Transport and deposition behaviour of model slurries in closed pipe flow

Hugh Patrick Rice

Submitted in accordance with the requirements
for the degree of Doctor of Philosophy

University of Leeds
School of Process, Environmental and Materials Engineering
Institute of Particle Science and Engineering

April 2013

Intellectual property and publication statements

The candidate confirms that the work submitted is his own and that appropriate credit has been given where reference has been made to the work of others.

Abstract

Suspensions of solid particles are ubiquitous in nature and industry. From sub-aqueous and aeolian dunes and ripples to plug flow in the minerals engineering industry, the complexity of the fluid dynamics and interparticle interactions in multiphase flow is such that specific applications require specific solutions.

The behaviour of suspensions of solid particles in a water carrier fluid in closed pipe flow is investigated over a range of flow regimes, from fully suspended, homogeneous flows to settled beds, using four particle species. The suspensions are intended to be simple analogues of more complex slurries that are encountered in the nuclear industry, the disposal and transport of which represent an ongoing challenge.

An off-the-shelf ultrasonic signal processing unit, with two ultrasonic transducers operating at 2 and 4 MHz, is used as both a Doppler velocimeter and an acoustic backscatter system. The results of a range of distinct measurements are presented. The effect of suspended particles of several types at several volume fractions on the first- and second-order flow statistics is described. The dependence of two critical velocities that delineate the homogeneous, heterogeneous and moving-bed flow regimes on the flow and particle properties is described, and the results are compared to two correlations of critical transport velocity in the literature. A model was developed to measure the scattering and attenuation properties of arbitrary solid particles in suspensions, and the measured values are incorporated into an inversion method in order to construct particle concentration profiles in pipe flow. Lastly, the behaviour of stable and time-dependent bedforms, which have been studied in natural and rectangular channels extensively, is investigated in closed pipe flow, and phase diagrams of bedform types are presented and compared with a similar diagram in the literature.

A full set of particle characterisation results is also presented in terms of size, density, shape and packing fraction, and the effect of the particle properties on the results is discussed in detail.

Table of contents

1 Background and introduction 1

1.1 Characteristics of UK nuclear industry radioactive waste 1

1.2 Objectives and overview of thesis 5

2 Literature review 8

2.1 Physical processes in insonified suspensions of particles 8

2.1.2 Regimes and dependences of scattering and absorption 11

2.2 Fluid mechanics of multiphase pipe flow 14

2.2.1 Coordinates, velocity and stress fields in turbulent pipe flow 14

2.2.2 Mean and turbulent velocities and Reynolds stresses 18

2.2.3 Turbulent scales 23

2.2.4 Basic multiphase flow parameters 26

2.2.5 Influence of suspended particles on multiphase flow 26

2.2.6 Slurries and high-concentration flows 31

2.2.7 Models and correlations of slurries and concentrated suspensions 33

2.3 Summary and identification of opportunities 36

3 Experimental method 38

3.1 Review and selection of measurement methods 38

3.2 Specification of flow loop and ultrasonic measurement system 43

3.2.1 Main flow loop 43

3.2.2 Basic operation of *UVP-DUO* ultrasonic measurement system 48

3.3 Data processing method 55

3.4 Choice of coordinate system and notation: reiteration 57

3.5 Selection and characterisation of particle species 58

3.5.1 Particle sizing 60

3.5.2 Particle density measurement 62

3.5.3 Packing fraction measurement 62
3.5.4 Determination of particle shape 63
3.5.5 Summary of particle characterisation studies 65
3.6 Calibration and data validation 67
3.6.1 Influence of suspended particles on sound speed 67
3.6.2 Consideration of flow parameters and instrumental resolution 70
3.6.3 Probe position calibration 72
3.6.4 Flow rate calibration 76
3.6.5 Statistical analysis and filtering of experimental data 79
3.6.6 Validation of single-phase data: inner variables and law of wall 83
3.7 Bed and shear layer thickness measurement 89
4 First- and second-order turbulence statistics and critical velocities in turbulent pipe flow 94
4.1 Experimental method 94
4.1.1 Decomposing velocity and stress components 95
4.1.2 Critical flow velocity 1, U_{c1} (homogeneous transition velocity) 96
4.1.3 Critical flow velocity 2, U_{c2} (limit deposition velocity) 97
4.2 Results and discussion 100
4.2.1 Homogeneous suspensions at low volume fractions 101
4.2.2 Homo- and heterogeneous suspensions at moderate volume fractions 107
4.2.3 Settling suspensions at low volume fractions 111
4.2.4 Heterogeneous and settling suspensions at high volume fractions 115
4.2.5 Summary: trends in first- and second-order flow statistics 121
4.2.6 Critical flow velocity 1, U_{c1} (homogeneous transition velocity) 124
4.2.7 Critical flow velocity 2, U_{c2} (limit deposition velocity) 127
4.3 Summary and conclusions 133

5 Concentration gradients in suspensions in closed pipe flow 135
5.1 Literature review: Thorne *et al.* model of backscatter strength 135
5.2 Homogeneous case: determination of backscatter and attenuation coefficients of arbitrary suspensions 138
5.2.1 Derivation 139
5.2.2 Testing for homogeneity in stirred mixing vessel 141
5.2.3 Measurements and results: attenuation constant, ξ_h 143
5.2.4 Measurements and results: combined backscatter and system constant, K_h 149
5.2.5 Discussion and summary: measured backscatter and attenuation coefficients 154
5.3 Heterogeneous case: measurement of the particle concentration profile using the dual-frequency inversion method 159
5.3.1 Derivation 159
5.3.2 Calculation of particle concentration profiles 162
5.3.3 Discussion: measured concentration profiles 174
6 Bedforms in closed pipe flow 178
6.1 Literature review: bedforms 178
6.1.1 Inception of particle motion and shear flow 179
6.1.2 Bedforms in natural systems and rectangular channels 184
6.1.3 Stability of plane beds and evolution of bedforms 188
6.1.4 Bedforms in closed conduits 191
6.1.5 Expected and observed differences between types of conduit 195
6.2 Experimental method 196
6.3 Results and discussion 197
6.3.1 Thickness of settled, upper plane beds and shear layers 198
6.3.2 Path-dependent behaviour of upper plane beds 201
6.3.3 Categorisation of observed bedforms 206

6.3.4 Hysteresis and ripple wash-out 211
6.3.5 Evolution and scaling of height and axial symmetry of time-dependent bedforms 215
6.3.6 Phase diagrams of bedforms in closed pipe flow 227
6.4 Summary and conclusions 237
7 Conclusions 239
7.1 Review of methods and results 239
7.1.1 Experimental method 239
7.1.2 Flow statistics, critical velocities and bed depth 240
7.1.3 Acoustic coefficients and concentration profiles 242
7.1.4 Universal scalings 243
7.2 Suggestions for future exploitation 244
8 References 249
A Appendix: Propagation of experimental errors 258
A.1 Beam divergence angle 258
A.2 Probe mounting angle 260
A.3 Speed of sound 261
A.4 Summary of uncertainties 263
A.5 Wall-normal distance 264
A.6 Mean axial velocity 266
A.7 Acoustic attenuation due to water 268
A.8 Discussion 269

List of figures

Figure 2-1: Attenuation spectra, normalised for particle mass concentration and path length, showing peaks for viscous absorption (peak to left of figure) and scattering (right). Note that solid black line is locus of viscous absorption peak, which shifts to higher particle sizes at higher frequencies. From Richards *et al.* (1996)..... 12

Figure 2-2: Diagram showing geometry of pipe flow, with notation for coordinates and velocity components used in this study shown..... 15

Figure 2-3: Stresses acting on a fluid element (Schlichting and Gersten, 2000) in Cartesian coordinate system, for illustration purposes. Note coordinates (x, y, z), and therefore shape of fluid element, differ from those used in this study (z, θ, y).18

Figure 2-4: Mean axial velocity relative to centreline value *vs.* distance from wall at two Reynolds numbers, Re = 50,000 and 500.000. Ordinate is equivalent to y/R in this study. From Laufer (1954). 21

Figure 2-5: Turbulence intensities *vs*. distance from wall. Solid, dashed and dotted lines correspond to axial, azimuthal and radial intensities in wall units, respectively, *i.e.* u'^{+}, v'^{+} and w'^{+} (Re = 44,000, numerical). Circles (Lawn, 1971) and diamonds (den Toonder and Nieuwstadt, 1997) are hot-wire and LDA experimental data at Re = 38,000 and 24,580, respectively. Ordinate is equivalent to $1 - r/R$ in this study. From Wu and Moin (2008)..... 22

Figure 2-6: Reynolds shear stress in z-r plane, nondimensionalised by shear velocity, $U\tau 2$, and double correlation coefficient, $u'w'$, at two Reynolds numbers, Re = 50,000 and 500,000; r' is radial distance from wall (*i.e.* y); a is pipe radius (R). From Laufer (1954). 22

Figure 2-7: Shape of mean axial flow velocity profile in multiphase pipe flow. (a) Three flow regimes with glass spheres (d = 2.07 mm, $\phi \approx 6$ %), where V_y/V_{max} corresponds to $U/Umax$ in this study, and C to ϕ. First frame: heterogeneous flow; second: flow with moving bed; third: flow with stationary bed. From Graf (1984), modified; (b) three flow rates with sand (d = 90 μm, ϕ = 19 %). From Gillies *et al.* (2004)..... 28

Figure 2-8: Reynolds stresses/RMS velocities *vs.* wall-normal distance, y/D, in multiphase pipe flow at five volume fractions; (a) mean and axial RMS velocities, u'

(upper frame) and w' (lower); (b) shear Reynolds stress, uw. Volume fraction c_v corresponds to ϕ in this study. Compiled from Zisselmar and Molerus (1979). 29
Figure 2-9: Turbulence intensity, $I = u'/U$, *vs*. distance from pipe centreline at Re = 29,100, with small plastic particles (d = 0.2 mm) at several mass loadings, m (ϕ_m in this study). From Tsuji and Morikawa (1982). 30
Figure 2-10: (a) Slurry flow regimes (Crowe, 2006); (b) homogeneous, moving bed and settled bed regimes in main flow loop, with Guyblast plastic beads (white bar in second frame is glare from lighting). 32
Figure 3-1: Main flow loop. (a) Diagram; (b) composite photograph. Inner diameter, D = 42.6 mm; entry length, L = 3.2 m. 45
Figure 3-2: Probe mounting geometry. (a) Diagram of probe arrangement; (b) photograph of probes attached to mounting clasp at 90 and 135 degrees to direction of mean flow. Inner pipe diameter, D = 42.6 mm; active transducer radii, a_t = 5 mm. 46
Figure 3-3: Geometry of sound field generated by a pulsed monostatic acoustic transducer. (a) View showing focal zone and near- and far-field regions. From *Met-Flow* (2002); (b) simpler view, in which T is transducer position and D is directivity, a measure of acoustic power, which varies with angle. From Hay and Sheng (1992). 49
Figure 3-4: Schematic diagram of measurement points. Distance to centre of measurement volume, *i.e.* distance to nominal measurement point, is r; distance between measurement points is s; width of each measurement volume is w. Minimum and maximum distances are r_0 and r_{max}, respectively. 53
Figure 3-5: Diagram showing geometry of pipe flow, with notation for coordinates and velocity components used in this study shown. Also shown in Figure 2-2. 57
Figure 3-6: Particle size distribution of Honite particle species. Data from *Mastersizer 2000*, Malvern Instruments..... 61
Figure 3-7: Particle size distribution of Guyblast particle species. Data from *Mastersizer 3000*, Malvern Instruments..... 61
Figure 3-8: Optical micrograph of Honite 22 glass spheres. 63
Figure 3-9: Optical micrograph of Honite 16 glass spheres. 64
Figure 3-10: Optical micrograph of Guyblast 40/60 plastic beads. 64
Figure 3-11: Optical micrograph of Guyblast 30/40 plastic beads. 65

Figure 3-12: Diagram of geometry used in calibration of probe position, where a_{off} is an offset distance, y is wall-normal distance, y' is distance measured along probe axis, ψ is angle between flow direction and probe axis and c is a reference distance (R or D). 73
Figure 3-13: RMS echo voltage profile with Guyblast 40/60 at Q = 3.08 l s^{-1} and ϕ = 0.01 %. Position of opposite (lower) pipe wall is shown by a vertical dashed line at measurement channel 121. 74
Figure 3-14: Mean Doppler velocity profile along probe axis with Guyblast 40/60 at Q = 2.68 l s^{-1} and ϕ = 0.01 %. Position of peak in profile (assumed to coincide with centreline of pipe) is shown by a vertical dashed line at measurement channel 90. 75
Figure 3-15: Diagram illustrating flow rate calibration method. First frame shows geometry in y-r plane; second frame is mean axial velocity profile. 77
Figure 3-16: Normality, P, of on-axis mean axial velocity *vs.* measurement channel number for Honite 22 at Q = 3.63 l s^{-1} and ϕ = 0.1 %. Solid and dashed lines are velocity data before and after application of a three-sigma noise filter, respectively. Dashed-dotted line corresponds to P = 1, for reference. 80
Figure 3-17: Histogram of instantaneous on-axis velocity at measurement channel 80 (d = 31.3 mm) for Honite 22 at Q = 3.63 l s^{-1} and ϕ = 0.1 %. Histogram consists of on-axis velocity time-series data and dashed line to a normal fit of data. Dashed-dotted vertical lines correspond to filter window, $\mu \pm 3\sigma$. 81
Figure 3-18: Normality P of on-axis mean axial velocity *vs.* measurement channel number for Guyblast 30/40 at Q = 1.68 l s^{-1} and ϕ = 1 %. Solid and dashed lines: data before and after application of 3σ noise filter. Dashed-dotted line corresponds to P = 1. 82
Figure 3-19: Histogram of instantaneous on-axis velocity at measurement channel 80 (y = 31.3 mm) for Guyblast 30/40 at Q = 1.68 l s^{-1} and ϕ = 1 %. Dashed line: normal fit of data; dashed-dotted vertical lines: filter window at $\mu \pm 3\sigma$. 83
Figure 3-20: Schematic of regions and layers in pipe and channel flows where $R^+ = RU_\tau/\nu$. From Wosnik *et al.* (2000). 85
Figure 3-21: Near-wall axial velocity in pipe flow in linear units at two Reynolds numbers. R is Reynolds number, Re; U is mean axial velocity, U, and U_0 is maximum value thereof at pipe centreline, $Umax$; r'/a is dimensionless wall-normal distance

from upper pipe wall, y/R. From Laufer (1954). 86
Figure 3-22: Friction factor, f, *vs*. Reynolds number, Re. Dashed line: correlation used in this study (Haaland, 1983); crosses: den Toonder and Nieuwstadt (1997); circles: McKeon *et al*. (2004b); triangles: Wu and Moin (2008)..... 87
Figure 3-23: Near-wall velocity profile in wall units with Honite 22 at ϕ = 0.01 % and Q = 3.56 l s^{-1}. Dashed-dotted line: ideal behaviour in linear region; dashed line: that in log-law region. "Plus" symbols are correct data; crosses and stars are same data with distance calibration point (*i.e.* peak velocity position) modified by ±3 measurement points (±1.11 mm) from correct position, respectively..... 88
Figure 3-24: Bed geometry and definitions. H and h are fluid and bed depths, respectively; R and D are pipe radius and diameter; θ is angle subtended by bed at pipe centre; and c is chord length (*i.e.* bed width at top of bed)..... 90
Figure 3-25: Echo amplitude showing peaks at three flow rates. Run 1 (solid line): high Q, fully suspended (peak at measurement channel 111); run 2 (dashed): shear layer present (peak: 62); run 3 (dotted): stop-flow run, Q = 0, with settled bed (peak: 84). Runs 2 and 3 also shown in Figure 6-8..... 92
Figure 4-1: Bed geometry and definitions. H and h are fluid and bed depths, respectively; R and D are pipe radius and diameter; θ is angle subtended by bed at pipe centre; and c is chord length (*i.e.* bed width at top of bed). Also shown in Figure 3-24 in general methodology (Section 3.7) 98
Figure 4-2: Mean velocity relative to average (bulk) value vs. wall-normal distance from upper pipe wall with Honite 22, Re = 53,000, U_{ave} = 1.24 m s^{-1}, ϕ = 0.01 %; pluses, DNS results of Wu and Moin (2008) at Re = 44,000.....103
Figure 4-3: (a) Mean velocity relative to maximum (*i.e.* centreline) value *vs*. wall-normal distance from upper pipe wall; (b) Reynolds shear stress in wall units; with Guyblast 40/60, Re = 107,000, U_{ave} = 2.50 m s^{-1}, ϕ = 0.1 %; crosses in (a), Pitot-probe results of McKeon *et al*. (2004a) at Re = 75,000; pluses in (b), hot-wire results of Laufer (1954) at Re = 50,000. 105
Figure 4-4: (a) Axial RMS velocity in wall units *vs.* wall-normal distance from upper pipe wall; (b) radial RMS velocity in wall units; with Guyblast 40/60, Re = 107,000, U_{ave} = 2.50 m s^{-1}, ϕ = 0.1 %; dashed line in (a), hot-wire results of Perry *et al.* (1986) at Re = 75,000; dashed line in (b) hot-wire results of Laufer (1954) at Re = 50,000.....106

Figure 4-5: (a) Mean velocity relative to maximum (*i.e.* centreline) value *vs.* wall-normal distance from upper pipe wall; (b) Reynolds shear stress in wall units; with Guyblast 30/40, Re = 49,700, U_{ave} = 1.17 m s^{-1}, ϕ = 0.5 %; pluses in (a), hot-wire results of Laufer (1954) at Re = 50,000; crosses in (b), DNS results of Wu and Moin (2008) at Re = 44,000.....109
Figure 4-6: (a) Axial RMS velocity in wall units *vs.* wall-normal distance from upper pipe wall; (b) radial RMS velocity in wall units; with Guyblast 30/40, Re = 49,700, U_{ave} = 1.17 m s^{-1}, ϕ = 0.5 %; dashed line in (a), hot-wire results of Morrison *et al.* (2004) at Re = 55,000; dashed line in (b) DNS results of Wu and Moin (2008) at Re = 44,000.....110
Figure 4-7: (a) Mean velocity relative to maximum (*i.e.* centreline) value *vs.* wall-normal distance from upper pipe wall; (b) Reynolds shear stress in wall units; with Honite 22, Re = 26,100, U_{ave} = 0.612 m s^{-1}, ϕ = 0.1 %; pluses in both frames, LDA results of den Toonder and Nieuwstadt (1997) at Re = 24,600.....113
Figure 4-8: (a) Axial RMS velocity in wall units *vs.* wall-normal distance from upper pipe wall; (b) radial RMS velocity in wall units; with Honite 22, Re = 26,100, U_{ave} = 0.621 m s^{-1}, ϕ = 0.1 %; dashed line in (a), Pitot-probe results of Zagarola and Smits (1998) at Re = 25,000; crosses in (b), LDA results of den Toonder and Nieuwstadt (1997) at Re = 24,600.....114
Figure 4-9: Axial RMS velocity *vs.* wall-normal distance, with Honite 16, Re = 25,000, U_{ave} = 0.587 m s^{-1}, ϕ = 3 %; dashed lined, Pitot-probe results of Zagarola and Smits (1998) at Re = 25,000.....115
Figure 4-10: Mean velocity relative to maximum (*i.e.* centreline) value *vs.* wall-normal distance from upper pipe wall, with Honite 16, ϕ = 3 %, (a) Re = 25,000, U_{ave} = 0.587 m s^{-1}, (b) Re = 104,000, U_{ave} = 2.43 m s^{-1}; crosses in both frames, hot-wire results of Laufer (1954) at Re = 50,000.....118
Figure 4-11: (a) Mean velocity relative to maximum (*i.e.* centreline) value *vs.* wall-normal distance from upper pipe wall; (b) Reynolds shear stress in wall units; with Guyblast 30/40, ϕ = 1 %, Re = 24,300, U_{ave} = 0.570 m s^{-1} (solid lines) and Re = 102,000, U_{ave} = 2.38 m s^{-1} (dashed lines).....119
Figure 4-12: (a) Axial RMS velocity in wall units *vs.* wall-normal distance from upper pipe wall; (b) radial RMS velocity in wall units; with Guyblast 30/40, ϕ = 1 %, Re = 24,300, U_{ave} = 0.570 m s^{-1} (solid lines, "low *Q*") and 102,000, U_{ave} = 2.38 m s^{-}

[1] (dashed lines, "high Q")....120
Figure 4-13: Axial turbulence intensity, I, *vs*. wall-normal distance, with Honite 22 glass spheres at three nominal volume concentrations; solid line: ϕ = 0.01 %, dashed line: ϕ = 0.5 %, dashed-dotted line: ϕ = 3 %. 122
Figure 4-14: Axial turbulence intensity, I, *vs*. wall-normal distance, with Guyblast 30/40 at Re ≈ 88,000, U_{ave} ≈ 2.1 m s^{-1} and three nominal volume concentrations; solid line: ϕ = 0.01 %, dashed line: ϕ = 0.5 %, dashed-dotted line: ϕ = 3 %. 123
Figure 4-15: Shift in position of peak in mean axial velocity, $Umax$, *vs.* bulk flow velocity, U_{ave}, for Honite 22 glass spheres at three nominal volume fractions, ϕ..124
Figure 4-16: Shift in position of peak in mean axial velocity, $Umax$, *vs.* bulk flow velocity, U_{ave}, for Honite 16 glass spheres at three nominal volume fractions, ϕ..125
Figure 4-17: Shift in position of peak in mean axial velocity, $Umax$, *vs.* bulk flow velocity, U_{ave}, for Guyblast 40/60 plastic beads at three nominal volume fractions, ϕ....126
Figure 4-18: Shift in position of peak in mean axial velocity, $Umax$, *vs.* bulk flow velocity, U_{ave}, for Guyblast 30/40 plastic beads at three nominal volume fractions, ϕ....126
Figure 4-19: Bed depth, h, *vs.* bulk flow velocity, U_{ave}, with Honite 22 at nominal volume fraction of ϕ = 0.5 %. 127
Figure 4-20: Bed depth, h, *vs.* bulk flow velocity, U_{ave}, with Honite 16 at nominal volume fraction of ϕ = 3 %.....128
Figure 4-21: Bed depth, h, *vs.* bulk flow velocity, U_{ave}, with Guyblast 40/60 at nominal volume fraction of ϕ = 0.5 %. 128
Figure 4-22: Bed depth, h, *vs.* bulk flow velocity, U_{ave}, with Guyblast 30/40 at nominal volume fraction of ϕ = 3 %. 129
Figure 4-23: Critical flow velocity, U_{c2}, *vs*. nominal volume fraction of suspended solids for four particle species. 130
Figure 5-1: Stirred mixing vessel, diagram (a) and photograph (b). Probes were positioned at about 50 mm from, and perpendicular to, base. 141
Figure 5-2: Sampled *vs*. weighed (nominal) concentration by mass of all particle species in stirred mixing vessel....142
Figure 5-3: G *vs.* distance from 4 MHz probe with Honite 22 at two mean concentrations, M_w = 2.41 and 122 kg m^{-3}. Dashed lines through data are linear fits.

Dot-dashed vertical lines indicate region over which gradients were calculated (measurement channels 60 to 120, or $r \approx 24$ to 46 mm).....145
Figure 5-4: Gradient of G with respect to distance from probe *vs.* weighed concentration by mass, M_w, of Honite 22 in stirred mixing vessel at ultrasonic frequencies of $f = 2$ and 4 MHz.....145
Figure 5-5: G *vs.* distance from 4 MHz probe with Honite 16 at two mean concentrations, $M_w = 2.50$ and 122 kg m^{-3} in stirred mixing vessel. Dashed lines through data are linear fits. Dot-dashed vertical lines indicate region over which gradients were calculated (measurement channels 60 to 120, or $r = 24$ to 46 mm).
.....146
Figure 5-6: Gradient of G with respect to distance from probe *vs.* weighed concentration by mass, M_w, of Honite 16 in stirred mixing vessel at ultrasonic frequencies of $f = 2$ and 4 MHz.....146
Figure 5-7: G *vs.* distance from 4 MHz probe with Guyblast 40/60 at two mean concentrations, $M_w = 1.50$ and 14.7 kg m^{-3} in stirred mixing vessel. Dashed lines through data are linear fits. Dot-dashed vertical lines indicate region over which gradients were calculated (measurement channels 60 to 120, or $r = 24$ to 46 mm).
.....147
Figure 5-8: Gradient of G with respect to distance from probe *vs.* weighed concentration by mass, M_w, of Guyblast 40/60 in stirred mixing vessel at ultrasonic frequencies of $f = 2$ and 4 MHz.....147
Figure 5-9: G *vs.* distance from 4 MHz probe with Guyblast 30/40 at two mean concentrations, $M_w = 1.50$ and 14.7 kg m^{-3} in stirred mixing vessel. Dashed lines through data are linear fits. Dot-dashed vertical lines indicate region over which gradients were calculated (measurement channels 60 to 120, or $r = 24$ to 46 mm).
.....148
Figure 5-10: Gradient of G with respect to distance from probe *vs.* weighed concentration by mass, M_w, of Guyblast 30/40 in stirred mixing vessel at ultrasonic frequencies of $f = 2$ and 4 MHz.....148
Figure 5-11: Variation of combined backscatter and system constant, K_h, with distance from probe at $M_w = 12.2$ kg m^{-3} for Honite 22 plastic beads at ultrasonic frequencies of $f = 2$ and 4 MHz in stirred mixing vessel. Relative standard deviation, 2.2 and 2.4 %, respectively.....150

Figure 5-12: Distance-averaged mean of combined backscatter and system constant, K_h, *vs.* weighed concentration by mass, M_w, for Honite 22 glass spheres at ultrasonic frequencies of f = 2 and 4 MHz in stirred mixing vessel.....150
Figure 5-13: Variation of combined backscatter and system constant, K_h, with distance from probe at M_w = 12.2 kg m^{-3} for Honite 16 plastic beads at ultrasonic frequencies of f = 2 and 4 MHz in stirred mixing vessel. Relative standard deviation, 3.0 and 1.5 % respectively.....151
Figure 5-14: Distance-averaged mean of combined backscatter and system constant, K_h, *vs.* weighed concentration by mass, M_w, for Honite 16 glass spheres at ultrasonic frequencies of f = 2 and 4 MHz in stirred mixing vessel.....151
Figure 5-15: Variation of combined backscatter and system constant, K_h, with distance from probe at M_w = 7.38 kg m^{-3} for Guyblast 40/60 plastic beads at ultrasonic frequencies of f = 2 and 4 MHz in stirred mixing vessel. Relative standard deviation, 9.4 and 4.4 %, respectively. 152
Figure 5-16: Distance-averaged mean of combined backscatter and system constant, K_h, *vs.* weighed concentration by mass, M_w, for Guyblast 40/60 glass spheres at ultrasonic frequencies of f = 2 and 4 MHz in stirred mixing vessel.....152
Figure 5-17: Variation of combined backscatter and system constant, K_h, with distance from probe at M_w = 7.40 kg m^{-3} for Guyblast 30/40 plastic beads at ultrasonic frequencies of f = 2 and 4 MHz in stirred mixing vessel. Relative standard deviation, 8.2 and 3.5 %, respectively. 153
Figure 5-18: Distance-averaged mean of combined backscatter and system constant, K_h, *vs.* weighed concentration by mass, M_w, for Guyblast 30/40 glass spheres at ultrasonic frequencies of f = 2 and 4 MHz in stirred mixing vessel.....153
Figure 5-19: Concentration by mass, M, *vs.* vertical distance from upper pipe wall with Honite 22 glass spheres, ϕ = 0.1 %; M_w = 2.50 kg m^{-3}; runs 1, 2 and 3 with M_s = 2.73, 3.32 and 2.28 kg m^{-3} at Q = 3.62, 1.78 and 0.874 l s^{-1}, respectively. 166
Figure 5-20: Concentration by mass, M, *vs.* vertical distance from upper pipe wall with Honite 22 glass spheres, ϕ = 0.5 %; M_w = 12.4 kg m^{-3}; runs 1, 2 and 3 with M_s = 13.9, 13.4 and 12.0 kg m^{-3} at Q = 3.60, 1.78 and 0.862 l s^{-1}, respectively. 166
Figure 5-21: Concentration by mass, M, *vs.* vertical distance from upper pipe wall with Honite 22 glass spheres, ϕ = 1 %; M_w = 24.7 kg m^{-3}; runs 1, 2 and 3 with M_s = 27.6, 27.4 and 24.3 kg m^{-3} at Q = 3.57, 1.77 and 0.866 l s^{-1}, respectively. 167

Figure 5-22: Concentration by mass, M, *vs.* vertical distance from upper pipe wall with Honite 22 glass spheres, ϕ = 3 %; M_w = 72.8 kg m^{-3}; runs 1, 2 and 3 with M_s = 81.5, 79.9 and 67.0 kg m^{-3} at Q = 3.50, 1.75 and 0.856 l s^{-1}, respectively. 167
Figure 5-23: Concentration by mass, M, *vs.* vertical distance from upper pipe wall with Honite 16 glass spheres, ϕ = 0.1 %; M_w = 2.50 kg m^{-3}; runs 1, 2 and 3 with M_s = 3.00, 2.60 and 1.82 kg m^{-3} at Q = 3.54, 1.75 and 0.851 l s^{-1}, respectively. 168
Figure 5-24: Concentration by mass, M, *vs.* vertical distance from upper pipe wall with Honite 16 glass spheres, ϕ = 0.5 %; M_w = 12.4 kg m^{-3}; runs 1, 2 and 3 with M_s = 14.5, 13.6 and 7.30 kg m^{-3} at Q = 3.48, 1.72 and 0.841 l s^{-1}, respectively. 168
Figure 5-25: Concentration by mass, M, *vs.* vertical distance from upper pipe wall with Honite 16 glass spheres, ϕ = 1 %; M_w = 24.7 kg m^{-3}; runs 1, 2 and 3 with M_s = 26.6, 20.9 and 10.9 kg m^{-3} at Q = 3.50, 1.73 and 0.851 l s^{-1}, respectively. 169
Figure 5-26: Concentration by mass, M, *vs.* vertical distance from upper pipe wall with Honite 16 glass spheres, ϕ = 3 %; M_w = 72.8 kg m^{-3}; runs 1, 2 and 3 with M_s = 75.9, 54.8 and 28.2 kg m^{-3} at Q = 3.47, 1.71 and 0.838 l s^{-1}, respectively. 169
Figure 5-27: Concentration by mass, M, *vs.* vertical distance from upper pipe wall with Guyblast 40/60 plastic beads, ϕ = 0.1 %; M_w = 1.50 kg m^{-3}; runs 1, 2 and 3 with M_s = 1.68, 1.44 and 1.95 kg m^{-3} at Q = 3.57, 1.76 and 0.858 l s^{-1}, respectively. 170
Figure 5-28: Concentration by mass, M, *vs.* vertical distance from upper pipe wall with Guyblast 40/60 plastic beads, ϕ = 0.5 %; M_w = 7.46 kg m^{-3}; runs 1, 2 and 3 with M_s = 7.80, 6.71 and 4.80 kg m^{-3} at Q = 3.54, 1.75 and 0.855 l s^{-1}, respectively. 170
Figure 5-29: Concentration by mass, M, *vs.* vertical distance from upper pipe wall with Guyblast 40/60 plastic beads, ϕ = 1 %; M_w = 14.9 kg m^{-3}; runs 1, 2 and 3 with M_s = 16.9, 17.3 and 11.3 kg m^{-3} at Q = 3.52, 1.73 and 0.838 l s^{-1}, respectively. 171
Figure 5-30: Concentration by mass, M, *vs.* vertical distance from upper pipe wall with Guyblast 40/60 plastic beads, ϕ = 3 %; M_w = 43.7 kg m^{-3}; runs 1, 2 and 3 with M_s = 46.9, 40.5 and 21.4 kg m^{-3} at Q = 3.51, 1.72 and 0.826 l s^{-1}, respectively. 171
Figure 5-31: Concentration by mass, M, *vs.* vertical distance from upper pipe wall with Guyblast 30/40 plastic beads, ϕ = 0.1 %; M_w = 1.50 kg m^{-3}; runs 1, 2 and 3 with M_s = 2.15, 1.14 and 0.553 kg m^{-3} at Q = 3.46, 1.71 and 0.836 l s^{-1}, respectively. 172

Figure 5-32: Concentration by mass, M, *vs.* vertical distance from upper pipe wall with Guyblast 30/40 plastic beads, ϕ = 0.5 %; M_w = 7.46 kg m^{-3}; runs 1, 2 and 3 with M_s = 8.25, 5.49 and 4.01 kg m^{-3} at Q = 3.39, 1.67 and 0.812 l s^{-1}, respectively. 172
Figure 5-33: Concentration by mass, M, *vs.* vertical distance from upper pipe wall with Guyblast 30/40 plastic beads, ϕ = 1 %; M_w = 14.9 kg m^{-3}; runs 1, 2 and 3 with M_s = 16.1, 11.2 and 7.56 kg m^{-3} at Q = 3.40, 1.68 and 0.812 l s^{-1}, respectively. 173
Figure 5-34: Concentration by mass, M, *vs.* vertical distance from upper pipe wall with Guyblast 30/40 plastic beads, ϕ = 3 %; M_w = 43.7 kg m^{-3}; runs 1, 2 and 3 with M_s = 45.5, 34.3 and 15.7 kg m^{-3} at Q = 3.37, 1.63 and 0.755 l s^{-1}, respectively. 173
Figure 6-1: Variant of Shields diagram. τ^* (*i.e.* θ_s) is Shields parameter and R_p (*i.e.* Re$_p$) is particle Reynolds number, as defined in Equation [6.3]. From García (2000). 180
Figure 6-2: Variation of particle concentration with bed height. Y/D (*i.e.* y/D) is distance from pipe bottom relative to pipe diameter. From Pugh and Wilson (1999). 182
Figure 6-3: Examples of Rousean concentration profiles in an open rectangular channel. C is particle concentration or volume fraction (*i.e.* M or ϕ) and C_a is a reference value at $y = a$. Note y is upwards distance from base, not downwards distance from upper wall as in this study. From Allen (1997). 183
Figure 6-4: Bedforms in open channels with a free water surface. F is Froude number (*i.e.* Fr, as defined in Equation [6.17]), and d is particle diameter. From García (2008). 184
Figure 6-5: Bedform phase diagram, with median particle diameter, d_{50}, and particle parameter, d^*, on x-axis and transport stage parameter, T, on y-axis. From van Rijn (1984b). 188
Figure 6-6: (a) Observed bedform types with glass and acrylic beads ("Batch A" and "Batch C", d = 132 and 193 μm), respectively, and (b) bedform phase diagram for pipe flow in terms of Reynolds number, Re$_{pipe}$, and Ga$(h_f/d)^2$ (*i.e.* Ga$(H/d)^2$ in this study). From Ouriemi *et al.* (2009) 194
Figure 6-7: Bedform evolution in terms of dimensionless bedform height *vs.* time, A/D (*i.e.* h_b/D) *vs.* Ut/D (*i.e.* $U_{ave}t/D$) for two runs. Circles: "vortex dunes"; squares: "small dunes". From Ouriemi *et al.* (2009), to which the reader is referred for more

materials and run information. 195
Figure 6-8: Bed/shear layer thickness *vs.* time (Q = 1.07 to 0.856 l s^{-1} at t = 0, ϕ = 3 %) with stop-flow run (to Q = 0 at $t \approx$ 475 s). Horizontal dashed line indicates mean over region shown. 198
Figure 6-9: Bed/shear layer thickness *vs.* time (Q = 0.856 to 0.609 l s^{-1} at t = 0, ϕ = 3 %) with stop-flow run (to Q = 0 at $t \approx$ 475 s). Horizontal dashed line indicates mean over region shown. 199
Figure 6-10: Bed/shear layer thickness *vs.* time (Q = 0.609 to 0.509 l s^{-1} at t = 0, ϕ = 3 %) with stop-flow run (to Q = 0 at $t \approx$ 475 s). Horizontal dashed line indicates mean over region shown 200
Figure 6-11: Bed/shear layer thickness *vs.* time (Q = 0.408 to 0.342 l s^{-1} at t = 0, ϕ = 3 %) with stop-flow run (to Q = 0 at $t \approx$ 475 s). Horizontal dashed line indicates mean over region shown 200
Figure 6-12: Bed/shear layer thickness *vs.* time (Q = 0.342 to 0.277 l s^{-1} at t = 0, ϕ = 3 %) with stop-flow run (to Q = 0 at $t \approx$ 1,150 s). Horizontal dashed line indicates mean over region shown 201
Figure 6-13: Shear layer and settled bed thickness *vs.* flow rate (ϕ = 3 %). Black circles (left axis): shear layer thickness; red triangles (right axis): settled bed thickness 201
Figure 6-14: Bed/shear layer thickness *vs.* time, showing path-dependent equilibration time (run 1: Q = 1.51 to 1.29 l s^{-1} at t = 0, run 2: Q = 2.66 to 1.29 l s^{-1} at t = 0, ϕ = 3 %). 202
Figure 6-15: Bed/shear layer thickness *vs.* time, showing path-dependent equilibration time (run 1: Q = 1.28 to 1.07 l s^{-1} at t = 0, run 2: Q = 2.66 to 1.07 l s^{-1} at t = 0, ϕ = 3 %). 203
Figure 6-16: Bed/shear layer thickness *vs.* time, showing path-dependent equilibration time (run 1: Q = 1.07 to 0.856 l s^{-1} at t = 0, run 2: Q = 2.66 to 0.856 l s^{-1} at t = 0, ϕ = 3 %). 203
Figure 6-17: Bed/shear layer thickness *vs.* time, showing path-dependent equilibration time (run 1: Q = 0.856 to 0.609 l s^{-1} at t = 0, run 2: Q = 2.66 to 0.609 l s^{-1} at t = 0, ϕ = 3 %). 204
Figure 6-18: Bed/shear layer thickness *vs.* time, showing path-dependent equilibration time (run 1: Q = 0.609 to 0.509 l s^{-1} at t = 0, run 2: Q = 2.66 to 0.509 l

s^{-1} at t = 0, ϕ = 3 %). 205
Figure 6-19: Bed/shear layer thickness *vs.* time, showing path-dependent equilibration time (run 1: Q = 0.509 to 0.408 l s^{-1} at t = 0, run 2: Q = 2.66 to 0.408 l s^{-1} at t = 0, ϕ = 3 %). 205
Figure 6-20: Bed/shear layer thickness *vs.* time, showing path-dependent equilibration time (run 1: Q = 0.408 to 0.342 l s^{-1} at t = 0, run 2: Q = 2.66 to 0.342 l s^{-1} at t = 0, ϕ = 3 %). 206
Figure 6-21: Bed geometry and definitions. H and h are fluid and bed depths, respectively; R and D are pipe radius and diameter; θ is angle subtended by bed at pipe centre; and c is chord length (*i.e.* bed width at top of bed). Also shown in Figure 3-24 in general methodology (Section 3.7). 207
Figure 6-22: Bedform geometry and evolution. H and h are fluid and bed depths, respectively, with $h = h_b + h_s$, where h_b and h_s are the bedform height and settled bed depth, respectively; R and D are pipe radius and diameter; t_i is period between adjacent peak and trough. 208
Figure 6-23: Bed thickness *vs.* time: shallow, regular ripples (Q = 0.498 to 0.403 l s^{-1} at t = 0, ϕ = 0.1 %). 208
Figure 6-24: Bed thickness *vs.* time: ripples of increasing period (Q = 0.483 to 0.323 l s^{-1} at t = 0, ϕ = 0.5 %). 209
Figure 6-25: Bed thickness *vs.* time: unstable/chaotic ripples (Q = 0.383 to 0.287 l s^{-1} at t = 0, ϕ = 1 %). 210
Figure 6-26: Histogram of ripple frequencies from Figure 6-25 (Q = 0.383 to 0.287 l s^{-1} at t = 0, ϕ = 1 %). 210
Figure 6-27: Bed thickness *vs.* time, showing hysteresis behaviour, (a) Q = 0.483 to 0.323 l s^{-1} at t = 0, (b) Q = 0.323 to 0.483 l s^{-1} at t = 0 ($|\Delta Q|$ = 0.160 l s^{-1}, ϕ = 0.5 %). Runs were performed concurrently. 213
Figure 6-28: Bed thickness *vs.* time, showing hysteresis behaviour, (a) Q = 0.342 to 0.277 l s^{-1} at t = 0, (b) Q = 0.277 to 0.342 l s^{-1} at t = 0 ($|\Delta Q|$ = 0.065 l s^{-1}, ϕ = 3 %). Runs were *not* performed concurrently. 214
Figure 6-29: Total bed thickness, h, for case of bedform field of regular period (Q = 0.498 to 0.402 l s^{-1} at t = 0, ϕ = 0.1 %). Circles indicate local minima and maxima (*i.e.* peaks and troughs) 216
Figure 6-30: Total bed thickness, h, for case of bedform field of increasing period

(Q = 0.483 to 0.323 l s^{-1} at t = 0, ϕ = 0.5 %). Circles indicate local minima and maxima (*i.e.* peaks and troughs). 217
Figure 6-31: Total bed thickness, h, for case of chaotic, unstable bedform field (Q = 0.383 to 0.287 l s^{-1} at t = 0, ϕ = 1 %). Circles indicate local minima and maxima (*i.e.* peaks and troughs). Time period was chosen to show ripples on dunes. 218
Figure 6-32: Scaling and evolution of bedform height, h_b, relative to (a) pipe diameter, D, and (b) fluid height, H, *vs.* (a) dimensionless time variable, $U_{ave}t/D$, and (b) time, t, for case of bedform field of regular period (Q = 0.498 to 0.402 l s^{-1} at t = 0, ϕ = 0.1 %). 220
Figure 6-33: Scaling and evolution of bedform height, h_b, relative to (a) pipe diameter, D, and (b) fluid height, H, *vs.* (a) dimensionless time variable, $U_{ave}t/D$, and (b) time, t, for case of bedform field of increasing period (Q = 0.483 to 0.323 l s^{-1} at t = 0, ϕ = 0.5 %) 221
Figure 6-34: Scaling and evolution of bedform height, h_b, relative to (a) pipe diameter, D, and (b) fluid height, H, *vs.* (a) dimensionless time variable, $U_{ave}t/D$, and (b) time, t, for case of chaotic, unstable bedform field (Q = 0.383 to 0.287 l s^{-1} at t = 0, ϕ = 1 %) 222
Figure 6-35: Illustration of a suggested universal scaling for closed-conduit flows of any cross-sectional shape. 224
Figure 6-36: Bedform asymmetry factor, f_b, for case of bedform field of regular period (Q = 0.498 to 0.402 l s^{-1} at t = 0, ϕ = 0.1 %). 226
Figure 6-37: Bedform asymmetry factor, f_b, for case of bedform field of increasing period (Q = 0.483 to 0.323 l s^{-1} at t = 0, ϕ = 0.5 %). 227
Figure 6-38: Bedform asymmetry factor, f_b, for case of unstable, chaotic bedform field (Q = 0.383 to 0.287 l s^{-1} at t = 0, ϕ = 1 %). 227
Figure 6-39: Phase diagram of bedforms in pipe flow according to flow Reynolds number, Re_{flow}. Unfilled triangles: upper plane bed; stars: variable ripples; pluses: regular ripples; crosses: ripples with increasing period; filled triangles: no particle motion. Dashed lines indicate transitions between no particle motion, ripples and upper plane beds. 229
Figure 6-40: Phase diagram of bedforms in pipe flow according to Froude number, Fr. Unfilled triangles: upper plane bed; stars: variable ripples; pluses: regular ripples; crosses: ripples with increasing period; filled triangles: no particle motion.

Dashed lines indicate transitions between no particle motion, ripples and upper plane beds. 230
Figure 6-41: Phase diagram of bedforms in pipe flow according to bulk Reynolds number, Re_{pipe} *vs.* $Ga(H/d)^2$, as presented by Ouriemi *et al.* (2009). Unfilled triangles: upper plane bed; stars: variable ripples; pluses: regular ripples; crosses: ripples with increasing period; filled triangles: no particle motion. Dashed lines indicate transitions between no particle motion, ripples and upper plane beds. . 231
Figure 7-1: Probe mounting used by Admiral and García to investigate sand beds in a rectangular channel. "ACP" is an acoustic concentration profiler. 245
Figure A-1: Linear beam divergence from a point source, where r is distance from probe to measurement point, w is distance between measurement points, γ_0 is beam divergence angle, dr_1 is resulting uncertainty in r 259
Figure A-2: Mean axial flow velocity, U, *vs.* wall-normal distance, y, for example run (Honite 16, ϕ = 1%, Q = 1.72 l s^{-1}, U_{ave} = 1.21 m s^{-1}), with errors in y, dy, shown (horizontal bars). Note x-axis is truncated for better visualisation 265
Figure A-3: Mean axial flow velocity, U, *vs.* wall-normal distance, y, for example run (Honite 16, ϕ = 1%, Q = 1.72 l s^{-1}, U_{ave} = 1.21 m s^{-1}), with errors in U, dU, shown (vertical bars). Note x-axis is truncated for better visualisation. 267

List of tables

Table 1-1: Five examples of waste streams in the "sludges, flocs and liquids" category in the UK radioactive waste inventory (NDA, 2011, 2013). 4
Table 2-1: Classification of ultrasonic interactions with suspended particles. Adapted from several sources (Dukhin and Goetz, 2002; Shukla *et al.*, 2010; Thorne and Hanes, 2002). 11
Table 2-2: Summary of notation for coordinates and velocity/stress components used in this study. 17
Table 2-3: Single-phase and low-concentration pipe flow studies[1]. Reynolds number, Re, is defined in Equation [2.9] 20
Table 2-4: Important time- and length scales in multiphase flow. 24
Table 2-5: Flow regimes for suspensions of particles. Adapted from Poelma *et al.* (2007). 25
Table 2-6: Multiphase and high-concentration pipe and channel flow studies 27
Table 3-1: Comparison of characteristics of several common methods for measuring concentration, particle size, velocity and stresses in flows and suspensions. Adapted from Lemmin and Rolland (1997), Povey (1997) and Admiraal and García (2000); Laufer (1954) and Hultmark *et al.* (2012) also consulted as examples. 40
Table 3-2: Description of flow loop components and diagnostic equipment. See Figure 3-1 for photograph of flow loop and Figure 3-2 for photograph of transducer assembly 44
Table 3-3: Transducer dimensions and beam characteristics 50
Table 3-4: Flow chart summarising overall data processing method, with references to sections where each procedure is described in more detail. 55
Table 3-5: *UVP-DUO* gain settings. Provided by Olivier Mariette, *Met-Flow SA*, Switzerland 56
Table 3-6: Summary of notation for coordinates and velocity/stress components used in this study. Also shown in Table 2-2. 58
Table 3-7: Properties of particle species considered for or used in this study. 66
Table 3-8: Density and compressibility of Honite (soda-lime glass) and Guyblast (urea formaldehyde) particles, and sensitivity of sound velocity at two particle

concentrations. 69
Table 3-9: Turbulent time- and lengthscales and entry lengths for a range of flow conditions in main flow loop (D = 42.6 mm, with water). Values of L/D from Equation [3.26] (Shames, 2003). 70
Table 3-10: List of runs used for flow meter calibration. 78
Table 3-11: Flow regions near a boundary (Gad-el-Hak and Bandyopadhyay, 1994; Roberson and Crowe, 1996; Schlichting and Gersten, 2000). 84
Table 4-1: Summary of all experiments, a selection of which is presented in Sections 4.2.1 to 4.2.4 under four distinct themes. 100
Table 4-2: Run parameters* and sample results for flow-loop runs presented in Sections 4.2.1 to 4.2.4 and Figure 4-2 to Figure 4-12. 101
Table 4-3: Comparison of limit deposition velocity, U_{c2}, results with correlations of Poloski *et al.* (2010) for Honite (Equations [2.19] and [2.20]) and Oroskar and Turian (1980) for Guyblast (Equation [2.18]). 132
Table 5-1: Constant of proportionality and goodness of fit of sampled (M_s) *vs.* weighed (M_w) concentration by mass of all particle species in stirred mixing vessel. 142
Table 5-2: Comparison of predicted and measured values of sediment attenuation constant, ξ_h, and combined backscatter and system constant, K_h. Values of ka are also given. (All results are given to three significant figures.) 154
Table 5-3: Run parameters and sample results for flow-loop runs shown in Figure 5-19 to Figure 5-34. 163
Table 6-1: Classification of bedforms in open and closed channels. Adapted from Acaroglu (1968) and Graf (1984). 185
Table 6-2: Studies of bedforms in closed conduits. 193
Table 6-3: Categories of bed/bedform identified in this study. 211
Table 6-4: Summary of example runs investigated in this section. 215
Table 6-5: Summary of experimental parameters of runs used to construct phase diagrams. (Total: 58.) 233
Table A-1: List of temperature measurements over three days. Example run was performed on second day. 261
Table A-2: Summary of nominal values of measured quantities in example run, with corresponding uncertainties. All results for f = 2 MHz at T = 20 °C and P = 10^5

Pa, with Honite 16 glass spheres (d_{50} = 77.0 μm, ρ_s = 2.46 × 10^3 kg m^{-3}) at volume fraction ϕ = 1 %. 263

Nomenclature

Roman symbols		
Symbol	**Definition**	**Dimensions**
Variables		
a_{off}	Offset distance	L
a	Particle radius	L
a_t	Radius of active face of transducer	L
A_{bed}	Cross-sectional area occupied by bed	L^2
A_{flow}	Flow cross-sectional area	L^2
c	Chord length	L
	Speed of sound	$L\ T^{-1}$
C'	Particle Chézy coefficient	$L^{0.5}\ T^{-1}$
d, d_{50}, d_{90}	Particle diameter, 50th percentile, 90th percentile	L
d^*	Particle parameter	1
$\mathrm{d}c$	Total error in speed of sound, c	$L\ T^{-1}$
$\mathrm{d}c_1$	Error in c due to uncertainty in temperature, $\mathrm{d}T$	$L\ T^{-1}$
$\mathrm{d}c_2$	Error in c due to uncertainty in pressure, $\mathrm{d}P$	$L\ T^{-1}$
$\mathrm{d}r$	Total error in distance along probe axis, r	L
$\mathrm{d}r_1$	Error in r due to beam divergence	L
$\mathrm{d}r_2$	Error in r due to uncertainty in speed of sound, $\mathrm{d}c$	L
$\mathrm{d}y$	Total error in wall-normal distance, y	L
$\mathrm{d}y_1$	Error in y due to error in distance along probe axis, $\mathrm{d}r$	L
$\mathrm{d}y_2$	Error in y due to uncertainty in mounting angle, $\mathrm{d}\psi$	L
$\mathrm{d}\overline{U}$	Total error in mean axial velocity, $\overline{U}$	$L\ T^{-1}$
$\mathrm{d}\overline{U}_1$	Error in $\overline{U}$ due to uncertainty in mounting angle, $\mathrm{d}\psi$	$L\ T^{-1}$
$\mathrm{d}\overline{U}_2$	Error in $\overline{U}$ due to error in speed of sound, $\mathrm{d}c$	$L\ T^{-1}$
$\mathrm{d}\alpha_w$	Total error in attenuation due to water, α_w	L^{-1}
$\mathrm{d}\psi$	Uncertainty in mounting angle, ψ	1
$\mathrm{d}P$	Uncertainty in pressure, P	$M\ L^{-1}\ T^{-2}$
$\mathrm{d}T$	Uncertainty in temperature, T	K
D	Pipe/conduit inner diameter	L
	Transducer directivity (as D^2)	1
E	Elastic (Young's) modulus	$M\ L^{-1}\ T^{-2}$
	Raw echo amplitude	1

Roman symbols		
Symbol	**Definition**	**Dimensions**
E_{inst}	Instantaneous raw echo amplitude	V
f	Ultrasonic frequency	T^{-1}
	Darcy friction factor	1
	Particle form factor	1
	Frame size in polynomial filter algorithm	1
f_b	Bedform asymmetry factor	1
f_r	Doppler-shifted frequency	T^{-1}
F	Sampling/pulse repetition frequency	T^{-1}
g	Acceleration due to gravity	$L\ T^{-2}$
G	Range-corrected echo amplitude	-
h	Total bed depth	L
h_b	Bedform height	L
h_e	Equivalent total bed depth	L
h_s	Settled bed depth	L
h_v	Void fraction	1
H	Fluid depth	L
H_e	Equivalent fluid depth	L
I	Turbulence intensity	1
k	Wavenumber	L^{-1}
	Polynomial order in polynomial filter algorithm	1
k_s	Solid phase backscatter constant	$L\ M^{-1/2}$
k_t	Measurement system constant	$V\ L^{3/2}$
K	Bulk modulus	$M\ L^{-1}\ T^{-2}$
K_h	Combined scattering and system constant	$V\ L^{1/2}\ M^{-1/2}$
l_e	Integral lengthscale	L
L	Entry length for fully developed turbulent pipe flow	L
m	Minimum peak separation in peak-finding algorithm	1
M, M_s, M_w	Solid phase concentration by mass, sampled, weighed	$M\ L^{-3}$
n	Number of samples	1
N	Number of cycles per ultrasonic pulse	1
N_d	Quantisation/digitisation constant	1
p	Particle packing fraction	1
	Proportion of statistical outliers	1

Roman symbols		
Symbol	**Definition**	**Dimensions**
P	Pressure	M L^{-1} T^{-2}
	Ratio of observed to expected proportion of statistical outliers	1
Q, Q_i, Q_f	Volumetric flow rate, initial, final	L^3 T^{-1}
r	Distance from transducer along its axis	L
	Radial coordinate/distance from pipe centreline	L
r_0	Minimum measurable distance	L
r_f	Transducer focal distance	L
r_{max}	Maximum measurable distance	L
r_n	Transducer near-field distance	L
R	Pipe/conduit radius	L
s	Separation between measurement channel volumes	L
	Specific gravity of solid phase	1
t	Time	T
t_{eq}	Bedform equilibration (lag) time	T
T	Transport stage parameter	1
u	Fluctuating component of axial flow velocity	L T^{-1}
u^+	Dimensionless mean axial velocity in wall units	1
u'	Root-mean-square (RMS) axial turbulent velocity	L T^{-1}
u_p	Characteristic particle velocity	L T^{-1}
$\overline{u^2}$	Axial Reynolds normal stress	L^2 T^{-2}
$\overline{uw}$	Axial-radial Reynolds shear stress	L^2 T^{-2}
U	Instantaneous axial flow velocity	L T^{-1}
U_{ave}	Bulk averaged axial flow velocity	L T^{-1}
U_{bw}	Velocity bandwidth	L T^{-1}
U_{c1}	Critical flow velocity 1: homogeneous transition velocity	L T^{-1}
U_{c2}	Critical flow velocity 2: limit deposition velocity	L T^{-1}
U_{flow}	Flow-area averaged axial flow velocity	L T^{-1}
U_p, U_{pi}	Instantaneous Doppler velocity measured along axis of transducer, with *i*th transducer	L T^{-1}
U_τ	Friction/shear velocity	L T^{-1}
U'_τ	Particle bed shear velocity	L T^{-1}
$U_{\tau,cr}$	Critical bed shear velocity	L T^{-1}

Roman symbols		
Symbol	**Definition**	**Dimensions**
$\overline{U}$	Time-averaged mean axial flow velocity	L T^{-1}
$\overline{U}_{max}$	Maximum mean axial flow velocity	L T^{-1}
v	Fluctuating component of azimuthal flow velocity	L T^{-1}
v'	Root-mean-square (RMS) azimuthal flow velocity	L T^{-1}
V	Root-mean-square (RMS) of received voltage, *i.e.* echo amplitude	V
	Instantaneous azimuthal flow velocity	L T^{-1}
V_{inst}	Instantaneous echo voltage	V
$\overline{V}$	Time-averaged mean azimuthal flow velocity	L T^{-1}
w	Fluctuating component of radial or wall-normal flow velocity	L T^{-1}
	Width of measurement volume	L
	Particle settling velocity	L T^{-1}
w'	Root-mean-square (RMS) radial or wall-normal flow velocity	L T^{-1}
$\overline{w^2}$	Radial or wall-normal Reynolds normal stress	L^2 T^{-2}
W	Instantaneous radial or wall-normal flow velocity	L T^{-1}
$\overline{W}$	Time-averaged mean radial or wall-normal flow velocity	L T^{-1}
y	Wall-normal distance/coordinate from upper pipe wall	L
y^+	Dimensionless distance from pipe wall in wall units	1
z	Axial (*i.e.* streamwise) distance/coordinate	L
	Dimensionless distance relative to focal distance, r_f	1
z_0	Bed roughness length	L
Dimensionless numbers		
Ar	Archimedes number	
Fr	Froude number	
Ga	Galilei number	
Re	Reynolds number	
Re*	Shear Reynolds number	
Re_{flow}	Flow Reynolds number	
Re_{pipe}	Bulk Reynolds number	
Re_p	Particle Reynolds number	
Ro	Rouse number	
St	Stokes number	

Greek symbols		
Symbol	**Definition**	**Units**
α	Total attenuation	L^{-1}
α_s	Attenuation due to solid phase	L^{-1}
α_w	Attenuation due to water	L^{-1}
γ_0	Beam divergence angle	1
δ	Lag between local sediment rate and velocity	L
	Mean distance between randomly distributed particles	L
δ_v	Viscous sublayer thickness	L
δh	Bed depth correction	L
Δf_r	Doppler shift	T^{-1}
Δf_{max}	Maximum measurable Doppler shift	T^{-1}
ε	Dissipation rate of turbulent kinetic energy per unit mass	$L^2\ T^{-3}$
	Roughness coefficient	L
η	Kolmogorov lengthscale	L
θ	Angle subtended by bed at pipe centre	1
	Azimuthal coordinate/angle	1
θ_s	Shields parameter	1
κ	Compressibility	$L\ T^2\ M^{-1}$
	Von Kármán constant	1
λ	Ultrasonic wavelength	L
μ	Dynamic viscosity	$M\ T^{-1}\ L^{-1}$
	Mean	-
ν	Kinematic viscosity	$L^2\ T^{-1}$
ξ	Sediment attenuation constant	$L^2\ M^{-1}$
ρ	Density	$M\ L^{-3}$
ρ_f	Density of fluid phase	$M\ L^{-3}$
ρ_s	Density of solid phase	$M\ L^{-3}$
σ	Poisson's ratio	1
	Standard deviation	-
τ	Stress	$M\ L^{-1}\ T^{-2}$
τ_b	Bed shear stress	$M\ L^{-1}\ T^{-2}$
$\tau_{b,cr}$	Critical bed shear stress	$M\ L^{-1}\ T^{-2}$
τ_c	Average time between particle-particle collisions	T
τ_I	Integral timescale	T

Greek symbols		
Symbol	**Definition**	**Units**
τ_p	Particle relaxation timescale	T
τ_K	Kolmogorov timescale	T
τ_w	Wall shear stress	M L^{-1} T^{-2}
ϕ	Volume fraction of solid phase	1
ϕ_m	Mass fraction of solid phase	1
χ	Normalised total scattering and absorption cross-section	1
	Hindered settling factor	1
ψ	Angle between transducer axis and mean flow axis	1
	Near-field correction factor	1
ω	Angular frequency	T^{-1}

Subscripts, superscripts, abbreviations and acronyms	
Symbol	**Definition**
Subscripts	
f	Fluid phase
h	Homogeneous case
s	Solid phase
w	Water
Superscripts	
+	Wall units (*i.e.* nondimensionalised using suitable combination of U_τ and ν)
Abbreviations and acronyms	
ABS	Acoustic backscatter system
ACP	Acoustic concentration profiler
ADV	Acoustic Doppler velocimetry
FFT	Fast Fourier transform
HLW	High-level (radioactive) waste
HWA/HFA	Hot wire/film anemometry
ILW	Intermediate-level (radioactive) waste
LLW	Low-level (radioactive) waste
LDA/LDV	Laser Doppler anemometry/velocimetry
NDA	Nuclear Decommissioning Authority (UK)
PIV	Particle image velocimetry
PSD	Particle size distribution

Subscripts, superscripts, abbreviations and acronyms	
Symbol	**Definition**
RCP	Random close packing
RMS	Root-mean-square
RSD	Relative standard deviation
SMV	Stirred mixing vessel
SSC	Suspended sediment concentration
UDV	Ultrasonic Doppler velocimetry

1 Background and introduction

A brief review of the characteristics of sludges and slurries held in the inventory of the UK nuclear industry is presented in Section 1.1. With these characteristics in mind, the objectives of this study are presented in Section 1.2, along with an outline of the thesis.

1.1 Characteristics of UK nuclear industry radioactive waste

The slurries that were used in this study were intended to be simple, non-active analogues of real slurries in the UK radioactive waste inventory, so it is important to estimate the range of particle properties present in the inventory. The principal properties to know are particle size, density, shape, elemental composition and concentration, and the geometry of storage and transport vessels and conduits. In this section, the composition of the UK radioactive waste inventory, as assessed by the Nuclear Decommissioning Authority (NDA), is described.

The NDA is a non-departmental public responsible for overseeing the operation and decommissioning of the UK's nuclear sites and publishes an inventory of the UK's radioactive waste every three years. The most recent, published in 2011, corresponds to the inventory as of April 2010 (NDA, 2011). There follows a short summary of the nature of the waste in the UK's inventory, particularly those containing liquids.

Radioactive waste is divided into three categories according to the level and type of activity: low-level waste (LLW) has an activity up to 4 GBq per tonne of alpha radiation or 12 GBq per tonne of beta and gamma activity (where one Becquerel, Bq, is one decay per second); intermediate-level waste (ILW) has an activity exceeding that of LLW but does "not require heating to be taken into account in the design of storage or disposal facilities"; high-level waste (HLW), however, has a sufficiently high activity that the associated temperature rise that it must "be taken into account in the design of storage or disposal facilities" (NDA, 2011).

The total volume of the UK inventory is 4,720,000 m^3 (5,000,000 tonnes), of which 93.9 % by volume is LLW (4,430,000 m^3), 6.1 % ILW (278,000 m^3) and less than 0.1 % HLW (1,020 m^3). In terms of activity, HLW accounts for 95 % of the total (84 × 10^6 TBq), ILW 5 % and LLW 0.00005 %.

As to the material composition of the waste, HLW consists exclusively of material generated by the reprocessing of nuclear fuel at Sellafield, but is outside the remit of this study as none is liquid or sludge. The majority of ILW is described as steel, graphite, concrete, cement, sand, sludge and flocs; LLW consists mainly of "building rubble, soil and steel". The only category of waste by composition that is of interest from the perspective of this study is "sludges, flocs and liquids" (the categories "other metals", "other organics", "other inorganics" and "unspecified", which may contain liquids, suspensions and slurries, are not considered here), which for ILW comprises 31,000 tonnes (10 % of all ILW by mass) and 11,000 tonnes for LLW (0.2 % by mass). According to the NDA (2011), "[m]ost sludge and floc waste is from the treatment of liquid effluents and from the corrosion of stored Magnox fuel cladding waste".

Magnox (a contraction of "magnesium non-oxidising") is an alloy, principally magnesium and aluminium – ρ = 1.738 and 2.698 g cm^{-3}, respectively (Kaye and Laby, 1995) – with smaller amounts of other metals, that was used as the cladding material around uranium fuel elements in Magnox reactors, a kind operated since the 1950s of which two operating units remain (both at Wylfa, north Wales). Very little specific physical properties are given for either ILW or LLW in the NDA inventory (NDA, 2011), so it is difficult to compose a summary, but it is reasonable to assume that any magnox fragments and other solids present in sludge-type waste have a large range of particle sizes, densities and shapes. A few randomly chosen examples of individual entries in the inventory that fall into the category of "sludges, flocs and liquids" are given in Table 1-1. It is clear that there is a large variety of substances present.

It should be noted, however, that the actual amount of waste that remains to be processed is likely to be smaller than given above because a proportion is

"conditioned". Conditioning is "immobilisation of radioactive waste in a suitable medium", such as cement, glass or a polymer, "to produce a solid and stable wasteform within a container" (NDA, 2011). Clearly, once conditioned, waste no longer needs to be transported hydraulically. Of ILW, 10 % by mass of unconditioned waste (of a total of 230,000 tonnes) is categorised as "sludges, flocs and liquids". Of LLW, 99.3 % is unconditioned (total: 78,000 tonnes), but the proportion comprising "sludges, flocs and liquids" is not given.

Hastings *et al.* (2007) have described the general issues relating to management of nuclear sludge, and a short summary follows.

- Monitoring, retrieval and processing of waste are difficult due to radioactivity.
- The quality of existing characterisation studies are limited due to radioactivity and heterogeneity, and waste processing must be able to deal with "unduly broad feed envelopes", *i.e.* a large range of physical properties.
- Retrofitting is difficult as it may require opening containment structures, and storage, transport and processing structures must be shielded against radiation.
- Unlike the minerals processing industry, in which continuous pumping of high-concentration slurries is preferable for economic reasons, in the nuclear industry safety, the ability to account for heterogeneity, minimise intervention and prevent blockages are the primary concerns.

It is with these challenges in mind – in terms of heterogeneity of physical properties, and the difficulties associated with access and characterisation – that the objectives of this study are described in more detail in the next section.

Table 1-1: Five examples of waste streams in the "sludges, flocs and liquids" category in the UK radioactive waste inventory (NDA, 2011, 2013).					
Decription (waste stream identifier)	Category	Site (owner)	Volume (m^3)	Composition	Bulk density (10^3 kg m^{-3})
Hydraulic fluid (2C08)	LLW	Chapelcross (NDA)	0.9	Water-glycol; traces of steel and other ferrous metals, aluminium and copper	1.0
Pond water filtration sludge (3K18)	ILW	Hartlepool (EDF Energy)	2.9	Sludge, filter sand and "precoat material"	~1.375
Contaminated solvent and oils (5B20)	LLW	Dounreay (NDA)	137.4	Toluene, paraffin, trichloroethane, trichloroethylene, other oils and solvents	0.97
Concrete slurry (9A933)	LLW	Berkeley (NDA)	1.2	Sludge from concrete cutting	~1.5
Magnox fuel element debris dust/sludge (9B66)	ILW	Bradwell (NDA)	8.3	Mainly magnesium hydroxide powder; also fuel fragments and fittings, nimonic springs, zirconium alloy, filter elements, spent ion exchange resin elements	0.62

1.2 Objectives and overview of thesis

The overall aim of this study was to address some fundamental difficulties that are encountered by the nuclear industry by investigating the settling and deposition behaviour of suspensions of dense particles in closed cylindrical pipes using ultrasonic methods, with a view to contributing predictive information – to the nuclear industry in particular, in which there is a particular problem with slurries and sludges containing dense particulates, the properties of which vary between sites and which are often difficult to characterise due to radioactivity – on fundamental properties such as the onset of deposition and resuspension. Ultrasonic measurement systems are ideal in such situations, as they are physically robust, portable, versatile and cost-effective.

Although focused on addressing challenges in the nuclear industry, the novel models and acoustic measurement methods presented in this study have a much wider range of potential applications: in any industrial situation where rapid, *in-situ* diagnostic measurements of suspended solid particles are required. In fact, the principal model of ultrasonic scattering and absorption that is used was first developed by marine scientists, but applies equally to any situation where the scatterers (*i.e.* solid particles) are suspended in a fluid.

An overview of the structure and contents of the thesis follows. Every chapter and many sections also begin with overviews, to aid the reader.

Chapter 2 is the main, general literature review containing information that is relevant to all the results chapters. In Section 2.1, the scattering and absorption processes in suspensions of particles are summarised; in Section 2.2 the fluid dynamics of multiphase pipe flow is reviewed. Based on this main review, some opportunities for research are stated or restated in Section 2.3, and smaller, more focused reviews are given at the beginning of each results chapter (Chapters 4 to 6).

Chapter 3 is a thorough description of the experimental method, consisting of: a

review of experimental methods and the basis of process used to select the most appropriate methods for this study (Section 3.1); specification of the slurry flow loop, the method of operation of the *UVP-DUO* ultrasonic system (Section 3.2); a description of the general data processing method (Section 3.3); a discussion of the chosen coordinate system (Section 3.4); a thorough description of the particle characterisation studies that were performed on the four particle types that were used (Section 3.5); the data validation procedures that were followed, including calibration of the instruments and a statistical analysis of the Doppler velocity data (Section 3.6); and a description of the method that was used in two of the subsequent results chapters to measure the thickness of settled and moving beds and shear layers (Section 3.7). Chapter-specific methodologies are also included in each of the results chapters.

Chapter 4 is the first of the three main results chapters, which are grouped into distinct topics. The aim of the work presented in Chapter 4 was to investigate the effects of suspended particles on the fluid mechanics of pipe flow, and identify the boundaries between several flow regimes by quantifying two critical velocities that separate them. The first part of Chapter 4 is a chapter-specific experimental methodology (Section 4.1). The results are divided into three parts: mean and fluctuating (RMS) velocity profiles and Reynolds stresses in several flow regimes over a range of particle volume fractions (Sections 4.2.1 to 4.2.5); the homogeneous transition velocity, U_{c1} (Section 4.2.6); and the limit deposition velocity, U_{c2} (Section 4.2.7).

Chapter 5 contains the results of an investigation of the scattering and absorption properties of the four particle species that were chosen for this study, with the objective of using the measured properties to construct particle concentration profiles in pipe flow. In Section 5.1, the model of ultrasonic backscattering and attenuation that is used in this study is briefly reviewed; in Section 5.2, the model is adapted for use with homogeneous suspensions in order that the backscatter and attenuation properties of arbitrary particle species can be measured; in Section 5.3, the dual-frequency concentration inversion method is presented and the measured particle properties are employed in order to construct particle

concentration profiles in pipe flow in a range of flow conditions with the four particle species.

The aim in Chapter 6, the last results chapter, is to present a phase diagram of bedform types in pipe flow, which include settled beds, moving beds and rippled beds. A variety of behaviour was encountered, including hysteresis and flow-rate path-dependence. A chapter-specific review of bedforms in natural, open and closed channels is presented in Section 6.1, and Section 6.2 is a chapter-specific experimental methodology. A range of varied behaviour is described in the results section (Section 6.3), in particular: examples of measurements of settled, "upper-plane" beds (Section 6.3.1); path-dependent behaviour caused by sudden changes in applied flow rate (Section 6.3.2); the proposed categorisation of bedforms according to their mode of motion (Section 6.3.3); hysteretic behaviour, that is, observed differences in bedform development upon increase and decrease of applied flow rate (Section 6.3.4); the evolution and scaling of bedform heights and asytmmetry of bedform periods over time (Section 6.3.5), with comparisons to several predictions from the literature; and finally the presentation of bedform phase diagrams in terms of the Froude number, Fr, Reynolds number, Re, and Galilei number, Ga (Section 6.3.6).

A summary of the outcomes and findings of the study is presented in Chapter 7, and several suggestions are made for extensions of the work presented here.

Lastly, in Appendix A, the effects of uncertainties in several known quantities – beam divergence angle, probe mounting angle, temperature and pressure – on the measurement distance, the mean axial flow velocity and the total acoustic attenuation are assessed quantitatively by propagation of errors for one representative example run.

2 Literature review

A summary of the basic interactions of ultrasound with suspensions of solid particles is presented in Section 2.1. Section 2.2 contains a review of the fluid mechanics of multiphase pipe flow, including common coordinate systems (Section 2.2.1), the expected behaviour of the velocity and stress fields (Section 2.2.2), the relevant Kolmogorov scales and other fundamental quantities (Section 2.2.3) and observations of multiphase flow (Sections 2.2.4 and 2.2.5); Section 2.2.6 contains a summary of the various flow regimes found in the literature, from homogeneous suspensions to flows with a stationary bed, and the critical velocities that delineate them; lastly, in Section 2.2.7 the most commonly used correlations for predicting these critical velocities are reviewed and discussed.

There are shorter, chapter-specific literature reviews in some of the chapters that follow. For example, a review of some commonly used experimental techniques is presented in the methodology chapter (specifically, Section 3.1), but this is for a specific purpose: to identify the most suitable technique for this study. Similarly, in the section relating to validation of the single-phase flow data (Section 3.6.6), extensive reference is made to studies of the near-wall behaviour and the Darcy friction factor in pipe flow; and in the chapter containing concentration profiles (Chapter 5), several models are referred that are required for the derivations that are presented.

However, it is important to note that the chapter-specific reviews are strictly supplementary to the general one presented in this chapter. The review in the bedforms chapter (Section 6.1) is the most substantial; it was decided to present it separately because much of the information is highly specific to bedforms, and not to the topics covered in the rest of the thesis, being drawn largely from the sedimentology literature and that of closely related fields.

2.1 Physical processes in insonified suspensions of particles

As described in the general methodology (Chapter 3), an ultrasonic measurement

system was principally used in this study, and specific models were used to calculate particle concentration profiles in suspensions of particles (Chapter 5).

There follows a review of the various physical mechanism by which ultrasound and particles in a suspension interact. An attempt is made to draw together several disparate models of the interactions of ultrasound with suspensions of solid particles. As Dukhin and Goetz (2002) state, the purpose of any model is to relate macroscopic properties (*e.g.* speed of sound, attenuation, angular dependence of scattering) to the microscopic properties of the fluid and solid phases (*e.g.* chemical composition, structure, particle size distribution). The model used in this study is that of Thorne and Hanes (2002), as described in Section 5.1. This model applies to a single, monostatic transducer arrangement – like the one used in this study – and can be thought of as a special case in which only the sound scattered at an angle of 180 degrees is measured, neglecting multiple scattering effects. However, in the interests of completeness a general description of several models is presented here.

Any such model should satisfy the following three minimal requirements (Dukhin and Goetz, 2002):

1. Be valid over a wide range of particle sizes and ultrasonic frequencies;
2. Account for all the physical mechanisms that are present (as listed in the following section); and
3. Incorporate the effects of multiple scattering, inter-particle interactions and be valid in concentrated suspensions.

However, Dukhin and Goetz (2002) go on to state that the most common model – the ECAH model, which is named after its originators Epstein, Carhart, Allegra and Hawley (Allegra and Hawley, 1972; Epstein and Carhart, 1953) – only partially satisfies the second requirement and fails the third. In particular, the ECAH model is only valid in the long-wavelength regime (LWR) and neglects particle interactions, so is not valid at high concentrations.

The physical mechanisms present in an insonified suspension can be broadly

divided into two types: scattering and absorption (*i.e.* conversion of acoustic energy into heat, sometimes referred to as dissipation). By analogy to optics, these two mechanisms collectively contribute towards attenuation (classically referred to as extinction) of the emitted signal in an additive fashion by superposition in most situations (Dukhin and Goetz, 2002) and can be categorised further, as follows (Babick *et al.*, 1998; Richter *et al.*, 2007):

1. *Scattering,* α_{sc}*.* Diffuse reflection, refraction and diffraction, by which energy is redirected from the incident beam. Does not dissipate energy, but does contribute to attenuation because less energy reaches the receiver as a result; "significant for larger particles with a diameter exceeding roughly 3 microns" (Dukhin and Goetz, 2002), that is, in the intermediate and short wavelength regimes.
2. *Viscous (or visco-inertial) absorption,* α_{vi}*.* A hydrodynamic effect caused by shear friction – that is, "viscous deformation of the flow field" (Babick *et al.*, 1998) – in the boundary layer around the solid particles. The dominant form of dissipation in "small rigid particles with sizes less than 3 microns" (Dukhin and Goetz, 2002) and at long wavelengths. This component is very sensitive to inter-particle interactions, and even more so than is scattering, perhaps surprisingly.
3. *Thermal absorption,* α_{th}*.* A thermodynamic effect caused by heat transfer between the solid and liquid phases "due to different thermo-physical properties" (Babick *et al.*, 1998); dominates attenuation for soft particles.
4. *Intrinsic absorption,* α_{in} *or* α_{w}*.* Independent of particle size and wavelength and is "related to relaxation phenomena" in the liquid phase (Richter *et al.*, 2007), but of relative significance for small particles and at low concentrations, since other mechanisms tend to be less significant in those cases.
5. *Structural absorption,* α_{st}*.* Caused by oscillation of inelastic inter-particle bonds and links. Only significant at high concentrations, or if the solid phase consists of aggregates. Generally negligible.
6. *Electrokinetic absorption,* α_{el}*.* A result of the electric field generated by acoustically excited dipole oscillation of particles. Generally negligible.

Scattering simply redirects acoustic energy, but a complicating factor when

measuring the scattering properties of a suspension is that the scattered sound may reach the detector *via* several routes: by coherent, incoherent or multiple scattering (Dukhin and Goetz, 2002).

2.1.2 Regimes and dependences of scattering and absorption

In general, each form of scattering and absorption requires a separate model, and to present a thorough description is beyond the scope of this review. However, a summary of the various limiting cases in terms of particle size, ultrasonic wavelength and other parameters is given below for completeness and to aid the reader's understanding. A very broad summary of the regimes of ultrasonic interactions with suspended particles is presented in Table 2-1, where ka is defined as follows (Shukla *et al.*, 2010), with k the ultrasonic wavenumber and a is the particle radius:

$$ka = \frac{\omega a}{c} = \frac{2\pi f a}{c} = \frac{2\pi a}{\lambda}. \qquad [2.1]$$

Table 2-1: Classification of ultrasonic interactions with suspended particles. Adapted from several sources (Dukhin and Goetz, 2002; Shukla *et al.*, 2010; Thorne and Hanes, 2002).

Regime (by analogy to optical scattering)	Rayleigh	Mie	Geometric
Regime (by wavelength)	Long-wavelength regime (LWR)	Intermediate-wavelength regime (IWR)	Short-wavelength regime (SWR)
Particle size, ultrasonic wavelength and wavenumber	$ka \ll 1$	$ka \sim 1$	$ka \gg 1$
	$\lambda \gg a$	$\lambda \sim a$	$\lambda \ll a$
Dominant components of attenuation	Viscous absorption	Scattering usually dominant	Scattering
Backscatter form function, f	Depends on $(ka)^2$	Transitional between SWR and LWR dependences	Tends to constant value
Normalised total scattering and absorption cross-section, χ	Depends on $(ka)^4$	Transitional between SWR and LWR dependences	Tends to constant value

Dukhin and Goetz (2002) note that "sub-micron particles do not scatter ultrasound at all in the frequency range under 100 MHz" but "only absorb ultrasound"; they also note that "absorption and scattering are distinctly separated in the frequency domain", with absorption dominant at lower frequencies and scattering at higher frequencies, as illustrated in Figure 2-1 (Richards *et al.*, 1996), which is normalised for particle mass concentration and path length.

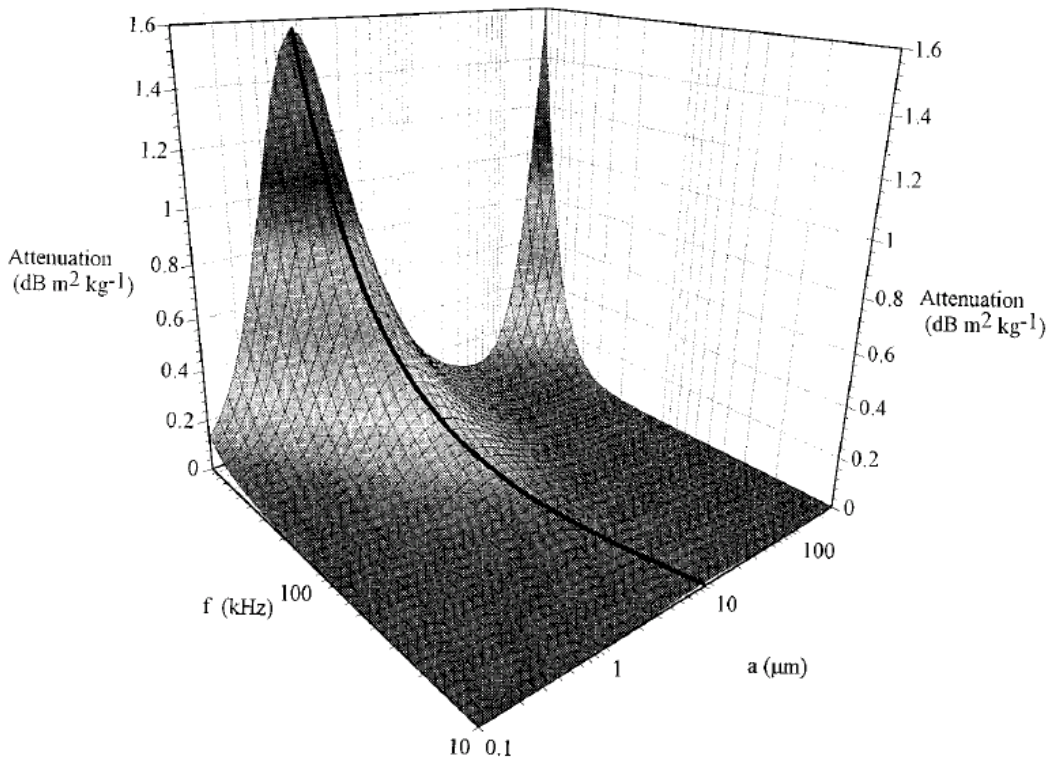

Figure 2-1: Attenuation spectra, normalised for particle mass concentration and path length, showing peaks for viscous absorption (peak to left of figure) and scattering (right). Note that solid black line is locus of viscous absorption peak, which shifts to higher particle sizes at higher frequencies. From Richards *et al.* (1996).

Babick *et al.* (1998) explain that in the long-wavelength regime (LWR, *i.e.* when $ka \ll 1$), "scattering effects are negligible" and attenuation is mainly due to absorption. However, in the intermediate-wavelength regime (IWR, *i.e.* when $ka \sim 1$), dissipation is negligible and "scattering, particularly by diffraction, increases enormously". Povey (1997) notes and that "the scattering intensity depends on the [inverse of the] fourth power of the wavelength" for both sound and light in the Rayleigh limit (*i.e.* low *ka*).

Several components of absorption can be neglected in the case of rigid, non-aggregating particles, as used in this study. In particular, thermal (due to particle rigidity), structural (because there is no aggregation) and electrokinetic absorption will be insignificant. Therefore the total attenuation is due to intrinsic absorption in water (α_w), viscous absorption (α_{vi}) and scattering (α_{sc}) (Richards *et al.*, 1996; Thorne and Hanes, 2002), that is:

$$\alpha = \alpha_w + \alpha_s = \alpha_w + \alpha_{vi} + \alpha_{sc}, \qquad [2.2]$$

where the subscripts w and s correspond to water and solids (or sediment), respectively, such that $\alpha_s = \alpha_{vi} + \alpha_{sc}$.

Attenuation due to particles has generally been found to vary linearly with concentration at relatively low concentrations. However, what constitutes "relatively low" depends strongly on the particle size and ultrasonic frequency. Hay (1991) measured the acoustic attenuation properties of sand in a particle-laden jet and found a linear relationship between the mean-squared (actually squared mean, to simplify computation) voltage and particle concentration in the absence of multiple scattering or strong "attenuation due to particles". Figure 6 of that paper shows that this linearity holds up to $M \approx 5$ g l^{-1} (or $\phi \approx 0.2$ %) at an acoustic frequency of 5 MHz, and up to a much higher concentrations – at least M = 25 g l^{-1} (or $\phi \approx 1$ %) – at 1 MHz, whereas at higher concentrations, "the observed local backscatter amplitude becomes independent of local particle concentration", an observation that was also made by Hipp *et al.* (2002) in a variety of suspensions in the 2-50 MHz range. In an earlier paper, Hay (1983) found a similar linear relationship using irregularly-shaped mine tailings "in the 10 to 10^3 mg l^{-1} range", as did Stakutis *et al* (1955) in suspensions of fine quartz sand and lycopodium spores at relatively low concentrations.

Richards *et al.* (1996) found a linear relationship, but their experiments with quartz-type sand were rather dilute (up to $M \approx 4$ kg m^{-3}, or $\phi \approx 0.15$ %). They note that this is to be expected, since Urick (1948, Figure 5) obtained similar results with sand and kaolin at concentrations up to $\phi = 10$ % or so. More recently, Sung *et*

al. (2008) found a linear relationship between attenuation and concentration, as did Greenwood *et al.* (1993), both of which groups used kaolin-water suspensions. The Greenwood group concluded that scattering was insignificant in their experiments, since $\lambda \gg a$, and found that attenuation was directly proportional to volume fraction if "there is no interaction between particles".

Using two ultrasonic frequencies (1.2 and 3.4 MHz) with glass and aluminium oxide beads in water and oil, Shukla *et al.* (2010) found that, in general, the relationship between attenuation and particle concentration was linear over a greater range of concentration for lower values of ka (*e.g.* for 114 μm particles at 1.2 MHz, such that $ka = 0.29$). A similar trend was observed by Carlson (2002) in suspensions of magnetite and dolomite particles of several sizes.

Similar acoustic methods are also used by marine scientists to measure suspended sediment concentration (SSC). Indeed, the model described in the review of acoustic methods in marine science by Thorne and Hanes (2002) is exploited in Chapter 5 to calculate concentration profiles in pipe flow.

2.2 Fluid mechanics of multiphase pipe flow

In Section 2.2.1, various conventions for representing the coordinates and velocity and stress fields are presented. One nomenclature is chosen, and the reasons for that choice are given. A review of the literature relating to the first- and second-order statistics of turbulent pipe flow are presented in Section 2.2.2, while Sections 2.2.3 and 2.2.4 contain an overview of the important parameters in multiphase flow. The influence of suspended particles on the fluid dynamics and bulk behaviour of multiphase flow is summarised in Section 2.2.5; in Sections 2.2.6 and 2.2.7, reviews of the literature relating to slurry flows, and the models most commonly used to predict their bulk behaviour, respectively, are presented.

2.2.1 Coordinates, velocity and stress fields in turbulent pipe flow

There are several forms of notation available for describing turbulent pipe flow in cylindrical polar coordinates. There follows a description of some of these

conventions, and the reasons for choosing the notation used in this study are described, in terms of: (a) the coordinates themselves; (b) the components of the velocity vector along each axis, and (c) the notation used for the mean and fluctuating parts of the velocity field, including the root-mean-square (RMS) of the fluctuating velocity components. These choices are reiterated in the general methodology (Section 3.4) for the reader.

General forms for the radial, azimuthal and axial coordinates in the mathematical literature are ρ, ϕ and z (Riley *et al.*, 2006). In the engineering literature, however, it is much more common for these coordinates to be expressed as r, θ and z (or sometimes x), respectively, or some similar combination. For this reason, these are the symbols used hereafter. For the instantaneous values of the velocity components in the axial (or streamwise), azimuthal and radial directions, the most common forms of notation are U, V and W, or U_z, U_r and U_θ, respectively (although other researchers use different forms of notation, *e.g.* Eggels *et al.*, 1994; Laufer, 1954). In order to simplify the typography as much as possible, U, V and W are used hereafter.

A diagram showing the axial and radial coordinates (in the z and r directions, respectively) and the instantaneous velocity components along those axes (U and W, respectively), as well as the distance from the upper pipe wall, y, is given in Figure 2-2.

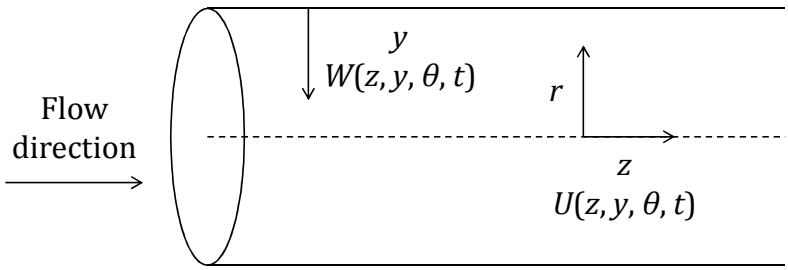

Figure 2-2: Diagram showing geometry of pipe flow, with notation for coordinates and velocity components used in this study shown.

Some important points should be taken from Figure 2-2, as follows:

1. The azimuthal component is not shown in because it was not considered in

this study: the ultrasonic probes were mounted in the vertical z–r plane, as shown in Figure 3-2 (general methodology, Chapter 3) and could not be rotated while experiments were running.

2. The wall-normal distance, y, is generally used in this study, rather than the radial coordinate, r. and the velocity component W is defined along the y axis. This means that $W = W(z, y, \theta, t) \neq W(z, r, \theta, t)$.

There follows a brief description of the method of Reynolds decomposition that is very frequently used in fluid mechanics to separate the mean and fluctuating parts of a quantity in a turbulent flow such as fluid velocity, temperature and pressure. In this study, the velocity, and as a result, the stress fields are the only quantities to which the decomposition is applied. The expressions that follow are based on those given in the books by Hinze (1959) and Schlichting and Gersten (2000). Hinze's notation is used here: it permits less ambiguity in the definition of the fluctuating component and its root-mean-square (RMS) value.

In general, a quantity A that varies randomly can be decomposed into a time-averaged component, $\bar{A}$, and a fluctuating component, a, such that $A(t) = \bar{A} + a(t)$. For two such quantities A and B, the time-averaged mean of their product, AB, is (Hinze, 1959):

$$\overline{AB} = \overline{(\bar{A} + a)(\bar{B} + b)} = \overline{\bar{A}\bar{B}} + \overline{\bar{A}b} + \overline{\bar{B}a} + \overline{ab} = \bar{A}\bar{B} + \overline{ab}, \qquad [2.3]$$

because $\bar{a} = \bar{b} = 0$, that is, the time-averaged mean of each fluctuating part is identically zero. When this principle is applied to turbulent pipe flow in cylindrical polar coordinates, the instantaneous axial velocity in the z (*i.e.* axial) direction is given by $U(z, r, \theta, t) = \overline{U}(z, r, \theta) + u(z, r, \theta, t)$, where $\overline{U}$ is the time-averaged mean and u is contrived to be the component that fluctuates randomly due to local turbulent motion, such that $\bar{u} = 0$.

It is conventional to use the root-mean-square (RMS) of the fluctuating part of the velocity as a measure of the strength of the turbulent fluctuations. Several symbols are used in the literature to represent this quantity, of which u_{rms} and u' (and permutations thereof) appear to be the most common (but see, for example, den

Toonder and Nieuwstadt, 1997; Wu and Moin, 2008). For simplicity of typography, u' is used hereafter to represent the RMS of the fluctuating component of the axial velocity.

For n samples, u' is given by the following expression:

$$u' = \sqrt{\overline{u^2}} = \left[\frac{1}{n}\sum_{i=1}^{n} u^2\right]^{1/2} = \left[\frac{1}{n}\sum_{i=1}^{n} (U - \bar{U})^2\right]^{1/2} \quad [2.4]$$

It is clear from Equation [2.4] that, if the substitution $u = U - \bar{U}$ is made, u' is identical to the standard deviation of the instantaneous velocity and can be calculated as such if it is more computationally efficient to do so. Lastly, the so-called turbulence intensity can be calculated as follows:

$$I = \frac{u'}{\bar{U}} \quad [2.5]$$

With reference to Equation [2.5], the term "turbulence intensity" is sometimes used to describe u', v' and w' (for example, Wu and Moin, 2008). However, in this study it refers only to I.

Table 2-2: Summary of notation for coordinates and velocity/stress components used in this study.

Direction/axis, symbol	Velocity components			
	Instantaneous	Mean instant.	Fluctuating	"RMS"
Axial, z	$U(z, \theta, y, t)$	$\bar{U}(z, \theta, y)$	$u(z, \theta, y, t)$	$u'(z, \theta, y)$
Azimuthal, θ	$V(z, \theta, y, t)$	$\bar{V}(z, \theta, y)$	$v(z, \theta, y, t)$	$v'(z, \theta, y)$
Wall-normal, y	$W(z, \theta, y, t)$	$\bar{W}(z, \theta, y)$	$w(z, \theta, y, t)$	$w'(z, \theta, y)$

The definitions of, and relationships between, U, $\bar{U}$, u and u' that have been described in the axial direction apply analogously to the components in the radial and azimuthal directions. In the interests of clarity, the various coordinates and velocity components used hereafter are summarised in Table 2-2. It should be noted that the wall-normal distance, y, from the upper pipe wall (*i.e.* that closest to

the probes) was used in this study when calculating the velocity and stress fields rather than the radial distance from the pipe centreline, r, because it could not be assumed (and, in fact, was found to be the case) that the flow was symmetrical about $r = 0$. However, r is referred to in this literature review rather than y if it was thought the choice would aid understanding by the reader, and r should not be confused with the distance from the probe used in other parts of this study.

2.2.2 Mean and turbulent velocities and Reynolds stresses

Figure 2-3 shows the various normal and shear stresses acting on a fluid element in Cartesian coordinates. Although cylindrical polar coordinates are used in this study, the choice between Cartesian and cylindrical polar is irrelevant because the transducers were mounted vertically, *i.e.* in the z-r plane. This means that only three elements of the Reynolds stress tensor could be measured, namely the axial and radial normal stresses (z-z and r-r) and the shear stress (z-r), which are of the same form in both coordinate systems (although different symbols are sometimes used in the literature to represent each component).

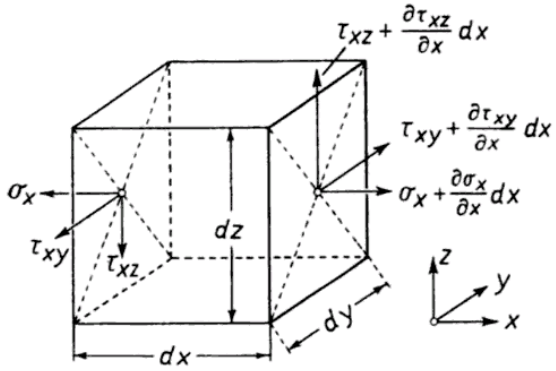

Figure 2-3: Stresses acting on a fluid element (Schlichting and Gersten, 2000) in Cartesian coordinate system, for illustration purposes. Note coordinates (x, y, z), and therefore shape of fluid element, differ from those used in this study (z, θ, y).

The three corresponding components of the total stress that contain turbulent parts that could be measured in this study are as follows (Hinze, 1959; Schlichting and Gersten, 2000):

$$\tau_{zz} = \sigma_z = -\bar{P} + 2\mu\frac{\partial \bar{U}}{\partial z} - \rho\overline{u^2}, \quad [2.6]$$

$$\tau_{rr} = \sigma_r = -\bar{P} + 2\mu\frac{\partial \bar{W}}{\partial r} - \rho\overline{w^2}, \quad [2.7]$$

$$\tau_{zr} = \mu\left(\frac{\partial \bar{U}}{\partial r} + \frac{\partial \bar{W}}{\partial z}\right) - \rho\overline{uw}, \quad [2.8]$$

in which ρ and μ are the fluid density and the dynamic viscosity, respectively, and $\bar{P}(z, \theta, r)$ is the time-averaged mean of the instantaneous pressure, $P(z, \theta, r, t)$, which is a (scalar) function of time and space and can be decomposed into mean and fluctuating parts in a manner exactly analogous to each component of velocity, *i.e.* $P = \bar{P} + p$. However, it is important to note that the viscous stresses in Equations [2.6], [2.7] and [2.8] could not be calculated in this study since no pressure transducers were used.

If the fluid behaviour – in the form of the mass (*i.e.* continuity), momentum (or Reynolds) and kinetic energy (or *k*-) equations, which can be found in Schlichting and Gersten (2000), for example – in any turbulent flow is to be fully resolved and understood, it is a minimum requirement of an experimental measurement system or numerical scheme that the pressure, velocity and stress terms described above - and their first and second derivatives – can be measured, and that they can be measured at a sufficiently high spatial and temporal resolution that the motion of the smallest turbulent motions are accounted for.

The first two terms in Equations [2.6] and [2.7], and the first one in Equation [2.8], are the viscous stresses, which "can frequently be neglected, apart from in the regions directly at the wall" (Schlichting and Gersten, 2000), while the last terms are the Reynolds (or apparent turbulent) stresses.

A summary of some of the most relevant studies of pipe flow in which velocity and Reynolds stress profiles were presented is given in Table 2-3, data from many of which are used for comparison in the results sections that follow. (Table 2-6 is

focused on multiphase studies, which are described later, in Sections 2.2.5 to 2.2.7.) The Reynolds number, Re, is defined as follows:

$$\mathrm{Re} = U_{ave} D/\nu, \qquad [2.9]$$

where U_{ave} is the mean axial velocity averaged over the pipe cross-section and D is the pipe diameter and ν is the kinematic viscosity.

Table 2-3: Single-phase and low-concentration pipe flow studies[1]. Reynolds number, Re, is defined in Equation [2.9].

Reference	Method (and notes)	Diameter, D (mm)	Reynolds number, Re (10^3)
Laufer (1954)	Hot wire	123	50 and 500
Lawn (1971)	Hot wire	144	37-250
Perry *et al.* (1986)	Hot wire	99	75-200
Kim *et al.* (1987)	DNS (channel flow)	-	3.3
Eggels *et al.* (1994)	DNS, hot wire, LDA, PIV (with oil droplets, 1-2 μm)	95.4	6.95-7.35
Den Toonder and Nieuwstadt (1997)	LDA (with pigmented TiO_2 particles)	40	4.9-25.3
Zagarola and Smits (1998)	Pitot probe	130	31.3-35,000
McKeon *et al.* (2004a)	Pitot probe	130	31.3-35,000
Morrison *et al.* (2004)	Hot wire	130	55-5,700
Wu and Moin (2008)	DNS	-	5.3 and 44
Hultmark *et al.* (2010)	Hot wire	130	24-145
Hultmark *et al.* (2012)	Hot wire	130	81-6,000

[1] A similar table for single-phase studies was given by Hultmark *et al.* (2010).

Although a complete review of the current knowledge of the behaviour of turbulence in wall-bounded flows is beyond the scope of this study, there follows an outline of the expected trends in the mean and RMS velocity, and the normal and shear Reynolds stress profiles and the current state of knowledge thereof.

The expected mean axial velocity profiles in pipe flow at two Reynolds numbers,

Re = 50,000 and 500,000, are shown in (Laufer, 1954), while Figure 2-5 shows the three components of normal stress in pipe flow at Re = 44,000 (Wu and Moin, 2008). All show peaks of various magnitudes at various distances from (but close to) the wall and decrease to minimum values at the pipe centreline. The strength and proximity of the peaks to the wall has been found to increase with Reynolds number.

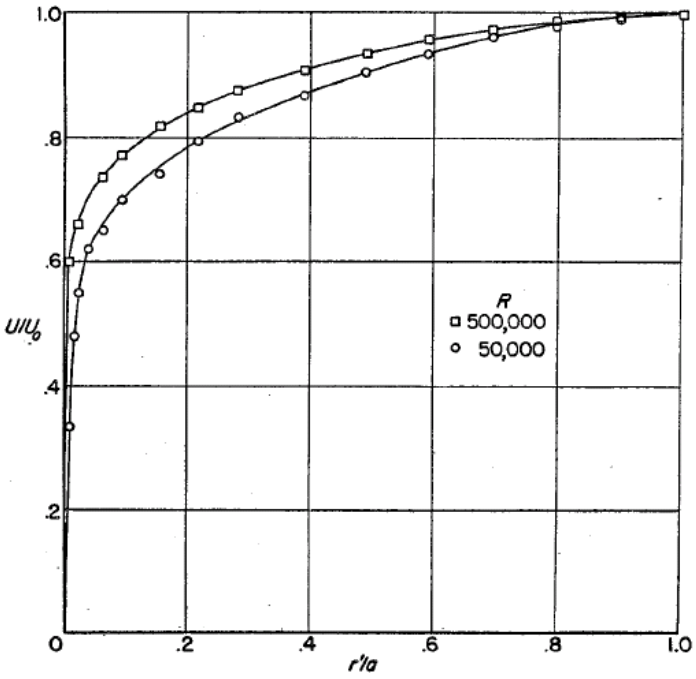

Figure 2-4: Mean axial velocity relative to centreline value *vs.* distance from wall at two Reynolds numbers, Re = 50,000 and 500.000. Ordinate is equivalent to y/R in this study. From Laufer (1954).

On the other hand, the variation in Reynolds shear stress as a function of radial distance at two Reynolds numbers is shown in Figure 2-6 (Laufer, 1954), from which it can be seen that $\overline{uw}/U_\tau^2$ is expected to reach a strong peak near the wall and decrease approximately linearly to zero at the pipe centreline.

A topic of intensive current interest is whether a region in which the mean velocity follows a universal logarithmic scaling – of the kind described in Section 3.6.6 – exists for all types of wall-bounded flows (see, for example, Monty *et al.*, 2009); that this seemingly fundamental question has remained unanswered into the twenty-first century has been attributed to the fact that data at very high Reynolds numbers are necessary to resolve the issue, but obtaining such data is both expensive and experimentally challenging for a number of reasons (see, for

example, George, 2007).

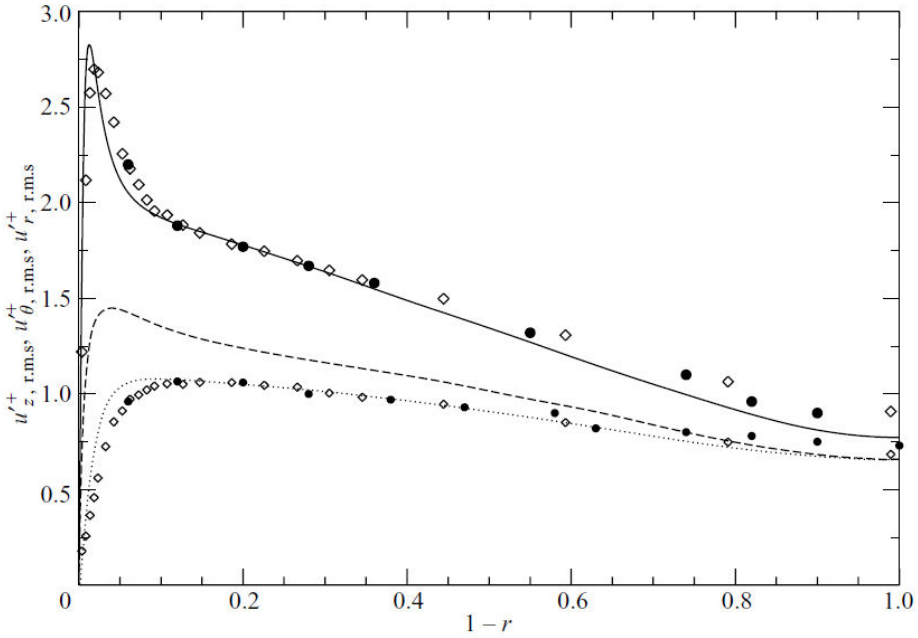

Figure 2-5: Turbulence intensities *vs.* distance from wall. Solid, dashed and dotted lines correspond to axial, azimuthal and radial intensities in wall units, respectively, *i.e.* u'^+, v'^+ and w'^+ (Re = 44,000, numerical). Circles (Lawn, 1971) and diamonds (den Toonder and Nieuwstadt, 1997) are hot-wire and LDA experimental data at Re = 38,000 and 24,580, respectively. Ordinate is equivalent to $1 - r/R$ in this study. From Wu and Moin (2008).

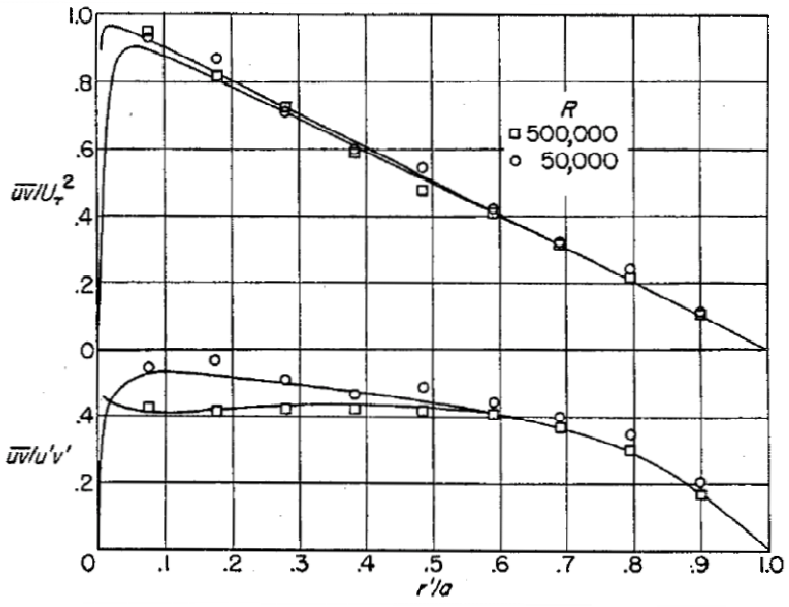

Figure 2-6: Reynolds shear stress in *z*-*r* plane, nondimensionalised by shear velocity, U_τ^2, and double correlation coefficient, *u*'*w*', at two Reynolds numbers, Re = 50,000 and 500,000; *r*' is radial distance from wall (*i.e. y*); *a* is pipe radius (*R*). From Laufer (1954).

Only very recently was a universal logarithmic region confirmed by Marusic *et al.* (2013), who compared several sets of data from a variety of bounded flows (boundary layers, pipe flow and atmospheric surface layer) and found logarithmic dependences over common regions (in terms of $y^+ = yU_\tau/\nu$, the wall-normal distance in wall units (described in more detail in Section 3.6.6) in both the axial mean velocity ($\overline{U}^+ = \overline{U}/U_\tau$) and turbulence intensity ($\overline{u^2}^+ = \overline{u^2}/U_\tau^2$) profiles.

2.2.3 Turbulent scales

Turbulent fluid flow is characterised by chaotic motions superimposed on the main fluid flow, such that translational energy is converted to rotational energy in the form of coherent vortical structures (eddies) that can be thought of as "instability waves rolling up into vortices" (Kulick *et al.*, 1994).

English translations of the classical papers of Kolmogorov on the structure and dissipation of turbulence are available (Kolmogorov, 1991a, b). A turbulent eddy has a corresponding Kolmogorov timescale (τ_K), length scale (η) and energy that depend on its size and the flow characteristics and geometry. The largest eddies have a size of the order of the channel that is referred to as the integral length scale, l_e, while the size of the smallest is determined by viscous forces and is known as the Kolmogorov length scale, η, such that (Shirolkar *et al.*, 1996):

$$\eta = \left(\frac{\nu^3}{\varepsilon}\right)^{1/4}, \qquad [2.10]$$

where ε is the mean dissipation rate of the turbulence kinetic energy per unit mass, which can be approximated as follows:

$$\varepsilon \approx \frac{(u')^3}{l_e}, \qquad [2.11]$$

where u' is the axial RMS velocity. The Kolmogorov timescale is, correspondingly,

$$\tau_K = \left(\frac{\nu}{\varepsilon}\right)^{1/2}. \qquad [2.12]$$

The mechanism of spectral energy transfer, that is, transfer of energy from larger to smaller eddies (since an eddy's kinetic and rotational energy depends on its size) in single-phase flows is a result of stretching under the action of velocity gradients in the fluid, which acts to break up the larger eddies into smaller ones until turbulent energy is dissipated as heat in the fluid, a process referred to as turbulent decay, or the "energy cascade" (Shirolkar *et al.*, 1996).

Table 2-4: Important time- and length scales in multiphase flow.

Quantity	Description	References
Timescales		
τ_c	Average time between particle-particle collisions.	Crowe (2006); Tsuji (2000)
τ_K	Kolmogorov timescale. Lifetime of smallest eddies in turbulent flow.	Tennekes and Lumley (1972)
τ_l	Integral timescale. Lifetime of largest eddies in turbulent flow.	
τ_p	Particle relaxation timescale. Response time of particle to difference in velocity between it and fluid.	Crowe (2006); Shirolkar *et al.* (1996)
Length scales		
l_e	"Integral" or "outer length scale": characteristic length of most energetic (*i.e.* largest) eddies in turbulent flow	Tennekes and Lumley (1972)
η	Kolmogorov length scale or 'inner' turbulence scale. Size of smallest eddies in turbulent flow.	
L or D	Conduit diameter	

Table 2-4 contains a summary of the most important time- and length scales in turbulent multiphase flow. From these we can define the particle Stokes number, *St*, is the ratio of the particle relaxation time, τ_p, to τ_k, as follows (Ouellette *et al.*, 2006):

$$\mathrm{St} = \frac{\tau_p}{\tau_k} = \frac{\left(\rho_p - \rho_f\right)}{18\rho_f}\left(\frac{d}{\eta}\right)^2. \qquad [2.13]$$

If St ≪ 1 a particle has time to respond to changes in the fluid velocity, and its velocity approaches that of the carrier fluid, while if St ≫ 1 the particle will not follow the fluid motion closely because particles cannot respond quickly to changes in the fluid velocity (Poelma *et al.*, 2007).

Table 2-5 summarises a number of regimes for characterising fluid flow. A flow can be considered disperse if τ_p/τ_c < 1, in which case the particles have time to respond to local fluid forces before the next collision: particle motion is controlled by the fluid forces, *i.e.* drag and lift. On the other hand, if τ_p/τ_c > 1, then the particle has no time to respond to the fluid forces before the next collision and the flow is dense. In this case the motion of particles is determined by collisions, *i.e.* granular contact. Crowe (2006) further classifies dense flows as collision-dominated, as in fluidised beds, and contact-dominated, as in granular flow.

Table 2-5: Flow regimes for suspensions of particles. Adapted from Poelma *et al.* (2007).

Quantity	Description	References
$\frac{\delta}{d}$	Mean spacing between randomly distributed particles • δ/d < 10: particle-particle interactions (hydrodynamic, collisions) • $\delta/d \gg 1$: interparticle collisions negligible	Poelma *et al.* (2007)
$\frac{\tau_p}{\tau_c}$	Ratio of particle response time to mean collision timescale • $\tau_p/\tau_c < 1$: collision-free or disperse flow • $\tau_p/\tau_c > 1$: collision-dominated or dense flow • $\tau_p/\tau_c \to \infty$: contact-dominated or very dense (*i.e.* granular) flow	Crowe (2006); Tsuji (2000)
St	Particle Stokes number • St ≪ 1: particle follows fluid motion as "tracers" • St ≈ 0.1-1: "preferential concentration" • St ≫ 1: particle lags fluid motion and slip velocity exists	Eaton and Fessler (1994); Poelma and Ooms (2006)

2.2.4 Basic multiphase flow parameters

The volume fraction of suspended particles can be defined in a number of ways, for example (Crowe, 2006):

$$\phi = \lim_{\delta V \to V_0} \frac{\delta V_s}{\delta V} = \frac{Q_s}{Q_s + Q_l}, \qquad [2.14]$$

where δV_s is the volume of solid in a volume element, δV, of suspension; V_0 is the smallest volume of fluid in which a stationary average can be taken; and Q_s and Q_l are the solid- and liquid-phase volumetric flow rates, respectively. On the other hand, the porosity or void fraction, h_v, is similarly defined as follows:

$$h_v = \lim_{\delta V \to V_0} \frac{\delta V_l}{\delta V} = \frac{Q_l}{Q_s + Q_l} = 1 - \phi, \qquad [2.15]$$

where V_l is the volume of liquid in a volume element. Of course, the total volume fraction is unity, that is:

$$\phi + h_v = 1. \qquad [2.16]$$

The mean slurry density, ρ_m, is given by:

$$\rho_m = \phi \rho_s + h_v \rho_l, \qquad [2.17]$$

where ρ_s and ρ_l are the mass densities of solid and liquid fractions respectively.

2.2.5 Influence of suspended particles on multiphase flow

A brief review of the most important concepts and observations relating to the fluid mechanics of single-phase and low-concentration pipe flow was given in Sections 2.2.2 and 2.2.3, while the literature regarding the prediction of bulk flow properties of concentrated suspensions, *i.e.* sludges and slurries, is described later in Section 2.2.6.

Table 2-6 contains a summary of some studies of the intervening kind, *i.e.* multiphase and high-concentration flows, that will be referred to in the results sections. Based on the studies that are summarised in Table 2-6, there follows an overview (in the form of a numbered list) of the most important aspects of the influence of suspended particles on the form of the flow.

Table 2-6: Multiphase and high-concentration pipe and channel flow studies.

Reference	Method	Diameter (mm)	Re (10^3)	Particle properties
Shook *et al.* (1968)	Gamma rays	24.7 × 101 (channel)	Not applicable	Sand, d = 153-510 μm; nickel, d = 135 μm
Karabelas (1977)	Sampling	50.4 and 75.3	≈ 3-55	Resin, d = 210 and 290 μm, = 1.126 × 10^3 kg m^{-3}
Zisselmar and Molerus (1979)	LDA	50	≈ 50	Glass, d = 12-120 μm, $\phi \leq$ 5.6 %
Tsuji and Morikawa (1982)	LDV, Pitot probe	30.5	11.7-38.9	Plastic, d = 0.2 and 3.4 mm, $\phi \leq$ 6 %; "fine" KCl
Admiraal and Garcia (2000)	ACP	300 × 100 (channel)	Not applicable	Sand, d = 120 and 580 μm
Gillies *et al.* (2004)	Resistivity probe	103	134-309	Sand, d_{50} = 90 and 270 μm, ϕ = 19 %
Ekambara *et al.* (2009)	Numerical	50-500	Not given	d = 90-480 μm, ϕ = 19-20.3 %

1. A shift in the mean axial velocity profile has been observed such that the peak is above the centreline because the mean velocity profile becomes asymmetrical. Some examples of this effect are shown in Figure 2-7(a), in which the velocity profiles for three flow regimes – heterogeneous flow, flow with a moving bed and flow with a stationary bed – are shown (Graf, 1984, Figure 15.20). Surprisingly, this asymmetry was clearly observed even at very high flow rates and volume fractions by Gillies *et al.* (2004, Figure 5), as shown in Figure 2-7(b) (D =0.103 m, Re = 134,000, 206,000 and 309,000, ϕ = 19 % and d = 90 μm). The latter experimental results were compared with the numerical results of Ekambara *et al.* (2009) at Re = 309,000, in which the

asymmetry was reproduced. A similar asymmetry in the mean velocity profile was observed by Tsuji and Morikawa (1982, Figure 10).

(a)

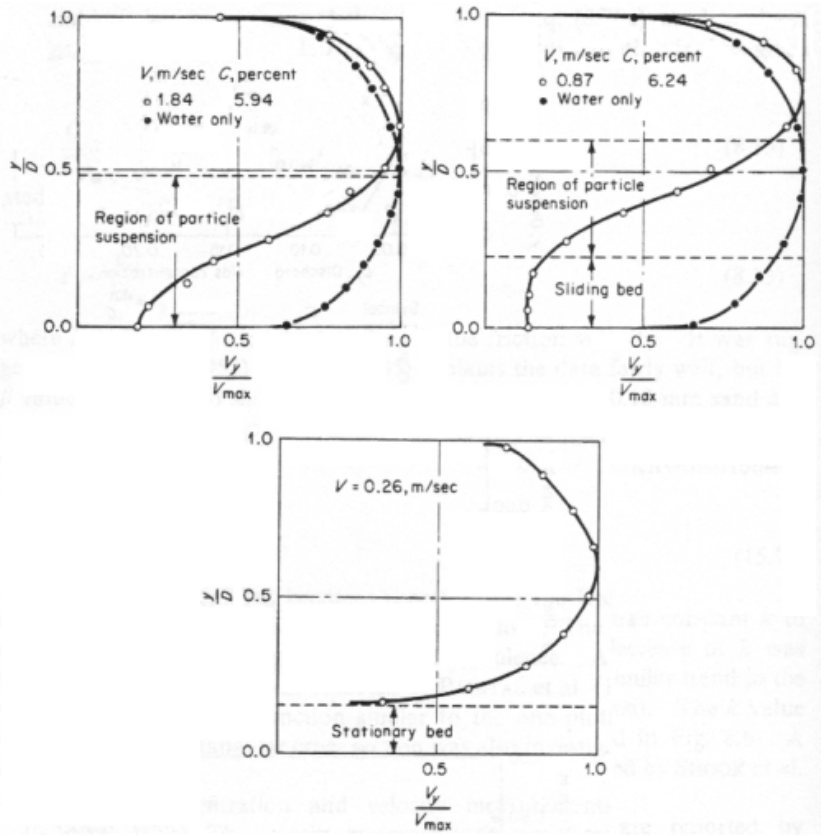

(b)

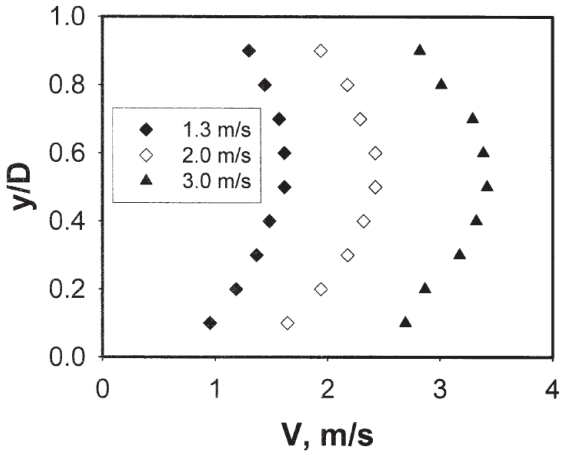

Figure 2-7: Shape of mean axial flow velocity profile in multiphase pipe flow. (a) Three flow regimes with glass spheres (d = 2.07 mm, $\phi \approx 6$ %), where V_y/V_{max} corresponds to $\overline{U}/\overline{U}_{max}$ in this study, and C to ϕ. First frame: heterogeneous flow; second: flow with moving bed; third: flow with stationary bed. From Graf (1984), modified; (b) three flow rates with sand (d = 90 µm, ϕ = 19 %). From Gillies *et al.* (2004).

2. A flattening of the mean axial velocity profile (in terms of $\overline{U}/\overline{U}_{max}$) at high flow rates and particle volume fractions was observed by Tsuji and Morikawa

(1982, Figure 11), who used two particle sizes (d = 0.2 and 3.4 mm) in air-solid pipe flow. The effect was found to be stronger in the case of the smaller particles.

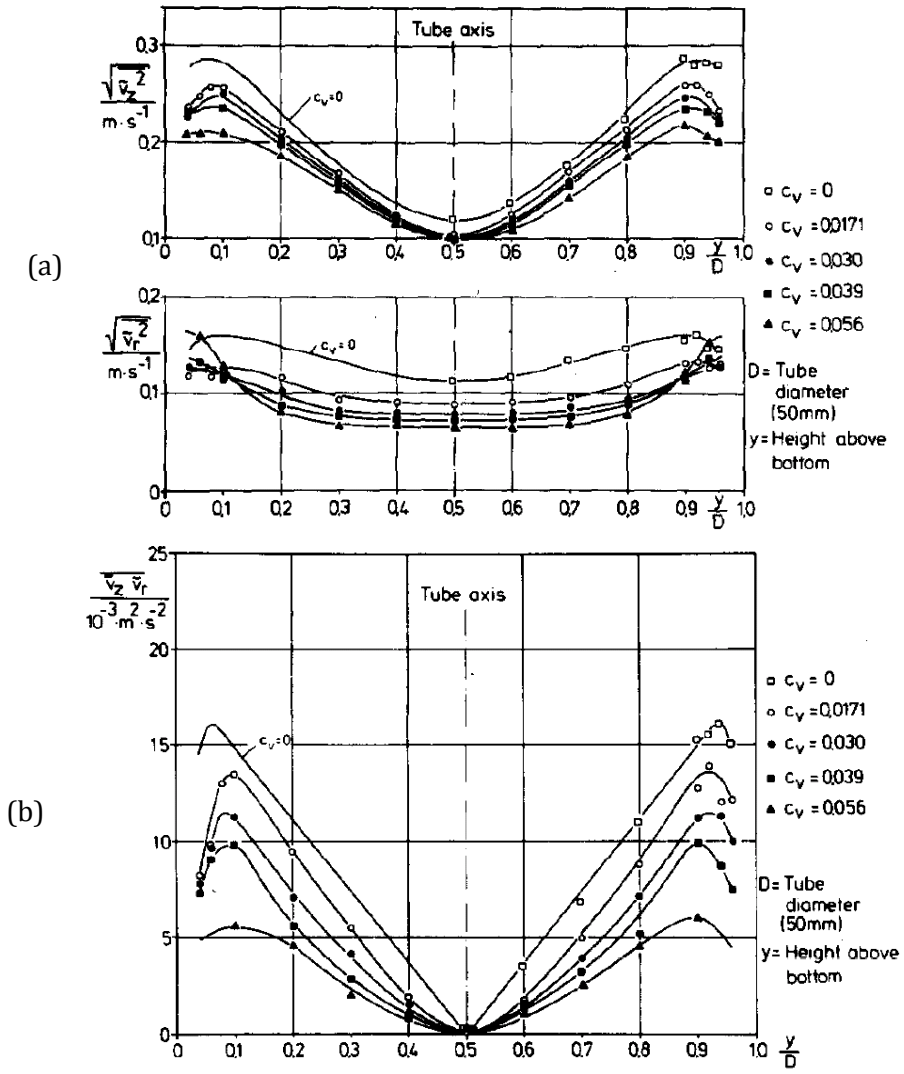

Figure 2-8: Reynolds stresses/RMS velocities *vs.* wall-normal distance, y/D, in multiphase pipe flow at five volume fractions; (a) mean and axial RMS velocities, u' (upper frame) and w' (lower); (b) shear Reynolds stress, $\overline{uw}$. Volume fraction c_v corresponds to ϕ in this study. Compiled from Zisselmar and Molerus (1979).

3. The normal and shear Reynolds stresses (u', w' and $\overline{uw}$) are suppressed in absolute terms in suspensions relative to water alone (Zisselmar and Molerus, 1979) as the solid volume fraction is increased (up to ϕ = 5.6 %; u', w' and $\overline{uw}$, Figures 7, 8 and 10 of that paper, respectively, with D = 50 mm and "Re ≈ 100k"). These results are given in Figure 2-8.

4. The axial turbulence intensity, $I = u'/\overline{U}$, as defined in Equation [2.5], was found by Tsuji and Morikawa (1982) to be enhanced at all mass loadings with the larger of two particle species (d = 3.4 mm) in air-solid flow relative to that with air alone, particularly in the lower part of the pipe (which the authors attributed to the concentration profile), whereas the smaller particles (d = 0.2 mm) suppressed the turbulence intensity, as shown in Figure 2-9. This particle size-dependent enhancement/suppression effect is referred to more generally as turbulence modulation and has been studied extensively (Gore and Crowe, 1989, 1991; Poelma and Ooms, 2006).

The four effects described above are investigated later in this study. All are explored in a general sense through the velocity and stress profiles (method: Section 4.1.1; results: Sections 4.2.1 to 4.2.4); the first is also used as a method for determining the transition from homogeneous to heterogeneous flow (method: Section 4.1.2; results: Section 4.2.5), with these flow regimes being described further below, in Section 2.2.6.

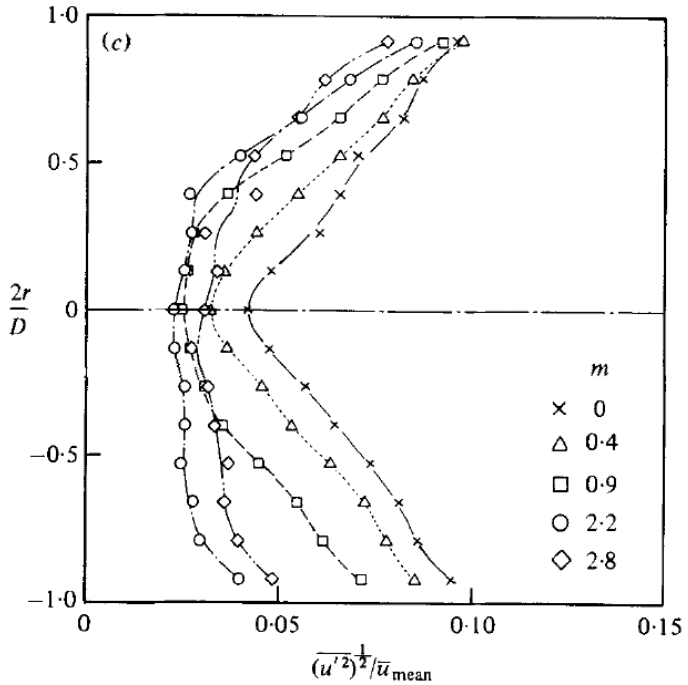

Figure 2-9: Turbulence intensity, $I = u'/\overline{U}$, *vs.* distance from pipe centreline at Re = 29,100, with small plastic particles (d = 0.2 mm) at several mass loadings, m (ϕ_m in this study). From Tsuji and Morikawa (1982).

2.2.6 Slurries and high-concentration flows

A slurry can be defined as "a suspension of solid particles in a carrier fluid" (Crowe, 2006). However, it is necessary to make a distinction between simple monodisperse suspensions and more complex bi-, polydisperse and polydense suspensions. Whereas the flow characteristics and rheology of simpler suspensions can be predicted from first principles, those of the more complex kinds that are commonly encountered in industry cannot. Instead it is necessary to rely more on empirical correlations that predict bulk behaviour, and while these methods give reasonable predictions for some flow quantities under certain conditions, they give no insight into the microscopic or fluid dynamical effects or particle-fluid interactions that occur.

Slurry flow has generally been characterised as follows (Crowe, 2006; Doron and Barnea, 1995; Wasp *et al.*, 1977):

1. Non-settling, in which the particles remain suspended in the carrier fluid;
2. Unhindered-settling, in which suspended particles can freely settle under gravity; or
3. Hindered-settling, in which hindrance to downward-moving particles is provided by upward-moving carrier fluid.

Alternatively, five slurry flow regimes, and various combinations thereof, are commonly described as:

1. Homogeneous (or pseudo-homogeneous), in which all particles are suspended and the concentration and velocity is constant across the diameter of the channel;
2. Heterogeneous, in which a concentration gradient exists in the suspension;
3. Flow with a moving bed, or sometimes "saltation" flow, in which some fraction of the suspended particles has settled and formed a sediment bed that moves along the channel;
4. Flow with a stationary bed, in which at least part of the sediment is stationary relative to the channel; or

5. Plug flow, in which the solids span the diameter of the channel and move *en masse*.

These regimes, with the exception of plug flow, as described more thoroughly by Crowe (2006), are shown schematically in Figure 2-10.

(a)

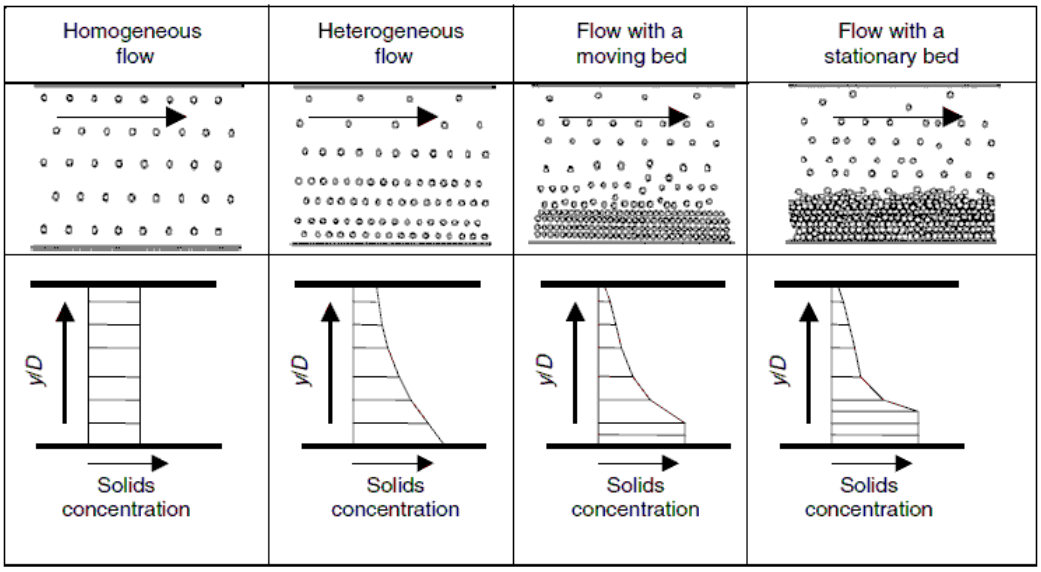

(b)

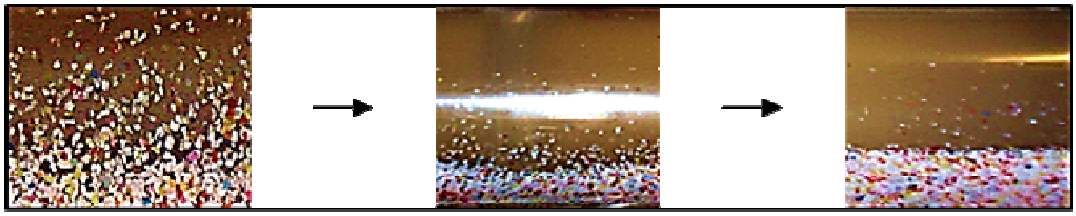

Figure 2-10: (a) Slurry flow regimes (Crowe, 2006); (b) homogeneous, moving bed and settled bed regimes in main flow loop, with Guyblast plastic beads (white bar in second frame is glare from lighting).

At low shear rates and low volume fraction (ϕ < 0.4 or so), fluid-particle suspensions (*viz.*, homogeneous and heterogeneous slurries and the suspended part of moving- and stationary-bed slurries) generally behave as Newtonian fluids, are shear-thinning (that is, pseudoplastic) at higher volume fractions (ϕ > 0.4), and a yield stress is often observed at very high volume fractions (that is, at ϕ > 0.5) (Crowe, 2006; Stickel and Powell, 2005).

Most commonly, the five flow regimes described above are delineated by the transition velocities U_{c1} to U_{c4}, respectively (Crowe, 2006). Of these, U_{c1} represents the velocity above which all solids are suspended homogeneously, while U_{c2} (or U_c)

is the velocity above which solids begin to settle out of a heterogeneous suspension and form a sediment bed. Some confusion exists because the term "critical velocity" (U_{min}) has also been used to describe the velocity at which the pressure drop reaches a minimum (Doron and Barnea, 1993; Doron *et al.*, 1987).

However, such confusion is avoided in this study, since U_{c1} is referred to as the homogeneous transition velocity hereafter, and U_{c2} as the limit deposition velocity, although they have been given several other names in the literature ("critical velocity", "minimum transport velocity" or "deposition velocity": Crowe, 2006; Harbottle, 2008). Methods for measuring, and measurements of, both U_{c1} (method: Section 4.1.2; results: Section 4.2.6) and U_{c2} (method: Section 4.1.3; results: Section 4.2.7) are presented in this study, and the reader is referred to those sections for more information.

2.2.7 Models and correlations of slurries and concentrated suspensions

There follows a summary of some models and experimental studies of concentration profiles in heterogeneous suspensions in pipes and channels. Karabelas (1977) derived a model for vertical particle concentration in pipes and channels and found excellent agreement with experimental results (plastic spheres, d_{50} = 210 and 290 μm, in kerosene, oil, and mixtures thereof) and those of Durand (1952) (sand, d_{50} ≈ 180 μm, in water).

Admiraal and García (2000) measured the particle concentration above a sand bed (d_{50} ≈ 120 and 580 μm) in a water channel using a predecessor of the model used in this study and the same UVP equipment. Gillies *et al.* (2004) presented concentration profiles for sand in pipe flow (d_{50} ≈ 90 and 270 μm, in water); it is also interesting to note that group's "two-layer" or "SRC" (Saskatchewan Research Council) model (Gillies and Shook, 2000) very accurately predicted the amount of suspended particles in high-concentration suspensions.

The numerical simulations of Ekambara *et al.* (2009) closely matched several sets of experimental pipe-flow data in terms of concentration, velocity and pressure drop. In one of several related papers, Matoušek (2009) presented concentration

profiles above a partially stationary sand bed (d_{50} ≈ 370 μm) and modelled the solid fraction as being composed of three layers – a stationary bed, a shear layer and a fully suspended layer – in contrast to the two-layer model of Gillies *et al.* (2004). Furlan *et al*. (2012) found good agreement between experimental and numerical results in horizontal and vertical pipe flow with glass beads (d_{50} = 210 μm) in water.

Lastly, it is interesting to note that, despite there being around sixty correlations for critical and limit deposition velocities in the literature (Estey and Hu, 1998; Kaushal *et al.*, 2002; Turian *et al.*, 1987), which were described earlier in Section , none has been properly verified (Majumder, 2007), despite there being obvious industrial applications. There follows a brief review of the prevalent slurry flow models; several more thorough reviews exist (Crowe, 2006; Matoušek, 2005). However, it should be noted that many models have been excluded for brevity, (most notably: Durand, 1953; Durand and Condolios, 1952; Eskin and Scarlett, 2005; Karabelas, 1977; Richardson and Zaki, 1954), since they are incorporated into the models described below, or are not considered definitive.

i. Roco, Shook and Gillies (or SRC) group

The "two-layer" model of Gillies *et al.* (1991), which was tested against experiments, actually incorporates three layers: a layer of suspended "fines", *i.e.* buoyant particles, and carrier fluid, and a bed with two components, a "contact load" which dissipates energy through friction with the wall, and a "suspended load", whose weight is held by the carrier fluid.

The model has been verified very successfully against experimental concentration profile data for coarse particles (sand, d = 0.18–2.4 mm) by Gillies and Shook (1994), and has undergone a number of refinements, including extension to higher volume fractions around the deposition velocity (ϕ > 35% or so) (Gillies *et al.*, 2000) and higher velocities (Gillies *et al.*, 2004).

ii. Turian and Oroskar group

The empirical pressure drop correlations of Turian and Yuan (1977) are based on a very large body of experimental data and have found wide application; they also provide a method of delineating the different flow regimes. The limit deposition velocity model of Oroskar and Turian (1980) and Turian *et al.* (1987) "showed good agreement ... with the experiment", and although "this model was oversimplified and not intended for dense slurries" (Eskin *et al.*, 2004), it is "the most sophisticated" and "most thorough" model available, even for suspensions in which $\phi < 25\%$ and $d < 50$ μm (Estey and Hu, 1998), although it was based on data from particles with diameters of hundreds of microns.

The limit deposition velocity correlation of Oroskar and Turian (1980) is described in detail here, as it is definitive and is used for comparison with the experimental results for the plastic (*i.e.* Guyblast) particle species presented in Section 4.2.7.

$$U_{c2} = 1.85[gd(s-1)]^{0.59}\phi^{0.1536}(1 - \phi)^{0.3564}\left(\frac{D}{d}\right)^{0.378}\left(\frac{D}{\nu_w}\right)^{0.09}\chi^{0.3}, \quad [2.18]$$

where s is the ratio of the solid to liquid densities and ν_w is the kinematic viscosity of water and χ is a hindered settling factor (which is close to unity for low volume fractions).

iii. Doron and Barnea group

A phenomenological two-layer model was presented by Doron *et al.* (1987) in which the slurry flow is treated as a moving bed with a heterogeneous fluid layer above. The pressure drop and mean velocities in the two layers and the velocity profile in the dispersed layer can be calculated directly, while the critical velocity (in this case, the velocity associated with the minimum pressure drop) can be determined graphically. However, the model fails to predict a stationary bed, which is often observed experimentally.

The results from the extended, three-layer model (Doron and Barnea, 1993), which incorporates the concept of a minimal bed velocity and a bed consisting of

stationary and moving parts, "constitute a significant improvement" over the two-layer model. Calculations compare well to experimental results for the pressure gradient (Doron and Barnea, 1995; Turian and Yuan, 1977), limit deposition velocity (Gillies *et al.*, 1991; Turian *et al.*, 1987) and flow patterns (Doron and Barnea, 1996).

iv. Poloski et al. group

The limit deposition velocity correlation of Poloski *et al.* (2010) is described in detail here, as it is used for comparison with the experimental results for the glass (*i.e.* Honite) particle species presented in Section 4.2.7. It is particularly applicable to smaller particles, as quantified by the Archimedes number, Ar, which the authors of that study note are not accounted for in many similar correlation and models. The Archimedes number is the ratio of gravitational to viscous forces acting on a particle, so for small Ar, particles are more strongly influenced by viscosity.

The correlation for the limit deposition velocity, U_{c2}, for Ar < 80 is as follows:

$$U_{c2} = 0.59[gD(s-1)]^{0.5}\mathrm{Ar}^{0.15}, \qquad [2.19]$$

where Ar is defined as

$$\mathrm{Ar} = \frac{4}{3}\frac{gd^3(s-1)}{\nu^2}. \qquad [2.20]$$

2.3 Summary and identification of opportunities

In Section 2.1, the physical mechanisms governing the interaction of ultrasound with particles in suspension were reviewed, and it was made clear that no computationally simple ultrasonic method exists for measuring the particle concentration in the engineering literature, despite the very wide range of possible industrial applications. With this in mind, a novel and robust method for measuring the suspended particle concentration with off-the-shelf ultrasonic

equipment is derived in Chapter 5, and extensive results are presented.

In Sections 2.2.1 to 2.2.5, the fluid dynamics of turbulent pipe flow and the influence of particles thereon were reviewed. A major aim of this project was to reproduce some of the results obtained using much more complex, expensive or technically challenging measurement systems (such as particle image velocimetry, laser Doppler anemometry and hot wire anemometry) with ultrasonic methods, with a view to applying the results to industrial problems. To fulfil this objective, extensive first- and second-order flow statistics are presented for a range of flows are presented in Sections 4.2.1 to 4.2.5.

In Sections 2.2.6 and 2.2.7, the various slurry flow regimes and critical velocities in multiphase flow were reviewed. These flow regimes, and the critical flow velocities that delineate them, were identified as fertile areas for study. In particular, novel methods for measuring the two critical flow velocities dividing homogeneous, heterogeneous and moving-bed regimes were devised (see Sections 4.1.2 and 4.1.3), with the aim of testing some prevalent correlations of limit deposition velocity in the literature, which exhibit significant scatter and are defined in a variety of ways. Lastly, the moving bed and settled bed regimes, the influence of which has received very little attention in engineering flows, are reviewed and studied separately in Chapter 6. All flow regimes are, therefore, covered by this study.

3 Experimental method

In Section 3.1, a review of the most commonly used techniques for interrogation of multiphase flow is presented, and justification is given for the decision to use an ultrasonic system in this study. The process of development and detailed specification of the experimental apparatus are presented in Section 3.2.1; thorough descriptions of the method of operation of the ultrasonic measurement system (Section 3.2.2) and the data processing method (Section 3.3) are also given. The notation used for coordinates and the velocity and Reynolds stress fields in this study is reiterated in Section 3.4.

The process of selecting suitable particle species is described in Section 3.5, which contains a summary of all the measured particle properties (size, density, shape and experimental suitability) in Table 3-7.

A range of instrumental calibration and data validation procedures were performed and are described in Section 3.6. Most importantly, the methods used to calibrate the probe position and flow rate are presented in Sections 3.6.3 and 3.6.4, while the mean-flow and near-wall calibration procedure is described in Section 3.6.6. Lastly, a novel method for measuring the thickness of settled beds and shear layers, which is used in several subsequent chapters, is described in Section 3.7, with examples.

3.1 Review and selection of measurement methods

An ultrasonic signal processor – the *UVP-DUO*, manufactured by *Met-Flow*, Switzerland – with two transducers operating at 2 and 4 MHz were used as the principal diagnostic system in this study, and the reasons for this choice are described in detail in this section.

To begin, there follows a brief review of the operational characteristics of the most commonly used diagnostic methods for the investigation of settling and non-settling, multiphase suspensions, which can be categorised as follows (Shukla *et al.*,

2007; Williams *et al.*, 1990):

1. External radiation, *e.g.* ultrasound, X-rays, gamma rays, microwaves, optical light/lasers, neutrons;
2. Emitted or internal radiation, *e.g.* radioactive and magnetic tracers, NMR/MRI;
3. Electrical properties, *e.g.* capacitance, conductance/resistance, inductance and associated tomographic methods, hot-wire anemometry;
4. Physical properties, *e.g.* sedimentation balance, hydrometric/density measurements, pressure, rheology;
5. Direct methods, *e.g.* physical sampling, pumping, interruption.

Williams *et al.* (1990), Bachalo (1994) and Powell (1994), for example, have also given thorough reviews of the most prevalent experimental techniques used for investigating multiphase flows, and it is interesting to note that Povey (1997) described analogous wave equations and complex wave velocities that can be defined for both acoustic and electromagnetic waves, and that the acoustic signal is influenced by the elastic, thermophysical and density properties of the fluid and suspended particles, whereas the electromagnetic signal is influenced by the dielectric properties and permeability.

A number of criteria must be considered when choosing the appropriate measurement apparatus, such as cost, potential hazards, physical size, ease of use and versatility, intrusiveness and the kind and accuracy of flow data that is required. Some of the most important of these criteria have been summarised for acoustic, optical and manual sampling methods and are presented in Table 3-1, which was compiled from a broad variety of sources (Admiraal and García, 2000; Hultmark *et al.*, 2010; Laufer, 1954; Lemmin and Rolland, 1997; Povey, 1997).

Table 3-1: Comparison of characteristics of several common methods for measuring concentration, particle size, velocity and stresses in flows and suspensions. Adapted from Lemmin and Rolland (1997), Povey (1997) and Admiraal and García (2000); Laufer (1954) and Hultmark *et al.* (2012) also consulted as examples.				
Characteristic	Manual sampling/ siphoning	Hot-wire (or film) anemometry (HWA)	Ultrasonic Doppler velocimetry (UDV) and backscatter (at single frequency)	Laser Doppler anemometry (LDA) and optical backscatter
Temporal resolution	Low, ~10 s	Very high, < 0.01 s	High, < 0.1 s	High, < 0.1 s
Spatial resolution	Depends on size of vessel and skill of operator, ~ few mm for siphon tube	Very high, < 100 μm	Depends on ultrasonic frequency, ~ 100 μm	Depends on size of vessel and skill of operator, ~ few mm
Measuring volume	As above, ~ few mm^3 for siphon tube	As above	Frustum of cone, ~few degrees	Cone, ~ 15° half angle, ~ 1 cm^3 volume
Concentration range	Any	-	Can penetrate high concentrations, but penetration depth depends on frequency and particle size (see Section 2.1.2)	No more than ϕ = 1 %; sample dilution usually necessary
Intrusiveness/ influence on flow	Intrusive	Intrusive, but influence minimal	Can be non-intrusive	Can be non-intrusive
Measurements per sample	One (single point)	One (single point)	Multiple (spatial profile)	One (single point)

Table 3-1: Comparison of characteristics of several common methods for measuring concentration, particle size, velocity and stresses in flows and suspensions. Adapted from Lemmin and Rolland (1997), Povey (1997) and Admiraal and García (2000); Laufer (1954) and Hultmark *et al.* (2012) also consulted as examples.				
Characteristic	Manual sampling/ siphoning	Hot-wire (or film) anemometry (HWA)	Ultrasonic Doppler velocimetry (UDV) and backscatter (at single frequency)	Laser Doppler anemometry (LDA) and optical backscatter
Calibration requirements	Not necessary	Always necessary, nonlinear	Sediment properties must be known or approximated	Sediment properties must be known or approximated
Particle size measurement	Can be measured directly, *ex situ*; all sizes accessible	-	As above; range of at least 0.1 to 100 microns can be accessed	As above
On-line flow visualisation	Not possible	Not possible	Possible	Not possible
Signal processing requirements	None	Low	Low	High
Mobility	Easy	Easy	Easy	Difficult, requires precise positioning
Cost	Very low	Low	Low	High

The use of EIT (electrical impedance tomography) for concentration profile measurement and LDA/PDA (laser/phase Doppler anemometry) and PIV (particle image velocimetry) for particle velocity measurement was ruled out in this study due to time, space and cost restrictions. The *UVP-DUO* was chosen as the principal measurement system in this study for those reasons, and more: as is clear from Table 3-1, acoustic instruments have many advantages over optical systems, most importantly low cost, high mobility, ease of operation, low signal processing and calibration requirements and the ability to measure entire profiles, rather than single-point measurements.

Indeed, McClements (1991) has listed a range of suspension properties - *e.g.* volume fraction, particle compressibility, particle size – that can be measured, and a range of processes – *e.g.* creaming, sedimentation, phase inversion and other phase transitions – that can be monitored with ultrasonic systems using the speed of sound, attenuation and other, less commonly used ultrasonic properties (*e.g.* impedance, angular scattering profile). It should be noted that, although acoustic particle sizing techniques have found wide application, especially in the form of attenuation spectroscopy, such techniques are not the subject of this study. However, some aspects of acoustic sizing methods are included in Table 3-1 for the purpose of comparison and completeness.

Other, more recent reviews of ultrasonic measurement techniques have also been published from a general perspective with an emphasis on colloidal suspensions (Challis *et al.*, 2005) and from a marine perspective (Thorne and Hanes, 2002). The authors of the former review are particularly keen to emphasise the benefits of ultrasonic methods over others, a few of which are described in Table 3-1.

In fact, in addition to those listed above, several acoustic properties have been exploited by other researchers in the Nuclear Research Group at the University of Leeds to measure the properties of a range of flowing and settling suspensions, *e.g.* settled bed depth using a Doppler velocity threshold method (Hunter et al., 2011), the motion of a cloud front using the backscatter signal, and particle concentration from the gradient of the backscatter signal (Hunter *et al.*, 2012a; Hunter *et al.*,

2012b).

However, one capability of the *UVP-DUO* instrument in particular, and ultrasonic systems in general, is to interrogate suspensions of much higher concentrations than is possible with optical methods. This capability, along with the many advantages described above, formed the basis for the choice of the *UVP-DUO* as the principal diagnostic instrument in this study, as one important objective was to investigate suspensions with particle volume fractions of several per cent.

3.2 Specification of flow loop and ultrasonic measurement system

The method of operation of the main flow loop as a whole, and some specific aspects of the *UVP-DUO* system, are described in Sections 3.2.1 and 3.2.2, respectively.

3.2.1 Main flow loop

All experiments were performed in the Sorby Environmental Fluid Dynamics Laboratory (SEFDL) in the School of Earth and Environment at the University of Leeds. A summary of the components of the experimental rig is presented in Table 3-2 and a diagram and photograph of it are presented in Figure 3-1.

The recirculating flow loop was designed, commissioned and optimised by the author in its entirety specifically for this project. An existing flow loop (D = 25 mm) in the Sorby Laboratory (Harbottle, 2008) was available but considered to be unsuitable, for a number of reasons: the mixing tank was difficult to access and uncovered; the peristaltic pump lacked the necessary pumping power and, on account of operating peristaltically, produced a time-varying flow rate; and because a larger inner diameter was required, in order to maximise the spatial resolution of measurements.

As described in the preceding section (Section 3.1), an ultrasonic system was

chosen for several reasons, most importantly cost, portability, safety and versatility. For the on-line measurements reported in this study, a *UVP-DUO* signal processing unit manufactured by *Met-Flow* SA (Switzerland) was used, with transducers manufactured by Imasonic, France.

Table 3-2: Description of flow loop components and diagnostic equipment. See Figure 3-1 for photograph of flow loop and Figure 3-2 for photograph of transducer assembly.

Component	Description	Supplier/ manufacturer
Mixing tank	Stainless steel, diameter 50 cm, height 80 cm. Circular lid divided into two parts, one of which is removable for water and solids entry, physical sampling and maintenance.	In-house
Mixer	Electromotor MA 71G-6, 0.25 kW rating, in-line assembly with inverter and control box. Attached to larger (fixed) section of mixing tank lid.	PH Pumps, Suffolk
Mixer shaft	700 mm total length (*i.e.* 100 mm from bottom of tank); three-vane impeller, total diameter 80 mm.	
Flow meter	ABB *Magmaster*, electromagnetic type, with inverter and control box	
Pump	Ebara DWO 200, centrifugal type, 2 kW rating, with inverter and control box.	
Pipework and fittings	UPVC pipe, clear and opaque, inner diameter D = 42.6 (and 50 mm outer). Some flexible steel-reinforced plastic hosing also used.	IPS Flow Systems, Pipestock Ltd.
Ultrasonic signal processor	*Met-Flow UVP-DUO* Doppler velocimeter.	*Met-Flow* SA, Switzerland
Transducers	Imasonic 2 and 4 MHz, piezoelectric, 5 mm active diameter, 8 mm including casing (plastic and steel, respectively).	

The transducers were attached to the flow loop at the point shown in Figure 3-1 in a novel manner such that the two probes of different frequencies (2 and 4 MHz) were mounted at different angles to the mean axial flow direction (135 and 90 degrees, respectively), as shown in Figure 3-2. In this novel arrangement, the

system offered the ability to make all the measurements necessary to reconstruct the mean and turbulent velocity and stress vectors (see Chapter 4, and Section 4.1.1 for the method of decomposing the axial and wall-normal components), as well as concentration profiles (using the dual-frequency inversion method, as described in Chapter 5).

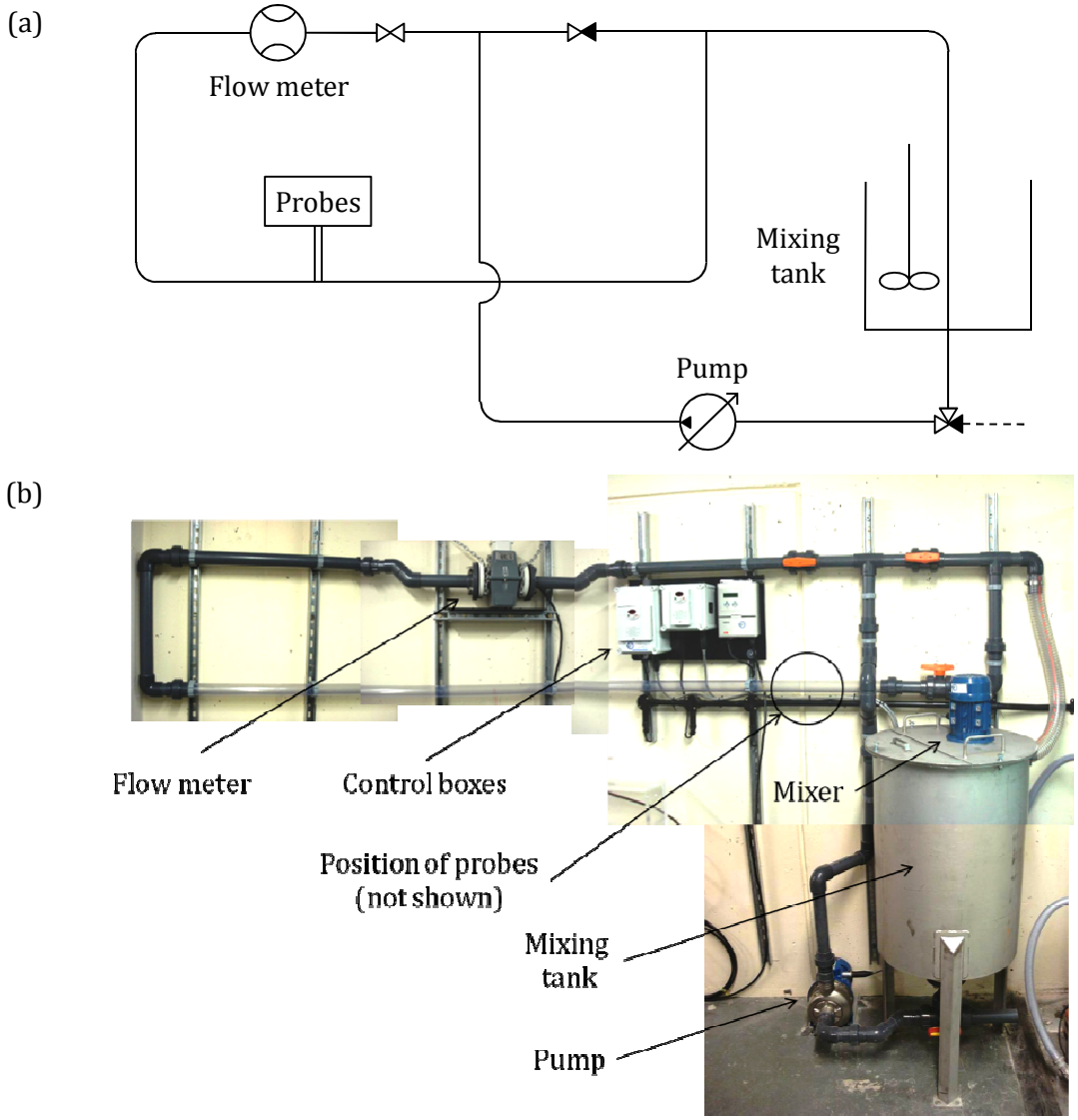

Figure 3-1: Main flow loop. (a) Diagram; (b) composite photograph. Inner diameter, D = 42.6 mm; entry length, L = 3.2 m.

It should also be noted that an angle of 135 degrees was chosen for the 2 MHz probe because the probe therefore pointed *upstream*, and so caused less flow disturbance than if it had been pointed *downstream*, that is, at 45 degrees. The choice of a mounting angle of 135 degrees, rather than, say, 120 or 160 degrees,

was chosen as a compromise: a shallower angle to the flow direction means the probe would project further into the flow and the on-axis distance from the probe to a given point in the flow (and the corresponding signal attenuation) would become larger, whereas a less shallow angle would reduce the accuracy of the axial velocity measurements.

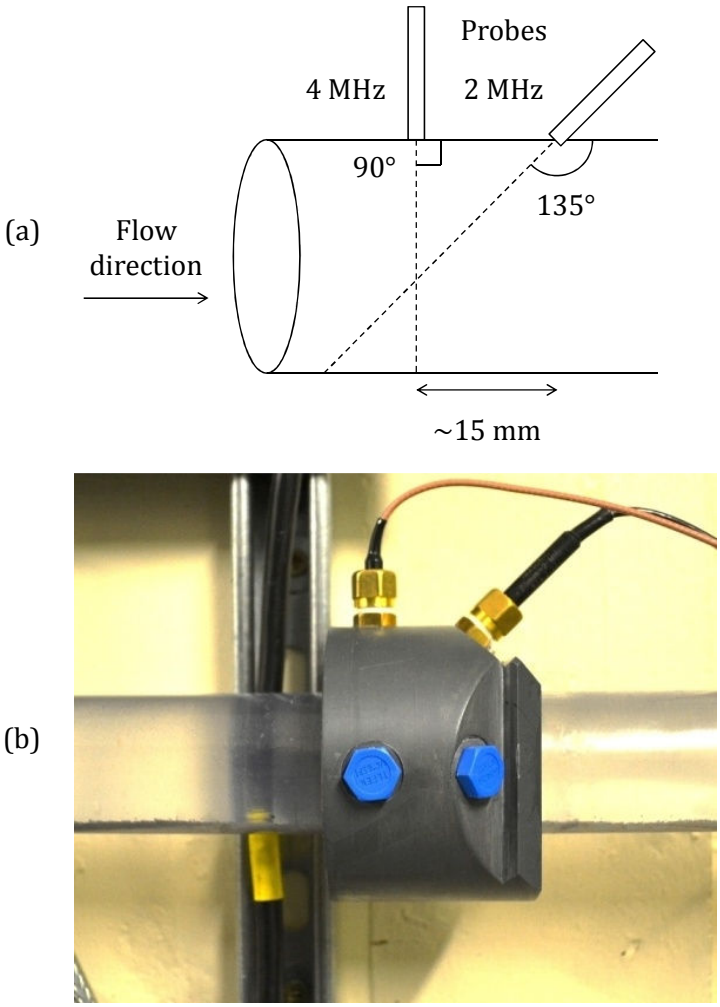

Figure 3-2: Probe mounting geometry. (a) Diagram of probe arrangement; (b) photograph of probes attached to mounting clasp at 90 and 135 degrees to direction of mean flow. Inner pipe diameter, D = 42.6 mm; active transducer radii, a_t = 5 mm.

It is important to note that the probes were in direct contact with the contents of the pipe: holes were drilled through the pipe wall and an outer clasp was attached through which the probes were inserted and secured so that (a) a watertight seal was achieved (using PTFE tape on the threads of the brass fastening nuts); and (b) the probe tips were positioned as close as possible to being parallel to the inner pipe wall (by inserting another, smaller-gauge pipe – with an outer diameter of 40

mm – into the test section, and fastening the nuts once the probes came into contact with the inner pipe, which was then retracted).

A non-intrusive arrangement was initially attempted, but a good and consistent contact with the pipe wall could not be achieved and the resulting data were not reliable, even though probe-shaped indentations were made part-way through the pipe wall and ultrasonic contact gel was used.

To summarise, the objective of building the flow loop in the manner described was to allow suspensions of particles of several per cent by volume to be generated and maintained indefinitely over a wide range of flow rates. The general experimental procedure was as follows:

1. The probes were attached to their mounting and checked for a watertight seal.
2. If necessary, the mixing tank was filled and the flow loop flushed to the drain several times to remove any sediment remaining from previous experiments.
3. The valve under the mixing tank was closed, and the mixing tank filled with 100 litres of mains water and left overnight so that the water could degas and its temperature could equilibrate.
4. The valve under the mixing tank was opened and water was pumped around the flow loop for several minutes so that leaks could be checked for.
5. The mixer was turned on to the maximum safe speed (25 Hz) and the suspension circulated through the flow loop for several minutes. The flow rate was varied using the pump control box. By opening or closing the two valves on the top section of the flow loop (red handles, Figure 3-1(b)), the flow rate through the test section (and the flow meter) could be varied over several orders of magnitude (at least $5{,}000 < \mathrm{Re} < 150{,}000$, *i.e.* $0.15 < Q < 4$ l s^{-1} or so) and maintained indefinitely.
6. A known, weighed mass of sediment was wetted and poured into the tank through the removable section of the lid and mixed for several minutes. In general, incremental masses were added in sequence, up to a maximum of $\phi = 3$ %.

7. The *UVP-DUO* was then set running, with echo voltage and Doppler velocity data from each transducer gathered in separate runs.

The data processing method is described thoroughly in a dedicated section later (Section 3.3). In terms of off-line measurements, a number of particle characterisation measurements were taken, as described in Section 3.5. In addition to the main flow loop, a smaller stirred mixing vessel (SMV) was used to produce homogeneous suspensions in order to measure the acoustic properties of each particle species, and is described in Section 5.2.2. Physical samples were also taken from both the mixing tank of the main flow loop and the SMV for validation purposes (3 × 60 ml samples in each run, of which the mean and standard deviation were taken).

3.2.2 Basic operation of *UVP-DUO* ultrasonic measurement system

In this study, two cylindrical piezoelectric transducers were used, and a brief description of their mode of operation follows. A diagram of the sound field generated by such a transducer – *i.e.* a "pulsed monostatic" transducer (Hay and Sheng, 1992) – is shown in Figure 3-3; the emission geometry and directivity pattern are shown. The important points to be taken from Figure 3-3 are as follows:

a. The directivity pattern (D^2 in the figure) varies with angle (Hay, 1991), where the directivity is a measure of emitted ultrasonic power density. The peaks in D^2 are referred to as main and side lobes, the distance between which provides the basis for one method of determining the angle of divergence of the ultrasonic pulse, γ_0. Another method is to measure the angle at which the intensity decreases to some proportion of the central value, as described below. Both methods were used by Hay (1991).
b. The beam reaches a focal point, in the vicinity of which the spatial accuracy of the probe is greatest. The distance to the focal point depends on the ultrasonic frequency and the size of the transducer's emitting face, as described below.

c. The measurement volume a disk in an ideal system with zero beam divergence (*i.e.* $\gamma_0 = 0$), but in real systems the zone is a conical section of a spherical annulus.

(a)

(b)

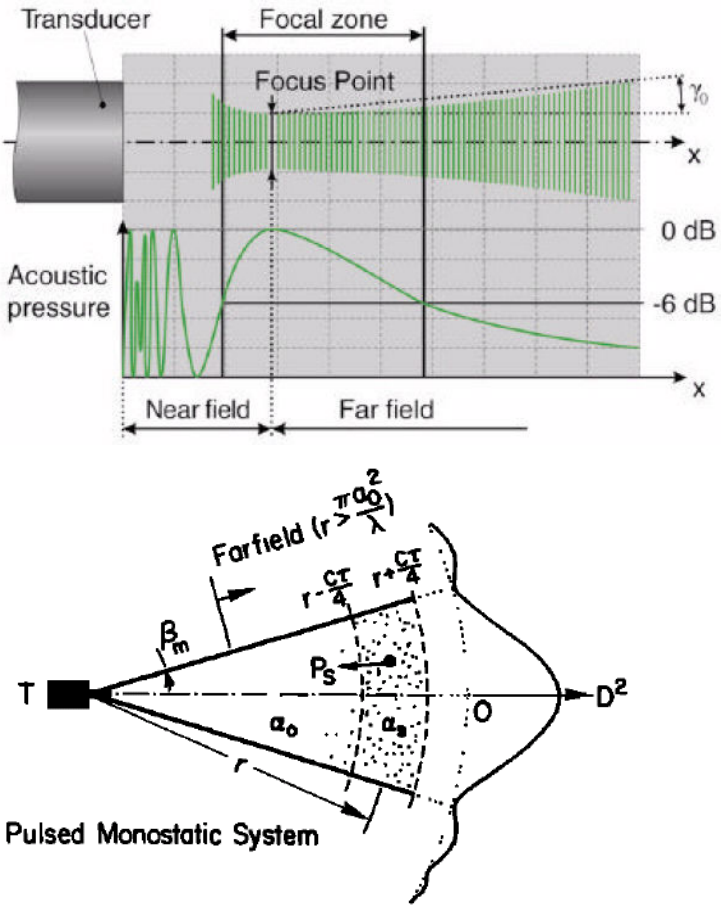

Figure 3-3: Geometry of sound field generated by a pulsed monostatic acoustic transducer. (a) View showing focal zone and near- and far-field regions. From *Met-Flow* (2002); (b) simpler view, in which *T* is transducer position and *D* is directivity, a measure of acoustic power, which varies with angle. From Hay and Sheng (1992).

Whereas Hay (1991) calculated the angle to the directivity "mainlobe half-widths at -3 and -12 dB", here the half-angle at which the sound pressure has decreased by -6 dB (*i.e.* to one half) is used as the beam divergence angle such that (*Met-Flow*, 2002):

$$\gamma_0 = \sin^{-1}\left(0.255\frac{\lambda}{a_t}\right). \qquad [3.1]$$

Zemanek (1971) studied the pressure field produced by a piston transducer and found that the distance from the active face to the point at which the pressure reaches a maximum, r_f, which is also the point at which the beam is narrowest, is:

$$z_f = 1 - \frac{0.25}{(a_t/\lambda)^2}, \qquad [3.2]$$

where

$$z = r/r_f, \qquad [3.3]$$

and $z_f = z(r_f)$ such that $z_f = 1$ in the limit of large a_t/λ. For the two transducers used in this study, the values z_f = 97.8 and 99.5 %, respectively, are obtained from Equation [3.2]. For this reason, r_f is hereafter approximated as a_t^2/λ and is referred to as the focal distance to avoid confusion with near-field distance, r_n (Downing *et al.*, 1995), that is used later in Chapter 5.

For reference, the values of various parameters for the two ultrasonic transducers used in this study are given in Table 3-3, including values for both r_f and r_n (where it should be noted that $r_n = \pi r_f$; see text and Equation [3.2]), and the beam divergence angle, γ_0 (Equation [1]). The effect of beam divergence on calculated quantities is described in detail in the appendix (Appendix A), as it was identified as being a possible source of experimental error, and is modelled as being linear with respect to distance.

Table 3-3: Transducer dimensions and beam characteristics.

Frequency, f (MHz)	Radius of active face, a_t (mm)	Focal distance, r_f (mm)	Near-field distance, r_n (mm)	Beam divergence angle, γ_0 (degrees)
2	2.5	8.45	25.3	4.33
4	2.5	16.9	50.7	2.16

In this study, voltage time-series data were recorded using the ultrasonic probes in order to calculate both the RMS of the echo voltage and the Doppler velocity, the latter being calculated by the *UVP-DUO* instrument using a fast Fourier transform

of the time series. The data processing method is described in more detail in Section 3.3. However, there follows a description of the basic principles of Doppler velocimetry and the method of operation of ultrasonic transducers and the *UVP-DUO* instrument.

It should be noted that, although the *UVP-DUO* is intended for use as a Doppler velocimeter, the time series of the received echo voltage – *i.e.* the voltage excited in the transducer by sound reflected by scattering particles in suspension – also contains a great deal of interesting information. So, the *UVP-DUO* is used for two purposes in this study, as follows:

1. *As a backscatter system*: the amplitude of the received voltage – as quantified by the root-mean-square (RMS) average of n samples – is used to detect the position of settled beds and shear layers (see Section 4.1.3 and Chapter 6, for example) and is also required by the dual-frequency inversion method in order to calculate the concentration of suspended particles (see Chapter 5);
2. *As a Doppler velocimeter*: the instrument performs a fast Fourier transform on the time-series of the received echo voltage; the resulting instantaneous Doppler velocity data, and their statistical variation in space and time in two dimensions, are used in this study to quantify the mean and turbulent flow behaviour and the normal and shear Reynolds stresses (see Chapter 4).

There follows a description of the measurement system and the method of determining the instantaneous echo voltage and Doppler velocity. The two transducers used in this study are of the piezo-electric type – *i.e.* ceramic cylinders of total diameter 8 mm (or 5 mm, not including plastic or steel casing), operating at frequencies of f = 2 and 4 MHz – that both emit and receive. The transducers are excited by an applied voltage (set to the maximum 150 V in this study) and emit an ultrasonic pulse of known duration and wavelength; scatterers in the flow (*i.e.* suspended particles) reflect or diffract some of the acoustic energy in the direction of the transducer axis, and the vibration excites a voltage in the transducer (in the range ± 2.5 V).

The *UVP-DUO* applies a variable gain to the voltage and records it as 14-bit data. The process of removing the gain and digitisation constant is described in more detail in the data processing methodology section (Section 3.3), but here the basic instrumental parameters are described, and the text is based on the *UVP-DUO* user manual (*Met-Flow*, 2002) and a standard signal processing reference (Orfanidis, 1996), to which the reader is referred for more information.

A schematic diagram of the measurement points is shown in Figure 3-4. The minimum measurement distance, r_0, can be set in the instrumental software (generally, r_0 = 2 mm in this study), whereas r_{max} is determined by the Nyquist sampling theorem, as described below. The distance to the centre of each measurement volume, r, is simply:

$$r = \frac{ct}{2}, \qquad [3.4]$$

where c is the speed of sound and t is the delay between the transmitted and received signal. It is therefore important that c be measured precisely, and the effect of the speed of sound on measurement distance is quantified by propagation of errors in the appendix (Appendix A). The measurement channel width, w, is determined by the wavelength of the emitted ultrasound, f (or alternatively the wavelength, λ), such that:

$$w = \frac{Nc}{2f} = \frac{N\lambda}{2}, \qquad [3.5]$$

where N is the number of cycles per emitted pulse, which is set in the instrumental software by the user.

The maximum measurable distance, r_{max}, is determined simply by the pulse repetition frequency, F, *i.e.* the sampling frequency:

$$r_{max} = \frac{c}{2F}. \qquad [3.6]$$

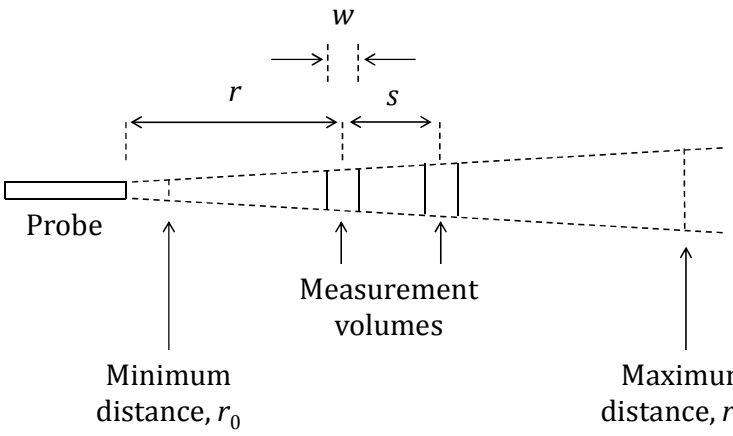

Figure 3-4: Schematic diagram of measurement points. Distance to centre of measurement volume, *i.e.* distance to nominal measurement point, is *r*; distance between measurement points is *s*; width of each measurement volume is *w*. Minimum and maximum distances are r_0 and r_{max}, respectively.

The *UVP-DUO* software performs a fast Fourier transform (FFT) on the received voltage, and the dominant frequency, f_r, of the frequency spectrum is related to the velocity (parallel to the probe axis) of the scatterers in the measurement volume, U_p, by the Doppler equation, which is as follows:

$$U_p = \frac{c\Delta f}{2f} = \frac{\Delta f \lambda}{2}, \qquad [3.7]$$

where Δf is the frequency shift relative to the frequency of the emitted pulse such that

$$\Delta f = f_r - f. \qquad [3.8]$$

The Nyquist sampling theorem requires that, for the sampled time-varying signal to be accurately represented by its samples, the sampling rate must be at least twice the maximum frequency shift, Δf_{max}. The sampling rate, *F*, is known, so the sampling theorem is incorporated in the following expression:

$$\Delta f_{max} = 2F. \qquad [3.9]$$

Equation [3.9] implies that, for a given sampling rate, *F*, there is a corresponding

limit on the Doppler shift (and therefore flow velocity) that can be measured if the sampled data are to be representative. However, the relationship between the frequency shift in the received signal and the underlying velocity of scatterers is fundamental to the principle of Doppler velocimetry, and the two quantities are related by the Doppler equation, as described above. As such, a limiting frequency shift corresponds to a limiting Doppler velocity, which is found by setting $\Delta f = \Delta f_{max} = F/2$ in Equation [3.7], to obtain the velocity bandwidth, U_{bw}, *i.e.*:

$$U_{bw} = \frac{cF}{2f}. \qquad [3.10]$$

Since the Doppler velocity (and, indeed, echo voltage) data were quantised into 14-bit data, each could take one of $N_d = 2^{14}$ values, so the velocity resolution, ΔU, as distinct from the velocity bandwidth, U_{bw}, was:

$$\Delta U = \frac{U_{bw}}{N_d}. \qquad [3.11]$$

Lastly, by multiplying the expressions for r_{max} (Equation [3.6]) and U_{bw} (Equation [3.10]), the following is obtained:

$$r_{max} U_{bw} = \frac{c^2}{4f}, \qquad [3.12]$$

from which an important conclusion can be drawn: the right-hand side is a constant for a particular system, so a compromise must always be made between the velocity bandwidth and the limit of the measurement window. In general, this limitation must always be considered. Although not found to be severe in this study, since the frequencies of the transducers was chosen such that it was minimised, the limitation set by Equation [3.12] did cause slight truncation of the velocity profiles at the highest flow rates (see, for example, Figure 4-3(a)), and consequently the echo amplitude profiles (*e.g.* Figure 5-20).

3.3 Data processing method

The software provided by *Met-Flow* for use with the *UVP-DUO* signal processing unit is not capable of combining pairs of datasets in order to construct velocity and stress vectors, as described in Chapter 4, or calculating certain quantities, such as the root-mean-square of the echo, which must be known if the dual-frequency concentration inversion method, as described in Chapter 5, is to be used. Therefore, a suite of MATLAB scripts was written to process and analyse the raw data (and present/plot the results).

A flow chart of the general data processing method, which covers the entire study, is presented in Table 3-4, which contains a number of links for the reader to the relevant sections. Then, a description follows of the procedure that was employed to remove the gain and digitisation constant that was applied by the *UVP-DUO* software to the echo voltage data.

Table 3-4: Flow chart summarising overall data processing method, with references to sections where each procedure is described in more detail.

	Procedure	See for more details
1	Echo voltage (±2.5 V) digitised by *UVP-DUO* into 14-bit data	Section 3.2.2
2	Fourier transform performed on echo time series by *UVP-DUO* to give instantaneous and mean Doppler velocity	Section 3.2.2
3	Echo and Doppler velocity data imported as text file into MATLAB	-
4	Gain and digitisation constant removed from echo to recover voltage (±2.5 V)	This section
5	Three-sigma (3σ) noise filter applied to echo and Doppler velocity data	Section 3.6.5
6	RMS voltage and Doppler velocity calculated for each set of n samples and for whole run (2,500 or 5,000 samples)	-
7	Distance calibrated for each probe	Section 3.6.3
8	Voltage, Doppler velocity and distance data projected onto common axis (perpendicular to upper pipe wall) by linear interpolation	Section 4.1.1

The excitement of the probe by backscattered sound generates a raw voltage (±2.5 V) that is converted to 14-bit data by the *UVP-DUO* software, in which a user-specified gain, g, is applied that is time-/distance-dependent in the general case.

Once the raw data has been imported into MATLAB, the first task was to remove the gain, and the second was to recover the raw voltages from the digitised values. MATLAB scripts were written by the author for this purpose. The gain settings, which apply to both the 2 and 4 MHz transducers, were kindly provided by Olivier Mariette of *Met-Flow* and are given in Table 3-5.

Table 3-5: *UVP-DUO* gain settings. Provided by Olivier Mariette, *Met-Flow SA*, Switzerland.

Setting	3	4	5	6	7	8	9
Absolute	0.91	1.76	3.41	6.67	15.00	25.00	60.00
Log. (dB)	-0.8	4.9	10.7	16.5	23.5	28.0	35.6

The user specifies the start and end, r_1 and r_2, of the measurement window and the gain settings $g_1 \equiv g(r_1)$ and $g_2 \equiv g(r_2)$ that are applied by the *UVP-DUO* software; $g(r)$ varies exponentially between those two points such that:

$$g = Ae^{B(r-r_1)}, \qquad [3.13]$$

where A and B are constants for a particular choice of window and gain settings. By applying the boundary conditions described above, it becomes clear that $A = g_1$ and $B = \ln(g_2/g_1)/(r_2 - r_1)$. When written out in full, the expression becomes:

$$g(r) = g_1 \exp\left[\ln\left(\frac{g_2}{g_1}\right).\frac{(r - r_1)}{(r_2 - r_1)}\right]. \qquad [3.14]$$

Alternatively, the expression can be written more simply as follows:

$$g(r) = A'e^{Br}, \qquad [3.15]$$

where B is as above and A is as follows:

$$A' = g_1 \exp(-Br_1). \qquad [3.16]$$

Then, the RMS of the voltage – *i.e.* the echo amplitude – is recovered from the RMS of the raw echo data, E, thus:

$$V(r) = \frac{5E(r)}{N_d g(r)} = \frac{3.052 \times 10^{-4} E(r)}{g(r)}, \qquad [3.17]$$

since N_d = 2^{14}, as described in Section 3.2.2. (It should be noted that E_{inst} is the instantaneous raw echo, from which the RMS, E, is calculated.)

3.4 Choice of coordinate system and notation: reiteration

For clarity, the choice of coordinate system and notation used in this study is reiterated in this section, and the reader is referred to the literature review (Section 2.2.1) for more information.

First, the symbols y, θ and z were chosen to represent the principal coordinates in the wall-normal, azimuthal and axial directions, respectively, because they appear to be the most common in the engineering literature. In particular, y is defined as the wall-normal distance from the upper pipe wall, through which the ultrasonic probes are mounted. The coordinates are illustrated in Figure 3-5.

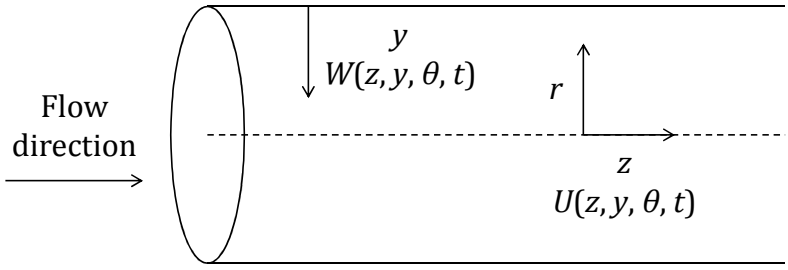

Figure 3-5: Diagram showing geometry of pipe flow, with notation for coordinates and velocity components used in this study shown. Also shown in Figure 2-2.

Second, the symbols U, V and W are used to represent the instantaneous velocities in the r, θ and z axes, respectively, and the various components of the Reynolds

decomposition process are shown in Table 3-6. The notation follows Hinze (1959).

Third, the ultrasonic probes used in this study were mounted vertically, *i.e.* in the *z*-*r* plane, so measurements in the azimuthal direction were not taken.

Table 3-6: Summary of notation for coordinates and velocity/stress components used in this study. Also shown in Table 2-2.				
Direction/axis, symbol	Velocity components			
	Instantaneous	Mean instant.	Fluctuating	"RMS"
Axial, z	$U(z,\theta,y,t)$	$\bar{U}(z,\theta,y)$	$u(z,\theta,y,t)$	$u'(z,\theta,y)$
Azimuthal, θ	$V(z,\theta,y,t)$	$\bar{V}(z,\theta,y)$	$v(z,\theta,y,t)$	$v'(z,\theta,y)$
Wall-normal, y	$W(z,\theta,y,t)$	$\bar{W}(z,\theta,y)$	$w(z,\theta,y,t)$	$w'(z,\theta,y)$

Fourth, the three components of the Reynolds stress tensor that were measured in this study were the axial and wall-normal stresses, *i.e.* $\overline{u^2}$ and $\overline{w^2}$, and the axial/wall-normal shear stress, $\overline{uw}$. The expected behaviour of these quantities in pipe flow was described in more detail in Section 2.2 (review of fluid dynamics). The simple relationship between RMS velocity, u' – that is, the RMS of the fluctuating part – and the normal stress, $\overline{u^2}$, in the axial direction, z, is as follows:

$$u' = \sqrt{\overline{u^2}} = \left[\frac{1}{n}\sum_{i=1}^{n} u^2\right]^{1/2} = \left[\frac{1}{n}\sum_{i=1}^{n} (U-\bar{U})^2\right]^{1/2}, \qquad [3.18]$$

and an analogous relationship exists for axial component, w, in the wall-normal direction, y.

3.5 Selection and characterisation of particle species

Several specific physical criteria were used in order to cover as large a parameter space as possible, such as: particle size and size distribution, density, shape and tendency to aggregate. In particular, particle species with a narrow size distribution and no tendency to form aggregates were preferred. However, the degree of monodispersity was generally found to vary in direct proportion to cost,

so a balance had to be found between those two criteria.

The nominal diameter of the particle species given by the manufacturer or supplier required verification, since several possible sources of inaccuracy exist. For example, samples may have been obtained from a larger bulk mass of powder in which segregation according to size had occurred due to settling; moreover, the quoted particle sizes were in many cases upper limits or mesh sizes of the sieve through which the batches had been passed.

However, a number of other, more general criteria also had to be considered when selecting particle species. Some of the most important of these were: cost; safety, *i.e.* toxicity, ease of disposal and the possibility of unwanted chemical reactions; and availability. A full summary of all the particle species that were tested for suitability is presented in Table 3-7. Ultimately, four species were chosen for use in the majority of the experimental programme, the reasons for which are presented in below. A fifth species, polyamide plastic, was also used in a small number of very low-concentration runs for the purpose of flow meter calibration (see Table 3-10 in Section 3.6.6), but was too expensive to be used extensively.

Initially, Sphericel hollow glass spheres were tested as tracer particles to be used in the low-concentration runs. Though ideal in terms of size and density, the cost was prohibitively high. A number of higher-density species were tested – silicon dioxide, titanium dioxide, manganese (III) oxide, chromium (IV) oxide, molybdenum carbide and tungsten carbide – but were excluded on the basis of cost, toxicity and the difficulty associated with keeping the species suspended in the flow loop. In addition, the suspensions and sludges that were created had to be disposed of as hazardous waste at considerable cost. Lastly, Turbobead steel particles were tested and, although non-toxic (and therefore suitable for disposal to the drain) and quite affordable, they caused severe rusting to the inside of the steel mixing tank after only 48 hours and were therefore rejected.

Because of the shortcomings of many of the particle species described above, and particularly the more dense ones (which tended to be more difficult to keep

suspended and dispose of), it was decided that less dense, more affordable and non-toxic particle species would be used in the main experimental runs. As a result, a number of blast media products from Guyson International (Skipton, U.K.) were identified – namely two Honite soda-lime glass and two Guyblast urea formaldehyde plastic species of two different sizes each. These species covered a large range of particle sizes, a moderate range of densities and exhibited different particle shapes. In addition, the densities of the Honite and Guyblast species are similar to those of magnesium and aluminium, respectively, which, as described in the introduction to this study (Section 1.1), are the main constituents of magnox fuel cladding, a common component of the UK radioactive waste inventory.

In addition, a small mass of polyamide particles – manufactured by Dantec Dynamics and typically used as fluid tracers in particle image velocimetry measurements – was used in the flow rate calibration runs described in Section 3.6.4.

A range of particle characterisation studies were performed on the selected species, which were as follows: particle sizing measurements (Section 3.5.1); (Section 3.5.2); packing fraction measurements (Section 3.5.3); and determination of particle shape by optical and scanning electron microscopy (Section 3.5.4). The results are summarised in Table 3-7 and discussed in Section 3.5.5.

3.5.1 Particle sizing

Mastersizer 2000 and *3000* particle sizing machines (Malvern Instruments, UK) were used to perform the measurements. The instruments use laser diffraction to measure the diameter of sample particles in suspension in deionised water.

Small amounts (~mg) of sample were added to a stirred vessel within the apparatus and diluted automatically by the machine until the correct level of attenuation necessary for diffraction to occur was attained. For each sample, the stirrer speed was varied so that results were only accepted if the particle size showed no variation over time. That is, data were rejected if aggregation was

thought to be occurring during a run. Averages over ten runs were taken and the data outputted as CSV-type files.

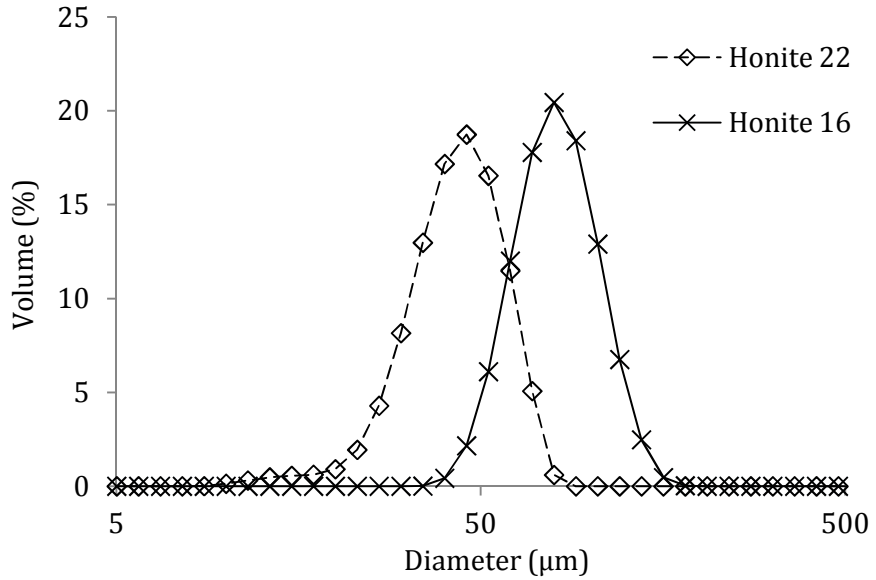

Figure 3-6: Particle size distribution of Honite particle species. Data from *Mastersizer 2000*, Malvern Instruments.

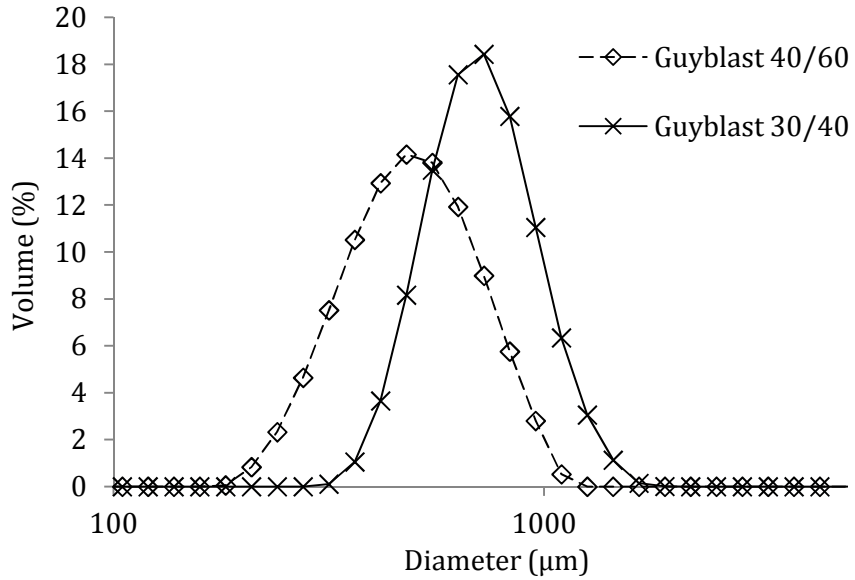

Figure 3-7: Particle size distribution of Guyblast particle species. Data from *Mastersizer 3000*, Malvern Instruments.

The particle size distributions for the Honite and Guyblast particle species are shown in Figure 3-7 and Figure 3-6, respectively, and it should be noted that the x-axis is logarithmic in both cases. With the exception of Honite 22, which shows a

small secondary peak in the range $10 < d < 30$ μ or so, the distributions for all particle species show a single peak, *i.e.* they are unimodal. This means that, although they are not strictly (or even approximately) monodisperse in the sense that all the particles have the same diameter, their size distributions are approximately log-normal and are accurately described by a mean and standard deviation; this also means that, to first order, their behaviour in suspension can be estimated more accurately than species with bimodal or even more complex size distributions.

3.5.2 Particle density measurement

A Micrometrics AccuPyc 1330 pycnometer was used to measure the particle densities. A small sample of a known mass (5-10 g) of each particle species was put into a small aluminium vessel, and a sealed cap placed over it. The machine then pumps in a measured volume of noble gas and the volume occupied by the species is calculated according to the ideal gas laws. The results are averaged by the apparatus over at least five runs and outputted as ASCII-type text files.

3.5.3 Packing fraction measurement

It was necessary to measure the packing fraction, p, for use in the bed depth calculations in Section 4.2.7 and Chapter 6. This was done manually using standard volumetric flasks and scales: known volumes were weighed and the packing fraction calculated using the measured particle densities. To rule out wall effects – that is, the tendency of vessel walls to influence the measured packing fraction if the vessel's size is similar to that of the particle diameter – p was measured using at least three flasks of different volumes (50, 100, 250 and 500 ml).

The relative standard deviation (RSD, *i.e.* the standard deviation divided by the mean, σ/μ) was of the order of 1 % for all four species, *i.e.* wall effects appear to have been insignificant. This was to be expected, since the diameter of even the smallest vessel was much larger than the diameter of the largest particle species.

3.5.4 Determination of particle shape

A number of optical micrographs were taken of each particle species with a Olympus BX51 optical microscope at various magnifications in order to investigate their shape and tendency to aggregate. Micrographs are also presented for the four species, as follows: Guyblast 40/60, Figure 3-10; Guyblast 30/40, Figure 3-11; Honite 22, Figure 3-8; and Honite 16, Figure 3-9.

It is clear from micrographs that the Honite particles are well approximated as spheres, whereas the Guyblast particles are irregular and jagged. This difference in shape was one reason that they were chosen, *i.e.* so that the effect of particle shape could be investigated, and it is discussed in the relevant results section.

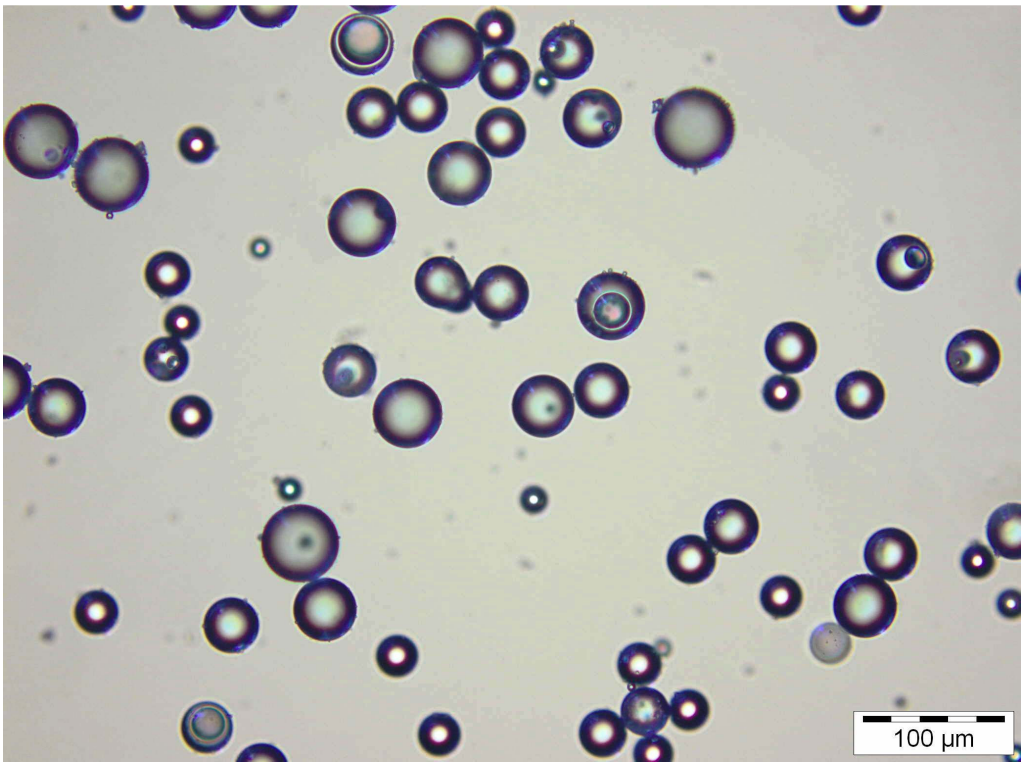

Figure 3-8: Optical micrograph of Honite 22 glass spheres.

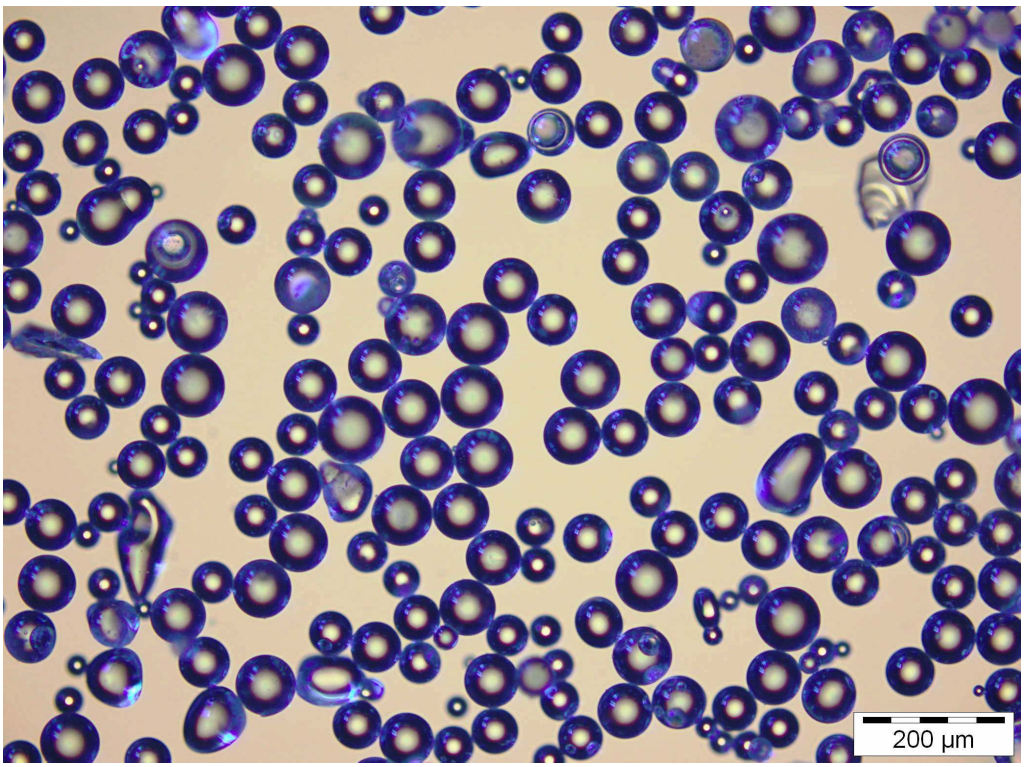

Figure 3-9: Optical micrograph of Honite 16 glass spheres.

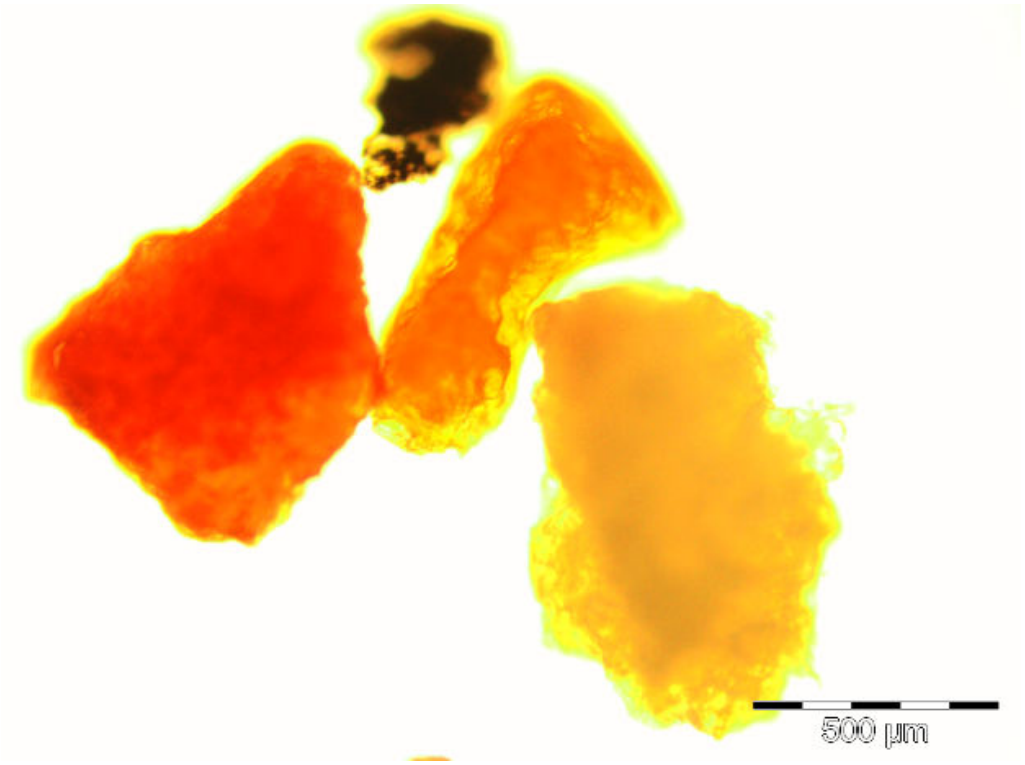

Figure 3-10: Optical micrograph of Guyblast 40/60 plastic beads.

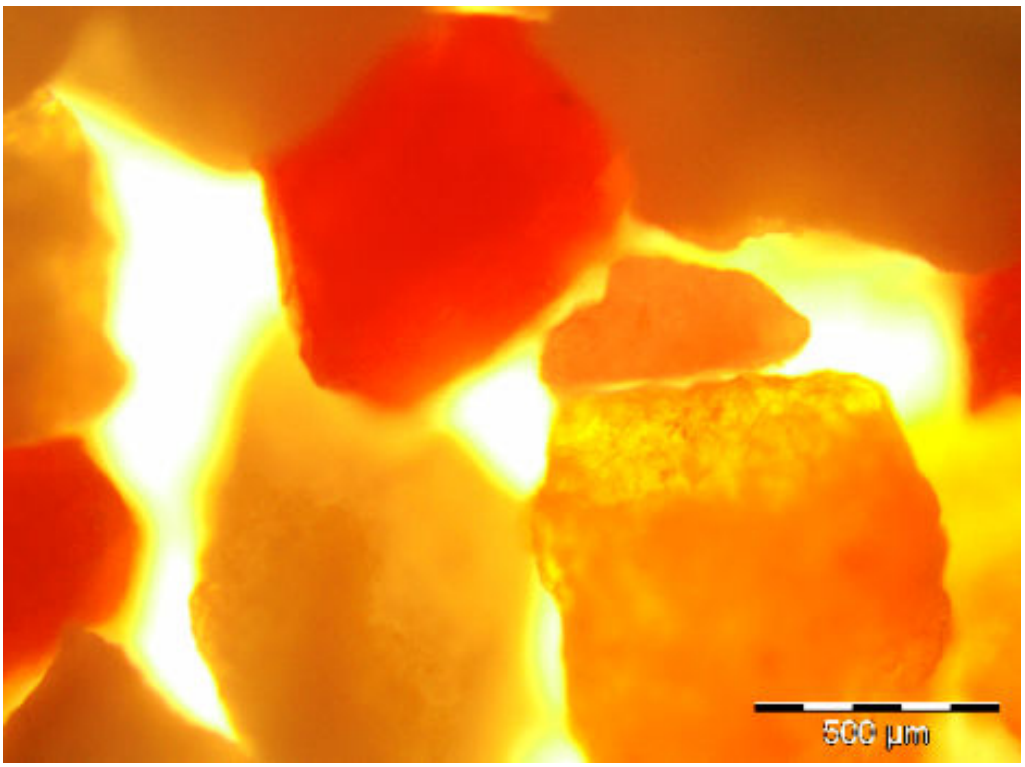

Figure 3-11: Optical micrograph of Guyblast 30/40 plastic beads.

3.5.5 Summary of particle characterisation studies

A summary of all the particle characterisation results is given in Table 3-7, which is intended to serve as a reference table hereafter.

Other relatively inexpensive particle species that would be suitable as for use in fluid flow experiments and are readily available as blast media from companies such as Guyson and Airblast (Peterborough, U.K.) include: polystyrene (spherical and neutrally buoyant: $\rho_s \approx 1.05$); olivine, *i.e.* naturally occurring magnesium iron silicate (angular, $\rho_s \approx 3.3$); zirconia-alumina (spherical, $\rho_s \approx 3.8$); and alumina (angular, $\rho_s \approx 4$).

Table 3-7: Properties of particle species considered for or used in this study.						
Species name and composition	Supplier	Diameter, d_{50} (μm)[1]	Density, ρ_s (10^3 kg m^{-3})[2]	Packing fraction[3]	Shape[4]	Selected for use (Y/N) and reason(s)
"Sphericel" hollow glass	Potters Ballotini	11*	1.1*	-	Spherical	N; availability
Silicon dioxide (SiO_2)	Sigma Aldrich	4.20	2.63*	-	Irregular	N; cost, aggregation
Titanium dioxide (TiO_2)	Sigma Aldrich	0.657	4.23*	-	Irregular	N; cost, aggregation
Manganese (III) oxide (Mn_2O_3)	Sigma Aldrich	6.26	4.50*	-	Irregular	N; cost, toxicity, disposal
Chromium (IV) oxide (Cr_2O_3)	Sigma Aldrich	2.08	5.22*	-	Irregular	N; cost, toxicity, disposal
"Turbobead" steel shot	Guyson International	-	7.8*	-	Spherical	N; corrosion
Molybdenum carbide (Mo_2C)	Alfa Aesar	< 44*	8.9*	-	Irregular	N; cost, toxicity, disposal
Tungsten carbide (WC)	Alfa Aesar	1*	15.8*	-	Irregular	N; cost, toxicity, disposal
Polyamide	Dantec Dynamics	18.5	1.03*	-	Approx. spherical	Y
"Guyblast 40/60" plastic	Guyson International	468	1.54	0.514	Jagged	Y
"Guyblast 30/40" plastic	Guyson International	691	1.52	0.513	Jagged	Y
"Honite 22" soda-lime glass	Guyson International	41.0	2.46	0.619	Spherical	Y
"Honite 16" soda-lime glass	Guyson International	77.0	2.45	0.616	Spherical	Y
* Commonly accepted value or nominal value according to supplier/manufacturer. [1] Malvern *Mastersizer 2000* and *3000* laser diffraction particle sizers; [2] Micrometrics AccuPyc 1330 pycnometer; [3] Standard volumetric flasks and scales; [4] Olympus BX51 optical microscope, also see micrographs, Figure 3-10 onwards.						

3.6 Calibration and data validation

A comprehensive range of calibration and validation experiments are described in this section. In particular, the probable influence of suspended particles on the speed of sound was quantified (Section 3.6.1) and the effect of instrumental resolution on the experimental results is discussed (Section 3.6.2). The procedures that were used to calibrate the position of the probes and the flow rate are described in Section 3.6.3 and 3.6.4. In the final two parts (Sections 3.6.5 and 3.6.6), the velocity time series of some example runs are tested to verify that they have the expected normal distribution, and the near-wall behaviour of some mean axial velocity profiles are compared with the literature, for validation.

3.6.1 Influence of suspended particles on sound speed

In this section, the influence of suspended particles on the mean density and compressibility, and therefore speed of sound, of a suspension of particles is assessed for two ideal species. The reader is referred to Appendix A for a more general and thorough analysis of experimental errors.

The velocity of sound in a medium depends on its mean density, ρ, and mean compressibility, κ, according to the Urick equation, as follows (Povey, 1997; Urick, 1948):

$$c = (\kappa\rho)^{-1/2}, \qquad [3.19]$$

where, for a medium with several constituents,

$$\kappa = \sum \phi_i \kappa_i, \qquad [3.20]$$

$$\rho = \sum \phi_i \rho_i, \qquad [3.21]$$

where the subscript i corresponds to the ith constituent. For a suspension of solid

particles of volume concentration ϕ, the mean density and compressibility are (Povey, 1997):

$$\kappa = \phi\kappa_s + (1-\phi)\kappa_w \qquad [3.22]$$

and

$$\rho = \phi\rho_s + (1-\phi)\rho_w, \qquad [3.23]$$

where the subscripts *s* and *w* refer to the solid and water phases, respectively.

The velocity of sound in all the experiments performed in this study was assumed to be 1480 m s^{-1} and was set to that value in the instrumental software. However, in order to test the validity of this assumption, the sensitivity of the velocity of sound to the particle concentration was estimated at three concentrations – ϕ = 0.1, 3 and 64 % – which correspond to low- and high-concentration runs and the random close packing (RCP) limit that is approached in a settled bed of spherical, monodisperse particles (although see Table 3-7 in Section 3.5 for packing fraction measurements of particle species, which were significantly lower than the RCP limit in all cases). The relative change in sound velocity, $\Delta c/c_0$, was calculated, where

$$\Delta c = c - c_0 \qquad [3.24]$$

and c_0 is the velocity in water alone, using Equations [3.19], [3.22] and [3.23].

In order to calculate the sound speed of suspensions, the compressibility must be known (according to Equation [3.22]), but no compressibility data could be found for either soda-lime glass (Honite) or urea formaldehyde (Guyblast), and so data for similar substances were sought.

In particular, data for "crown glass" given by Kaye and Laby (1995) were used for Honite; for Guyblast, however, an approximate value of Poisson's ratio of σ = 0.25

was assumed since "[t]he value of Poisson's ration is usually positive and lies between 0 and +1/2" (1995) in combination with a value of the elastic (Young's) modulus of E = 8.75 GPa (Martienssen and Warlimont, 2006). The bulk modulus, K, was then calculated as follows (Kaye and Laby, 1995):

$$K = \frac{E}{3(1-2\sigma)}. \qquad [3.25]$$

The compressibility, κ, was then straightforward to calculate, since $\kappa = 1/K$. The value of K for water is taken from Kaye and Laby (1995), and the corresponding values of κ and ρ yield a value for the velocity of sound in pure water, c_0. (The value thus calculated, c_0 = 1431 m s^{-1}, was used only in the sensitivity analysis presented in this section as an approximate reference value, and not elsewhere in the study; a value of c_0 = 1,480 m s^{-1} was used in the instrumental software.)

The results of the analysis are given in Table 3-8. Based on the expressions and material data presented above, the calculated values of $\Delta c/c_0$ demonstrate that the presence of solid particles at the concentrations used in this study (*i.e.* ϕ = 0.1 to 3 %) have a negligible effect on the velocity of sound in the suspensions: the relative change is less than 1 % for both Honite and Guyblast.

Table 3-8: Density and compressibility of Honite (soda-lime glass) and Guyblast (urea formaldehyde) particles, and sensitivity of sound velocity at two particle concentrations.

Material		Water	Honite	Guyblast
Density, ρ (10^3 kg m^{-3})*		1	~1.5	~2.5
Poisson's ratio, σ		-	-	0.25*
Elastic modulus, E (GPa)		-	-	8.75*
Bulk modulus, K (10^9 Pa)		2.05	41.2*	5.83
Compressibility, $\kappa = 1/K$ (Pa^{-1})		4.88×10^{-10}	2.43×10^{-11}	1.71×10^{-10}
$\Delta c/c_0$	ϕ = 0.1 %	-	-0.27 %	+0.0075 %
	ϕ = 3 %	-	-0.75 %	+0.24 %
	ϕ = 64 %	-	+14 %	+14 %

* Approximate value (see text for details).

However, it should be noted that this conclusion only strictly holds for homogeneous suspensions: if there is strong segregation or a bed, then the results for ϕ = 64 % suggest that the sound velocity may increase in that region, but even in that case the increase in sound speed would be quite modest (for both Honite and Guyblast). On the other hand, in the case of strong segregation (*i.e.* a strong concentration gradient, shear layer or settled bed, for more details of which the reader is referred to Chapters 5 and 6), the distance coordinate was always calibrated independently (see Section 3.6.3), thus precluding the possibility of variations in sound speed influencing the results.

3.6.2 Consideration of flow parameters and instrumental resolution

An overview of the principles of Doppler velocimetry and operation of the *UVP-DUO* was presented in Section 3.2.2 and included a description of the limiting measurable distance *etc.*, *i.e.* the spatial, temporal and velocity resolution. In order to verify whether the particles used in this study were capable of tracing the turbulent fluid motions, whether the flow would be fully developed at the measurement point and whether the instrumentation would be capable of resolving the smallest scales of turbulent motion, values for some of the parameters described in Section 2.2.3 for a representative range of flow and particle parameters were calculated and are presented in Table 3-9.

Table 3-9: Turbulent time- and lengthscales and entry lengths for a range of flow conditions in main flow loop (D = 42.6 mm, with water). Values of L/D from Equation [3.26] (Shames, 2003).

Q (l s^{-1})	U_{ave} (m s^{-1})	Re (10^3)	L/D	η (μm)	τ_K (ms)	St	
						Particle 1*	Particle 2**
0.2	0.140	5.98	18.8	333	111	3.00×10^{-4}	0.0400
1	0.702	29.9	24.5	100	9.93	3.36×10^{-3}	0.447
5	3.51	149	32.1	29.8	0.889	0.0375	5.00

* Particle 1: d = 20 μm, $\rho_s = 2.5 \times 10^3$ kg m^{-3} (Honite analogue).

** Particle 2: d = 400 μm, $\rho_s = 1.5 \times 10^3$ kg m^{-3} (Guyblast analogue).

In particular, two idealised particle types were used, one to broadly represent the

two glass (Honite) species used in this study (d = 20 μm, ρ_s = 2.5 × 10^3 kg m^{-3}) and another to represent the two plastic (Guyblast) species (d = 400 μm, ρ_s = 1.5 × 10^3 kg m^{-3}). In all cases, the pipe diameter, D, was 42.6 mm and the kinematic viscosity of water, ν, was 10^{-6} m^2 s^{-1} and it was assumed that $l_e \approx 0.1\ D$ and $u' \approx 0.05\ U_{ave}$ (Hinze, 1959; Laufer, 1954). The ratio of entry length, L, to pipe diameter, D, was calculated as follows (Shames, 2003):

$$\frac{L}{D} = 4.4\mathrm{Re}^{1/6}. \qquad [3.26]$$

First, it is clear from Table 3-9 that the flow would be fully developed at the measurement point – around 3.2 m from the nearest fitting, *i.e.* at $L/D \approx 75$ – even at the highest flow rate (Q = 5 l s^{-1},which is above the maximum flow rate that the pump can actually maintain), at which flow rate the flow is fully developed by L/D = 32.1 according to Equation [3.26] (Shames, 2003).

An alternative expression for entry has been provided by Zagarola and Smits (1998) based on the Darcy friction factor, f, as follows:

$$\frac{L}{D} = \frac{0.5}{f} + \frac{5}{f^{1/2}}, \qquad [3.27]$$

where f is found using the expression given by Haaland (1983), which is considered in more detail later (Section 3.6.6, Equation [3.43]). At the highest flow rate considered in this section (*i.e.* Q = 5 l s^{-1}, Re = 149,000), f = 0.0168, so L/D = 68.5, and although that value differs significantly from the one calculated using the expression of Shames (2003), it is still smaller than the actual entry length of the flow loop ($L/D \approx 75$). To conclude, it is very reasonable to assume the flow was fully developed at the point of measurement. However, it is interesting to note that, although Eggels *et al.* (1994) used an entry length of L/D = 102 at Re = 7,000, Laufer (1954) found the flow to be fully developed at just L/D = 30 at Re = 50,000.

Second, the values of the Stokes number, St, at all flow rates for the glass analogue (particle 1) and at the lowest flow rate for the plastic analogue (particle 2) given in

Table 3-9 suggest that such particles follow the flow closely and are therefore good tracers of turbulent motions. However, at the highest flow rate the plastic analogue will act as a poor tracer and will not respond to the finest turbulent motions.

Third, it is important to consider whether the *UVP-DUO* is capable of interrogating the flow with sufficient spatial and temporal resolution. The minimum measurement channel width, w, at 2 and 4 MHz are 0.37 and 0.74 mm (*i.e.* 370 and 740 μm) respectively. This is slightly larger than the Kolmogorov lengthscale at even the lowest flow rate considered in Table 3-9 (η = 333 μm at Q = 0.2 l s^{-1}) and therefore more than an order of magnitude larger than would be necessary to resolve the finest turbulent motions. Moreover, the sample rate attainable by the *UVP-DUO* – 25-40 ms at 2 MHz and 40-50 ms at 4 MHz – is considerably lower than would be necessary: at Q = 5 l s^{-1}, a sample rate of around 90 μs or less – *i.e.* one tenth of the Kolmogorov timescale, τ_K – would be required.

Finally, the effect of the particle size distributions of the species used should be borne in mind: particles at the upper and lower limits of the particle size distribution (PSD) respond very differently to turbulent motions. All the observations made in this section have implications for the interpretation of experimental results presented later and are discussed in the relevant results sections.

3.6.3 Probe position calibration

Some basic calibration procedures are described in this section. Two novel methods for the calibration of distances measured by ultrasonic transducers – the first relying on the mean Doppler velocity profile, and the second on the RMS echo profile – are described and applied to some representative experimental data, for illustration and validation.

The 2 and 4 MHz probes were mounted at 135 and 90 degrees to the direction of mean flow, respectively, as shown in Figure 3-2. It was essential to calibrate the positions of both probes as accurately as possible relative to the pipe centreline

and the inner pipe wall (*i.e.* the wall through which the probes were inserted and secured) so that all results could be projected onto a common axis. In general, the position of a probe mounted at an angle ψ to the axial flow direction can be calibrated according to the following linear transformation:

$$y = y' \sin\psi - a_{off}, \qquad [3.28]$$

where y is the perpendicular distance from the upper pipe wall (through which the probes are mounted), y' is the distance measured along the probe axis and a_{off} is an offset such that a_{off} is positive if the probe (or more strictly, the centre of its active face) does not protrude into the flow and is retracted into the pipe wall. This geometry is illustrated in Figure 3-12, in which c is a known reference distance such as the pipe radius, R, or diameter, D. Clearly, through Equation [3.28], the probe mounting geometry is a potential source of experimental error in terms of the mounting angle, which has an associated precision. This error is assessed quantitatively for an example case in the appendix (Appendix A).

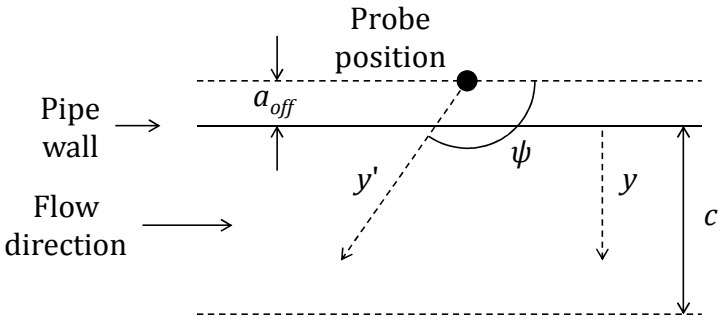

Figure 3-12: Diagram of geometry used in calibration of probe position, where a_{off} is an offset distance, y is wall-normal distance, y' is distance measured along probe axis, ψ is angle between flow direction and probe axis and c is a reference distance (R or D).

The position of the 4 MHz probe could be calibrated in a straightforward fashion by inspecting the echo voltage profile, which showed a very strong peak due to reflection by the opposite (*i.e.* lower) pipe wall at $c = D = 42.6$ mm and $\psi = 90°$. An example is shown in Figure 3-13 (Guyblast 40/60 at a very high flow rate, with ϕ = 0.01 %, *i.e.* very low concentration).

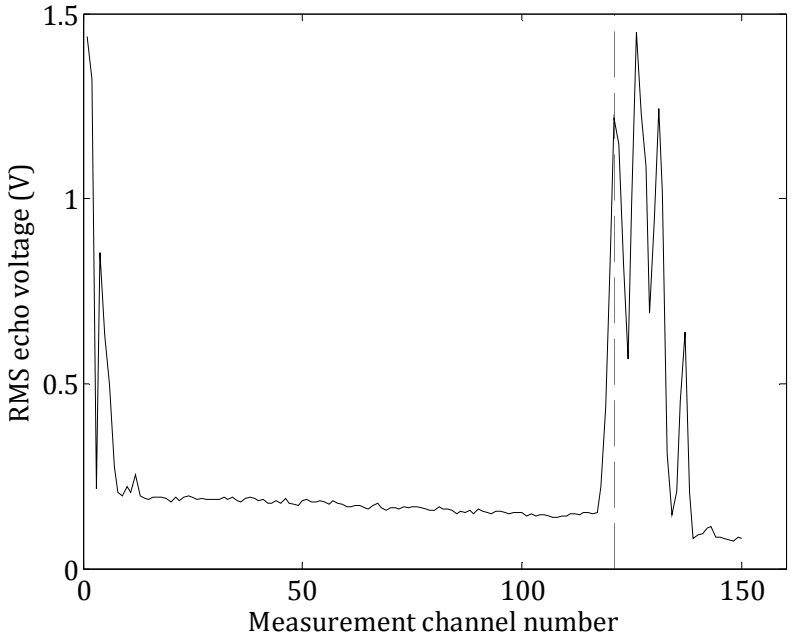

Figure 3-13: RMS echo voltage profile with Guyblast 40/60 at Q = 3.08 l s^{-1} and ϕ = 0.01 %. Position of opposite (lower) pipe wall is shown by a vertical dashed line at measurement channel 121.

To summarise, the echo amplitude profile shown in Figure 3-13 was obtained from the raw echo data in the manner described in the data processing methodology (Section 3.3): the gain and digitisation constant were removed from the echo data produced by the *UVP-DUO* and the RMS taken over the whole run (n = 2,500 samples in this case) with MATLAB. The distance corresponding to each measurement channel could then be calculated in a trivial way, since the distance to the first channel, and the separation between each subsequent channel, s, was known.

The first peak at measurement channel 121, *i.e.* y = 46.44 mm, corresponds to the position of the opposite (lower) pipe wall. Because ψ = 90° for the 4 MHz probe (so that sin ψ = 1), it only remains to find the offset a_{off}. Equation [3.28] yields a_{off} = 46.44 – 42.6 = 3.84 mm, *i.e.* the active face of the probe is at a position 3.84 mm retracted into the wall of the pipe. This offset would then be applied to all subsequent runs using this particular probe arrangement.

It should be noted that the kind of echo amplitude profile shown in Figure 3-13 is

used extensively in the chapters on concentration profiles (Chapter 5) and bedforms (Chapter 6). The large peak close to the probe (*i.e.* in the first 10 measurement channels) is thought to arise from flow disturbances.

The position of 2 MHz probe, which is angled at ψ = 135° to the main flow, cannot be calibrated in the same as the 4 MHz because there is no reflection from the lower pipe wall and therefore no peak in the RMS echo profile. Instead, the calibration for the 2 MHz probe is performed based on the distance to the peak in the mean Doppler velocity profile, which can be assumed to be at the centreline of the pipe, *i.e.* $c = R$ = 21.3 mm. An example is shown in Figure 3-14 at a high flow rate with Guyblast 40/60 at very low particle concentration (ϕ = 0.01 %). To be clear, the mean axial Doppler velocity profile shown in Figure 3-14 was obtained from the instantaneous velocity data produced by the *UVP-DUO*, and the mean at each measurement channel was then taken over the whole run (n = 2,500 samples in this case) using MATLAB, as described in the data processing methodology (Section 3.3).

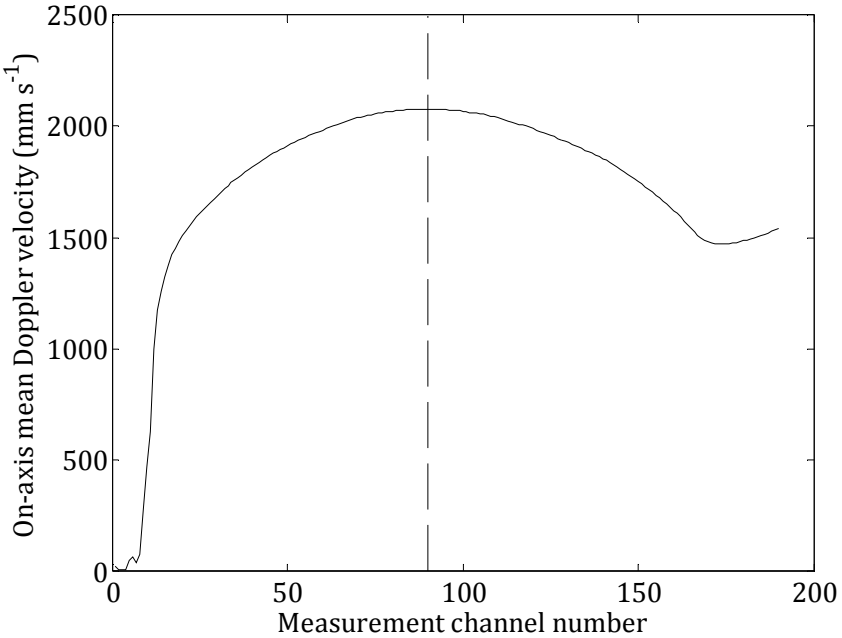

Figure 3-14: Mean Doppler velocity profile along probe axis with Guyblast 40/60 at Q = 2.68 l s^{-1} and ϕ = 0.01 %. Position of peak in profile (assumed to coincide with centreline of pipe) is shown by a vertical dashed line at measurement channel 90.

The mean velocity profile reaches a peak at measurement channel 90, *i.e. y'* = 34.97 mm. With ψ = 135°, Equation [3.28] yields an offset a_{off} = 3.43 mm, which means the (centre of) the active face of the 2 MHz probe is positioned 3.43 mm into the pipe wall in the run shown.

The upward curvature of the mean velocity profile in Figure 3-14 between the 150th and 200th measurement channels is thought to be a result of a combination of beam divergence and reflections from the lower pipe wall, and was present in all the mean axial velocity profiles.

In general, the probe positions were measured in the manner described in this section whenever the probe position changed (for maintenance, *etc.*). It is also useful to note that the radial distance from the pipe centreline, *r*, can easily be calculated from *y* as follows:

$$r = |R - y|. \qquad [3.29]$$

As well as mean axial velocity profiles – like the one shown in Figure 3-14 – the fluctuating parts of the velocity time series in both the wall-normal and axial directions were also calculated (using MATLAB, see Section 3.3), as described in Section 4.1.1, and the first- and second-order statistics of a range of flows are described in detail in Sections 4.2.1 to 4.2.4.

3.6.4 Flow rate calibration

Following completion of all experimental runs, the flow meter was re-recalibrated (ABB Ltd., Stonehouse, Gloucestershire), as it was installed around three years before these runs were performed, during which it had not been calibrated, and the discrepancy between the true and measured flow rate was found to have been -0.7 % (mean of three runs). A corresponding correction factor (*i.e.* 1.007) was applied to all flow rate measurements presented in this study.

In addition, an independent flow rate calibration method is outlined in this section

and some example results are presented. The total flow rate, Q, through a cross-section of a cylindrical pipe can be written as follows:

$$Q = U_{ave} A_{\text{flow}} \approx \sum_i \overline{U}_i \Delta A_i, \qquad [3.30]$$

where U_{ave} is the average (bulk) flow velocity, A_{flow} is the flow area, which for fully suspended flow in which there is no bed is equal to is $A_{\text{flow}} = A_{\text{pipe}} = \pi R^2$, $\overline{U}_i$ is the mean velocity in the ith annulus and ΔA_i is an annular increment of cross-sectional area, as shown in Figure 3-15.

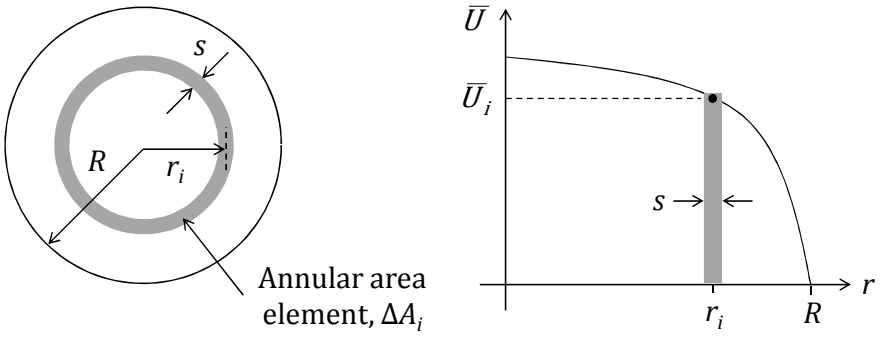

Figure 3-15: Diagram illustrating flow rate calibration method. First frame shows geometry in y-r plane; second frame is mean axial velocity profile.

If the thickness of each concentric annulus is s – *i.e.* the distance between measurement channels – then the following expression for ΔA_i is obtained:

$$\Delta A_i = \pi \left(r_i + \frac{s}{2} \right)^2 - \pi \left(r_i - \frac{s}{2} \right)^2 = 2\pi r_i s, \qquad [3.31]$$

where r_i is the ith radial distance from the pipe centreline.

In order to test the accuracy of the flow meter, the flow rate was calculated using the numerical integration method described above. The mean Doppler velocity profile was integrated between the pipe centreline and the pipe wall closest to the probe (*i.e.* over the interval $0 < r/R < 1$). The flow rate was found for 12 runs with five different particle species, the results of which are shown in Table 3-10; the chosen runs were quasi-single-phase (with volume fractions of ϕ = 0.01 and 0.1 %

by volume) and at very high flow rates so that it could be assumed that the profiles were symmetric about the centreline. The position of the pipe centreline was found using the distance calibration method described in Section 3.6.3, and the radial distance from the centreline was found using the transformation given in Equation [3.29].

Table 3-10: List of runs used for flow meter calibration.

Particle species	Volume fraction, ϕ (%)	Flow rate, Q (l s^{-1})		
		From flow meter (uncorrected)	By numerical integration	Discrepancy (%)*
Honite 22	0.01	3.97	3.60	-9.28
		3.54	3.06	-13.6
Polyamide	0.01	3.96	3.51	-11.5
		3.53	2.88	-18.4
Honite 16	0.01	3.95	3.37	-14.8
		3.5	2.99	-14.5
Guyblast 40/60	0.01	3.57	3.09	-13.6
	0.1	3.97	3.57	-10.1
		3.54	3.05	-13.8
Guyblast 30/40	0.01	3.44	3.10	-9.85
	0.1	3.87	3.46	-10.5
		3.44	2.92	-14.8
* Mean and standard deviation, μ and σ, of all data: -12.9 ± 2.7 %.				

It is clear from Table 3-10 that there is no trend with respect to particle type or flow rate. It was found that the flow rate found by numerical integration was lower than that measured by the flow meter: the mean value and standard deviation of the discrepancy for the 12 runs listed was -12.9 ± 2.7 %.

It is thought that the majority of this discrepancy can be accounted for by known experimental uncertainties, in particular: the acoustic beam divergence angle, the probe mounting angle, pressure and temperature, as described in detail and quantified for an example run in the appendix (Appendix A). The relative

uncertainties in the wall-normal distance and mean axial velocity (both of which are required for the numerical integration described in this section) amount to $\mathrm{d}y/y$ = 6.3 % and $\mathrm{d}\overline{U}/\overline{U}$ = 5.3 % at the pipe centreline in the example run described in Appendix A.

It is clear from inspection of Equation [3.30] that

$$\frac{\mathrm{d}Q}{Q} = \frac{\mathrm{d}\overline{U}_i}{\overline{U}_i} + \frac{\mathrm{d}(\Delta A_i)}{\Delta A_i}. \qquad [3.32]$$

Through Equations [3.29] and [3.31], it is also clear that

$$\frac{\mathrm{d}(\Delta A_i)}{\Delta A_i} = \frac{\mathrm{d}r_i}{r_i} = \frac{\mathrm{d}y_i}{y_i}, \qquad [3.33]$$

so that $\mathrm{d}Q/Q \approx$ 5.3 % + 6.3 % = 11.6 %, based on the error analysis presented in Appendix A. This accounts for most of the actual discrepancy (12.9 %) between the measured flow rate and that calculated by numerical integration of the mean velocity profile. However, the errors due nonlinear beam divergence and flow disturbance near the tips of the probes, although present in reality, were not quantified in the analysis in Appendix , but are likely to contribute to the flow rate discrepancy and to the total experimental error in general.

3.6.5 Statistical analysis and filtering of experimental data

Turbulent fluid motion is random and so should be the motion of particles suspended in it if those particles follow the fluid motion and there exists no slip velocity between the two phases. A brief review of the fluid mechanics of pipe flow is given in Section 2.2. In this section, the aim is to verify that the velocity statistics recorded by the *UVP-DUO* instrument are, indeed, normally distributed and are not significantly affected by noise and contributions from other objects in the water (*i.e.* bubbles and dirt in the mains water).

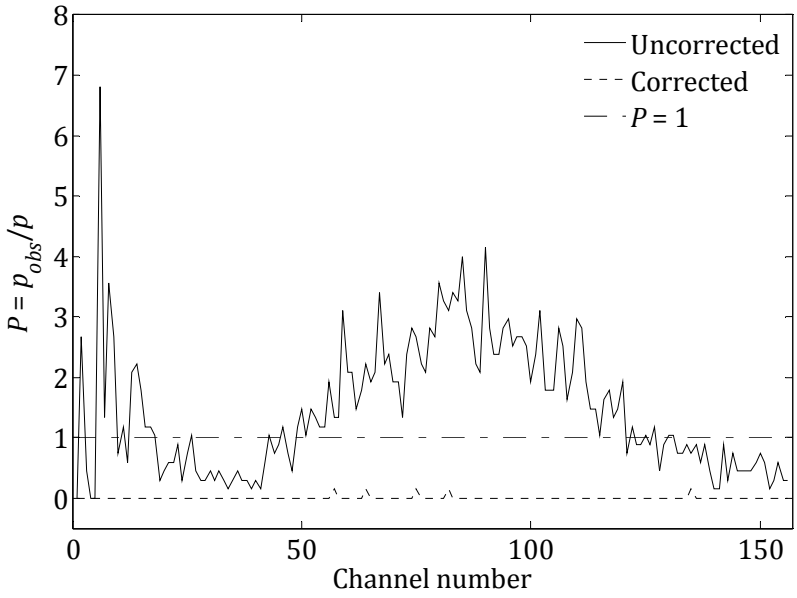

Figure 3-16: Normality, P, of on-axis mean axial velocity *vs.* measurement channel number for Honite 22 at Q = 3.63 l s^{-1} and ϕ = 0.1 %. Solid and dashed lines are velocity data before and after application of a three-sigma noise filter, respectively. Dashed-dotted line corresponds to P = 1, for reference.

Let p_{obs} be the observed proportion of outliers, that is, the proportion of measured data falling outside the range $\mu \pm n\sigma$, where μ is the mean and σ the standard deviation of the time series data, and p be the expected proportion of outliers for a normal distribution, in particular:

$$p = 1 - \mathrm{erf}\left(\frac{n}{\sqrt{2}}\right), \qquad [3.34]$$

where "erf" is the error function. In addition, the normality P is defined as

$$P \equiv p_{obs}/p, \qquad [3.35]$$

such that $P > 1$ if the data are more widely distributed about the mean than would be expected if they were normally distributed, and $P < 1$ if they are less widely distributed.

As part of the data processing method described in Section 3.3, a three-sigma (3σ) noise filter was applied to all the echo voltage and Doppler velocity data using

MATLAB; that is, all data falling outside the range $\mu \pm 3\sigma$ were excluded and replaced by randomly sampled values from the same distribution. The normality of the data and the efficacy of the noise filter were tested for the smallest and largest particle species (Honite 22 and Guyblast 30/40, respectively) at a high and intermediate flow rate (Q = 1.68 and 3.63 l s^{-1}) and at low and high volume concentrations (ϕ = 0.1 and 1 %), of which a representative selection of runs are presented below.

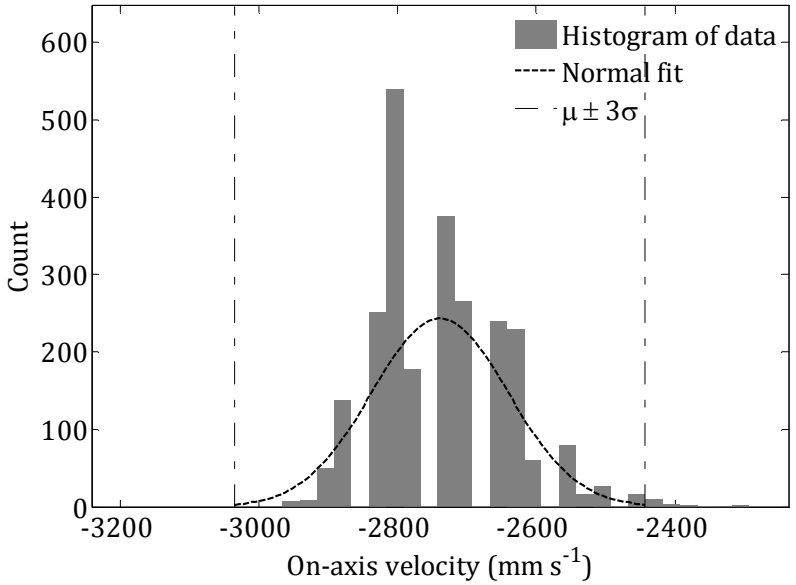

Figure 3-17: Histogram of instantaneous on-axis velocity at measurement channel 80 (d = 31.3 mm) for Honite 22 at Q = 3.63 l s^{-1} and ϕ = 0.1 %. Histogram consists of on-axis velocity time-series data and dashed line to a normal fit of data. Dashed-dotted vertical lines correspond to filter window, $\mu \pm 3\sigma$.

Figure 3-16 shows P for the mean axial velocity measured with the 2 MHz probe (at 135° to the mean flow direction) with Honite 22, the smallest particle species used, at a high flow rate and low volume concentration. The proportion of outliers is rather higher than expected (P > 1) very close to the probe and the middle region (between channels 50 and 130), although the absolute number of data falling outside the range is very small (for a run with 2,500 samples, P = 4 is equivalent to about 27 samples). It is also clear from Figure 3-16 that the noise filter was effective in removing data outside the range $\mu \pm 3\sigma$: the value of P is zero for the uncorrected data for the majority of measurement channels.

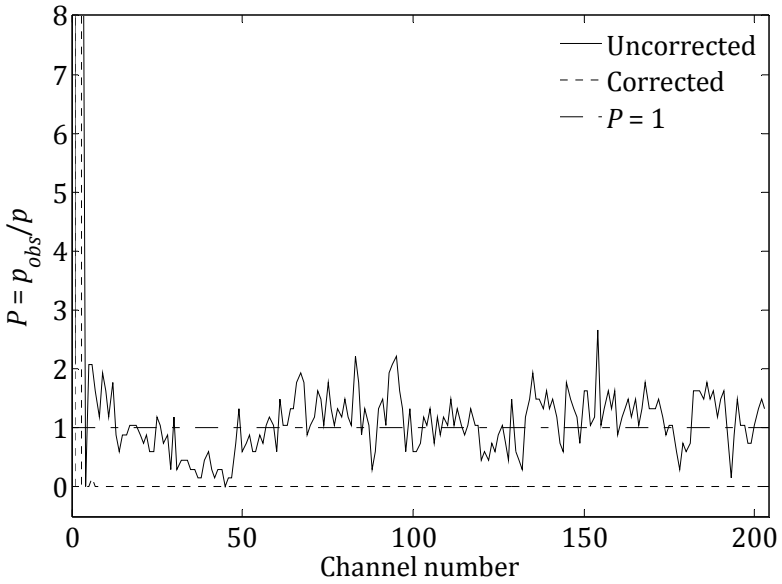

Figure 3-18: Normality P of on-axis mean axial velocity *vs.* measurement channel number for Guyblast 30/40 at Q = 1.68 l s^{-1} and ϕ = 1 %. Solid and dashed lines: data before and after application of 3σ noise filter. Dashed-dotted line corresponds to P = 1.

Figure 3-17 shows a histogram of instantaneous Doppler velocities from the same run as shown in Figure 3-16 and described above. Both the quantisation of velocity data and the normal distribution that they follow are evident. Figure 3-18 and Figure 3-19 show the same results as above for Guyblast 30/40, the largest particle species used, at an intermediate flow rate and a higher volume concentration. It is clear from Figure 3-18 that the value of P across the measurement region is close to unity, suggesting that the distribution of instantaneous velocities is normal. There was no significant trend in the behaviour of P with flow rate for either particle species.

To summarise, the degree to which the instantaneous velocity data follow normal distributions varies according to particle size and concentration. This is to be expected: the smaller the particles and the lower the concentration, the greater contribution that dust and microbubbles in the fluid (mains water) will have to the received signal. If the signal from these contaminants is regarded as noise, then their presence will tend to contribute to the proportion of outliers in the data. Indeed, the proportion of outliers, although relatively small, is greater for Honite 22 at a lower concentration that for Guyblast 30/40 at a higher concentration.

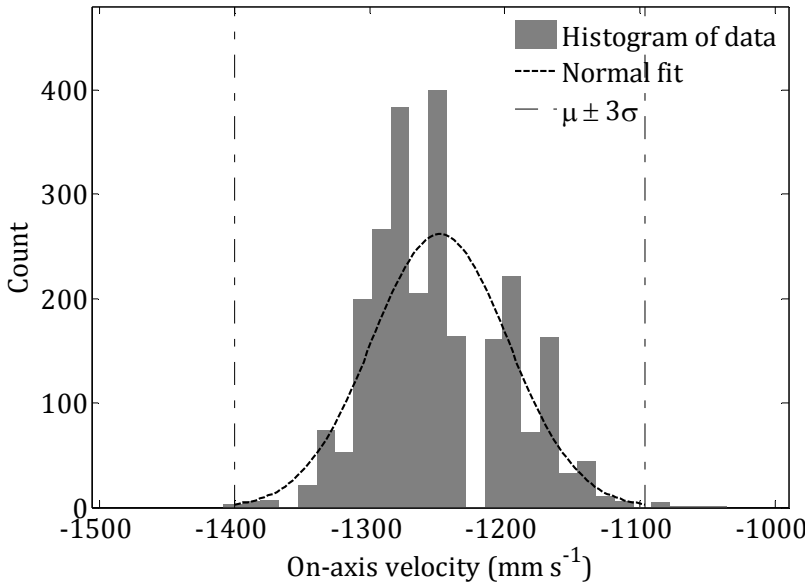

Figure 3-19: Histogram of instantaneous on-axis velocity at measurement channel 80 (y = 31.3 mm) for Guyblast 30/40 at Q = 1.68 l s^{-1} and ϕ = 1 %. Dashed line: normal fit of data; dashed-dotted vertical lines: filter window at $\mu \pm 3\sigma$.

3.6.6 Validation of single-phase data: inner variables and law of wall

In this section, the behaviour of the fluid flow very near the wall is investigated in order to test the accuracy of the measurement method. Table 3-11 contains a summary of the regions nearest to a solid boundary in pipe flow, and Figure 3-20 contains a schematic diagram of the same regions.

A number of variables in Table 3-11 require definitions. A very common way of visualising the flow behaviour near the wall is to non-dimensionalise the flow parameters using the friction (or shear) velocity, U_τ, which is defined below, and express them in the so-called inner variable (or wall units) which are defined as follows:

$$y^+ = yU_\tau/\nu, \qquad [3.36]$$

$$u^+ = \overline{U}/U_\tau. \qquad [3.37]$$

As stated in Table 3-11, the viscous sublayer is commonly described as extending from the solid boundary to a distance of y^+ = 5, so if the sublayer thickness is

denoted by δ_v, then by setting $y = \delta_v$ and rearranging Equation [3.36], the following expression for the viscous sublayer thickness is obtained:

$$\delta_v = 5\nu/U_\tau. \qquad [3.38]$$

Table 3-11: Flow regions near a boundary (Gad-el-Hak and Bandyopadhyay, 1994; Roberson and Crowe, 1996; Schlichting and Gersten, 2000).

Name		Location	Form of mean velocity profile
Viscous sublayer	Viscous region	$0 \leq y^+ < 5$	Linear dependence: $u^+ = y^+$.
Buffer layer		$5 < y^+ < 30$	See, for example, Schlichting and Gersten.
Log-law or overlap region		$y^+ > 30$ and $y/R < 0.2$	Logarithmic dependence: $u^+ = (1/\kappa) \ln y^+ + C^+$, where $\kappa = 0.41$ (von Kármán constant) and $C^+ = 5$ in smooth conduits.
Core region		$y/R > 0.2$	Velocity defect law applies: $(\overline{U}_{max} - \overline{U})/U_\tau = f(y/\delta_v)$.

The friction velocity, U_τ, is defined as (and can be most directly measured according to) the following expression (Laufer, 1954):

$$U_\tau^2 = -\nu \left(\frac{\partial \overline{U}}{\partial r} \right)_{\text{wall}}, \qquad [3.39]$$

where $\partial \overline{U}/\partial r$ is the gradient of the mean axial velocity, $\overline{U}$, with respect to the radial distance, r, from the pipe centreline. The notation used here for co-ordinates and velocity is described in detail in Section 2.2.1, to which the reader is referred for more information, and is reiterated in Section 3.4. Examples of two mean velocity profiles close to the pipe wall are shown in Figure 3-21 (Laufer, 1954), in which the pipe radius, R, was 123 mm and the Reynolds numbers, Re, were 50,000 and 500,000. The measurement resolution was of the order of 0.05 mm (*i.e.* 50 μm) and a hot-wire anemometer was used.

However, the method of calculating the velocity gradient described by Laufer (1954) – *i.e.* directly from velocity data – is not possible with the measurement

system used in this study, for a number of reasons, which follow.

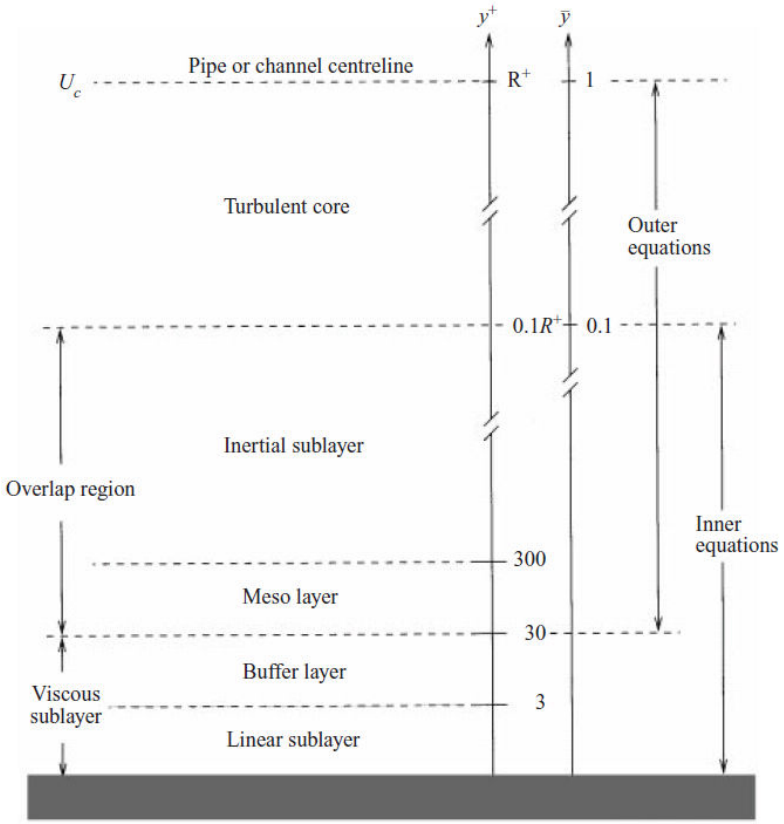

Figure 3-20: Schematic of regions and layers in pipe and channel flows where $R^+ = RU_\tau/\nu$. From Wosnik *et al.* (2000).

1. The probes are inserted into the pipe wall, and thus influence the flow near the wall. (This would be true whether the probes protruded into the flow or even if the probes were retracted slightly into the pipe wall, as was generally the case, because in that case a small recess would exist.) Measurements near the probe are not reliable for this reason, although this problem could be avoided if a transmission tube and film arrangement were used (Admiraal and García, 2000). Echo data near the probe are unreliable for the same reason.

2. The spatial resolution is not sufficient. For example, in the flow loop (D = 42.6 mm) at Re = 50,000, the viscous sublayer thickness, δ_ν, is about 40 μm, *i.e.* significantly less than the distance between measurement points for either probe (260 and 370 μm for the 135- and 90-degree probes,

respectively). If a much shallower probe angle were used, this problem would be avoided, but such an arrangement would cause other, equally limiting, problems.

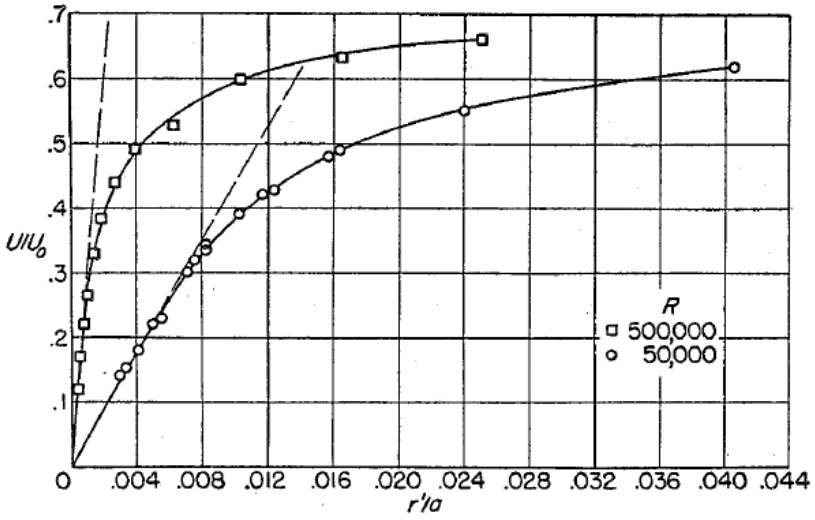

Figure 3-21: Near-wall axial velocity in pipe flow in linear units at two Reynolds numbers. R is Reynolds number, Re; U is mean axial velocity, $\overline{U}$, and U_0 is maximum value thereof at pipe centreline, $\overline{U}_{max}$; r'/a is dimensionless wall-normal distance from upper pipe wall, y/R. From Laufer (1954).

Instead, the wall shear stress and friction velocity were found using a more general method (Roberson and Crowe, 1996; Schlichting and Gersten, 2000). The friction velocity and wall shear stress, τ_w, are calculated as follows:

$$U_\tau = (\tau_w/\rho)^{1/2}, \qquad [3.40]$$

$$\tau_w = \frac{f\rho U_{ave}^2}{8}. \qquad [3.41]$$

where f is the Darcy friction factor and U_{ave} is the average flow velocity such that

$$U_{ave} = Q/A_{\text{flow}}. \qquad [3.42]$$

A variety of implicit and explicit expressions exist for f, of which the following is explicit, accurate and simple to implement (Haaland, 1983):

$$f^{-1/2} = -1.8\log\left[\frac{6.9}{\mathrm{Re}} + \left(\frac{\varepsilon}{3.7D}\right)^{1.11}\right], \qquad [3.43]$$

where ε is the roughness coefficient.

The method described above for calculating the friction factor, f, and friction velocity was validated using several datasets available in the literature (den Toonder and Nieuwstadt, 1997; McKeon *et al.*, 2004b; Wu and Moin, 2008), as shown in Figure 3-22. It is clear that the agreement is very good.

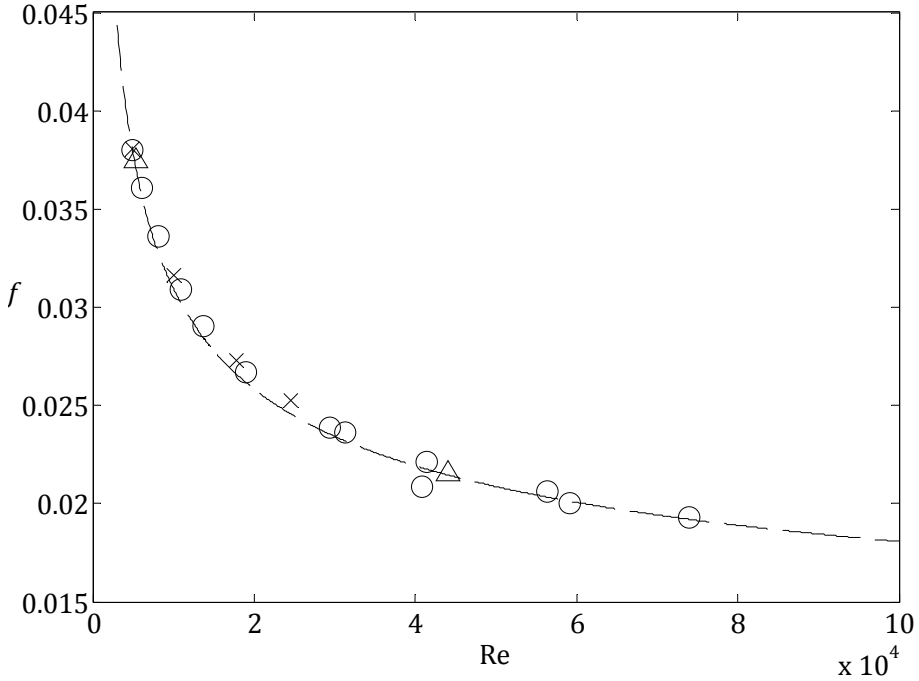

Figure 3-22: Friction factor, *f*, *vs*. Reynolds number, Re. Dashed line: correlation used in this study (Haaland, 1983); crosses: den Toonder and Nieuwstadt (1997); circles: McKeon *et al*. (2004b); triangles: Wu and Moin (2008).

In order to validate the experimental data, a plot of the near-wall behaviour of the mean velocity is shown in Figure 3-23 for a representative quasi-single-phase (*i.e.* very low-volume-fraction) run, in particular with Honite 22 glass beads at ϕ = 0.01 % and Q =3.56 l s^{-1} (Re = 106,000, U_{ave} = 2.50 m s^{-1}). In this example, for the smooth, plastic flow loop used in this study (D = 42.6 mm), the following parameters are obtained using the expressions presented in this section: f = 0.0177, τ_w = 13.8 kg m^{-1} s^{-2} and U_τ = 0.118 m s^{-1}, assuming ε = 0.0015 mm (Moody,

1944; Roberson and Crowe, 1996). This corresponds to a velocity gradient in the viscous sublayer of $|\partial\overline{U}/\partial y| = 13.8 \times 10^3$ s^{-1}, according to Equation [3.39].

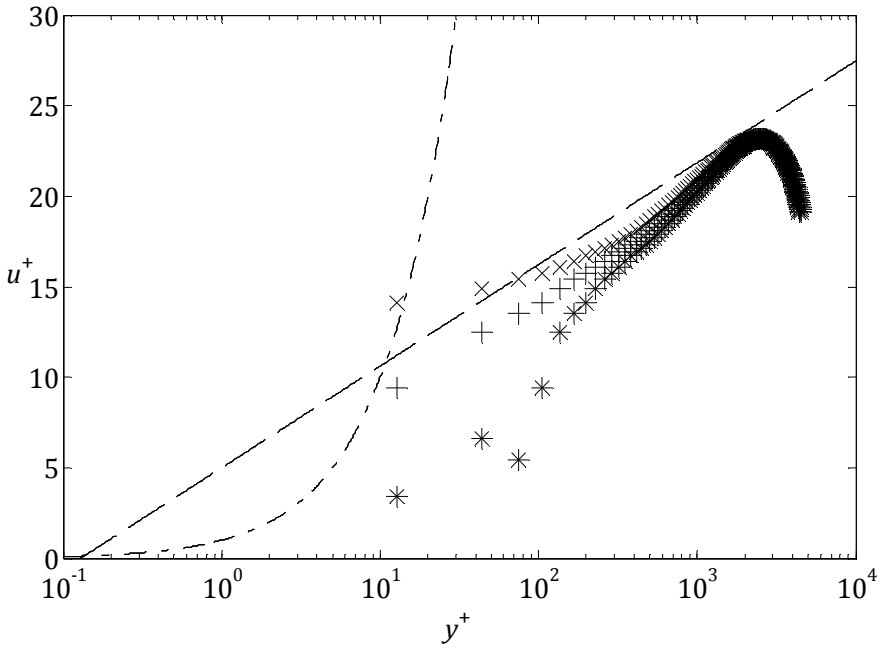

Figure 3-23: Near-wall velocity profile in wall units with Honite 22 at ϕ = 0.01 % and Q = 3.56 l s^{-1}. Dashed-dotted line: ideal behaviour in linear region; dashed line: that in log-law region. "Plus" symbols are correct data; crosses and stars are same data with distance calibration point (*i.e.* peak velocity position) modified by ±3 measurement points (±1.11 mm) from correct position, respectively.

A number of important conclusions can be drawn from Figure 3-23, as follows.

1. The correct data ("plus" symbols) fall close to, but below, the expected values (dashed line) in the log-law region, suggesting the measurements are quite accurate in this region (but see Section 3.6.4 for a detailed account of the discrepancy); this observation is supported by the fact that the Stokes number for this run is St = 0.0913 (according to Equation [2.13]), such that the particles follow the turbulent fluid motions very closely.
2. At lower values, *i.e.* in the viscous sublayer (dashed-dotted line), the instrumental resolution is insufficient and no data are present. The viscous sublayer thickness in this case is δ_v = 48.3 μm (*i.e.* y^+ = 5) and the Kolmogorov lengthscale is η = 42.5 μm (according to Equation [2.10]); therefore, an

instrumental resolution of the order of around 4 μm (*i.e.* one tenth of η) would be necessary to fully resolve the behaviour therein. However, the actual spatial resolution of the data (*i.e.* the measurement channel separation) in this run is 370 μm, that is, two orders of magnitude larger than would be necessary to resolve the motion of the smallest eddies.

3. The cross and star symbols correspond to the same data, but with the distance calibration point (*i.e.* that at the peak of the mean velocity) shifted by ±3 measurement channels (*i.e.* 1.11 mm) in order to illustrate the sensitivity of this type of plot, and how important it is to accurately calibrate the position of the probe.

To summarise this section, two possible methods for calculating the friction velocity, U_τ, and wall shear stress, τ_w, were described, of which one (direct measurement of the velocity gradient in the viscous sublayer) was found not to be viable with the measurement system used in this study on the grounds of resolution. However, the second method (using the correlation of Haaland, 1983) was found to be very accurate.

Some examples of near-wall velocity profiles, expressed in wall units, were presented for one example run (Honite 22, *i.e.* small glass, at Q = 3.56 l s^{-1}) and it was confirmed that the profile followed the expected behaviour (Figure 3-23), albeit with a small discrepancy (for more details of which, see Section 3.6.4); the sensitivity of the measurement method was also illustrated. It was also confirmed that the viscous sublayer could not be resolved using the *UVP-DUO* system.

3.7 Bed and shear layer thickness measurement

The thickness of settled beds and shear layers – *i.e.* the region above a moving bed in which the particles move as a sheet – requires definition here, as these regions were measured extensively in this study in two contexts: firstly, the variation of bed depth with flow rate was used to predict the critical flow velocity at which no bed formed (method: Section 4.1.3; results: Section 4.2.7); and secondly, the

behaviour of stable and time-dependent bedforms was investigated in detail, the results of which are presented in Chapter 6.

The flow Reynolds number, $\mathrm{Re}_{\mathrm{flow}}$, is defined as follows:

$$\mathrm{Re}_{\mathrm{flow}} = \frac{U_{\mathrm{flow}} H}{\nu}, \qquad [3.44]$$

and h, H and D are the bed depth, fluid depth and inner pipe diameter, respectively, as shown in Figure 3-24. U_{flow} is the mean axial flow velocity in the flow area, A_{flow}, *i.e.* the cross-sectional area not occupied by the bed, and is calculated as follows:

$$U_{\mathrm{flow}} = \frac{Q}{A_{\mathrm{flow}}}. \qquad [3.45]$$

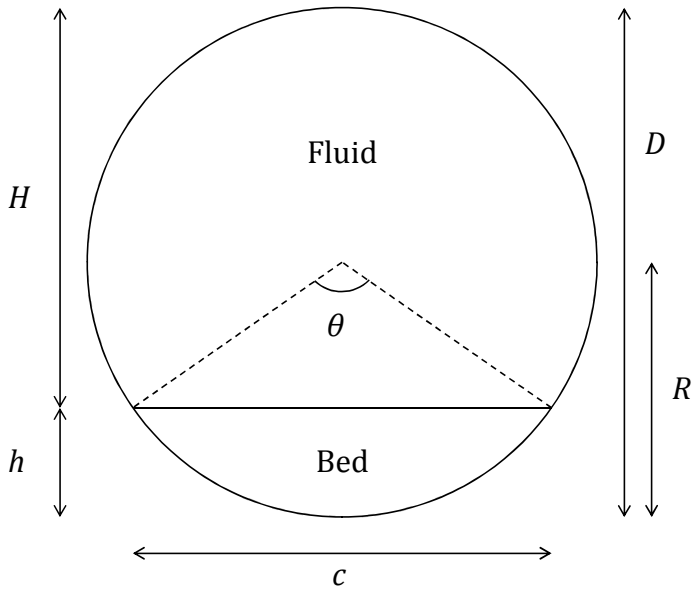

Figure 3-24: Bed geometry and definitions. H and h are fluid and bed depths, respectively; R and D are pipe radius and diameter; θ is angle subtended by bed at pipe centre; and c is chord length (*i.e.* bed width at top of bed).

Geometrically speaking, in a cross-section of the pipe the settled bed is a chord of length, c, such that (Weisstein):

$$c = 2\sqrt{h(2R - h)} = 2\sin(\theta/2), \qquad [3.46]$$

where θ, the angle subtended by the bed at the centre of the pipe, is:

$$\theta = 2\cos^{-1}\left(\frac{R-h}{R}\right). \quad [3.47]$$

and R is the pipe radius (R = 42.6 mm).

The cross-sectional areas occupied by the bed, A_{bed}, and by the flow area, A_{flow}, are then:

$$A_{\text{bed}} = \frac{1}{2}R^2(\theta - \sin\theta), \quad [3.48]$$

$$A_{\text{flow}} = A - A_{\text{bed}} = R^2\left[\pi - \frac{1}{2}(\theta - \sin\theta)\right]. \quad [3.49]$$

A distinct interface such as a settled bed typically acts as a strongly reflective surface (and more measurably so if a suitable acoustic impedance mismatch exists between the two media), and the echo signal will exhibit a strong peak. However, in the more general case of a gradual variation in particle concentration with distance, for example, at a softer interface like a bed with a moving component, the physical significance of the peak in the echo amplitude, V (as defined in Section 3.2.2), if one exists, requires more interpretation. In this study, the position of the peak in V is assumed to correspond to the top of either the settled bed or shear layer, depending on the flow regime.

At high flow rates, the particulate phase remains fully suspended and no vertical concentration gradient exists (as confirmed by the comparison of nominal, *i.e.* weighed, *vs.* sampled particle concentration measurements that were taken in the stirred mixing vessel, as presented in Section 5.2.2; the reader is also referred to the description of Rousean concentration profiles in Section 6.1.1). At intermediate flow rates, a concentration gradient develops, and a saltating or moving bed forms along the bottom of the pipe. At low flow rates, some or all of the bed is stationary

and a shear layer, spanning some or all of the pipe diameter, exists above it. The reader is referred to Section 6.1.1 for more details of the commonly observed properties of shear layers; to avoid duplication, only their effect on the ultrasonic signal and the method for measuring their thickness are described in this section.

In the presence of a shear layer a significant proportion of the ultrasonic energy is absorbed before it reaches the stationary part of the bed (*i.e.* the lower, immobile part of the bed), whilst at very low flow rates (at which the bed is mainly or wholly settled and the shear layer is very thin or non-existent) the top part of the bed acts as a simple reflective surface. The root-mean-square of the echo profile – referred to here as the echo amplitude, V – was found to reach a maximum at a certain distance from the probe. This distance was assumed to correspond to the top of the stationary bed or shear layer, depending on the flow regime.

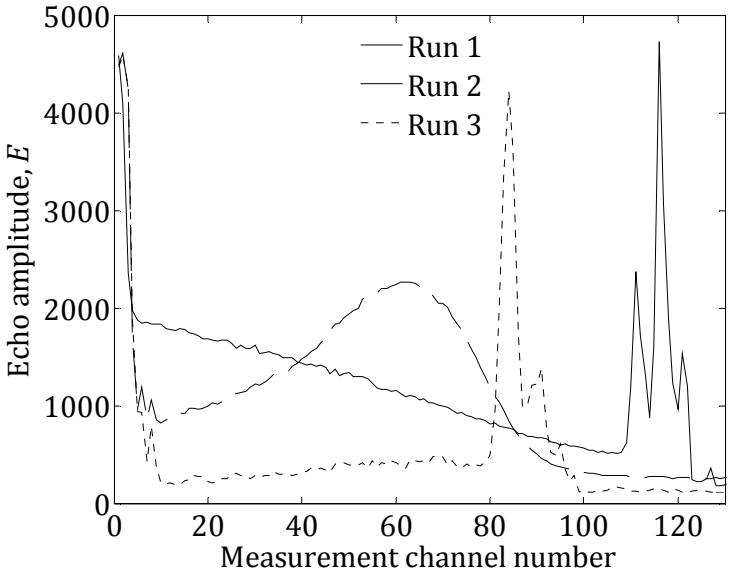

Figure 3-25: Echo amplitude showing peaks at three flow rates. Run 1 (solid line): high Q, fully suspended (peak at measurement channel 111); run 2 (dashed): shear layer present (peak: 62); run 3 (dotted): stop-flow run, Q = 0, with settled bed (peak: 84). Runs 2 and 3 also shown in Figure 6-8.

To illustrate this method, the echo amplitude (with the RMS taken over the whole of each run, n = 2,500, 5,000 and 500, respectively, for runs 1, 2 and 3) at three flow rates are shown in Figure 3-25. In run 1, the flow rate was very high (Q = 3.61 l s^{-1}): the particles are fully suspended and the first peak (at measurement channel

111) corresponds to the position of the lower pipe wall and was therefore used as a reference run. In run 2, at an intermediate flow rate (Q = 0.856 l s^{-1}) a shear layer is present, the top of which corresponds to the peak in echo amplitude at channel 62. Lastly, the pump was turned off in run 3 and the moving bed and suspended sediment were allowed to settle; in this case a peak in V was observed at the top of the bed, at channel 84. The distance between channels 62 and 84, and between channels 84 and 111, were then the thicknesses of the shear layer (8.14 mm) and settled bed (9.99 mm), respectively.

To summarise, the distance to the opposite pipe wall is found using a reference run; in practice this meant the flow rate had to be high enough that that the sediment was fully suspended and a settled bed (the top of which would act as a reflective surface itself) was not present. The settled bed and/or shear layer thickness could then be calculated in a simple fashion, as described above and illustrated in Figure 3-25.

4 First- and second-order turbulence statistics and critical velocities in turbulent pipe flow

The first objective in this section was to investigate the mean and RMS axial and radial (or rather, wall-normal) velocity profiles, and normal and shear Reynolds stresses, in turbulent, multiphase pipe flow in order to determine the effects of suspended particles on the flow and settling behaviour. The second objective was to delineate homogeneous, heterogeneous and settling flow regimes through the quantification of the corresponding critical flow velocities, U_{c1} and U_{c2}.

Experimental procedures that were specific to this part of the study are described in Section 4.1, in particular the method of decomposing the two components of velocity and stress (Section 4.1.1) and for determining the two critical flow velocities (Section 4.1.2 and 4.1.3).

The results for the first part are presented in four themed sections: for homogeneous suspensions at low particle volume fractions (Section 4.2.1), homo- and heterogeneous suspensions at moderate volume fraction (Section 4.2.2), settling suspensions at low volume fractions (Section 4.2.3), and settling suspensions at high volume fractions (Section 4.2.4). The results for the second part are presented in Sections 4.2.5 and 4.2.7. Lastly, a summary of all the results is given (Section 4.3).

4.1 Experimental method

A general description of the experimental methods used in this study was given in Chapter 3. However, in the sections that follow more thorough details are presented of some specific techniques that were used, in particular the decomposition of velocity and stress fields into their axial and radial (or wall-normal) components (Section 4.1.1) and the determination of the two critical velocities, U_{c1} (Section 4.1.2), which corresponds to the transition between homogeneous and heterogeneous flow regimes, and U_{c2} (Section 4.1.3), which corresponds to the velocity below which a bed begins to form.

4.1.1 Decomposing velocity and stress components

It is clear from Section 2.2.1, and specifically from Equations [2.6], [2.7] and [2.8], that the quantities $\overline{u^2}$, $\overline{w^2}$ and $\overline{uw}$ must be known if the Reynolds stresses are to be calculated. These terms, along with U, W and $\overline{U}$, constitute the six variables that were to be measured or calculated in this study.

To resolve both the axial and radial (or wall-normal) components of the velocity and stresses, at least two independent measurements at different angles to the direction of flow are required. For the ith probe mounted at an angle ψ_i to the mean flow direction, the measured instantaneous velocity along the probe axis is:

$$U_{pi} = U \cos\psi_i + W \sin\psi_i. \qquad [4.1]$$

Taking the mean of Equation [4.1], and noting that the means of the fluctuating parts and $\overline{W}$ in pipe flow are all zero, yields:

$$\overline{U_{pi}} = \overline{U} \cos\psi_i. \qquad [4.2]$$

Unless contrived to be so by the physical arrangement of the transducers (Lemmin and Rolland, 1997; Lhermitte and Lemmin, 1994; Pedocchi and Garcia, 2012) or by a suitable choice of parameters in the instrumental software, which is very difficult in practice, the measurement points will not be co-located in general. This is, of course, true for the specific case of two probes mounted at ψ = 90° and 135° to the direction of flow, as in this study, and has two implications: first, in order to resolve the velocity components the flow field must be assumed not to vary with axial distance, z, *i.e.* the flow is fully developed; second, it is necessary to project all data onto a common axis and evaluate them at a set of co-located points along this axis. In this study, linear interpolation was used and the distance from each probe (and from the pipe wall) was calibrated accurately, using the method described in Section 3.6.3.

Evaluating Equation [4.1] for ψ_1 = 135° and ψ_2 = 90°, as shown in 3.2.2, yields the following expressions for the instantaneous velocities:

$$W = U_{p2}, \quad [4.3]$$

$$U = U_{p2} - \sqrt{2}U_{p1}, \quad [4.4]$$

where it was necessary to (linearly) interpolate the U_{p2} data since the measurement points for each probe were not collocated. The interpolation and all other data processing were performed using MATLAB scripts written for this purpose by the author.

As mentioned in Section 2.2, P could not be measured because no pressure transducers were installed in this study. However, several components of the Reynolds stresses (in particular $\rho\overline{u^2}$, $\rho\overline{w^2}$ and $\rho\overline{uw}$) were measured: once U and W were known (*via* Equations [4.3] and [4.4]) the normal and shear stresses could be calculated according to the rules given in Equation [2.3], since it was more computationally efficient, as follows:

$$\overline{uw} = \overline{UW} - \overline{U}\overline{W}, \quad [4.5]$$

$$\overline{u^2} = \overline{U^2} - \overline{U}^2, \quad [4.6]$$

$$\overline{w^2} = \overline{W^2} - \overline{W}^2, \quad [4.7]$$

and the RMS turbulent velocities, u' and w', could then be calculated according to Equation [2.4], *i.e.* $u' = \sqrt{\overline{u^2}}$ and $w' = \sqrt{\overline{w^2}}$.

4.1.2 Critical flow velocity 1, U_{c1} (homogeneous transition velocity)

Whereas at very high flow rates, the mean axial velocity profile in a suspension of particles is expected to be symmetrical about the pipe centreline, at lower flow rates this has been found not to be the case, as described in Section 4.2.4. A method

is proposed for determining U_{c1}, the homogeneous transition velocity, based on the shift in the position of the peak in the mean axial velocity profile with respect to the flow rate (and therefore the bulk or average flow velocity). For example, a clear shift is evident in Figure 4-11, Guyblast 30/40, ϕ = 1 %.

The method is as follows. First, the distance from the probe to the maximum value of the mean axial velocity was measured at a high flow rate at which it was assumed the flow was symmetrical about the centreline (in every case Q > 3 l s^{-1}, Re > 90,000). Second, the position of the peak was measured at progressively lower flow rates and compared to the position at the highest flow rate.

This process was repeated for all four particle species at three nominal volume concentrations, ϕ = 0.5, 1 and 3 %. It was intended that the flow rates used covered the range from very high (and therefore fully suspended/homogeneous) to moderately low (heterogeneous/moving bed), but not so low that time-dependent bedforms were present, as this topic is covered separately in another chapter (Chapter 6). The results of this technique for all (*i.e.* four) particle species over a range of flow rates and nominal volume fractions are given in Section 4.2.5.

4.1.3 Critical flow velocity 2, U_{c2} (limit deposition velocity)

As described in Section 2.2.7, there are many models and correlations in the literature for predicting U_{c2}, the critical flow velocity necessary to keep the solid phase fully in suspension. In this section, a method is presented for determining U_{c2}, the limit deposition velocity, based on measurements of the position of the first peak in the RMS echo profile (which is assumed to correspond to the position of the opposite pipe wall) with respect to flow rate (and therefore bulk or average flow velocity). The variables R, D, h and H are as defined in the general methodology (Section 3.7): R and D are the radius and diameter of the pipe, respectively; h and H are the bed and flow depths such that

$$D = h + H. \qquad [4.8]$$

The diagram is repeated in Figure 4-1, below, for the reader.

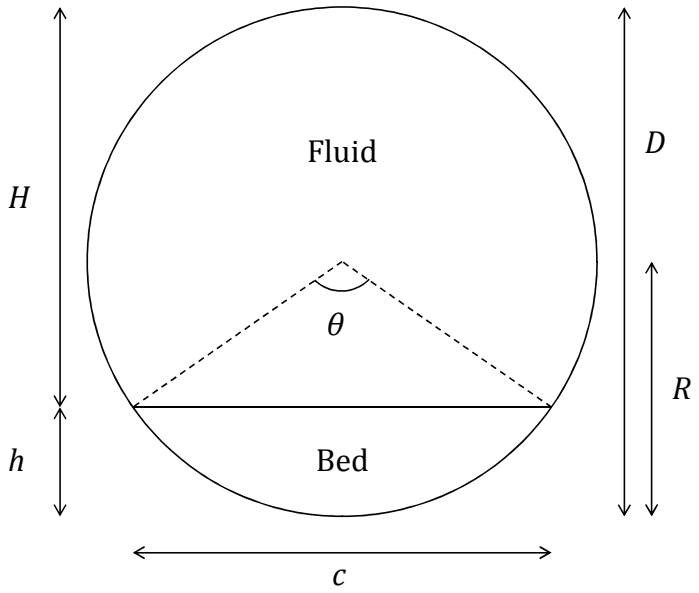

Figure 4-1: Bed geometry and definitions. *H* and *h* are fluid and bed depths, respectively; *R* and *D* are pipe radius and diameter; θ is angle subtended by bed at pipe centre; and *c* is chord length (*i.e.* bed width at top of bed). Also shown in Figure 3-24 in general methodology (Section 3.7)

The bed depth was found by inspection of the peak in the echo RMS profile, *V*, in a stop-flow run (*i.e.* one in which the pump was turned off and the bed and ambient suspended sediment were allowed to form a settled bed), with the distance to the pipe wall found from high-flow-rate reference runs corresponding to each set of stop-flow runs, except in the cases of both Guyblast plastic species at ϕ = 3 %, in which cases a peak at the lower pipe wall could not be seen due to high attenuation; in those cases the lower pipe wall was assumed to be at the same position as in the ϕ = 1 % sets.

The chord length, *c*, and angle subtended by the bed at the pipe centre, θ, are as described in the general methodology (Section 3.7) but are repeated here for the reader (Weisstein):

$$c = 2\sqrt{h(2R - h)} = 2\sin(\theta/2), \qquad [4.9]$$

$$\theta = 2\cos^{-1}\left(\frac{R-h}{R}\right). \qquad [4.10]$$

The cross-sectional area occupied by the bed, A_{bed}, and the flow, A_{flow}, are as described in Section 3.7 (Equations [3.48] and [3.49], respectively).

Because the bed depths were measured during stop-flow runs, it was necessary to apply a correction, δh, to the bed depth to account for sediment that settles when the flow was stopped but which would otherwise remain suspended. To calculate this correction, it was assumed that the volume fraction occupied by the suspended particles, ϕ, which is calculated directly from the sampled mass concentration, M, as follows:

$$\phi = M/\rho_s, \qquad [4.11]$$

where ρ_s is the material density of the solid particles, is equal to the area fraction occupied by the suspended particles when they settle. A further, trivial simplification – that the chord length, c, is constant within the increment δh – was also made such that the following expression, which also incorporates the particle packing fraction, p (which was measured using dry samples in volumetric flasks of several sizes, the results of which measurements were presented in Section 3.5.3), can be written:

$$pc\delta h = \phi A_{\text{flow}}. \qquad [4.12]$$

The mass concentration, M, was calculated assuming a linear variation with flow rate using the runs at which no bed was observed. The depth correction δh, was calculated *via* Equation [4.12]; the uncorrected and corrected bed depths, h_{uncorr} and h_{corr}, are related as follows:

$$h_{uncorr} = h_{corr} + \delta h \qquad [4.13]$$

The results of this technique for all particle species over a range of flow rates and nominal volume fractions are given in Section 4.2.7.

4.2 Results and discussion

Such was the size of the available experimental parameter space that it was necessary to be selective when presenting the results. A summary of the parameter space is given in . Although the entire dataset is presented in Section 4.2.7 (U_{c2}), and a less comprehensive (but nevertheless thorough and representative) dataset in Section 4.2.5 (U_{c1}), the same was not possible for the velocity and stress data in general.

Table 4-1: Summary of all experiments, a selection of which is presented in Sections 4.2.1 to 4.2.4 under four distinct themes.	
Particle species	Honite 22, Honite 16, Guyblast 40/60, Guyblast 30/40 (properties given in Table 3-7)
Pump setting	5 to 45 Hz
Volumetric flow rate, Q	≈ 0.4 to 4 l s^{-1}
Bulk mean velocity, U_{ave}	≈ 0.28 to 2.8 m s^{-1}
Reynolds number, Re	≈ 12,000 to 120,000
Nominal concentration by volume, ϕ	0.01, 0.1, 0.5, 1 and 3
Runs per species per concentration	14
Total number of runs	280

The results were grouped into four themed sections, as follows: homogeneous suspensions at low volume fractions (Section 4.2.1); homo- and heterogeneous suspensions at moderate volume fractions, including a detailed case study (Section 4.2.2); settling suspensions at low volume fractions (Section 4.2.3); and heterogeneous and settling suspensions at high volume fractions (Section 4.2.4). A summary of the run parameters are given in Table 4-2.

All four particle species are represented in the results sections that follow, and the effects of particle size and flow rate/bulk flow velocity are discussed in detail. In particular, three Reynolds numbers were investigated: Re ≈ 25,000, 50,000 and 100,000. The velocity and stress results, in particular, were compared to a wide range of data taken from the literature (all of which, and more, are listed in Table

2-3 for reference).

4.2.1 Homogeneous suspensions at low volume fractions

The mean velocity (relative to the bulk or average value, U_{ave}) for a very low-volume fraction run (ϕ = 0.01 %) with Honite 22 at a high flow rate (Q = 1.76 l s^{-1}, Re = 53,000) at which the flow is homogeneous, is shown in Figure 4-2. The agreement with the data from Wu and Moin (2008) at Re = 44,000 is very good, although there is a slight overestimate in the core region of the flow. The effects of beam divergence and reflections from the opposite (*i.e.* lower) pipe wall are apparent around y/R = 2.

Table 4-2: Run parameters* and sample results for flow-loop runs presented in Sections 4.2.1 to 4.2.4 and Figure 4-2 to Figure 4-12.

ϕ (%)	M_w (kg m^{-3})	M_s (kg m^{-3})	Q (l s^{-1})	Re (10^3)	U_{ave} (m s^{-1})	Profile
Homogeneous suspensions at low volume fractions (Section 4.2.1)						
Honite 22 (small glass)						
0.01	0.250	-	1.76	53.0	1.24	Figure 4-2: $\overline{U}/U_{ave}$
Guyblast 40/60 (small plastic)						
0.1	1.50	1.68	3.57	107	2.50	Figure 4-3(a): $\overline{U}/\overline{U}_{max}$; (b): $\overline{uw}^+$
						Figure 4-4(a): u'^+; (b): w'^+
Homo- and heterogeneous suspensions at moderate volume fractions (Section 4.2.2)						
Guyblast 30/40 (large plastic)						
0.1	7.46	5.49	1.67	49.7	1.17	Figure 4-5(a): $\overline{U}/\overline{U}_{max}$; (b): $\overline{uw}^+$; Figure 4-6(a): u'^+; (b): w'^+
Settling suspensions at low volume fractions (Section 4.2.3)						
Honite 22 (small glass)						
0.1	2.50	2.28	0.874	26.1	0.612	Figure 4-7(a): $\overline{U}/\overline{U}_{max}$; (b): $\overline{uw}^+$
						Figure 4-8(a): u'^+; (b) w'^+
Settling suspensions at high volume fractions (Section 4.2.4)						
Honite 16 (large glass)						
3	72.8	28.2	0.838	25.0	0.587	Figure 4-9: u'^+

Table 4-2: Run parameters* and sample results for flow-loop runs presented in Sections 4.2.1 to 4.2.4 and Figure 4-2 to Figure 4-12.						
ϕ (%)	M_w (kg m^{-3})	M_s (kg m^{-3})	Q (l s^{-1})	Re (10^3)	U_{ave} (m s^{-1})	Profile
		28.2	0.838	25.0	0.587	Figure 4-10(a): $\overline{U}/\overline{U}_{max}$; (b): $\overline{U}/\overline{U}_{max}$
		75.9	3.47	104	2.43	
Guyblast 30/40 (large plastic)						
1	14.9	7.56	0.812	24.3	0.570	Figure 4-11(a): $\overline{U}/\overline{U}_{max}$; (b): $\overline{uw}^+$; Figure 4-12(a): u'^+; (b): w'^+
		16.1	3.40	102	2.38	
*ϕ = nominal volume fraction; M_w = weighed particle concentration; M_s = sampled particle concentration; Q = flow rate; Re = Reynolds number; U_{ave} = bulk flow velocity.						

Figure 4-3(a) shows the mean axial velocity profile for Guyblast 40/60 at a very high flow rate (Q = 3.57 l s^{-1}, Re = 107,000) with a low particle volume fraction (ϕ = 0.1 %). The region very close to the probe and within the pipe wall (*i.e.* $y/R < 0$) is also shown: rather than being an underestimate, however, the discrepancy between the measured results and those of McKeon *et al*. (2004a) in the upper half of the pipe (*i.e.* $0 < y/R < 1$) suggests that there is a real flow disturbance around the tips of the probes and in the pipe-wall recesses (which are of the order of 3-4 mm).

However, the agreement with the data of McKeon *et al.* (2004a) in the lower half of the pipe (*i.e.* $1 < y/R < 2$) in Figure 4-3(a) is excellent, although it should be noted that no data could be gathered beyond $y/R \approx 1.8$: this was the maximum measurement distance at such a high flow rate, as determined by the compromise between maximum measurable velocity and distance (which were described in Section 3.2.2 of the general methodology in Chapter 3). This was found to be the case for all runs at the highest flow rates (*i.e.* Re ≈ 100,000). The kind of plot shown in Figure 4-3(a) (*i.e.* $\overline{U}/\overline{U}_{max}$) is the most suitable for inspecting the shape of a velocity profile since several datasets can be readily compared, like for like.

The mean axial velocity results for every particle species were generally very good at the lowest volume fractions (*i.e.* "single-phase", in which the particles do not influence the flow, ϕ = 0.01 and 0.1 %). The discrepancy in Figure 4-2 can be

explained by inaccuracies in the flow rate and distance calibration and overall, the results demonstrate the limits of accuracy of the intrusive probe mounting that was used.

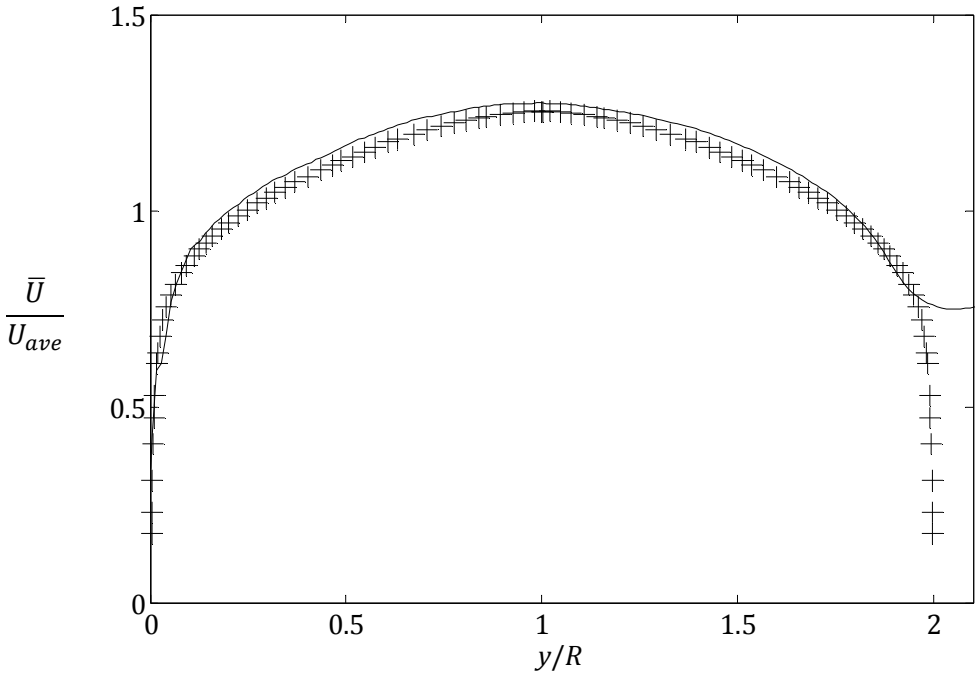

Figure 4-2: Mean velocity relative to average (bulk) value vs. wall-normal distance from upper pipe wall with Honite 22, Re = 53,000, U_{ave} = 1.24 m s^{-1}, ϕ = 0.01 %; pluses, DNS results of Wu and Moin (2008) at Re = 44,000.

The Reynolds shear stress profile, $\overline{uw}^+$, for the same conditions as in Figure 4-3(a) (Guyblast 40/60, Re = 107,000, ϕ = 0.1 %) is shown in Figure 4-3(b) and was found to be strongly underestimated relative to the hot-wire results of Laufer (1954) at Re = 50,000, and although the discrepancy was strongest at such high flow rates, it was present at all flow rates, as can be seen from the sections that follow. Putative explanations are given in Section 4.2.5.

The axial and radial RMS velocities for the same conditions are shown in Figure 4-4(a) and (b), respectively. The agreement of u'^+ with the results of Perry *et al*. at Re = 75,000 is very good in the region $0.5 < y/R < 1$ (Figure 4-4(a)), but the turbulence is suppressed near the probe ($0 < y/R < 0.2$), presumably because of the intrusive probe arrangement. On the other hand, w'^+ is underestimated by a factor of 2.5 through the entire profile (Figure 4-4(b)), an observation that is common to

all the runs presented in this results chapter. The results suggest that the present system accurately measures the structure of both the radial/wall-normal and axial turbulence statistics, notwithstanding the discrepancy in the *magnitude* of w'^{+}, and the flow disturbance caused by the probes that is most evident in Figure 4-4(a) in the near-probe region.

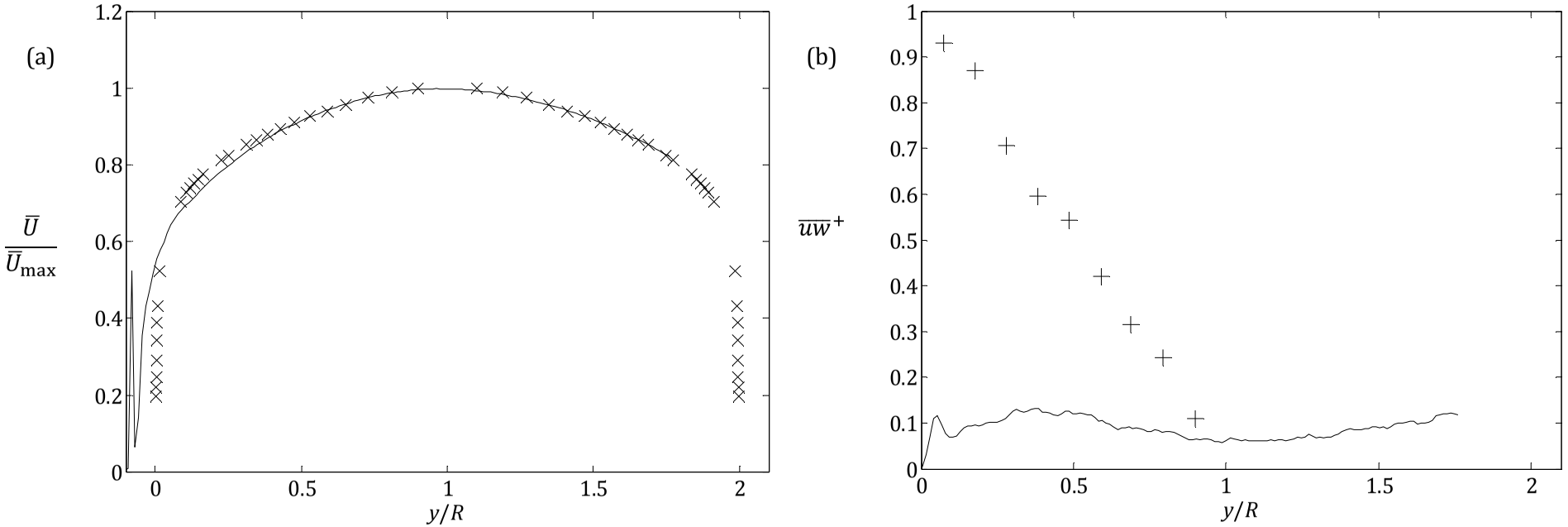

Figure 4-3: (a) Mean velocity relative to maximum (*i.e.* centreline) value *vs.* wall-normal distance from upper pipe wall; (b) Reynolds shear stress in wall units; with Guyblast 40/60, Re = 107,000, U_{ave} = 2.50 m s^{-1}, ϕ = 0.1 %; crosses in (a), Pitot-probe results of McKeon *et al.* (2004a) at Re = 75,000; pluses in (b), hot-wire results of Laufer (1954) at Re = 50,000.

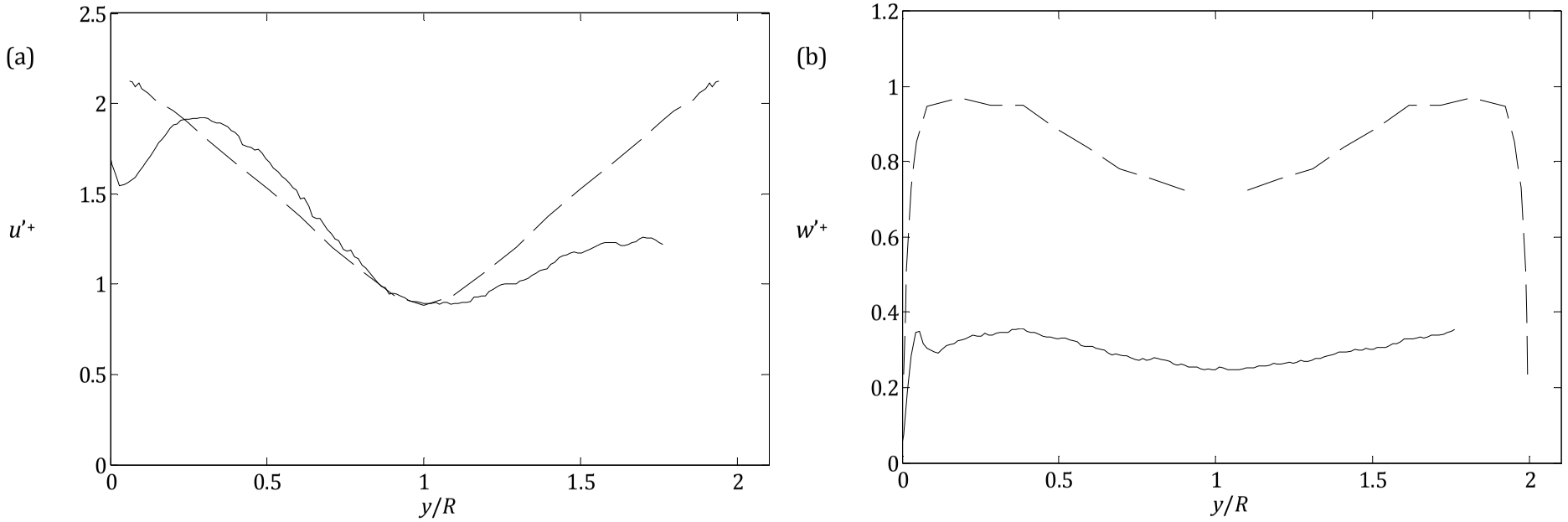

Figure 4-4: (a) Axial RMS velocity in wall units *vs.* wall-normal distance from upper pipe wall; (b) radial RMS velocity in wall units; with Guyblast 40/60, Re = 107,000, U_{ave} = 2.50 m s^{-1}, ϕ = 0.1 %; dashed line in (a), hot-wire results of Perry *et al.* (1986) at Re = 75,000; dashed line in (b) hot-wire results of Laufer (1954) at Re = 50,000.

4.2.2 Homo- and heterogeneous suspensions at moderate volume fractions

In order to examine the mean and turbulence statistics (*i.e.* the mean axial and RMS axial and wall-normal velocities and Reynolds shear stress), a single representative case study is presented in this section. The run parameters were as follows: Guyblast 30/40 at a moderate volume fraction, ϕ = 0.5 %, and a high flow rate, Re = 49,700 (Q = 1.67 l s^{-1}), and both Figure 4-5 and Figure 4-6 show the results for these conditions.

Figure 4-5(a) shows the mean axial velocity profile, $\overline{U}/\overline{U}_{max}$ The agreement with the results of Laufer (1954) at Re = 50,000 is good, but there is a small under-prediction in the lower half of the pipe ($1 < y/R < 2$) that is most likely to have been caused by a slight concentration gradient. Such an asymmetry is consistent with the modification of the mean axial velocity profile observed by several researchers (Gillies and Shook, 2000; Graf, 1984).

As in Figure 4-2 in the previous section, the effect of beam divergence at the opposite (lower) wall is evident at $y/R > 2$. The Reynolds shear stress in wall units, $\overline{uw}^+ = \overline{uw}/U_\tau^2$, is presented in Figure 4-5(b). The agreement with the data of Wu and Moin (2008) at Re = 44,000 is poor: $\overline{uw}^+$ was under-predicted by a factor of four to five, and flow disturbance near the probe and within the probe recess produced unreliable results in the region $0 < y/R < 0.1$. As shown in Figure 4-6(a), the magnitude and structure of the axial RMS velocity, u', are very good in the upper half of the pipe ($0 < y < 1$). A near-wall peak in u' is apparent in the Morrison *et al.* (2004) data at Re = 55,000. However, because this peak has a width of $\Delta y/R \approx 0.04$, *i.e.* $\Delta y \approx 0.85$ mm, which is only slightly larger than the spatial resolution of the present measurements (0.37 mm), and because of flow disturbance near the tips of the probes, this peak was not observed.

Figure 4-6(b) shows the wall-normal RMS velocity, w', compared to the DNS results of Wu and Moin (2008) at Re = 44,000. As with the shear stress, w' is underestimated, although the general shape of the profile is correct, *i.e.* the profile

is (approximately) symmetrical about, and exhibits a minimum at, the pipe centreline and reaches peaks near the pipe walls.

The tendency of $\overline{uw}^+$ and w'^+ to be under-predicted at low and moderate volume fractions (*e.g.* Figure 4-3(a) and Figure 4-4(b), respectively) was observed for all particle species, and the degree of under-prediction was found to increase with Reynolds number. The most obvious hypothesis for the cause of the discrepancy is that the ultrasonic probes do not have sufficient spatial and/or temporal resolution to record the motion of the smallest turbulent eddies. There is some further evidence for this: the Stokes number for Guyblast 30/40 particles under the flow conditions specified in this section, for example, was St = 2.39, which means the particles were only reasonably good tracers of the fluid motion. Moreover, the Kolmogorov timescale was estimated to be τ_K = 5.75 ms, which is significantly smaller than the actual sample interval, Δt = 41 ms.

On the other hand, under-predictions of similar magnitudes were observed for all particle species at all flow rates, suggesting a Stokes-number effect was not responsible, since St was of the order of 10^{-4} in some cases (*i.e.* the particles acted as excellent tracers). That conclusion leaves the spatial and/or temporal resolution of the instrument as the most likely cause of the discrepancy, but it must be noted that in the runs that are presented here, the *UVP-DUO* was operating at the limit of its resolution.

However, why the wall-normal RMS velocity, w', was under-predicted but not the axial component, u', in an analogous way remains unclear, since the measurement volumes were approximately the same for both transducers – $\pi a^2 \times w$ – and the sample rate for each differed only by factor of order unity. No calculation errors could be found; indeed, data from both probes were processed with a common MATLAB code.

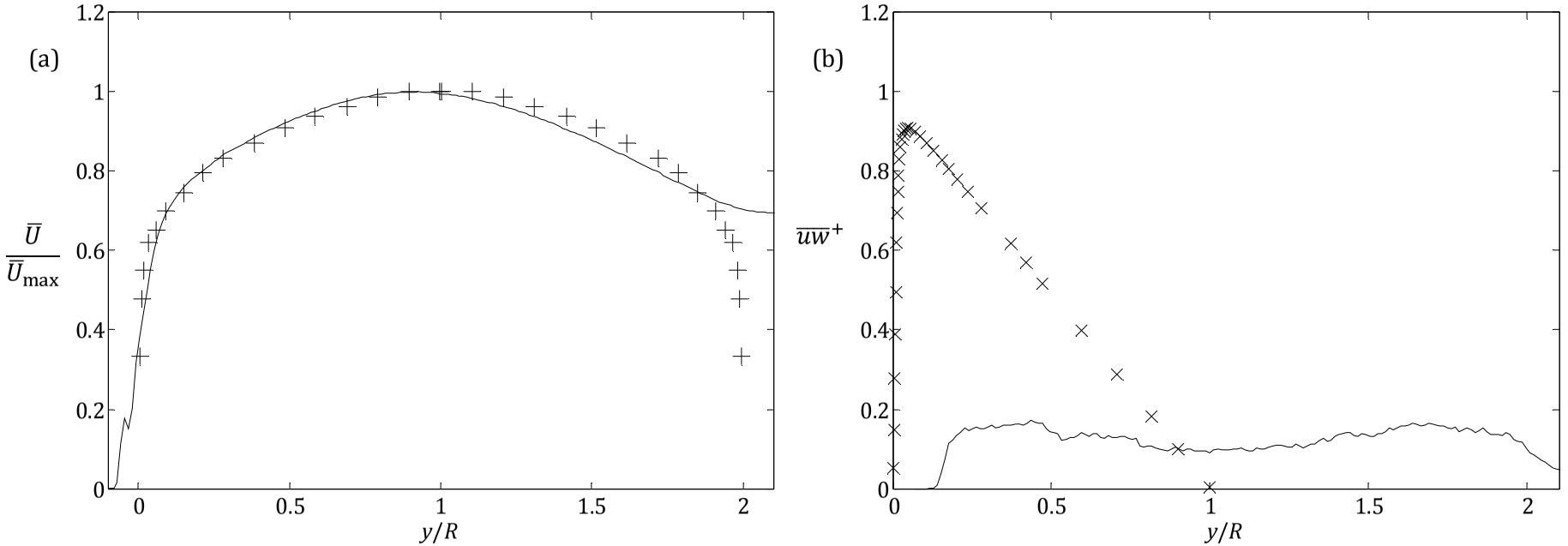

Figure 4-5: (a) Mean velocity relative to maximum (*i.e.* centreline) value *vs.* wall-normal distance from upper pipe wall; (b) Reynolds shear stress in wall units; with Guyblast 30/40, Re = 49,700, U_{ave} = 1.17 m s^{-1}, ϕ = 0.5 %; pluses in (a), hot-wire results of Laufer (1954) at Re = 50,000; crosses in (b), DNS results of Wu and Moin (2008) at Re = 44,000.

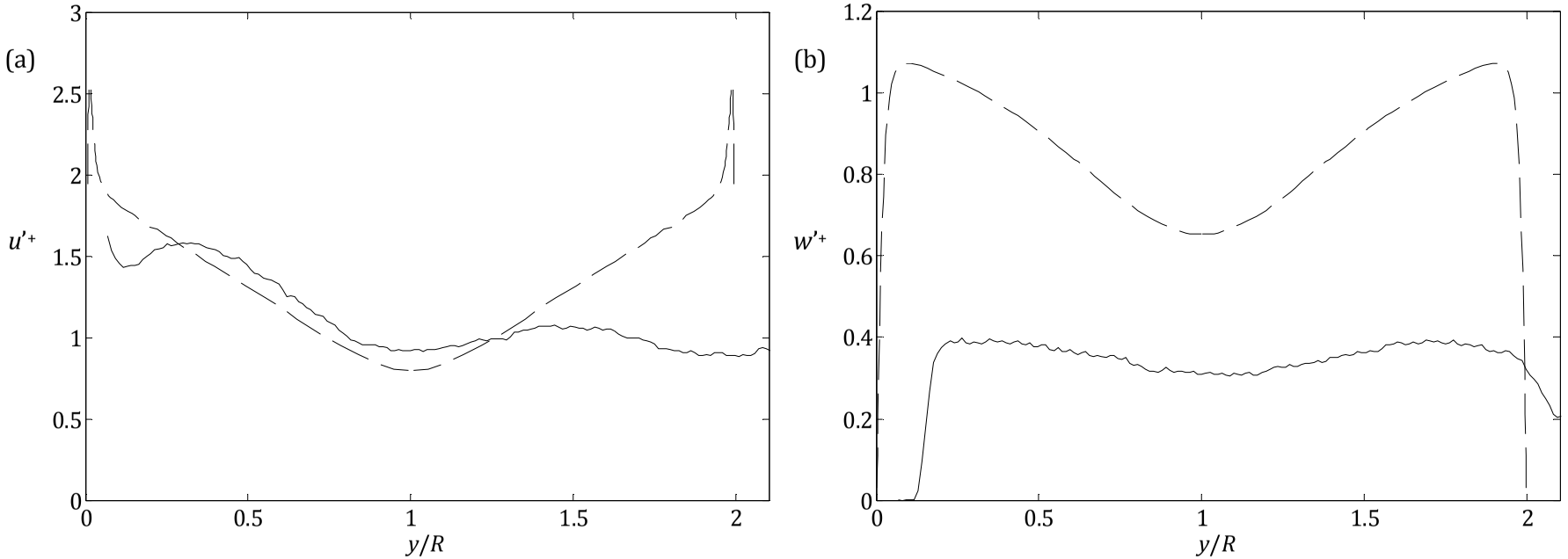

Figure 4-6: (a) Axial RMS velocity in wall units *vs.* wall-normal distance from upper pipe wall; (b) radial RMS velocity in wall units; with Guyblast 30/40, Re = 49,700, U_{ave} = 1.17 m s^{-1}, ϕ = 0.5 %; dashed line in (a), hot-wire results of Morrison *et al.* (2004) at Re = 55,000; dashed line in (b) DNS results of Wu and Moin (2008) at Re = 44,000.

4.2.3 Settling suspensions at low volume fractions

In this section a case study with Honite 22 at a low volume fraction (ϕ = 0.1 %) and moderate flow rate (Re = 26,100, Q = 0.880 l s^{-1}) is presented in order to illustrate the effects of settling on the first- and second-order statistics.

The mean axial velocity profile in Figure 4-7(a) agrees well in the core region (0.8 < y/R < 1.5) with the results of den Toonder and Nieuwstadt (1997) at Re = 24,600, but there is a significant discrepancy near the bottom of the pipe (*i.e.* 1.8 < y/R < 2). That a similar discrepancy exists in the u'^{+} profile in the same region (see Figure 4-8(a)) suggests a real physical effect is present, most likely a shear layer or region of relatively high local particle concentration.

Although it is possible that the observed peak – which is posited as being caused by a thin shear layer above the lower pipe wall – could be caused by a combination of wall reflections and a distance contraction due to enhancement of sound speed by a high concentration of suspended particles in that region, it is thought to be very unlikely, and the reader is referred to Section 3.6.1 for a quantitative justification. A variation of several tens of per cent would be necessary to produce the observed peak, were it caused by wall reflections, and such a variation is not physically possible at a mean concentration of ϕ = 0.1 %.

It is surprising that a local enhancement in particle concentration was observed at such low nominal volume fractions. However, a strong peak in the local concentration was indeed observed in this run but not at higher flow rates, as shown in Figure 5-21 (Chapter 5). It is interesting to note that the effects of beam divergence may cause the putative shear layer to appear to be thicker than it is in reality. This is left as a topic for further study. Notwithstanding the peak near the lower pipe wall, the u'^{+} results are very good, in terms of both magnitude and structure.

Lastly, the wall-normal RMS velocity, w'^{+}, and the Reynolds shear stress, $\overline{uw}^{+}$, for the same runs described above are shown in Figure 4-7(b) and Figure 4-8(b),

respectively. As was observed in the two previous sections at two higher Reynolds numbers (Section 4.2.1: Re = 107,000; Section 4.2.2 Re = 49,700), both w'^{+} and $\overline{uw}^{+}$ are underestimated relative to data in the literature, but to a lesser degree at this, lower, Reynolds number (Re = 26,100). To be clear, the degree of under-prediction of w'^{+} and $\overline{uw}^{+}$ appears to increase with Reynolds number. The reader is invited to compare the w'^{+} profiles in Figure 4-4 (Re = 107,000), Figure 4-6 (Re = 49,700) and Figure 4-8 (Re = 26,100).

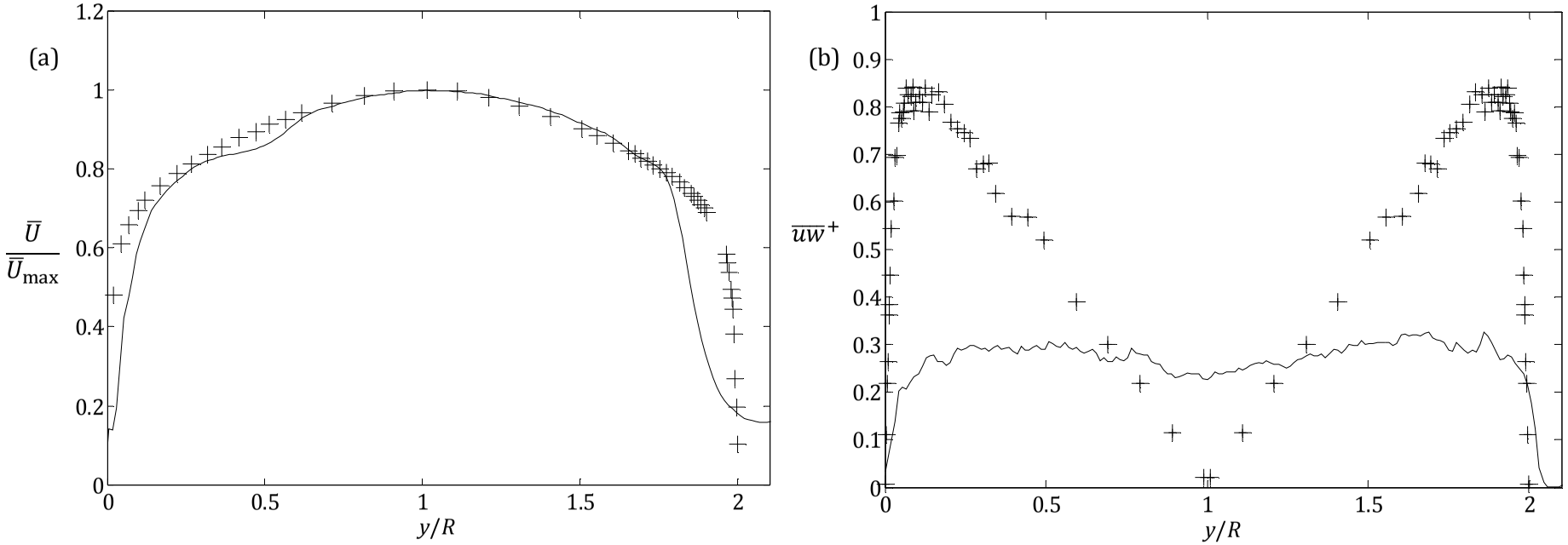

Figure 4-7: (a) Mean velocity relative to maximum (*i.e.* centreline) value *vs.* wall-normal distance from upper pipe wall; (b) Reynolds shear stress in wall units; with Honite 22, Re = 26,100, U_{ave} = 0.612 m s^{-1}, ϕ = 0.1 %; pluses in both frames, LDA results of den Toonder and Nieuwstadt (1997) at Re = 24,600.

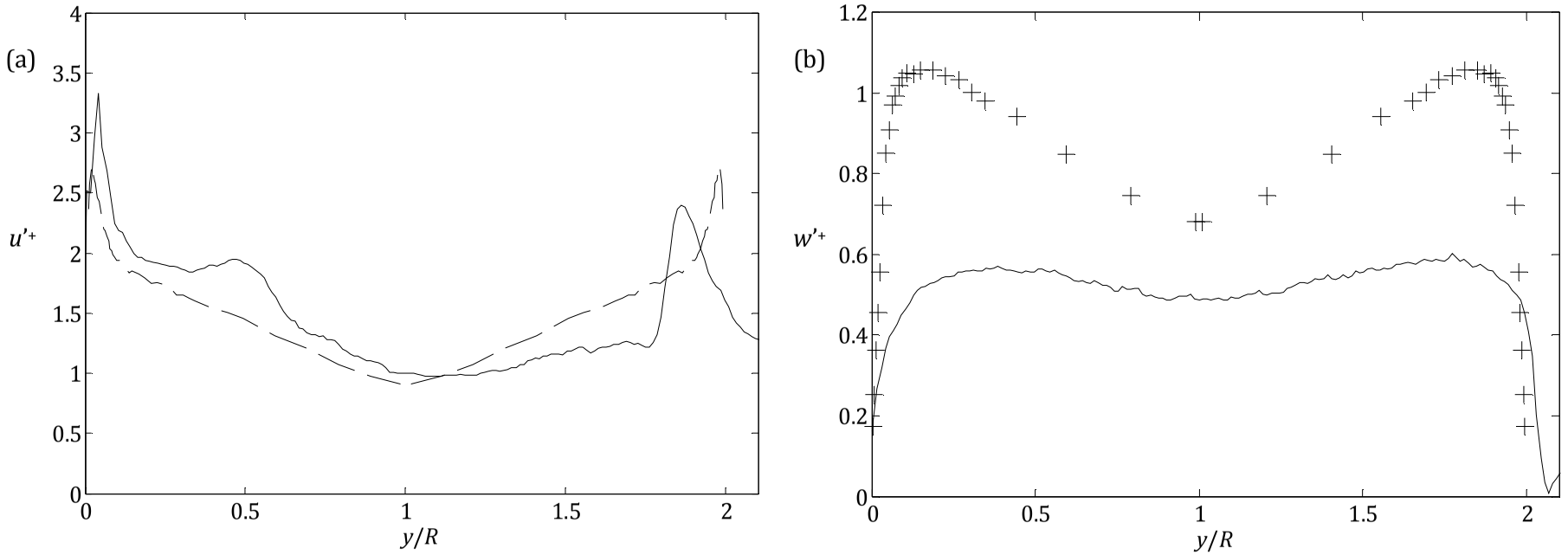

Figure 4-8: (a) Axial RMS velocity in wall units *vs.* wall-normal distance from upper pipe wall; (b) radial RMS velocity in wall units; with Honite 22, Re = 26,100, U_{ave} = 0.621 m s^{-1}, ϕ = 0.1 %; dashed line in (a), Pitot-probe results of Zagarola and Smits (1998) at Re = 25,000; crosses in (b), LDA results of den Toonder and Nieuwstadt (1997) at Re = 24,600.

4.2.4 Heterogeneous and settling suspensions at high volume fractions

In this section, the last of four on velocity and stress fields, the effects of high volume fractions on the flow are investigated. First, shear-layer phenomena in a suspension of Honite 16 at ϕ = 3 % are described and compared to similar observations at lower volume fractions that were made in Section 4.2.3. Second, a case study of Guyblast 30/40 at ϕ = 3 % is given.

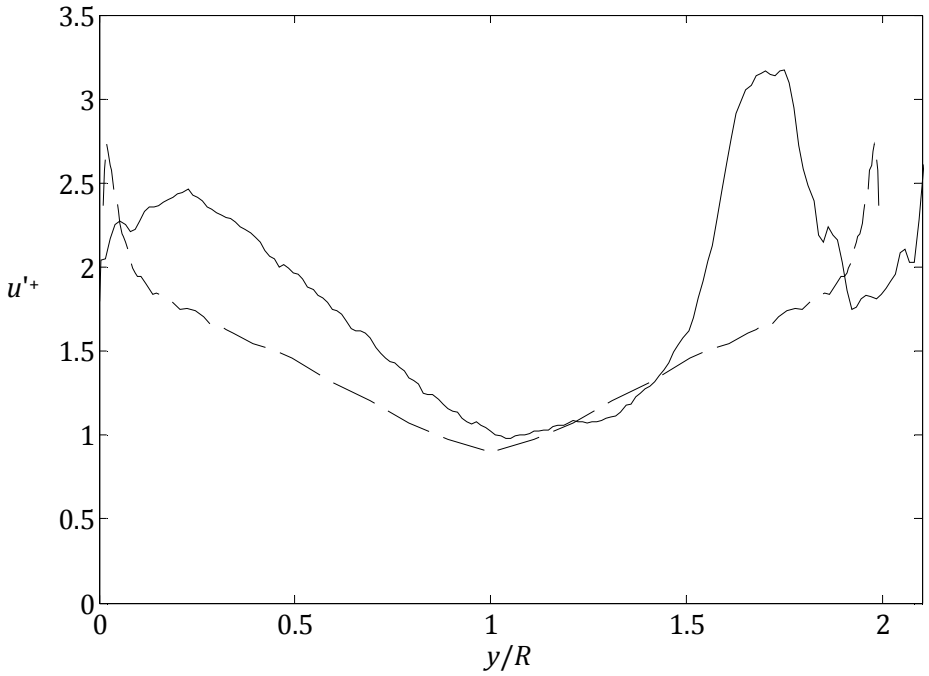

Figure 4-9: Axial RMS velocity *vs.* wall-normal distance, with Honite 16, Re = 25,000, U_{ave} = 0.587 m s^{-1}, ϕ = 3 %; dashed lined, Pitot-probe results of Zagarola and Smits (1998) at Re = 25,000.

In a suspension of Honite 16 at a high volume fraction (ϕ = 3 %) and a moderate flow rate (Re = 25,000, Q = 0.838 l s^{-1}) a strong enhancement in the axial turbulence was observed (Figure 4-9) relative to the single-phase Pitot-probe results of Zagarola and Smits (1998) at Re = 25,000. This enhancement was similar to, but more pronounced than, that observed with Honite 22 and ϕ = 0.1 % (Figure 4-8(a), Section 4.2.3): the flow in the majority of the lower half of the pipe, *i.e.* at least 1.5 < y/R < 2, appears to be affected. This is to be expected, since a high nominal volume fraction means that, if a shear layer were present, then the local enhancement in particle concentration would also have be stronger. Indeed, a

strong increase in the concentration profile was observed (see, for example, Figure 5-26, Chapter 5).

A corresponding suppression of $\overline{U}/\overline{U}_{max}$ in the same region can be seen in Figure 4-10(a), *i.e.* $1.5 < y/R < 2$, and this combination of an enhancement in u' and a suppression of $\overline{U}$ was also observed with Honite 22 at ϕ = 0.1 % (Section 4.2.3). The mean velocity profile for the same nominal volume fraction at a higher flow rate (Re = 104,000, Q = 3.47 l s^{-1}) is shown in Figure 4-10(b) for comparison, and the hot-wire data of Laufer (1954) at Re = 50,000 is given in both frames of Figure 4-10 as a common standard to aid the comparison. The structure and magnitude of the discrepancy in Figure 4-10(a) is quite clear: the mean velocity is more strongly peaked at the lower flow rate. This is, of course, to be expected if the mean flow in the lower part of the pipe is suppressed and a similar effect (as well as strong asymmetry) can be seen in the literature, as shown in Figure 2-7 (Gillies *et al.*, 2004; Graf, 1984). Indeed, this asymmetry, and the corresponding shift in the position of the peak in the mean axial velocity field, was investigated quantitatively in the form of U_{c1} (method: Section 4.1.2; results: Section 4.2.5).

Lastly, a case study is presented with Guyblast 30/40, the largest (and therefore most highly attenuating and readily settling) of the four particle species, at a high volume fraction (ϕ = 1 %) and moderate flow rate (Re = 24,300, Q = 0.812 l s^{-1}) at which a moving bed was thought to form (as tentatively confirmed by the concentration profile presented in Figure 5-33, in which a small peak in concentration was observed, and "tentatively" because the attenuation was severe). In all frames of Figure 4-11 and Figure 4-12, the results are compared with those at the same nominal volume fraction but a much higher flow rate (in particular, Re = 102,000, Q = 3.40 l s^{-1}) in order to isolate and elucidate the effects of flow rate.

Figure 4-11(a) shows $\overline{U}/U_{ave}$ (as this format is best for showing a change in shape); Figure 4-11(b), $\overline{uw}^{+}$; Figure 4-12(a), u'^{+}; Figure 4-12(b), w'^{+}. As described in Sections 4.2.2 and 4.2.3 for both Honite species at lower volume fractions, a suppression of $\overline{U}$ (Figure 4-11(a)) and an enhancement of u'^{+} (Figure 4-12(a)) are

seen in a common region in the lower half of the pipe (centred on $y/R \approx 1.2$ in this case), suggesting the presence of a shear layer of measurable thickness.

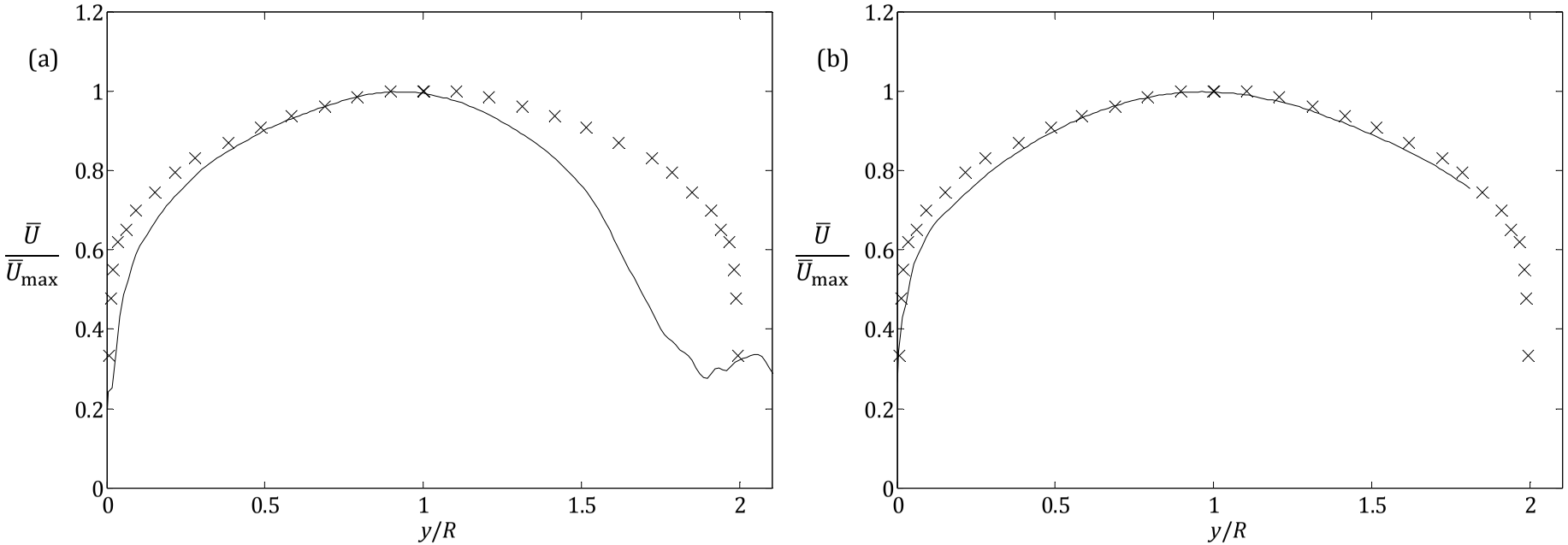

Figure 4-10: Mean velocity relative to maximum (*i.e.* centreline) value *vs.* wall-normal distance from upper pipe wall, with Honite 16, ϕ = 3 %, (a) Re = 25,000, U_{ave} = 0.587 m s^{-1}, (b) Re = 104,000, U_{ave} = 2.43 m s^{-1}; crosses in both frames, hot-wire results of Laufer (1954) at Re = 50,000.

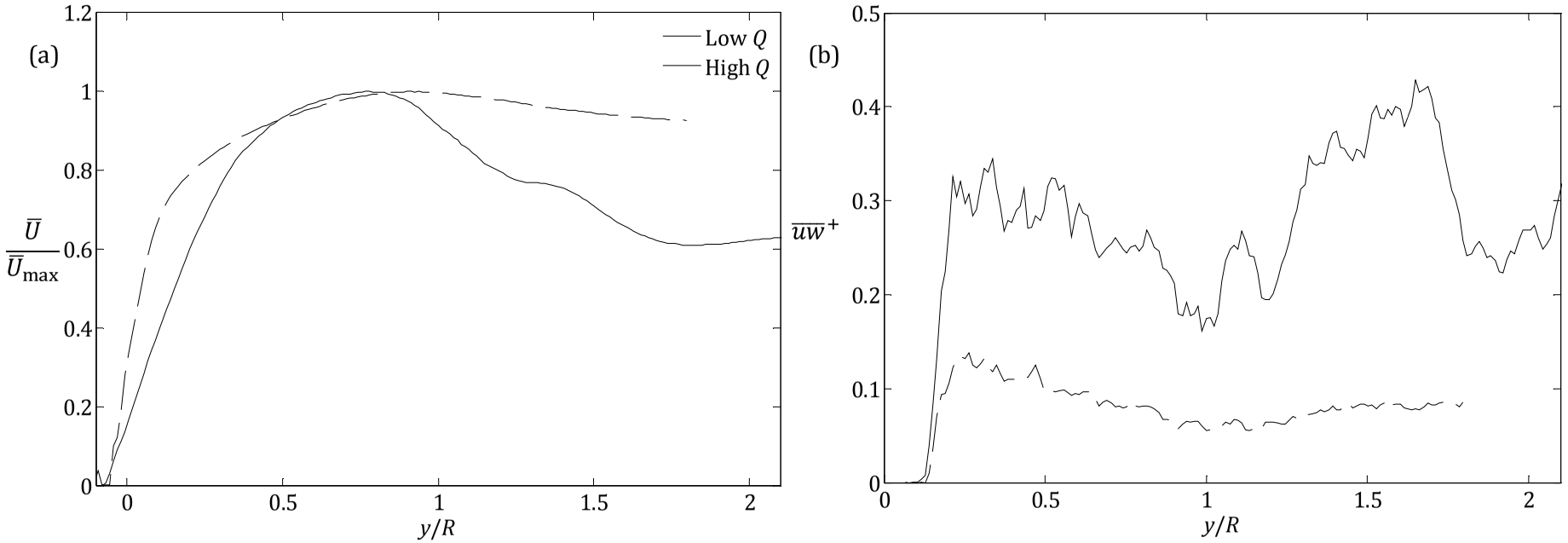

Figure 4-11: (a) Mean velocity relative to maximum (*i.e.* centreline) value *vs.* wall-normal distance from upper pipe wall; (b) Reynolds shear stress in wall units; with Guyblast 30/40, ϕ = 1 %, Re = 24,300, U_{ave} = 0.570 m s^{-1} (solid lines) and Re = 102,000, U_{ave} = 2.38 m s^{-1} (dashed lines).

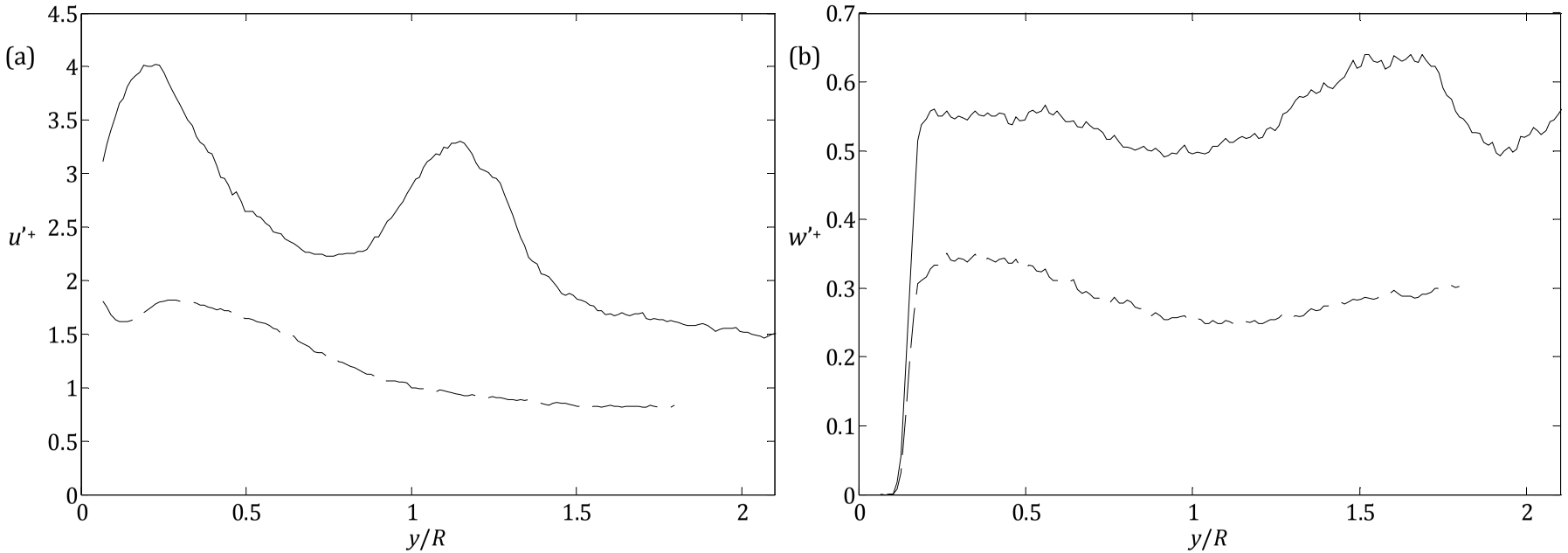

Figure 4-12: (a) Axial RMS velocity in wall units *vs.* wall-normal distance from upper pipe wall; (b) radial RMS velocity in wall units; with Guyblast 30/40, ϕ = 1 %, Re = 24,300, U_{ave} = 0.570 m s^{-1} (solid lines, "low Q") and 102,000, U_{ave} = 2.38 m s^{-1} (dashed lines, "high Q").

4.2.5 Summary: trends in first- and second-order flow statistics

A brief overview of the results presented in Sections 4.2.1 to 4.2.4 follows. The observed trends are summarised, and several issued to be resolved are described.

The mean axial velocity profiles were generally very good, especially at lower particle concentrations. At high concentration, however, there was evidence of segregation. The putative modification of the mean velocity profiles by segregation of particles to the lower part of the pipe, even at low particle concentration, was observed in the corresponding regions of the axial RMS velocity profiles, suggesting a real physical process was present, and that a combination of these two fields and the concentration profiles presented in Chapter 5 represent a powerful method of diagnosing changes in the flow regime.

The radial RMS velocity and shear stress profiles were generally small in magnitude than would be expected, by comparison with data in the literature, and this shortfall showed a tendency to increase as the Reynolds number was increased. It is thought that this shortfall could be mitigated if the spatial and temporal resolution of the measurements were increased. However, despite these discrepancies, both $w'+$ and $\overline{uw}$ were within an order of magnitude of the expected values in all cases, and in many cases within a factor of two.

The first question to be addressed is why the axial mean and RMS velocity fields do not show the same degree of under-prediction shown in the $w'+$ and $\overline{uw}$ fields. That the two variables that rely on measurements taken with the 4 MHz probe (*i.e.* $w'+$ and $\overline{uw}$) are the two that show the most marked under-prediction relative to data in the literature suggests the cause is instrumental, but very thorough checking of the data processing method revealed no errors.

The second question, which applies particularly to Guyblast because it is larger than Honite and therefore scatters and attenuates more strongly, is which of the observed effects are real in the sense that the results accurately capture actual changes in the mean flow and the turbulence statistics, and which are artefacts of the severe attenuation that is known to occur at volume fractions above $\phi \approx 1$ % or

so with Guyblast (with reference to the scattering and attenuation coefficients compiled in Section 5.2.5 of Chapter 5). This is a general question that the author has attempted to answer in the preceding results sections, but which is left as a subject of further study in general.

The third and final question to be answered is how the observed profiles at high volume fractions (*i.e.* those presented in Section 4.2.4) compare to what is expected in such multiphase flows. The trends in the relevant literature, *cf.* Gillies *et al*. (2004) and Ekambara *et al.* (2009), were described in Section 2.2.5, and the following points are numbered as they were in that section. Each point is reiterated and commented on.

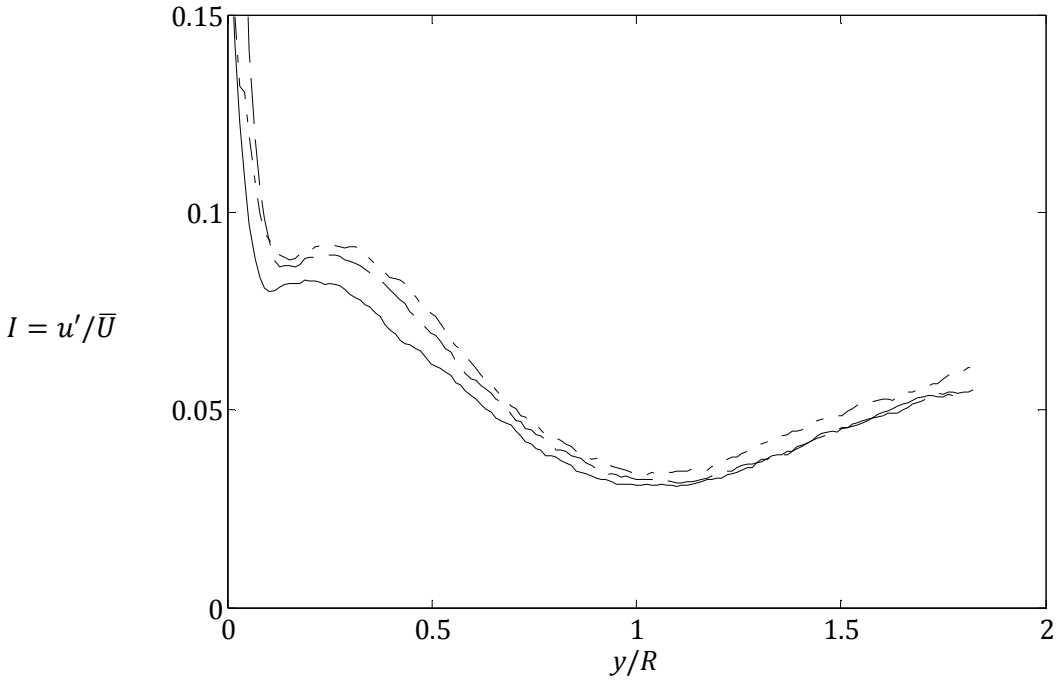

Figure 4-13: Axial turbulence intensity, *I*, *vs*. wall-normal distance, with Honite 22 glass spheres at three nominal volume concentrations; solid line: ϕ = 0.01 %, dashed line: ϕ = 0.5 %, dashed-dotted line: ϕ = 3 %.

1. *Shift in the mean axial velocity profile.* This effect was, indeed, observed very commonly with all particle species (*e.g.* "low-*Q*" runs at Re ≈ 25,000: Honite 16 at ϕ = 3 %: Figure 4-10(a); Guyblast at ϕ = 1 %: Figure 4-11(a)), but particularly noticeably with Guyblast. The reader is referred to the relevant sections on the homogeneous transition velocity, U_{c1}, in which this effect is discussed in detail as a distinct topic (method: 4.1.2; results: Section 4.2.6).

2. *Flattening of the mean axial velocity profile*. This effect was also observed, most strongly with the Guyblast plastic species at the highest concentration (ϕ = 3 %: see "high-Q" run in Figure 4-11(b)).

3. *Suppression of normal and shear Reynolds stresses relative to fluid alone*. This effect was not observed, although a higher volume fraction may have been necessary. However, the radial (or wall-normal) and shear Reynolds stresses were generally suppressed to a degree that increased with Reynolds number, as described earlier.

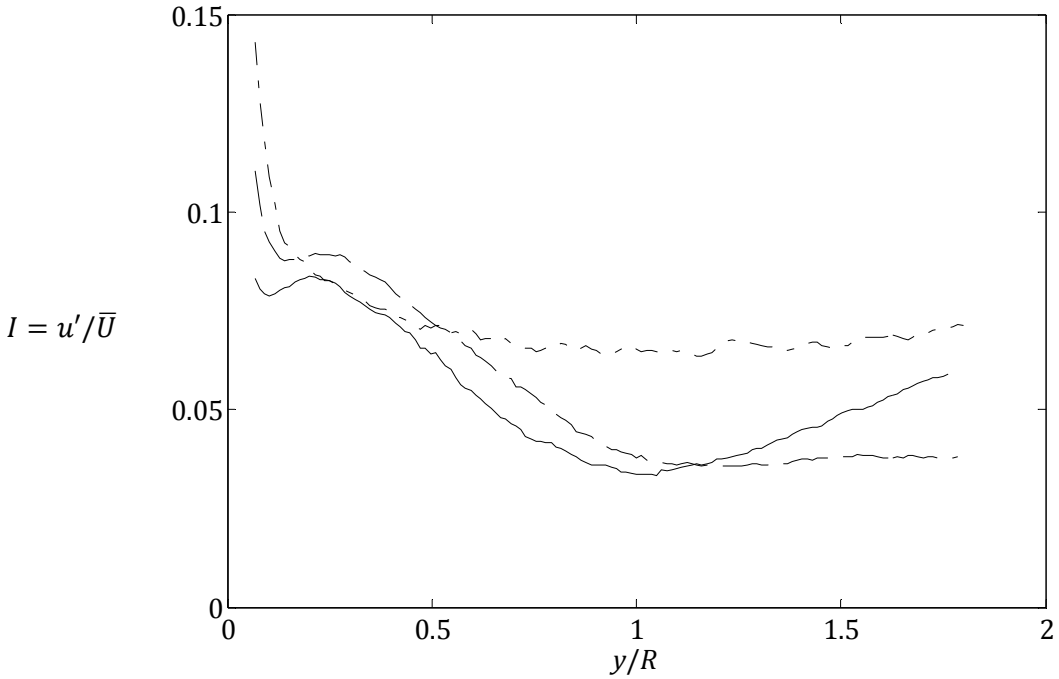

Figure 4-14: Axial turbulence intensity, I, *vs.* wall-normal distance, with Guyblast 30/40 at Re ≈ 88,000, U_{ave} ≈ 2.1 m s^{-1} and three nominal volume concentrations; solid line: ϕ = 0.01 %, dashed line: ϕ = 0.5 %, dashed-dotted line: ϕ = 3 %.

4. *Enhancement of axial turbulence intensity, I, with larger particle species relative to fluid alone; suppression with smaller particles*. This effect, noted by Tsuji and Morikawa (1982), was not observed. In fact, I was enhanced slightly for all particle types, even though all would qualify as "small" according to the criterion of Tsuji and Morikawa (*i.e.* d_{50} < 0.2 mm). Axial turbulence intensity profiles at three nominal volume fractions (ϕ = 0.01, 0.5 and 3 %) are shown for Honite 22 (d_{50} = 41.0 μm) and Guyblast 30/40 (d_{50} =

691 μm) at high Reynolds numbers in Figure 4-13 and Figure 4-14, respectively. For Honite 22 (Figure 4-13) the trend is very clear: the turbulence intensity is enhanced to a degree that increases with concentration. However, the trend for Guyblast 30/40 (Figure 4-14) is less clear and appears to comprise an enhancement factor due to concentration, as observed with Honite 22, and another factor that causes a flattening of the u'^{+} profile in the region $y/R > 1$ at ϕ = 0.5 % and $/R > 0.5$ at ϕ = 3 %. A similar effect was also observed in the mean velocity profile of Guyblast at ϕ = 1 % (see Figure 4-11(a)). So, although the observations of Tsuji and Morikawa (1982) were not reproduced, a great deal of clear, interesting information can be gleaned from the results under this topic.

4.2.6 Critical flow velocity 1, U_{c1} (homogeneous transition velocity)

As described in the literature review (Section 2.2.6) and the methodology (Section 4.1.2), U_{c1} is referred to here as the homogeneous transition velocity, and is that below which the flow becomes heterogeneous and a significant concentration gradient develops. A method for measuring this transition velocity, based on the shift in the position of the peak in the mean axial velocity profile, $\overline{U}$, was proposed in Section 4.1.2, and in the following section results are presented that were gathered using this method for all four particle species over a range of flow rates.

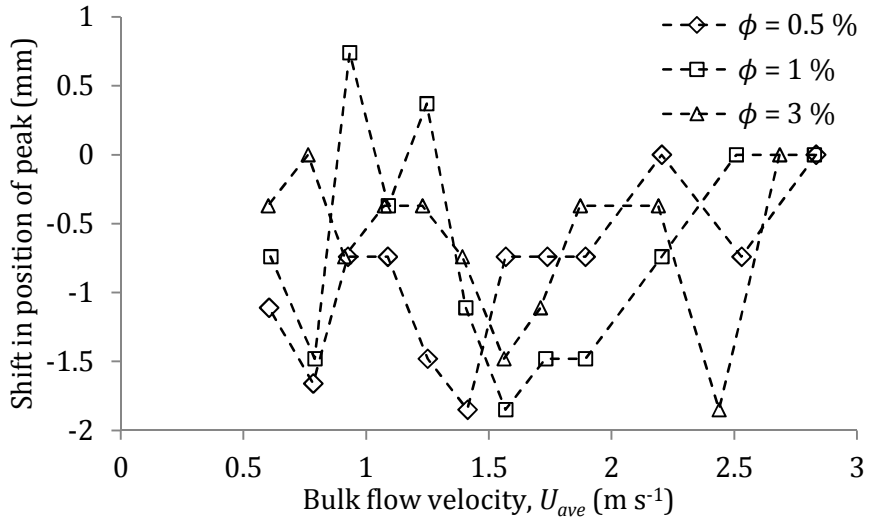

Figure 4-15: Shift in position of peak in mean axial velocity, $\overline{U}_{max}$, *vs.* bulk flow velocity, U_{ave}, for Honite 22 glass spheres at three nominal volume fractions, ϕ.

In particular, the results for Honite 22, Honite 16, Guyblast 40/60 and Guyblast 30/40 are presented in Figure 4-15, Figure 4-16, Figure 4-17 and Figure 4-18, respectively. To clarify, the distances shown are those between the position of the peak in the mean axial velocity measured with the particle types and volume fractions shown, and that from reference runs at very low volume fractions, in which the velocity profile is not affected by the presence of suspended particles, such that the peak was at the centreline of the pipe.

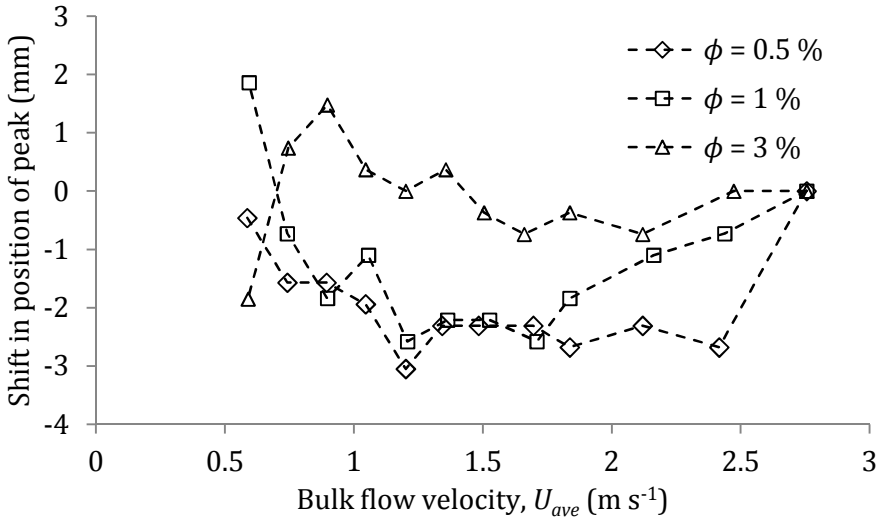

Figure 4-16: Shift in position of peak in mean axial velocity, $\overline{U}_{max}$, *vs.* bulk flow velocity, U_{ave}, for Honite 16 glass spheres at three nominal volume fractions, ϕ.

Overall, no clear transition to heterogeneous flow *in terms of bulk flow velocity* is apparent in Figure 4-15 to Figure 4-18, and so it can be concluded that the proposed method was not successful in the form it was proposed: there appears to be no trend in the position of the peak in the mean velocity profile for Honite 22 at all volume fractions, Honite 16 at ϕ = 0.5 % and for both Guyblast species at ϕ = 0.5 and 1 %.

However, it clear from Figure 4-16 that there is a consistent shift of several millimetres for Honite 16 at ϕ = 1 and 3 %, and a much more significant shift for both Guyblast species at ϕ = 3 % (Figure 4-17 and Figure 4-18). Overall, whether the inability of the method to measure a sharp shift in the position of the peak in the mean velocity due to real changes in the flow structure or is an artefact caused

by high attenuation, as described in Section 4.2.4 in the context of its effect on the velocity and stress profiles at high volume fractions, remains to be discussed.

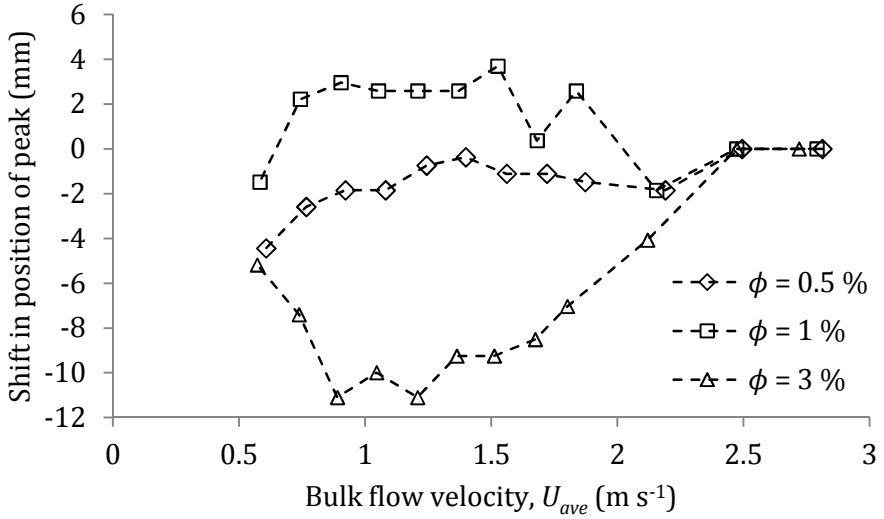

Figure 4-17: Shift in position of peak in mean axial velocity, $\overline{U}_{max}$, *vs.* bulk flow velocity, U_{ave}, for Guyblast 40/60 plastic beads at three nominal volume fractions, ϕ.

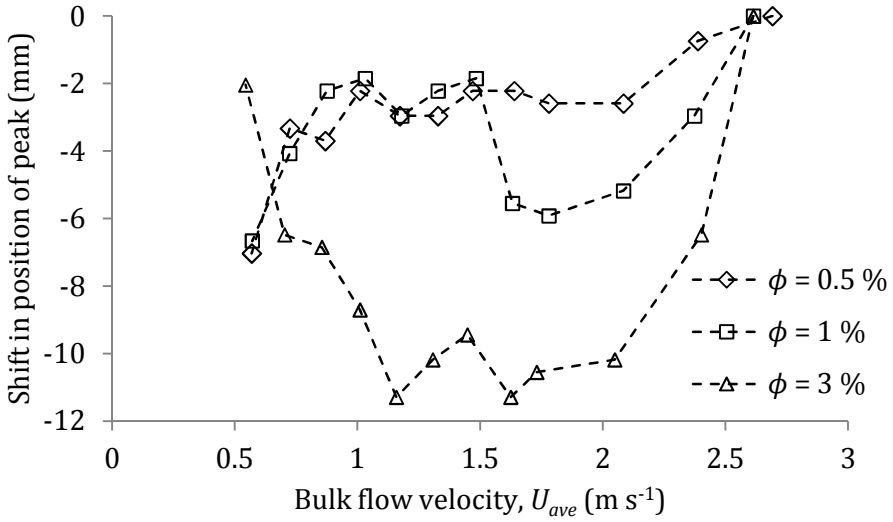

Figure 4-18: Shift in position of peak in mean axial velocity, $\overline{U}_{max}$, *vs.* bulk flow velocity, U_{ave}, for Guyblast 30/40 plastic beads at three nominal volume fractions, ϕ.

Although attenuation may be a significant factor in the Guyblast runs, the same cannot be said of the Honite runs. The attenuation properties of Honite (as described and measured in Chapter 5) suggest this was not a problem. This leaves real, physical flow structure as the cause, at least in the case of Honite. This uncertainty aside, at the very least the method that has been presented allows the following to be identified: the volume fraction at which a significant, consistent

flow asymmetry is observed, ϕ = 1 % for Honite 16 and ϕ = 3 % for both Guyblast species. It is certain, however, that spatial resolution was not the issue, since shifts of the order of millimetres could be measured quite easily with the present system.

4.2.7 Critical flow velocity 2, U_{c2} (limit deposition velocity)

As described in the literature review (Section 2.2.6), U_{c2} is referred to in this study as the limit deposition velocity, and is that below which a moving bed forms, the method for measuring which was presented in detail earlier (Section 4.1.3).

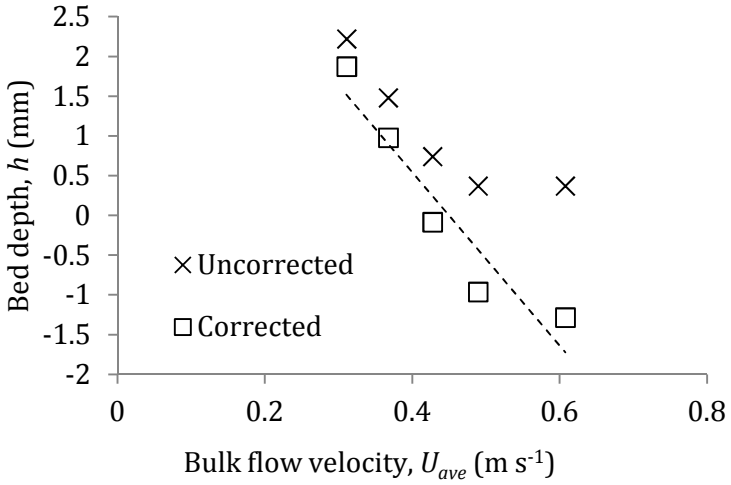

Figure 4-19: Bed depth, h, *vs.* bulk flow velocity, U_{ave}, with Honite 22 at nominal volume fraction of ϕ = 0.5 %.

In this section, the variation in bed depth with measured bulk/average flow velocity is given at one nominal volume fraction for each particle species as examples, in the interests of brevity. These results serve to illustrate the method in detail and are intended to be a representative selection from a larger parameter space. In particular, Figure 4-19 shows the results for Honite 22 at ϕ = 0.5 %, Figure 4-20 for Honite 16 at ϕ = 3 %, Figure 4-21 for Guyblast 40/60 at ϕ = 0.5 % and Figure 4-22 for Guyblast 30/40 at ϕ = 3 %.

To reiterate, the bed depth is measured during so-called stop-flow runs, *i.e.* runs in which the pump is turned off and the bed *and suspended sediment* are allowed to settle, since the bed depth is unambiguous in this case. Using a stop-flow run

excludes the possibility of a shear layer being present, which would make the bed depth measurement more ambiguous. (Measurements of the shear layer thickness under a variety of conditions are presented in the bedforms chapter, Chapter 6.) A correction was then made to the measured bed depth to account for sediment that would otherwise be in suspension, were the pump turned on (and this correction is described in Section 4.1.3). This accounts for the "uncorrected" and "corrected" data shown in the figures that follow.

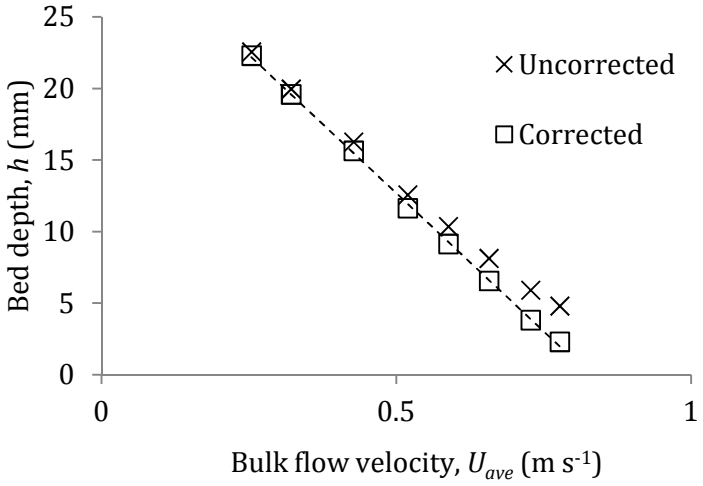

Figure 4-20: Bed depth, h, *vs.* bulk flow velocity, U_{ave}, with Honite 16 at nominal volume fraction of ϕ = 3 %.

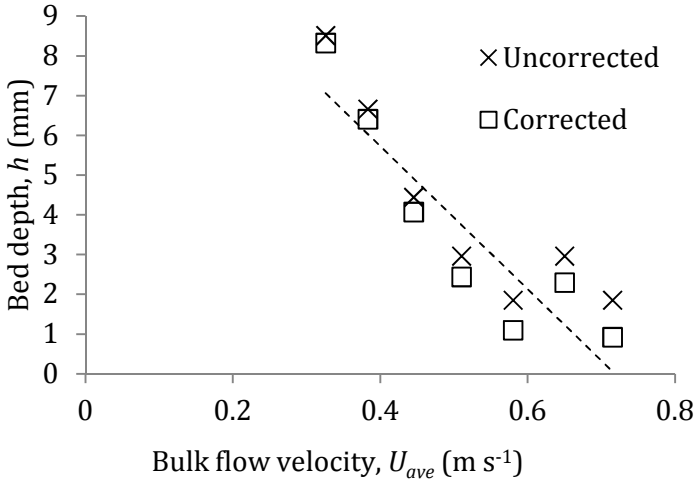

Figure 4-21: Bed depth, h, *vs.* bulk flow velocity, U_{ave}, with Guyblast 40/60 at nominal volume fraction of ϕ = 0.5 %.

It should also be made clear that the critical velocity, U_{c2}, is that at which a linear fit

to the measured bed depths *vs.* flow velocity intercepts the x-axis, *i.e.* the flow velocity at which the bed depth is zero.

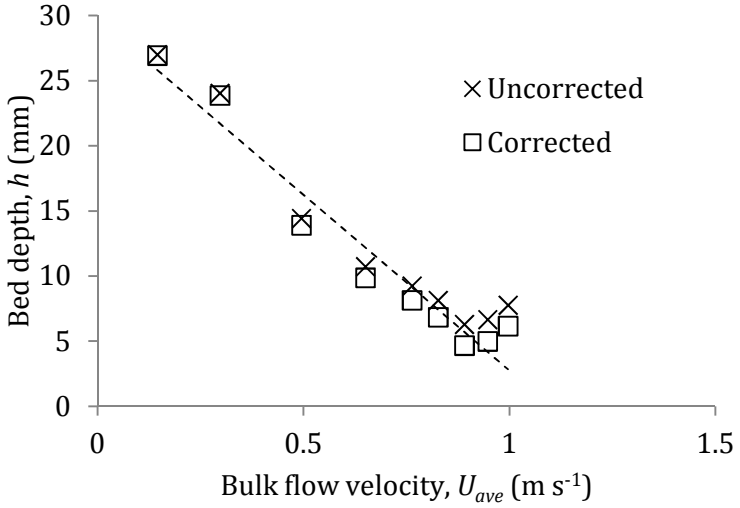

Figure 4-22: Bed depth, h, *vs.* bulk flow velocity, U_{ave}, with Guyblast 30/40 at nominal volume fraction of ϕ = 3 %.

Lastly, a compilation of the results for all four particle species at three nominal volume fractions are presented in Figure 4-23, and the trends are discussed in detail and compared to two correlations for the limit deposition velocity, U_{c2}, in the literature. There are several conclusions to be drawn from the figures above. First, it should be noted that there were generally fewer data at lower volume fractions (*e.g.* compare Figure 4-19 at ϕ = 0.5 % to Figure 4-20 at ϕ = 3 %): a narrower range of flow rates was accessible at lower ϕ because ripples were more likely to form on shallower beds. (Time-dependent bedforms, such as ripples, are investigated in detail in Chapter 6, to which the reader is referred for more information.) The existence of ripples would have made bed depth measurements more difficult (since a suitable average would have had to be taken).

Second, it is clear that the correction for suspended sediment that was applied to all the runs (compare the "corrected" and "uncorrected" results in each figure) had a very significant effect on the resulting point of intersection with the x-axis. Moreover, the effect of the correction was greater at lower volume fractions (*e.g.* compare Figure 4-19 and Figure 4-20) since thinner beds formed in that case: the chord length of thin beds is much smaller than for thick beds, so a smaller amount

of settled material leads to a greater change in bed depth. This sensitivity also explains the negative bed depths shown in Figure 4-19: it is not a shortcoming of the method, but merely an indication that no bed would be present. That is, the method of correcting the bed depth for suspended sediment is most sensitive at low volume concentrations, since the chord length is smallest for shallow beds.

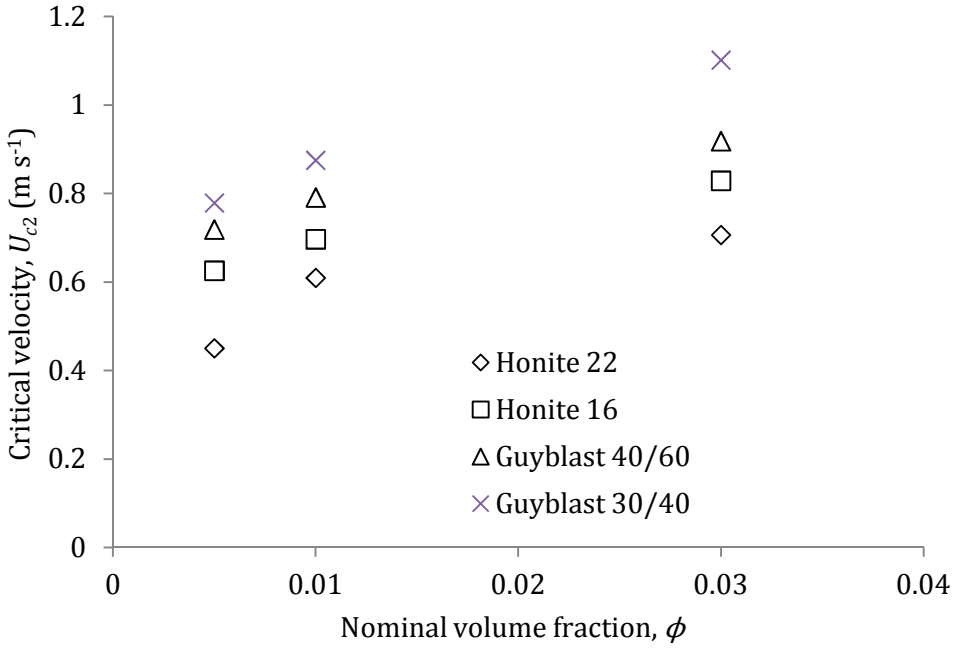

Figure 4-23: Critical flow velocity, U_{c2}, *vs*. nominal volume fraction of suspended solids for four particle species.

The measurements of bed depth *vs.* bulk flow velocity, a representative selection of which were presented in Figure 4-19 to Figure 4-22, were compiled and are shown in Figure 4-23, from which it is clear that the measured limit deposition velocity, U_{c2}, increases with particle size and volume fraction, as expected. In order to verify the experimental results for the limit deposition velocity obtained using the zero-bed-depth method, they were compared with values calculated using the correlations of Poloski *et al*. (2010) for the two Honite glass particle species (as described in Section 2.2.7 and Equations [2.19] and [2.20]) and Oroskar and Turian (1980) for the two Guyblast plastic species (Equation [2.18], in which it was assumed that $\chi = 1$). The values are shown in Table 4-3.

In addition to the U_{c2} results, the equivalent particle diameters necessary to

reproduce the experimentally determined values of U_{c2} using both correlations from the literature are also given in Table 4-3, as well as the corresponding percentile range of the measured particle size distribution, since several of the correlations presented in the literature review (specifically, Section 2.2.7) use a particular percentile of the PSD as a representative diameter. Several interesting points should be made about the results presented in Table 4-3. First, all the experimentally determined values of U_{c2} exceed those predicted by the correlations of Poloski *et al.* (2010) and Oroskar and Turian (1980) (with the exception of the Honite species at the lowest volume fraction (ϕ = 0.5 %), in which the under-prediction of U_{c2} is nevertheless slight). That is, the two correlations are not conservative, and generally underpredict the measured critical velocities.

Second, the measured values exceed the predicted values particularly strongly for the Guyblast plastic particles, for which the discrepancy is a factor of more than two in all cases. The correlation used in that case was that of Oroskar and Turian (1980), which was based on 357 data from suspensions of various solids (coal, iron, limestone, potash and sand) in various liquids (brine, ethylene glycol, kerosene and water). However, the density difference, as quantified by $s - 1$, was much larger for 301 of the 357 data ($2.16 \lesssim s - 1 \lesssim 4.82$) than in the experiments described here for Guyblast ($s - 1 \approx 0.5$), and so that parameter is posited as the cause of the discrepancy, all other parameters being in the same range. In fact, the strongest dependence in Equation [2.18] is on $s - 1$, such that

$$U_{c2} \propto (s-1)^{0.59}. \qquad [4.14]$$

Third, the equivalent particle sizes that would be necessary to give the measured critical flow velocities according to each correlation were also calculated. For the Honite species, the corresponding particle sizes were within the measured PSDs for four of the six data, but for Guyblast the particle sizes were unrealistically large (of the order of centimetres). Again, the cause is thought to be the density difference, as quantified by $s - 1$, which appears to have a much greater effect on the critical velocity than is predicted by the Oroskar and Turian (1980) correlation.

Table 4-3: Comparison of limit deposition velocity, U_{c2}, results with correlations of Poloski *et al.* (2010) for Honite (Equations [2.19] and [2.20]) and Oroskar and Turian (1980) for Guyblast (Equation [2.18]).			
	ϕ = 0.5 %	ϕ = 1 %	ϕ = 3 %
Honite 22 (Ar = 1.30)			
Limit deposition velocity, U_{c2} (m s^{-1})			
This study	0.450	0.609	0.706
Poloski *et al.* (2010)	0.477	0.477	0.477
Particle size, d (μm)			
Actual median particle size, d_{50}	41.0		
Equivalent particle size in correlation	35.6	69.8	97.0
Percentile range of actual PSD	30-40 %	90-100 %	> 100 %
Honite 16 (Ar = 8.73)			
Limit deposition velocity, U_{c2} (m s^{-1})			
This study	0.625	0.696	0.829
Poloski *et al.* (2010)	0.638	0.638	0.638
Particle size, d (μm)			
Actual median particle size, d_{50} (μm)	77.0		
Equivalent particle size in correlation	73.5	93.3	138
Percentile range of actual PSD	40-50 %	80-90 %	90-100 %
Guyblast 40/60 (Ar = 719)			
Limit deposition velocity, U_{c2} (m s^{-1})			
This study	0.719	0.791	0.918
Oroskar and Turian (1980)	0.340	0.377	0.443
Particle size, d (μm)			
Actual median particle size, d_{50} (μm)	468		
Equivalent particle size in correlation	16,100	15,400	14,500
Percentile range of actual PSD	> 100 %	> 100 %	> 100 %
Guyblast 30/40 (Ar = 2,240)			
Limit deposition velocity, U_{c2} (m s^{-1})			
This study	0.778	0.875	1.10
Oroskar and Turian (1980)	0.362	0.401	0.472
Particle size, d (μm)			
Actual median particle size, d_{50} (μm)	691		
Equivalent particle size in correlation	25,700	27,300	37,500
Percentile range of actual PSD	> 100 %	> 100 %	> 100 %

Overall, then, the method described for determining the limit deposition velocity, U_{c2}, appears to be very effective and give precise, unambiguous results. The expected trends were, indeed, observed: the value of U_{c2} increased with particle size and concentration. Moreover, the results compare very well with some correlations in the literature, although the results were found to be generally conservative, particularly for the Guyblast plastic particles. The reason for this discrepancy is thought to be a result of the smaller density difference between Guyblast and water, and that of the suspensions used to derive the correlation of Oroskar and Turian (1980).

4.3 Summary and conclusions

A number of conclusions can be drawn from the velocity and stress results presented in this chapter. The measurements of the mean and RMS axial velocity fields were generally very good at lower volume fractions and quite good at higher volume fractions. However, the wall-normal (or radial) RMS velocity and Reynolds shear stress were under-predicted in general to a degree that increased with flow velocity. On the other hand, a correlation between $\overline{U}$ and u', which showed a suppression and enhancement, respectively, in the presence of a significant concentration gradient, was observed without ambiguity with all four particle species at moderate and low flow velocities, and was supported by the presence of gradients in the corresponding concentration profiles presented in Chapter 5. It is suggested that this effect could be exploited further, in a qualitative manner, at least, since the processing requirements are slight and a great deal of information about the flow can be gained.

The method that was presented for determining U_{c1}, the homogeneous transition velocity, was not successful in its original purpose. However, as a qualitative method for measuring the degree of flow asymmetry that results from moderate and high particle volume fractions, it is illuminating and novel. On the other hand, the method for determining U_{c2}, the limit deposition velocity, was shown to yield simple, unambiguous results that compared well with one correlation in the literature (Poloski *et al.*, 2010) but not another (Oroskar and Turian, 1980),

suggesting the latter is not accurate universally.

A general difficulty exists – with reference to the velocity and stress results in general, and also the results for U_{c1} presented in Section 4.2.5 – in identifying which errors and inaccuracies are due to the instrument itself (*e.g.* beam divergence and transducer radius) or the measurement method (*e.g.* position calibration), and which are due to actual properties of the suspended particles (*e.g.* attenuation, which depends on the particle size and ultrasonic frequency, and therefore a poor signal/multiple scattering in the far field, change in sound speed) or the flow (*i.e.* real changes in the turbulence field and velocity and concentration profiles).

It is thought that, despite some inaccuracies in the wall-normal statistics (as presented in Sections 4.2.1 to 4.2.4), the *UVP-DUO* system and the suite of novel techniques developed for it in this study are very powerful tools for investigating the properties of turbulent flow and the effect of suspended particles on them.

5 Concentration gradients in suspensions in closed pipe flow

The objective of this chapter is to present the development of a method for measuring concentration profiles of suspensions of particles of arbitrary physical properties in pipe flow. The model of Thorne and Hanes (2002) is described in detail in Section 5.1 below, and a novel acoustic method for determining the backscatter and attenuation properties of suspended particles is then presented (Section 5.2). This method is applied to Honite glass spheres and Guyblast plastic beads, and the resulting backscatter and attenuation coefficients that were measured (as tabulated in Section 5.2.5) are used to generate concentration profiles according to the dual-frequency inversion method of Hurther *et al.* (2011), which is described in detail and applied to the gathered experimental data (Section 5.3).

5.1 Literature review: Thorne *et al.* model of backscatter strength

An overview of some models of the interactions of ultrasound with suspended particles was given in the general literature review (in particular, Section 2.1). However, it should be made clear that the model of Thorne and Hanes (2002) was chosen for use in this study because it is simpler to implement than some other, similar formulations (Carlson, 2002; Furlan *et al.*, 2012; Ha *et al.*, 2011) and has a firm theoretical basis (Hay, 1991; Kytömaa, 1995; Richards *et al.*, 1996). As a result, it has been adopted and exploited by a number of groups (Admiraal and García, 2000; Hunter *et al.*, 2012a; Hurther *et al.*, 2011). In this section, the details of the model are described, with a view to developing it into a method for determining the properties of suspensions of arbitrary particles in the next section (Section 5.2).

In the model of Thorne and Hanes (2002), the backscattering and attenuation properties of the suspension are embodied in f, the backscatter form function, and χ, the "normalised total scattering cross-section", as described in more detail in

Section 5.1. Thorne and Hanes state that "[t]he sediment attenuation constant is due to absorption and scattering" which "for noncohesive sediments insonified at megahertz frequencies the scattering component dominates". However, this is only strictly true in the short-wavelength regime, that is, at larger values of ka, as is clear from Figure 2-1, and is not true for several of the suspensions used in this study. For example, $ka \approx 0.35$ for Honite 22 particles insonified at a frequency of f = 2 MHz, in which case both viscous absorption and scattering are significant (although both relatively small). For clarity, then, χ is hereafter referred to as the normalised total scattering and absorption cross-section, as in Table 2-1.

The expression for V, the root-mean-square (RMS) of the received instantaneous voltage, V_{inst}, which varies with distance from the transducer along its axis, r, is as follows (Thorne and Hanes, 2002):

$$V = \frac{k_s k_t}{\psi r} M^{1/2} e^{-2r\alpha}, \qquad [5.1]$$

$$\alpha = \alpha_w + \alpha_s, \qquad [5.2]$$

where k_s is the sediment backscatter constant and incorporates the scattering properties of the particles, k_t is a system parameter that must be measured, M is the concentration by mass of suspended particles, α_w and α_s account for attenuation by water and suspended particles, respectively, and ψ is a near-field correction factor (Downing *et al.*, 1995) that is written as follows:

$$\psi = \frac{1 + 1.35z + (2.5z)^{3.2}}{1.35z + (2.5z)^{3.2}}, \qquad [5.3]$$

where

$$z = r/r_n, \qquad [5.4]$$

$$r_n = \pi a_t^2/\lambda, \qquad [5.5]$$

a_t is the radius of the active face of the transducer and λ is the ultrasound wavelength. ψ tends to unity in the far field, *i.e.* when $r \gg r_n$. α_s and k_s are as follows:

$$\alpha_s = \frac{1}{r}\int_0^{r'} \xi(r)\, M(r)\mathrm{d}r, \qquad [5.6]$$

$$k_s = \frac{\langle f \rangle}{\sqrt{a\rho_s}}, \qquad [5.7]$$

$$\xi = \frac{3\langle \chi \rangle}{4\langle a \rangle \rho_s}, \qquad [5.8]$$

where ξ is the sediment attenuation constant and f is the backscatter form function, which "describes the backscattering characteristics of the scatterers" (Thorne and Buckingham, 2004). Angled brackets represent the average over the particle size distribution (PSD). In particular:

$$\langle f \rangle = \left(\frac{\langle a \rangle \langle a^2 f^2 \rangle}{\langle a^3 \rangle} \right)^{1/2}, \qquad [5.9]$$

$$\langle \chi \rangle = \frac{\langle a \rangle \langle a^2 \chi \rangle}{\langle a^3 \rangle}, \qquad [5.10]$$

where χ is the normalised total scattering and absorption cross-section. It is important to note that the derivation of Equation [5.1] requires that "the attenuation over the insonification volume [be] relatively small" (Thorne and Hanes, 2002). (A correction factor for when this condition is not satisfied has been given by Hay, 1991.)

Clearly, both k_s and ξ depend on the PSD and particle shape and therefore distance from the transducer in the general case, as do M and α_s. Empirical forms of f and χ are known for "sandy sediment" (*i.e.* quartz sand-type sediment) (Thorne and Meral, 2008) and are as follows:

$$f = \frac{x^2\left(1 - 0.35\exp\left[-\left(\frac{x-1.5}{0.7}\right)^2\right]\right)\left(1 + 0.5\exp\left[-\left(\frac{x-1.8}{2.2}\right)^2\right]\right)}{1 + 0.9x^2}, \quad [5.11]$$

$$\chi = \frac{0.29x^4}{0.95 + 1.28x^2 + 0.25x^4}, \quad [5.12]$$

where $x = ka$.

No such data are available for particle species other than quartz sand, and it is not feasible in this study to construct equivalent expressions for other particle species. However, order-of-magnitude estimates of ξ can be made using the equations above (as described in Section 5.2.5). Section 5.2 contains the description and validation of a novel method for determining the attenuation and backscatter coefficients of a wider range of particles.

5.2 Homogeneous case: determination of backscatter and attenuation coefficients of arbitrary suspensions

The objective in this section is to manipulate the expressions in the Thorne and Hanes (2002) model, as presented in Section 5.1, in order to extract a number of parameters for the case of an arbitrary prepared homogeneous suspension, that is, one in which M is known and does not vary with distance, but in which the backscatter and attenuation properties of the particle species, *i.e.* k_s and ξ, are not known and are to be measured.

To summarise, the aim of this chapter is to calculate values of ξ_h and K_h in order to use those values to construct concentration profiles in suspensions *via* the dual-frequency concentration inversion method (Hurther *et al.*, 2011), as described in detail in Section 5.3. It is with these objectives in mind that the following derivation is presented.

5.2.1 Derivation

The first stage of the derivation consists of defining the quantity G, the range-corrected echo amplitude, such that

$$G = \ln(\psi r V). \qquad [5.13]$$

By multiplying both sides of Equation [5.1] by ψr, taking the natural logarithm and then the derivative with respect to distance, r, the following expression is obtained:

$$\begin{aligned} \frac{\partial G}{\partial r} &= \frac{\partial}{\partial r}[\ln(\psi r V)] \\ &= \frac{\partial}{\partial r}\left[\ln(k_{sh}k_t) + \frac{1}{2}\ln M - 2r(\alpha_w + \alpha_{sh})\right], \end{aligned} \qquad [5.14]$$

where the h subscript signifies the specific case of homogeneity. This expression is similar to one given by Thorne and Buckingham (2004). Neither k_s, M nor α_s depend on r, so Equation [5.6] can be written in a simplified form, *i.e.*

$$\alpha_{sh} = \xi_h M \qquad [5.15]$$

where ξ_h is the sediment attenuation constant in the case of a homogeneous suspension) and the first two terms on the right-hand side of Equation [5.14] are zero. It can therefore be simplified, as follows:

$$\frac{\partial G}{\partial r} = \frac{\partial}{\partial r}[\ln(\psi r V)] = -2(\alpha_w + \xi_h M). \qquad [5.16]$$

That is, the right-hand side of Equation [5.16] varies linearly with M and this expression also provides a test for homogeneity. By taking the derivative with respect to concentration, an expression for ξ_h is obtained, as follows:

$$\xi_h = -\frac{1}{2}\frac{\partial^2 G}{\partial M\,\partial \mathrm{r}} = -\frac{1}{2}\frac{\partial}{\partial M}\left[\frac{\partial}{\partial r}[\ln(\psi r V)]\right]. \qquad [5.17]$$

This value of $\xi = \xi_h$ applies to a suspension in which the particle size distribution does not vary spatially. Results for the four particle species used in this study are given in Section 5.2.3.

Once ξ_h is known, it is then straightforward to find $K_h \equiv k_{sh}k_t$ for any combination of particle size and transducer frequency by rearrangement of Equation [5.1], that is:

$$K_h \equiv k_s k_t = \psi r V M^{-1/2} \exp\,[2r(\alpha_w + \xi_h M)], \qquad [5.18]$$

as described by Betteridge *et al.* (2008, Figure 7), Thorne and Hanes (2002, Figure 4) and Thorne and Buckingham (2004, Figure 4). Hereafter, K_h is referred to as the combined backscatter and system constant.

The evaluation of Equation [5.18] requires that α_w, the attenuation due to water, be known. It can be calculated by interpolation of the tabular data given by Kaye and Laby (1995) or preferably from the following expression for the specific case of zero salinity, adapted from a more general expression by Ainslie and McColm (1998), as follows:

$$\alpha_w = 0.05641 f^2 \exp\left(-\frac{T}{27}\right), \qquad [5.19]$$

where α_w is in Np m^{-1}, f is the ultrasonic frequency in MHz and T is the temperature in °C in the range -6 < T < 35 °C. Note that these units are different from those in the original Ainslie and McColm (1998) paper, and that this expression is accurate to within 10% of the data on which it is based (Francois and Garrison, 1982) in the range 1 Hz < f < 1 MHz, but the f^2 dependence is also known to hold "at least for the range 3-70 MHz" (Kaye and Laby, 1995).

Results for K_h are given in Section 5.2.4. A summary and discussion of the measured values of both are given in Section 5.2.5. To the author's knowledge, the

method for determining the acoustic properties of suspensions of particles described in this section is novel as a whole, particularly for species other than sand. Provided the stated assumptions are valid (*i.e.* distance-independent concentration and particle size distribution) – assumptions that were tested – then this method can be used to determine the acoustic properties of a very wide range of suspensions; alternatively, any deviation from the expected behaviour can be taken as an indication of heterogeneity, spatial variation in particle size distribution or significant attenuation.

5.2.2 Testing for homogeneity in stirred mixing vessel

As described in Section 5.2.1, ξ_h and K_h must be measured in homogeneous suspensions. Such suspensions of known concentrations were prepared in the stirred mixing vessel (SMV) in the School of Earth and Environment. The apparatus consists of a rotating plastic cylindrical tub, the contents of which are mixed with an impeller connected to a variable-speed mixer, as shown in Figure 5-1. Mains tap water (4 litres) was used as the fluid.

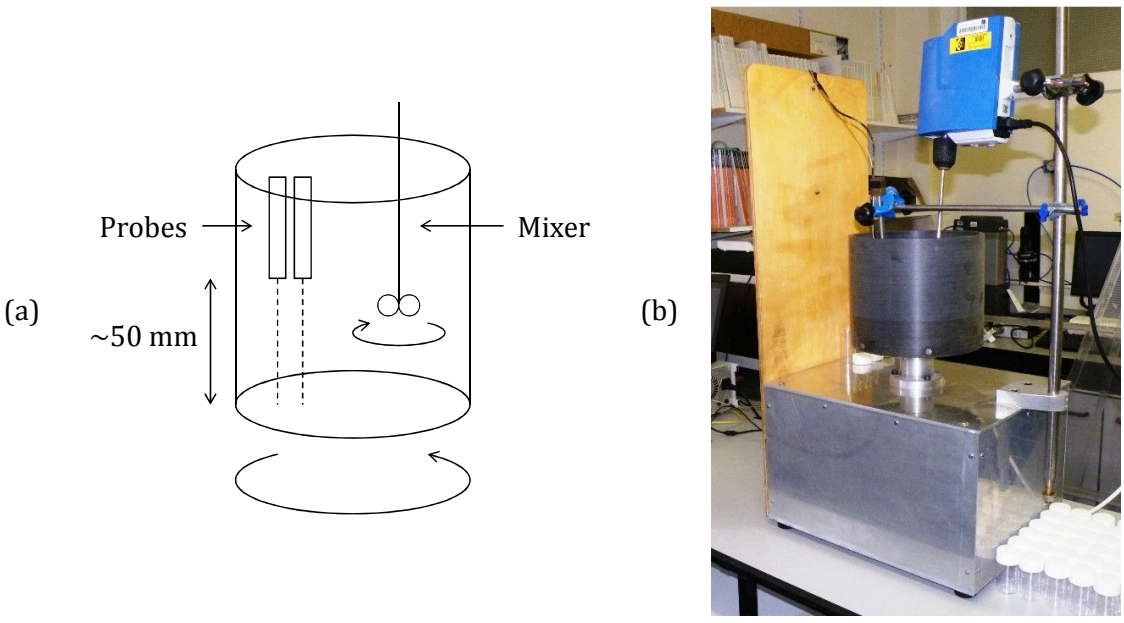

Figure 5-1: Stirred mixing vessel, diagram (a) and photograph (b). Probes were positioned at about 50 mm from, and perpendicular to, base.

A test for homogeneity was performed by taking physical samples from the mixing

vessel (3 × 60 ml samples at each concentration, as was the case for the main loop) and comparing them to the concentration of solids added by weighing. The masses of fluid and solids removed as physical samples were thoroughly accounted for when calculating the total mass at each concentration. Figure 5-2 shows the results of this comparison for the four particle species, and Table 5-1 gives the constant of proportionality and goodness of fit for the same data.

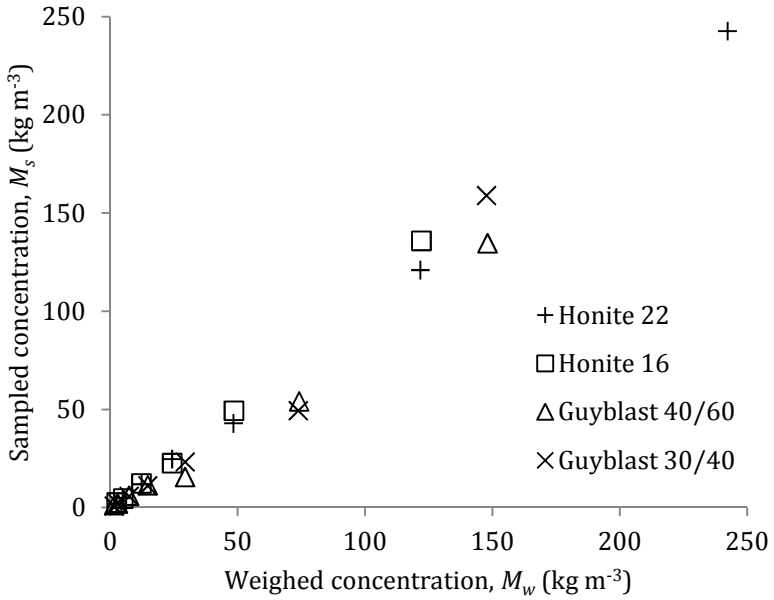

Figure 5-2: Sampled *vs*. weighed (nominal) concentration by mass of all particle species in stirred mixing vessel.

Table 5-1: Constant of proportionality and goodness of fit of sampled (M_s) *vs*. weighed (M_w) concentration by mass of all particle species in stirred mixing vessel.

Particle species	Constant of proportionality	Goodness of fit (R^2)
Honite 22	0.998	0.999
Honite 16	1.05	0.999
Guyblast 40/60	0.863	0.983
Guyblast 30/40	0.987	0.960

It is clear from Figure 5-2 and Table 5-1 that the suspensions prepared in the stirred mixing vessel are rather uniformly mixed, and particularly so in the cases of Honite 22, Honite 16 and Guyblast 30/40 (with constants of proportionality between sampled and weighed concentrations of 0.998, 1.05 and 0.987, respectively), although the Guyblast 40/60 suspension appears to have been

slightly less well mixed than the other particle species (constant of proportionality: 0.863).

5.2.3 Measurements and results: attenuation constant, ξ_h

In this section, results for the attenuation constant, ξ_h, are given. As specified in Equations [5.16] and [5.17], it was necessary to know the gradient of G with respect to distance, r, and mass concentration, M, in order to calculate ξ_h.

To reiterate, the following method was used. Raw echo profiles were taken with the *UVP-DUO* (n = 2,500 samples) at several nominal volume fractions/mass concentrations with both transducers in the stirred mixing vessel, and the data processed using the method described in Section 3.3 to yield the RMS echo voltage, V, from which G was calculated (according to Equation [5.13]). Then, for each run, the gradient, $\partial G/\partial r$, was calculated over the region $r \approx 24$ to 46 mm (*i.e.* measurement points 60 to 120) because it was found that the variation in G tended to be most linear over this region for all particles and at all concentrations. Then, the gradient of $\partial G/\partial r$ with respect to M was found by compiling the results over a range of values of M.

Figure 5-3 shows G *vs*. distance with the 4 MHz probe for Honite 22 at low and high concentrations (M_w = 2.41 and 121.7 kg m^{-3}), for illustration of the goodness of fit. For conciseness, only data for the 4 MHz probe are shown, but the linear fits to the 2 MHz data were equally good and showed very similar trends. The values of the gradient, $\partial G/\partial r$, over a range of concentrations are shown in Figure 5-4 for both the 2 and 4 MHz probes. Gradients and goodness of fit with respect to weighed concentration, M_w, are also shown.

The other figures (Honite 16: Figure 5-5 and Figure 5-6; Guyblast 40/60: Figure 5-7 and Figure 5-8; Guyblast 30/40: Figure 5-9 and Figure 5-10) follow the same sequence. Values of the attenuation constant, ξ_h, for all particle species and both transducers, calculated from $\partial^2 G/\partial r \partial M_w$ according to Equation [5.17], are listed in Table 5-2 in Section 5.2.5.

It should be noted that the nonlinearity in the plots of G *vs*. *r* (*e.g.* for Honite 22) is assumed to be caused by flow around the tip of the probes (in the region $r < 0.01$ m) and reflection from the base of the stirred mixing vessel ($r > 0.05$ m). Neither effect influences the results and nor are they indicative of a problem with the method.

5.2.3.1 Honite 22

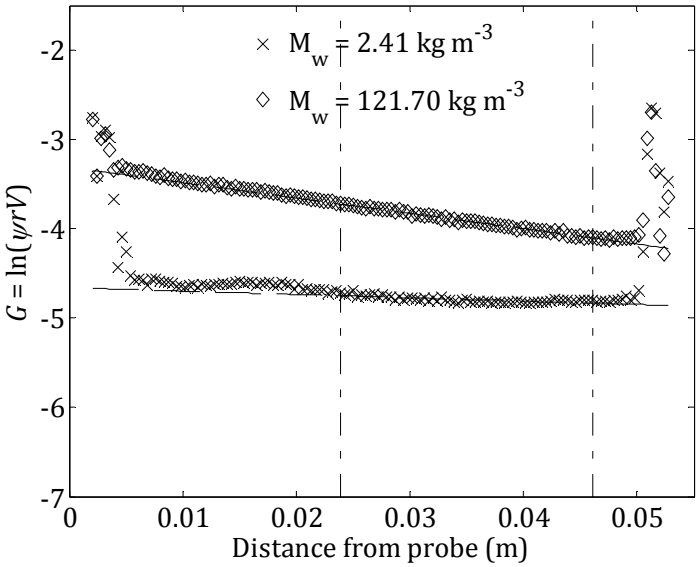

Figure 5-3: *G vs.* distance from 4 MHz probe with Honite 22 at two mean concentrations, M_w = 2.41 and 122 kg m^{-3}. Dashed lines through data are linear fits. Dot-dashed vertical lines indicate region over which gradients were calculated (measurement channels 60 to 120, or $r \approx$ 24 to 46 mm).

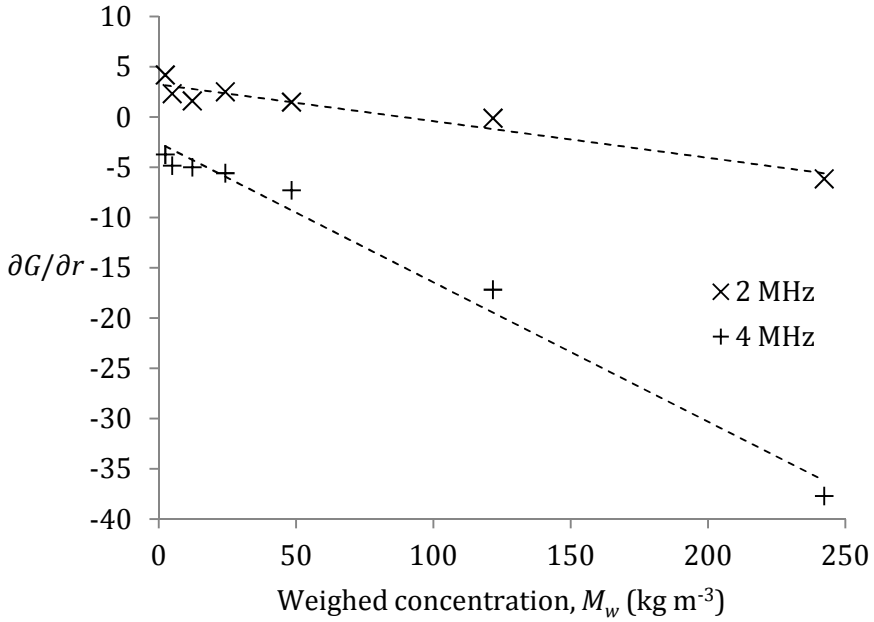

Figure 5-4: Gradient of G with respect to distance from probe *vs.* weighed concentration by mass, M_w, of Honite 22 in stirred mixing vessel at ultrasonic frequencies of f = 2 and 4 MHz.

5.2.3.2 Honite 16

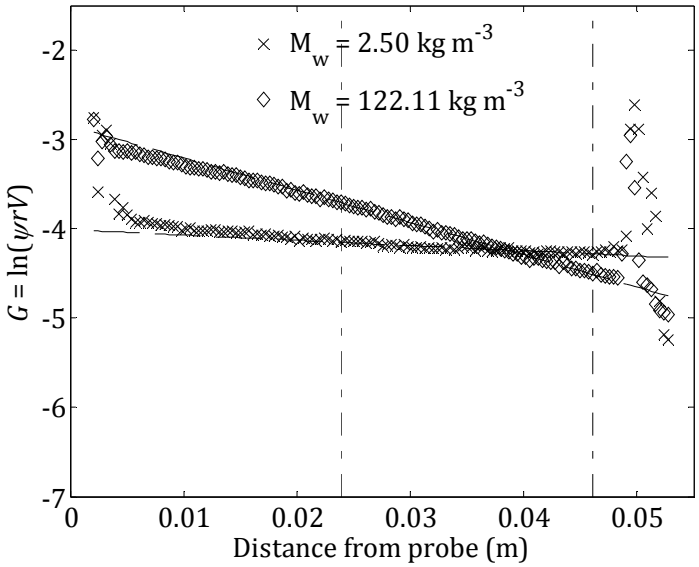

Figure 5-5: *G vs.* distance from 4 MHz probe with Honite 16 at two mean concentrations, M_w = 2.50 and 122 kg m^{-3} in stirred mixing vessel. Dashed lines through data are linear fits. Dot-dashed vertical lines indicate region over which gradients were calculated (measurement channels 60 to 120, or r = 24 to 46 mm).

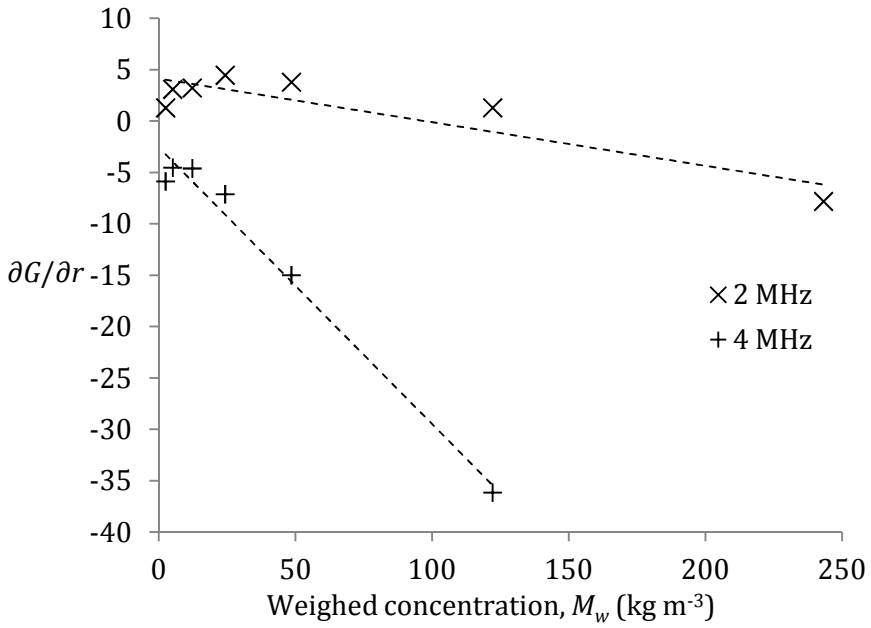

Figure 5-6: Gradient of G with respect to distance from probe *vs.* weighed concentration by mass, M_w, of Honite 16 in stirred mixing vessel at ultrasonic frequencies of f = 2 and 4 MHz.

5.2.3.3 Guyblast 40/60

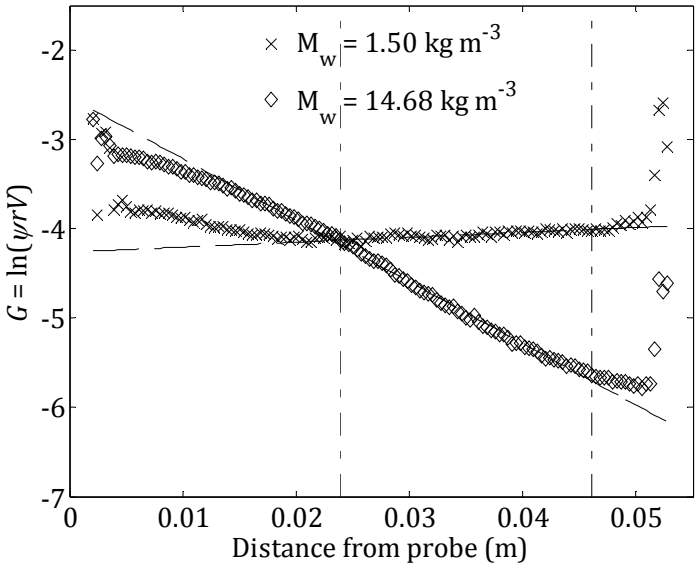

Figure 5-7: *G vs.* distance from 4 MHz probe with Guyblast 40/60 at two mean concentrations, M_w = 1.50 and 14.7 kg m^{-3} in stirred mixing vessel. Dashed lines through data are linear fits. Dot-dashed vertical lines indicate region over which gradients were calculated (measurement channels 60 to 120, or r = 24 to 46 mm).

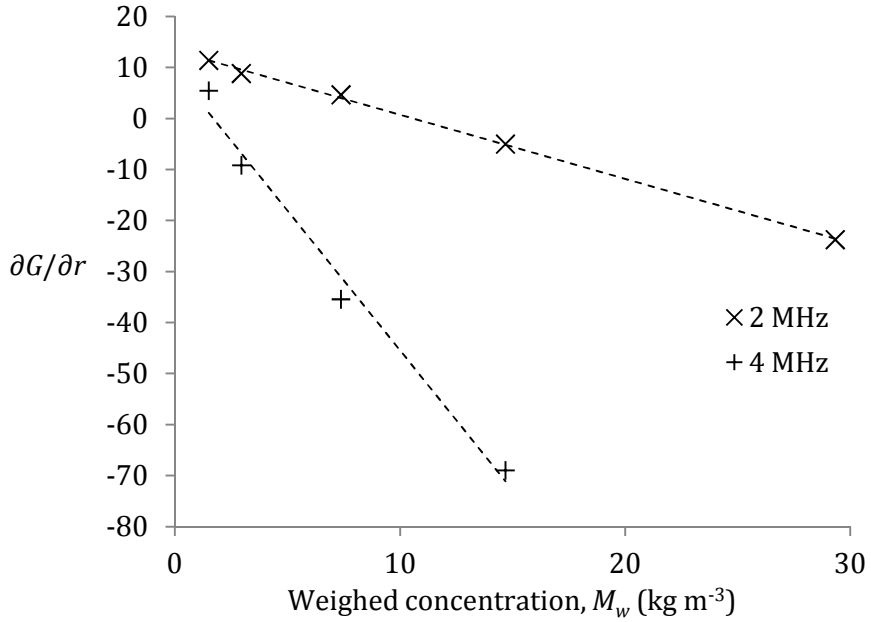

Figure 5-8: Gradient of G with respect to distance from probe *vs.* weighed concentration by mass, M_w, of Guyblast 40/60 in stirred mixing vessel at ultrasonic frequencies of f = 2 and 4 MHz.

5.2.3.4 Guyblast 30/40

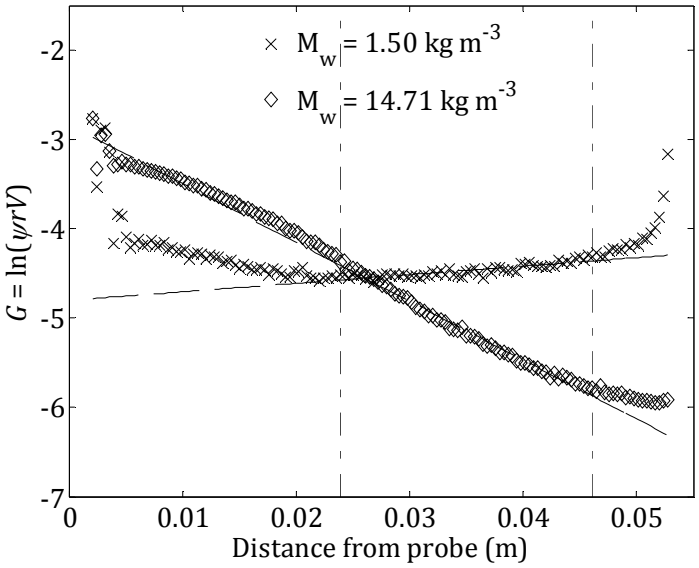

Figure 5-9: *G vs.* distance from 4 MHz probe with Guyblast 30/40 at two mean concentrations, M_w = 1.50 and 14.7 kg m^{-3} in stirred mixing vessel. Dashed lines through data are linear fits. Dot-dashed vertical lines indicate region over which gradients were calculated (measurement channels 60 to 120, or r = 24 to 46 mm).

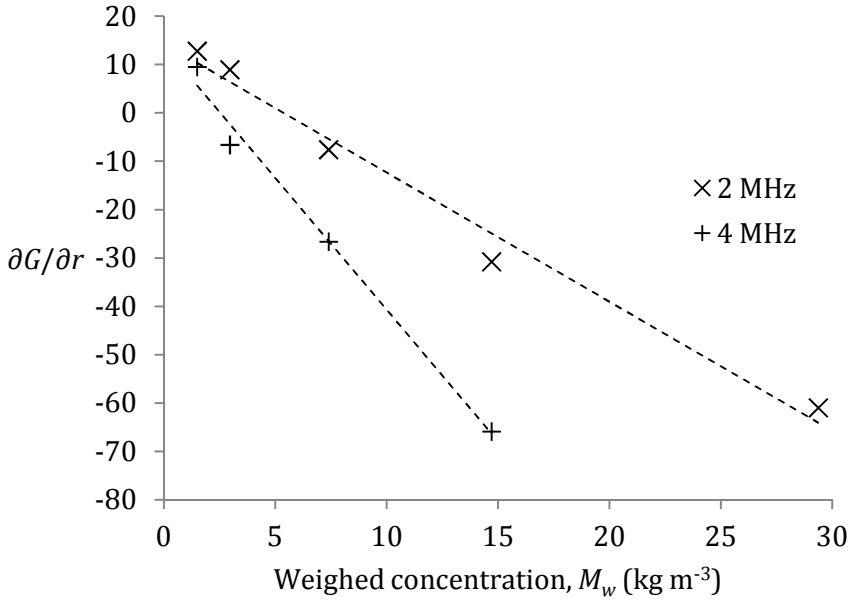

Figure 5-10: Gradient of G with respect to distance from probe *vs.* weighed concentration by mass, M_w, of Guyblast 30/40 in stirred mixing vessel at ultrasonic frequencies of f = 2 and 4 MHz.

5.2.4 Measurements and results: combined backscatter and system constant, K_h

In this section, results for the combined backscatter and system constant, K_h, are given. K_h was calculated according to Equation [5.18] once the corresponding values of ξ_h were known, from the same runs. In every case, the mean values of K_h were calculated over the region $r \approx 24$ to 46 mm (*i.e.* measurement points 60 to 120) in order to be consistent with the method of calculation of ξ_h.

As a representative example, Figure 5-11 shows K_h *vs*. distance with both the 2 and 4 MHz probes for Honite 22 at an intermediate concentration (M_w = 12.2 kg m^{-3}), for illustration of the degree of variation with distance. Relative standard deviations are given in the caption. For conciseness, only data at one concentration are shown, but the data at other concentrations were equally good. The distance-averaged mean values of K_h are shown in Figure 5-12 for both the 2 and 4 MHz probes. The other figures (Honite 16: Figure 5-13 and Figure 5-14; Guyblast 40/60: Figure 5-15 and Figure 5-16; Guyblast 30/40: Figure 5-17 and Figure 5-18) follow the same sequence.

Then, concentration-averaged mean values of K_h were calculated for all particle species and both ultrasonic frequencies, which are listed in Table 5-2 in Section 5.2.5 for reference.

5.2.4.1 Honite 22

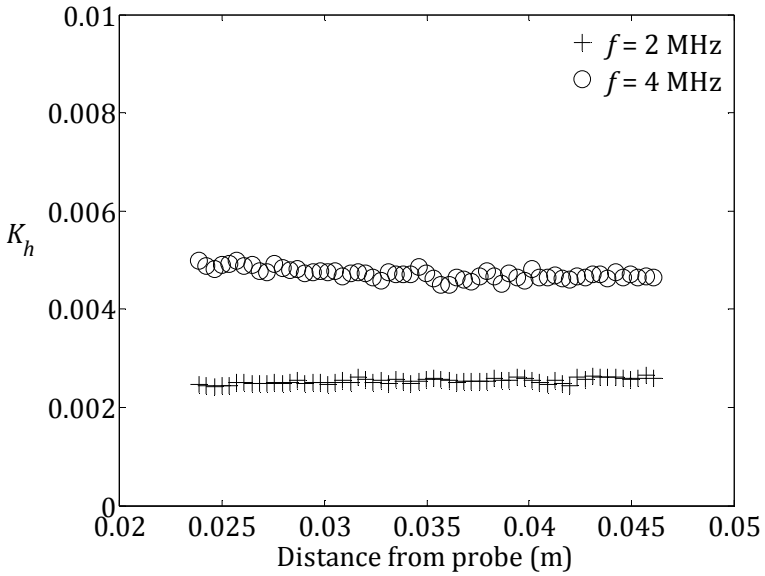

Figure 5-11: Variation of combined backscatter and system constant, K_h, with distance from probe at M_w = 12.2 kg m^{-3} for Honite 22 plastic beads at ultrasonic frequencies of f = 2 and 4 MHz in stirred mixing vessel. Relative standard deviation, 2.2 and 2.4 %, respectively.

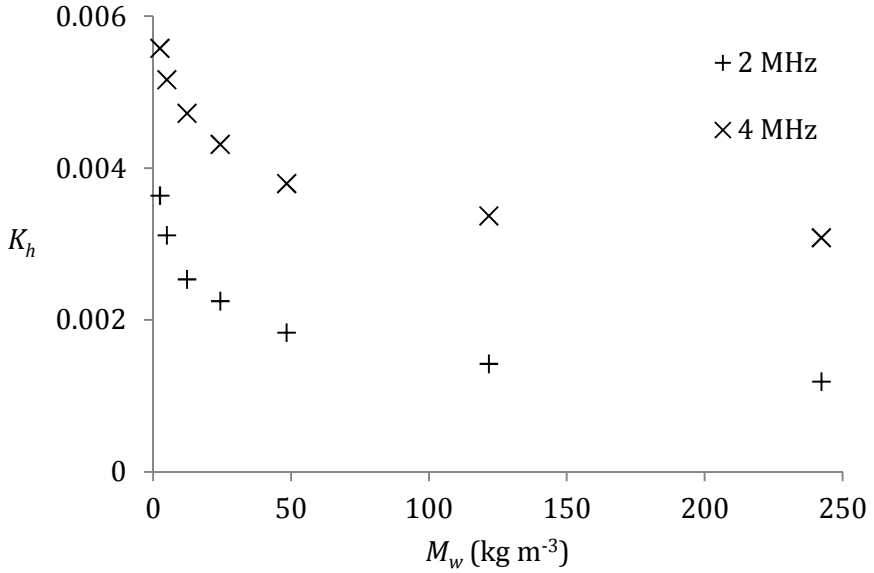

Figure 5-12: Distance-averaged mean of combined backscatter and system constant, K_h, *vs.* weighed concentration by mass, M_w, for Honite 22 glass spheres at ultrasonic frequencies of f = 2 and 4 MHz in stirred mixing vessel.

5.2.4.2 Honite 16

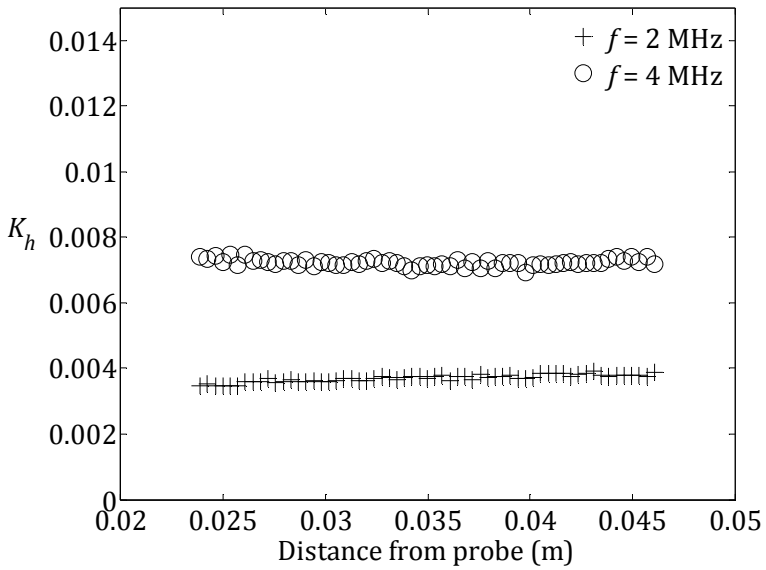

Figure 5-13: Variation of combined backscatter and system constant, K_h, with distance from probe at M_w = 12.2 kg m^{-3} for Honite 16 plastic beads at ultrasonic frequencies of f = 2 and 4 MHz in stirred mixing vessel. Relative standard deviation, 3.0 and 1.5 % respectively.

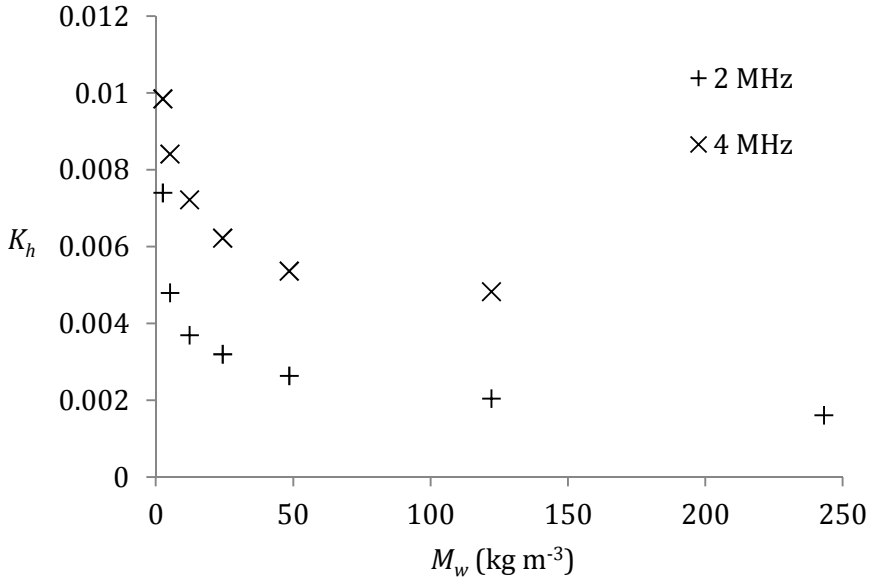

Figure 5-14: Distance-averaged mean of combined backscatter and system constant, K_h, *vs.* weighed concentration by mass, M_w, for Honite 16 glass spheres at ultrasonic frequencies of f = 2 and 4 MHz in stirred mixing vessel.

5.2.4.3 Guyblast 40/60

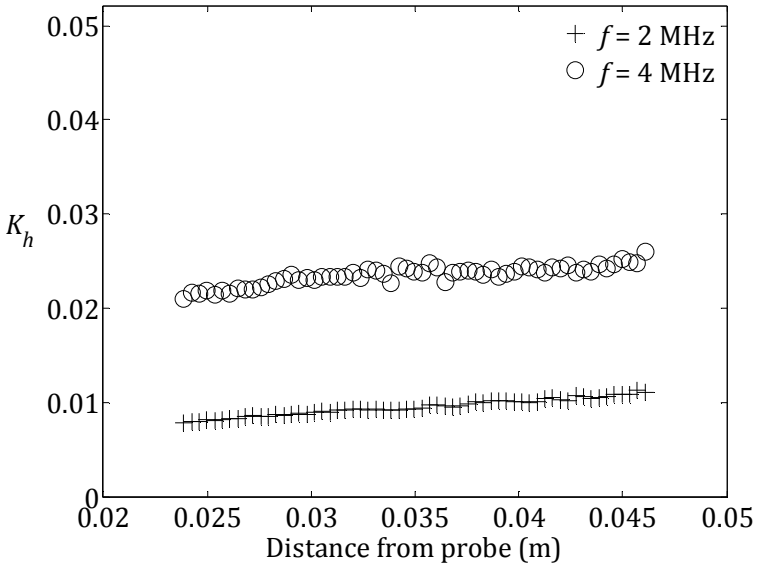

Figure 5-15: Variation of combined backscatter and system constant, K_h, with distance from probe at M_w = 7.38 kg m^{-3} for Guyblast 40/60 plastic beads at ultrasonic frequencies of f = 2 and 4 MHz in stirred mixing vessel. Relative standard deviation, 9.4 and 4.4 %, respectively.

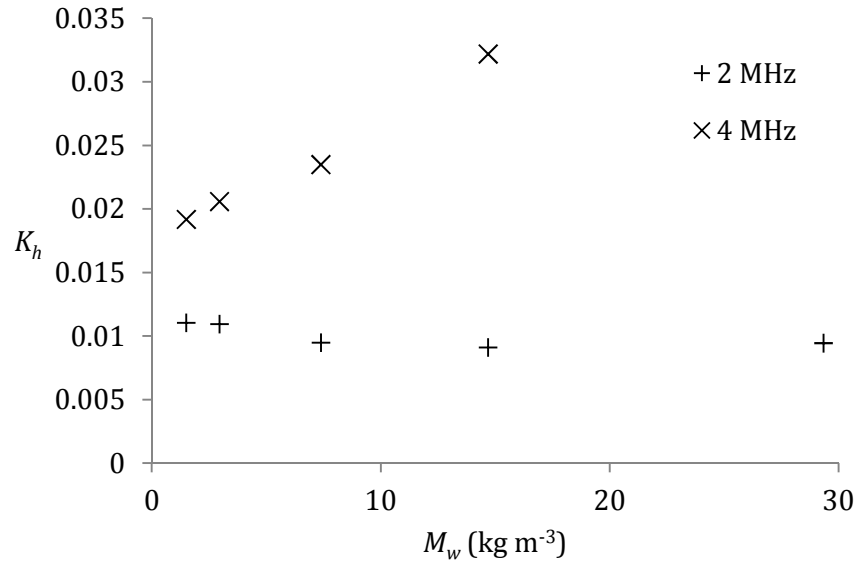

Figure 5-16: Distance-averaged mean of combined backscatter and system constant, K_h, *vs.* weighed concentration by mass, M_w, for Guyblast 40/60 glass spheres at ultrasonic frequencies of f = 2 and 4 MHz in stirred mixing vessel.

5.2.4.4 Guyblast 30/40

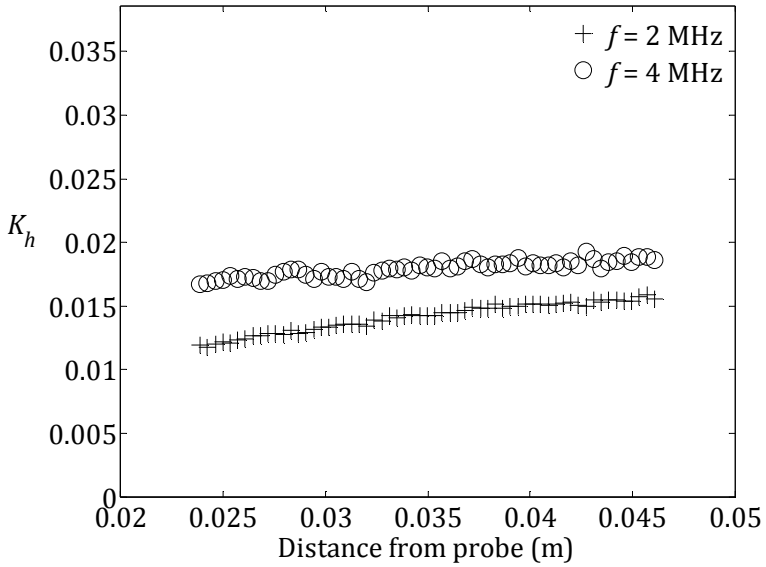

Figure 5-17: Variation of combined backscatter and system constant, K_h, with distance from probe at M_w = 7.40 kg m^{-3} for Guyblast 30/40 plastic beads at ultrasonic frequencies of f = 2 and 4 MHz in stirred mixing vessel. Relative standard deviation, 8.2 and 3.5 %, respectively.

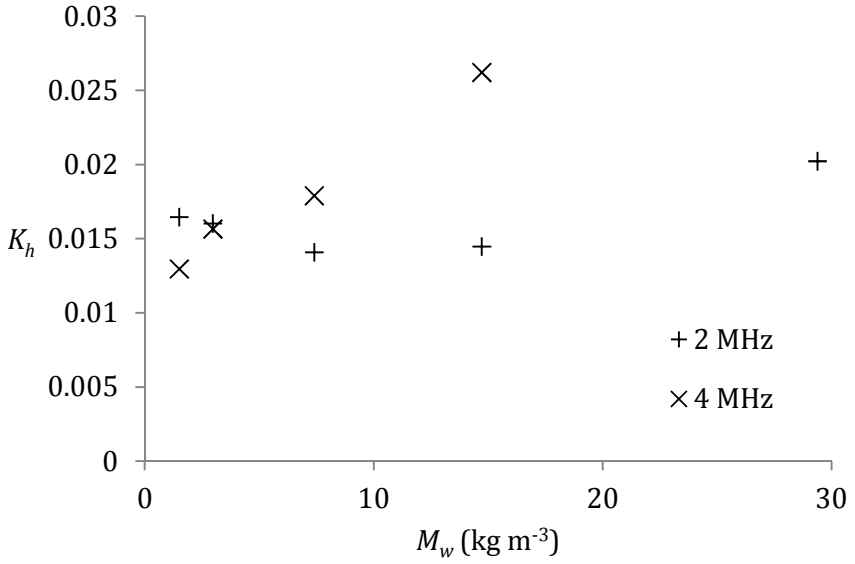

Figure 5-18: Distance-averaged mean of combined backscatter and system constant, K_h, *vs.* weighed concentration by mass, M_w, for Guyblast 30/40 glass spheres at ultrasonic frequencies of f = 2 and 4 MHz in stirred mixing vessel.

5.2.5 Discussion and summary: measured backscatter and attenuation coefficients

The measured values of the attenuation constant, ξ_h, and the combined scattering and system constant, K_h, are discussed in this section and have been compiled in Table 5-2 for reference.

Table 5-2: Comparison of predicted and measured values of sediment attenuation constant, ξ_h, and combined backscatter and system constant, K_h. Values of ka are also given. (All results are given to three significant figures.)

Particle species		Honite 22	Honite 16	Guyblast 40/60	Guyblast 30/40
ka (2 MHz)*		0.174	0.327	1.99	2.93
ka (4 MHz)*		0.348	0.654	3.97	5.87
ξ_h (2 MHz)	Predicted**	0.00400	0.0242	0.953	1.01
	Measured	0.0182	0.0212	0.627	1.34
ξ_h (4 MHz)	Predicted**	0.0570	0.274	1.807	1.44
	Measured	0.0694	0.135	2.74	2.73
K_h (2 MHz)		0.00229	0.00363	0.0100	0.0163
K_h (4 MHz)		0.00430	0.00699	0.0239	0.0182

* Value based on mean particle diameter, *i.e.* with $a = d_{50}/2$.

** Calculated *via* Equations [5.8] and [5.12] (Thorne and Hanes, 2002; Thorne and Meral, 2008) by setting $a = d_{50}/2$ and $\langle\chi\rangle = \chi(x = ka)$, as described in Section 5.1.

First, the results for the attenuation constant, ξ_h, are discussed. It was found that G, the range-corrected echo amplitude, varied very linearly with respect to r for all particle species (*e.g.* Figure 5-5, Honite 16) over the chosen region ($24 < r < 46$ mm), as the model requires (Equation [5.16]). Moreover, the variation of $\partial G/\partial r$ with respect to M_w was also found to be highly linear for all particle species, as was also expected (Equation [5.17]). Together, these two observations demonstrate two things: the success of the method as described, and that the suspensions in the stirred mixing vessel were, indeed, homogeneous.

However, it should be noted cursorily that the variation of $\partial G/\partial r$ with respect to

M_w was somewhat nonlinear at lower concentrations for both Honite species (*e.g.* Figure 5-6), and $\partial G/\partial r$ could be calculated for a much smaller range of M_w for the Guyblast species than for the Honite species. For example, the reader is invited to compare the x-axes of Figure 5-4 (Honite 22) and Figure 5-10 (Guyblast 30/40). As is clear from Table 5-2, this difference can be accounted for by the fact that attenuation is much higher in suspensions of Guyblast 30/40 (the largest of the particle species) than Honite 22 (the smallest), as would be expected, since the Guyblast particles are much larger (see Section 2.1.2).

Overall, then, the measured values of the attenuation coefficient, ξ_h, agree well with the predicted values, especially if the differences in material properties of the particle species are considered. The main conclusion to be drawn is that the degree of attenuation due to particles in the suspensions used, as quantified by the gradient of $\partial G/\partial r$ presented in Section 5.2.3, did indeed vary with mass concentration, as was expected and as has been found by many other researchers, and the reader is referred to Section 2.1.2 for a review of the relevant literature.

For completeness, several possible reasons exist for the observed (but not severe) nonlinearity in $\partial G/\partial r$, a numbered list of which is given below. A discussion of which are likely to be the most significant, and some suggestions of how they might be mitigated in the future, follow the list.

1. *The concentration is not uniform in the stirred tank mixer*. In general, particle size and density and mixer speed all have an effect on the concentration profile. The true concentration profile may, in reality, be quite Rousean (see Figure 6-3 in the bedforms chapter, Chapter 6, for more information), there may be some particles depositing on the bottom of the vessel, or there may be other, unknown effects caused by the motion of the impeller or vessel. However, the results presented in Section 5.2.2 suggest that the stirred mixing vessel produced a well mixed, homogeneous suspension for all the particle species.
2. *The probes are not functioning correctly or there are microbubbles on their active faces.* It is unlikely that any bubbles were present: none would remain

attached to the probes at the flow rates used here. As for other malfunctions, two probes did indeed fail during the experimental session and had to be replaced. Bad data were rejected.

3. *The near-field correction factor, ψ, is inaccurate.* The effective radius of the transducer, a_t, may be significantly smaller than the physical radius, perhaps by as much as 30% or so (Hay, 1991, Table II). Such a discrepancy would strongly influence the value of the near-field correction factor, ψ, since it depends on z such that the highest-order term in ψ is proportional to $z^{3.2}$ in Equation [5.3], and z depends on $(a_t)^{-2}$.
4. *The received signal is saturated or (oppositely) is attenuated very strongly with distance.* In the former case, the emitted voltage could be reduced, but it was found that none of the recorded echo data were saturated. In the latter case, one assumption of the model – that no significant attenuation occurs within each measurement volume – would not be valid. Attenuation was indeed very high, even at moderate concentrations with Guyblast, but such runs were excluded when calculating $\partial G/\partial r$ and ξ_h.
5. *Segregation by particle size is affecting the results*. Polydispersity, through its effect on ξ and χ (or K_h), strongly influences the scattering and attenuation properties of a suspension. Segregation according to particle size (even if the suspension is homogeneous in terms of concentration) will cause a variation in f and χ with distance, and potentially a strong one, because $f \propto (ka)^2$ and $\chi \propto (ka)^4$ for low values of ka. The effect of a wide PSD has been investigated in detail by Thorne and Meral (2008) and is discussed in more detail below.
6. *Turbulent motions are producing numerical errors.* The effects of nonlinearities (*e.g.* on time-averaging, as done in this study) have been identified previously (Admiraal and García, 2000; Hay, 1991; Pedocchi and Garcia, 2012) and it is reasonable to assume that such effects are present in the results of this study.
7. *Uncertainties in measured experimental parameters are affecting the results.* This possibility is explored quantitatively in Appendix A with respect to the beam divergence angle, probe mounting angle, temperature and pressure.

Of the possible sources of error listed above, points 1 and 2 are thought to be

insignificant and point three to be likely, although the quantitative effect is left as a subject for further study. Point four, although generally present in highly attenuating suspensions, is not thought to have affected the final results because it is quite clear when this effect is present, and data were excluded accordingly. As with point four, the effects of points five and six must be assumed to be present in general, but the strength of these effects is difficult to quantify and is left as a subject for future work.

Next, the results for the combined backscatter and system constant, K_h, are discussed. For all particle species, K_h was found to vary with particle concentration. However, the variation in K_h with concentration for the two Guyblast species was less severe than for the Honite species. Indeed, considering the complexity and novelty of the experimental method and the fact that the calculation of K_h relies on measurements of ξ_h, according to Equation [5.18], the observed variation in K_h with M_w is quite acceptable.

Moreover, several of the observed trends in K_h were indeed as expected: K_h was found to be very constant with distance (the maximum spatial variation, as quantified by the relative standard deviation, was 9.4 % for Guyblast 40/60 at f = 2 MHz: see Figure 5-15); and the distance-averaged values of K_h increased with both particle size and ultrasonic frequency (except for the two Guyblast species at f = 4 MHz).

For the purposes of validation and discussion, the measured values of ξ_h and K_h, are summarised and presented in Table 5-2, along with predicted values of ξ_h. The predicted values of ξ_h were calculated *via* Equations [5.8] and [5.12] (Thorne and Hanes, 2002; Thorne and Meral, 2008), in which the measured values of the particle density and size were used (see Table 3-7 in Section 3.5.5, particle characterisation), *i.e.* $a = \langle a \rangle = d_{50}/2$ and $\langle \chi \rangle = \chi(x = ka)$. (It was not possible to perform a similar comparison for K_h, as it contains a system constant, k_t, that could not be separated from the backscatter constant, k_s.)

It is clear from Table 5-2 that all the measured values of ξ_h are within a factor of

order unity of the predicted values. This is a particularly good result for the two Guyblast species, which differ in density (and other properties, such as compressibility) to sand, upon which the predicted values are based. More generally, the measured values of both ξ_h and K_h increase with ka, as expected: ξ and K are expected to be proportional to $(ka)^4$ and $(ka)^2$, respectively, at low ka (*i.e.* $ka < 1$) and approach constant values at high ka (*i.e.* $ka > 1$), where k is the ultrasonic wavenumber ($k = 2\pi/\lambda$) and a is the particle diameter (Thorne and Hanes, 2002). However, the discrepancies are not insignificant, and so there follows a discussion of some of the problems involved in estimating the attenuation properties from measured particle size distributions, as previously discussed by Thorne and Meral (2008) and more recently by Moate and Thorne (2013).

1. In the Rayleigh regime (low ka), $\langle\chi\rangle/\chi > 1$, *i.e.* χ is underestimated; in the geometric regime (high ka), $\langle\chi\rangle/\chi < 1$, *i.e.* χ is overestimated.
2. The discrepancy is stronger for low ka and is proportional to the width of the particle size distribution, quantified as κ by Thorne and Meral (2008). Therefore, measurements of ξ (which is related to χ through Equation [5.8]) will be most sensitive to uncertainties in the PSD in the case of small, polydisperse species insonified at low frequencies.
3. This trend is indeed observed in the results presented here: the measured values of ξ at lower ka are generally lower than those predicted, and higher than predicted at higher ka, as shown in Table 5-2.

Lastly, it is interesting to note the effect that particle shape is likely to have on scattering and attenuation properties, since at least one of the species used in the experiments presented here (Guyblast) is highly non-spherical in shape. According to Thorne and Buckingham (2004) in the geometric regime (*i.e.* at high ka) "a particle of irregular shape, having a similar volume to a sphere, would have a larger surface area and hence a higher geometric and scattering cross section", and it is reasonable to assume the attenuation properties of highly irregular particles – that is, their ability to absorb energy – would be enhanced for the same reasons, since such particles present a larger projected surface area to the emitted acoustic

beam than do spherical particles with the same volume. However, whether this enhancement of attenuation properties can fully account for the difference between the observed and predicted values at higher values of ka is left as a subject for further study.

To summarise, then, the discrepancy between the measured and estimated values of ξ_h (and, for analogous reasons, K_h) can be accounted for partly by recourse to experimental errors, the most likely of which were described in Section 5.2.3, partly by differences in the physical properties of quartz sand and the species used in this study, and partly by inaccuracies in the predicted values themselves, which are estimates based on mean particle size. However, overall, the measured values of ξ_h and K_h demonstrate that the method as a whole was very successful.

So, as stated earlier, such data only exist for quartz sand, and one objective of this study – which has been achieved – is to provide data for other kinds of particle species, in particular highly spherical glass (*i.e.* Honite) and highly non-spherical plastic (Guyblast). The main aim, however, is to use the measured values of ξ_h and K_h to calculate concentration profiles in suspensions, as described in the section that follows.

5.3 Heterogeneous case: measurement of the particle concentration profile using the dual-frequency inversion method

In this section, the expressions required to implement the dual-frequency inversion method (Hurther *et al.*, 2011) are derived and discussed. The values of ξ_h and K_h that were measured, as presented in Table 5-2, are then used to construct vertical concentration profiles in horizontally flowing suspensions in a closed circular pipe. The experimental method, including data processing, is described in detail.

5.3.1 Derivation

The dual-frequency method circumvents the inaccuracies associated with other methods: all suffer from numerical instability in the far-field, "with small errors due to uncertainties in the acoustic suspension scattering characteristics, positively feeding back into the inversion and accumulating with range" (Thorne *et al.*, 2011). The dual-frequency method, on the other hand, "has the major advantage that the calculated concentration at range *r* from the transducer is independent of the concentration profile between the transducer and *r*, which removes the attenuation feedback instability inherent in the iterative implicit approach" (Thorne *et al.*, 2011). A description of the model follows.

Equation [5.1] can be rewritten for the general case, using Equation [5.6], as described by Hurther *et al.* (2011) and Thorne *et al.* (2011), as follows:

$$V^2(r) = \Phi^2(r)J(r) \qquad [5.20]$$

$$\Phi^2(r) \equiv \left(\frac{k_s k_t}{\psi r}\right)^2 e^{-4r\alpha_w}, \qquad [5.21]$$

$$J(r) \equiv Me^{-4\int_0^r \xi(r)M(r)\mathrm{d}r} = V^2(r)/\Phi^2(r). \qquad [5.22]$$

If the PSD, and therefore ξ and k_s, do not vary with distance from the probe, which is a reasonable approximation if the particle species is neutrally buoyant, has a very narrow PSD or is very well mixed, the exponent in Equation [5.22] can be written as follows:

$$-4\int_0^r \xi(r)M(r)\mathrm{d}r = -4\xi\int_0^{r'} M(r)\mathrm{d}r, \qquad [5.23]$$

i.e. $\xi \neq \xi(r)$, and for two transducers that operate at different frequencies Equation [5.22] can be rewritten as follows:

$$J_i(r) = Me^{-4\xi_i\int_0^{r'} M(r)\mathrm{d}r}, \qquad [5.24]$$

where i = 1, 2 for probes/frequencies 1 and 2 (*i.e.* 2 and 4 MHz in this study). Taking the natural logarithm of Equation [5.24] and dividing both sides by ξ_i yields

$$\frac{1}{\xi_i}\ln\left(\frac{J_i}{M}\right) = -4\int_0^{r'} M(r)\mathrm{d}r. \qquad [5.25]$$

The right-hand side of Equation [5.25] is common, and so

$$\left(\frac{J_1}{M}\right)^{\xi_2} = \left(\frac{J_2}{M}\right)^{\xi_1}, \qquad [5.26]$$

and rearranging for M yields the following:

$$M^{\xi_1-\xi_2} = J_1^{-\xi_2}J_2^{\xi_1}. \qquad [5.27]$$

The explicit expression for particle mass concentration according to the dual-frequency inversion method is then obtained:

$$M = J_1^{(1-\xi_1/\xi_2)^{-1}}J_2^{(1-\xi_2/\xi_1)^{-1}}. \qquad [5.28]$$

In the general case, the PSD and detailed backscatter and attenuation properties are not known. Experimentally, J is evaluated by

$$J = V^2/\Phi^2, \qquad [5.29]$$

where V is measured directly and Φ must be calculated from known parameters, so a minimal requirement for closure is that k_s, k_t, ξ_i and α_w are known or can be measured. Whereas α_w can be calculated using Equation [5.19], as described in Section 5.2.1, k_s, k_t and ξ_i must be found empirically, as described in the section on homogeneous suspensions (Section 5.2). That is, ξ_i is calculated from Equation [5.17] (results: Section 5.2.3), and $K_h \equiv k_{sh}k_t$ is found using Equation [5.18] (results: Section 5.2.4). The measured values of ξ_h and K_h are summarised in Table 5-2.

Lastly, it must be noted that consideration should generally be given to the specific frequencies used. The form factor, f (and therefore k_s and K_h), and the scattering cross-section, χ (and therefore ξ_h), vary with $(ka)^2$ and $(ka)^4$, respectively, in the low-ka (*i.e.* Rayleigh) regime and approach constant values in the high-ka (*i.e.* geometric) regime (see, for example, Moate and Thorne, 2009), although the author is aware of such data only for "primarily quartz" sand (Thorne and Hanes, 2002). The reader is referred to Section 2.1 for a description of the various scattering regimes.

The dual-frequency method requires that the particle scattering properties, and therefore ξ_1 and ξ_2, vary with ka such that M can be evaluated accurately from Equation [5.28]. However, this condition – which dictates that the smaller of the two frequencies lies in the Rayleigh (*i.e.* low-ka) regime in which ξ depends very strongly on ka, such that ξ_1/ξ_2 is "sufficiently different from unity" – is not so stringent in practice, and is easily satisfied for particles sizes of a < 500 μm and frequencies in the range 1-5 MHz, because $\xi \propto (ka)^4$ (Hurther *et al.*, 2011).

It was found that the two frequencies used in this study, 2 and 4 MHz, were sufficiently different: the ratios of the measured values of ξ_1 to ξ_2 (or rather ξ_{h1} and ξ_{h2}) at f = 2 and 4 MHz, respectively, for all four particle species differed significantly from unity (see Table 5-2).

5.3.2 Calculation of particle concentration profiles

In this section, vertical profiles of the particle concentration, M, are presented for all four particle species over a range of nominal mean concentrations and flow rates in the main pipe flow loop, calculated *via* the dual-frequency inversion method of Hurther *et al.* (2011) that was described in Section 5.3.1. However, to begin, the experimental procedure is reiterated briefly for the reader.

First, echo amplitude profiles were recorded with both probes, since a requirement of the dual-frequency inversion method is that two frequencies are used. Then, the data were processed according to the general method presented

earlier (Section 3.3) and profiles of the RMS echo voltage, V, obtained for each transducer. Profiles of Φ and J were then generated using the measured values of ξ_h and K_h (presented in Table 5-2) *via* Equations [5.21] and [5.22], respectively. Finally, profiles of the mass concentration, M, were calculated using pairs of J profiles *via* Equation [5.28].

Note that the axes in all the figures in this section are inverted to aid visualisation. Particle mass concentrations measured by physical sampling are also given in the caption text; samples (3 × 60 ml for each run) were taken manually from the mixing tank of the pipe loop, the contents of which were stirred by an impeller. However, the mixing tank and test section were separated by a 1.5 m vertical riser pipe, so the concentration in the test section was expected (and, indeed, found) to be somewhat lower than that in the mixing tank: a slip velocity would exist between the fluid and particles being pumped upwards.

Run parameters and concentration profiles are shown in Table 5-3 and Figure 5-19 to Figure 5-34, respectively, at three flow rates (Re ≈ 25,000, 50,000 and 100,000) and four nominal volume fractions (ϕ = 0.1, 0.5, 1 and 3 %). Table 5-3 includes the weighed and sampled concentrations and the Reynolds number, Re.

Table 5-3: Run parameters and sample results for flow-loop runs shown in Figure 5-19 to Figure 5-34.

ϕ (%)*	M_w (kg m^{-3})*	M_s (kg m^{-3})*	Q (l s^{-1})*	Re (10^3)*	Profile
Honite 22 (small glass)					
0.1	2.50	2.73	3.62	108	Figure 5-19
		3.32	1.78	53.2	
		2.28	0.874	26.1	
0.5	12.4	13.9	3.60	108	Figure 5-20
		13.4	1.78	53.1	
		12.0	0.862	25.8	
1	24.7	27.6	3.57	107	Figure 5-21
		27.4	1.77	52.7	
		24.3	0.866	25.9	
3	72.8	81.5	3.50	105	Figure 5-22

Table 5-3: Run parameters and sample results for flow-loop runs shown in Figure 5-19 to Figure 5-34.					
ϕ (%)*	M_w (kg m^{-3})*	M_s (kg m^{-3})*	Q (l s^{-1})*	Re (10^3)*	Profile
		79.9	1.75	52.1	
		67.0	0.856	25.6	
Honite 16 (large glass)					
0.1	2.50	3.00	3.54	106	Figure 5-23
		2.60	1.75	52.3	
		1.82	0.851	25.4	
0.5	12.4	14.5	3.48	104	Figure 5-24
		13.6	1.72	51.3	
		7.30	0.841	25.1	
1	24.7	26.6	3.50	105	Figure 5-25
		20.9	1.73	51.6	
		10.9	0.851	25.4	
3	72.8	75.9	3.47	104	Figure 5-26
		54.8	1.71	51.1	
		28.2	0.838	25.0	
Guyblast 40/60 (small glass)					
0.1	1.50	1.68	3.57	107	Figure 5-27
		1.44	1.76	52.7	
		1.95	0.858	25.7	
0.5	7.46	7.80	3.54	106	Figure 5-28
		6.71	1.75	52.3	
		4.80	0.855	25.6	
1	14.9	16.9	3.52	105	Figure 5-29
		17.3	1.73	51.7	
		11.3	0.838	25.0	
3	43.7	46.9	3.51	105	Figure 5-30
		40.5	1.72	51.2	
		21.4	0.826	24.4	
Guyblast 30/40 (large plastic)					
0.1	1.50	2.15	3.46	103	Figure 5-31
		1.14	1.71	51.1	
		0.553	0.836	25.0	

Table 5-3: Run parameters and sample results for flow-loop runs shown in Figure 5-19 to Figure 5-34.					
ϕ (%)*	M_w (kg m^{-3})*	M_s (kg m^{-3})*	Q (l s^{-1})*	Re (10^3)*	Profile
0.5	7.46	8.25	3.39	101	Figure 5-32
		5.49	1.67	49.7	
		4.01	0.812	24.3	
1	14.9	16.1	3.40	102	Figure 5-33
		11.2	1.68	50.1	
		7.56	0.812	24.3	
3	43.7	45.5	3.37	101	Figure 5-34
		34.3	1.63	48.7	
		15.7	0.755	23.1	
* ϕ = nominal volume fraction; M_w = weighed particle concentration; M_s = sampled particle concentration; Q = flow rate; Re = Reynolds number.					

It is important to note why these particular flow rates were chosen. In a general sense, they are intended to be representative samples from a larger set of results, but more specifically they correspond broadly to three flow regimes: fully suspended, with an approximately uniform concentration profile (*i.e.* pseudo-homogeneous); segregating, with a significant concentration gradient (*i.e.* heterogeneous); and settling. These regimes were described in more detail in Section 2.2.6, and it should also be made clear that no time-dependent beds (*i.e.* beds with ripples and other complex phenomena) were observed in the runs presented in this section, since such bedforms are dealt with separately as a distinct topic in Chapter 6.

5.3.2.1 Honite 22

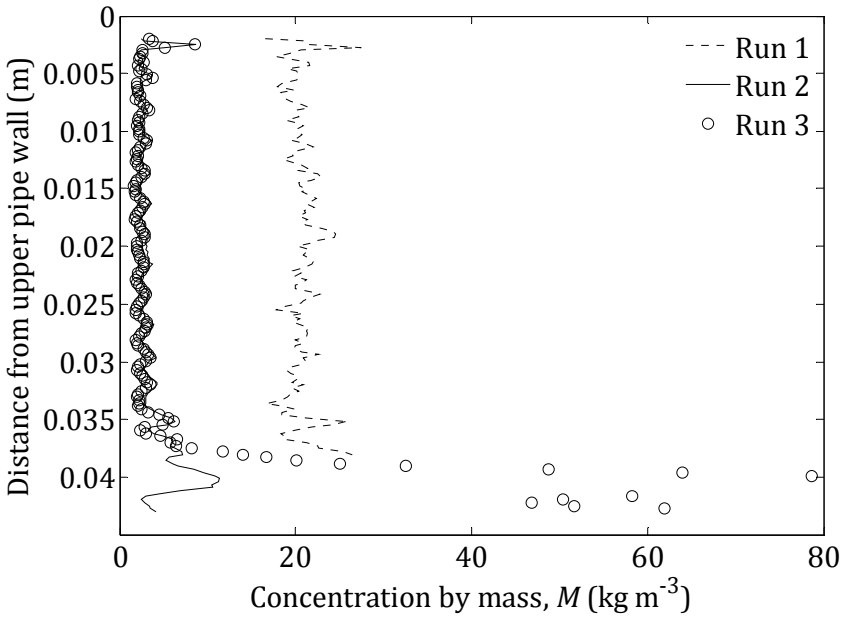

Figure 5-19: Concentration by mass, M, *vs.* vertical distance from upper pipe wall with Honite 22 glass spheres, ϕ = 0.1 %; M_w = 2.50 kg m^{-3}; runs 1, 2 and 3 with M_s = 2.73, 3.32 and 2.28 kg m^{-3} at Q = 3.62, 1.78 and 0.874 l s^{-1}, respectively.

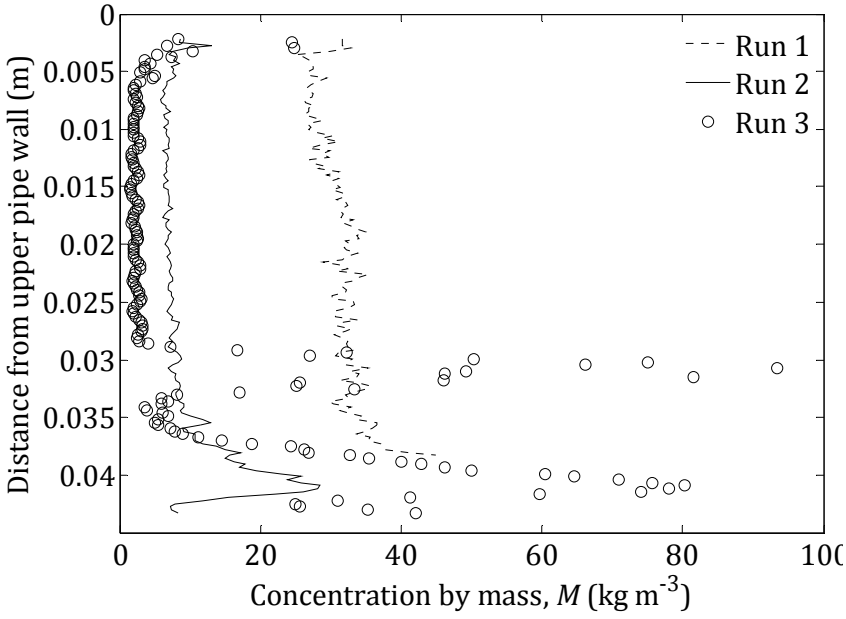

Figure 5-20: Concentration by mass, M, *vs.* vertical distance from upper pipe wall with Honite 22 glass spheres, ϕ = 0.5 %; M_w = 12.4 kg m^{-3}; runs 1, 2 and 3 with M_s = 13.9, 13.4 and 12.0 kg m^{-3} at Q = 3.60, 1.78 and 0.862 l s^{-1}, respectively.

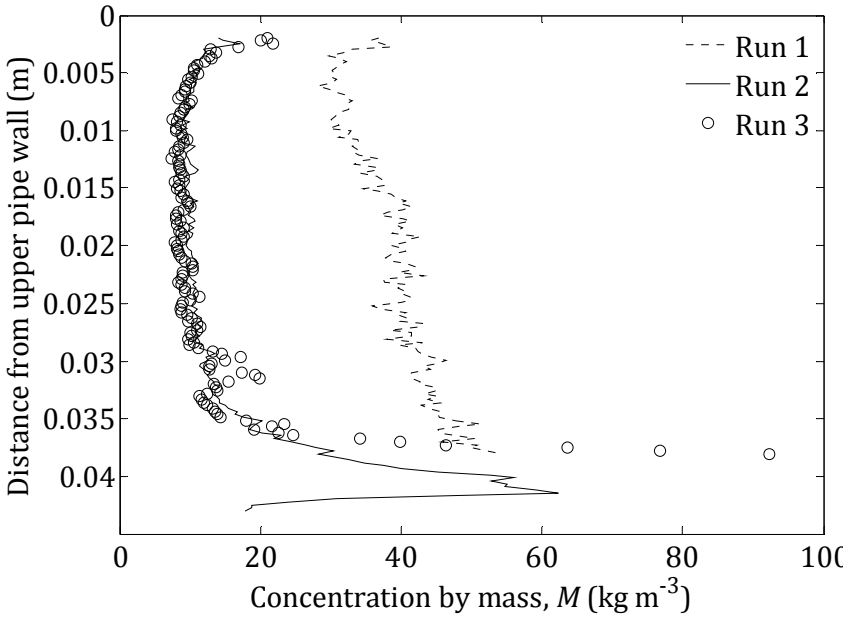

Figure 5-21: Concentration by mass, M, *vs.* vertical distance from upper pipe wall with Honite 22 glass spheres, ϕ = 1 %; M_w = 24.7 kg m^{-3}; runs 1, 2 and 3 with M_s = 27.6, 27.4 and 24.3 kg m^{-3} at Q = 3.57, 1.77 and 0.866 l s^{-1}, respectively.

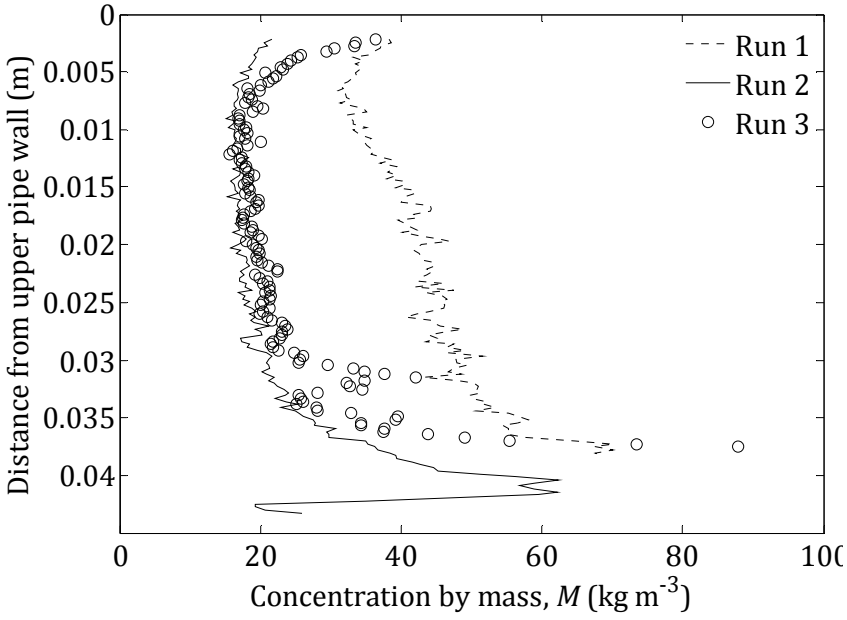

Figure 5-22: Concentration by mass, M, *vs.* vertical distance from upper pipe wall with Honite 22 glass spheres, ϕ = 3 %; M_w = 72.8 kg m^{-3}; runs 1, 2 and 3 with M_s = 81.5, 79.9 and 67.0 kg m^{-3} at Q = 3.50, 1.75 and 0.856 l s^{-1}, respectively.

5.3.2.2 Honite 16

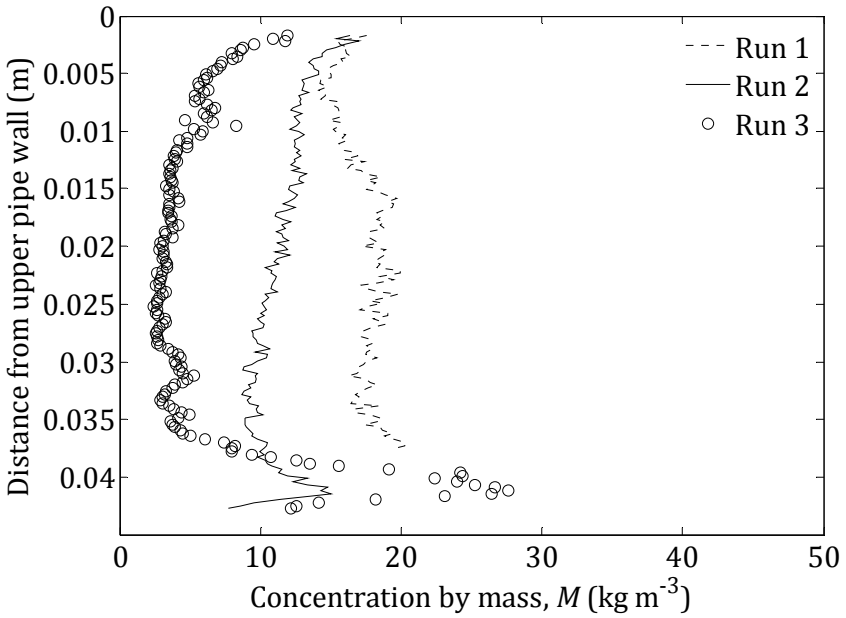

Figure 5-23: Concentration by mass, M, *vs.* vertical distance from upper pipe wall with Honite 16 glass spheres, ϕ = 0.1 %; M_w = 2.50 kg m^{-3}; runs 1, 2 and 3 with M_s = 3.00, 2.60 and 1.82 kg m^{-3} at Q = 3.54, 1.75 and 0.851 l s^{-1}, respectively.

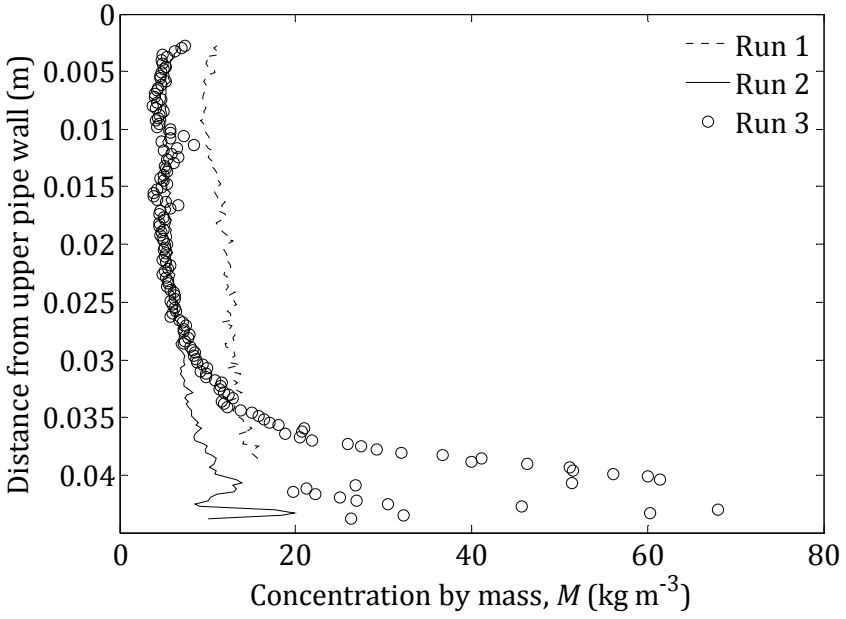

Figure 5-24: Concentration by mass, M, *vs.* vertical distance from upper pipe wall with Honite 16 glass spheres, ϕ = 0.5 %; M_w = 12.4 kg m^{-3}; runs 1, 2 and 3 with M_s = 14.5, 13.6 and 7.30 kg m^{-3} at Q = 3.48, 1.72 and 0.841 l s^{-1}, respectively.

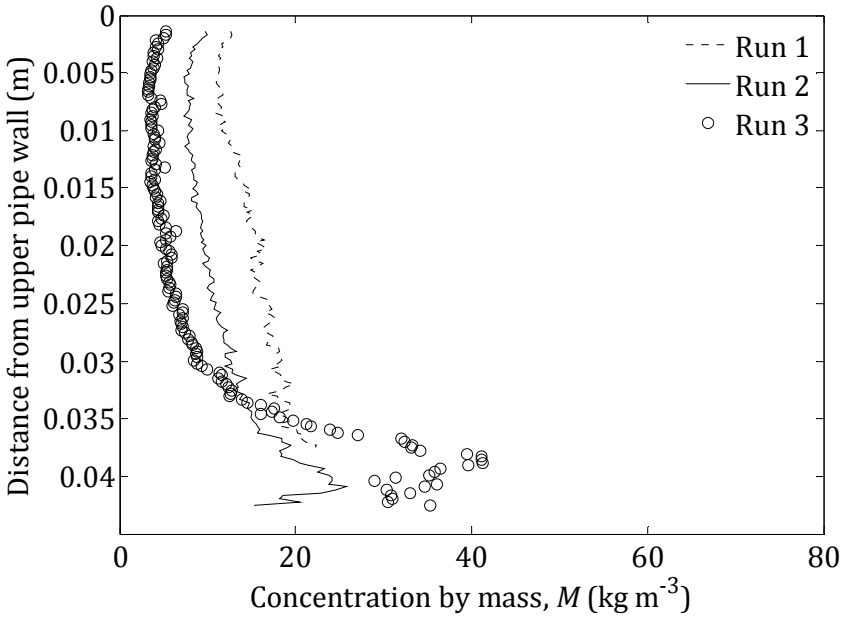

Figure 5-25: Concentration by mass, M, *vs.* vertical distance from upper pipe wall with Honite 16 glass spheres, ϕ = 1 %; M_w = 24.7 kg m^{-3}; runs 1, 2 and 3 with M_s = 26.6, 20.9 and 10.9 kg m^{-3} at Q = 3.50, 1.73 and 0.851 l s^{-1}, respectively.

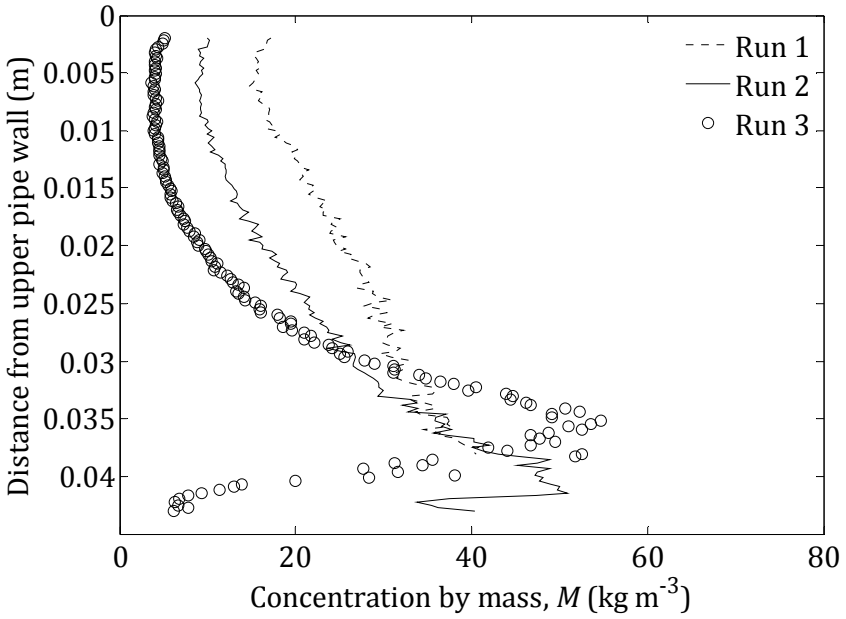

Figure 5-26: Concentration by mass, M, *vs.* vertical distance from upper pipe wall with Honite 16 glass spheres, ϕ = 3 %; M_w = 72.8 kg m^{-3}; runs 1, 2 and 3 with M_s = 75.9, 54.8 and 28.2 kg m^{-3} at Q = 3.47, 1.71 and 0.838 l s^{-1}, respectively.

5.3.2.3 Guyblast 40/60

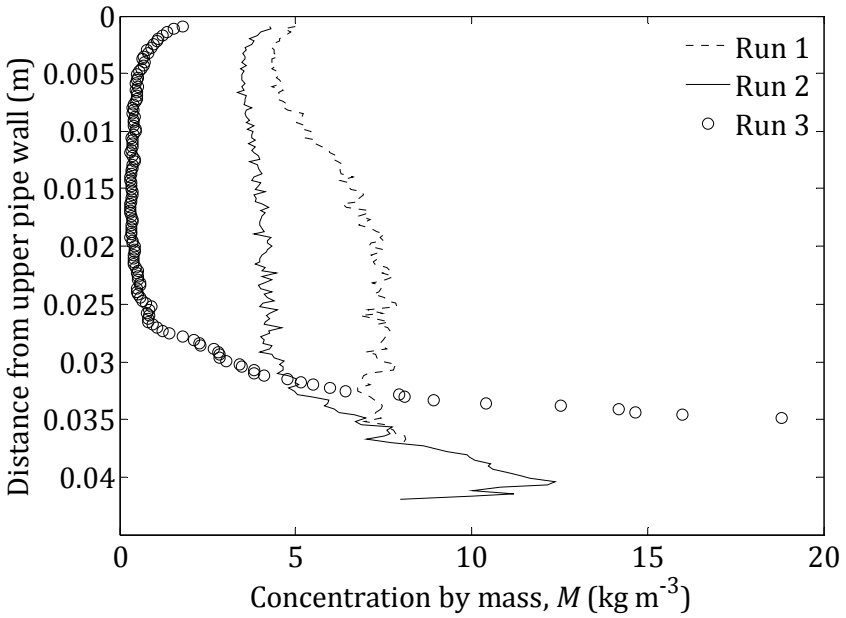

Figure 5-27: Concentration by mass, M, *vs.* vertical distance from upper pipe wall with Guyblast 40/60 plastic beads, ϕ = 0.1 %; M_w = 1.50 kg m^{-3}; runs 1, 2 and 3 with M_s = 1.68, 1.44 and 1.95 kg m^{-3} at Q = 3.57, 1.76 and 0.858 l s^{-1}, respectively.

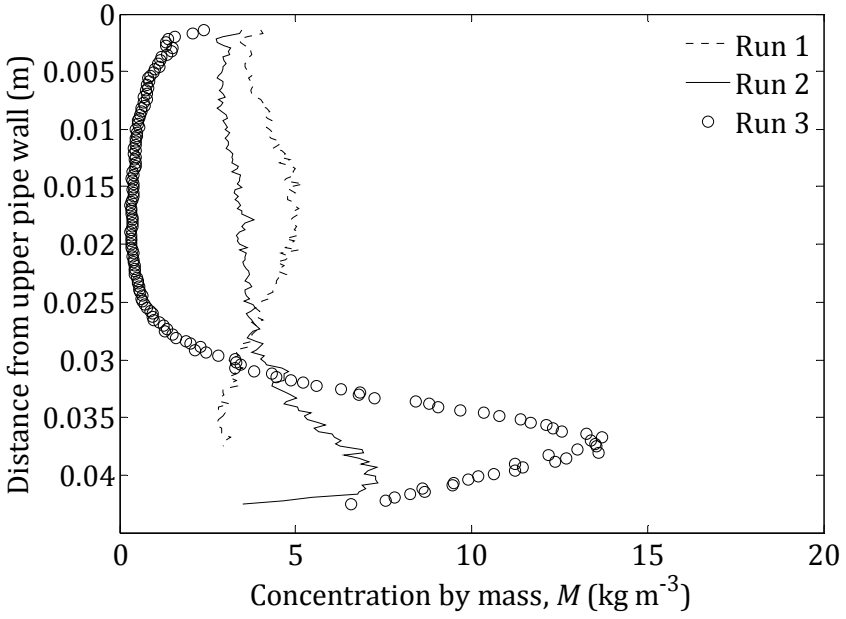

Figure 5-28: Concentration by mass, M, *vs.* vertical distance from upper pipe wall with Guyblast 40/60 plastic beads, ϕ = 0.5 %; M_w = 7.46 kg m^{-3}; runs 1, 2 and 3 with M_s = 7.80, 6.71 and 4.80 kg m^{-3} at Q = 3.54, 1.75 and 0.855 l s^{-1}, respectively.

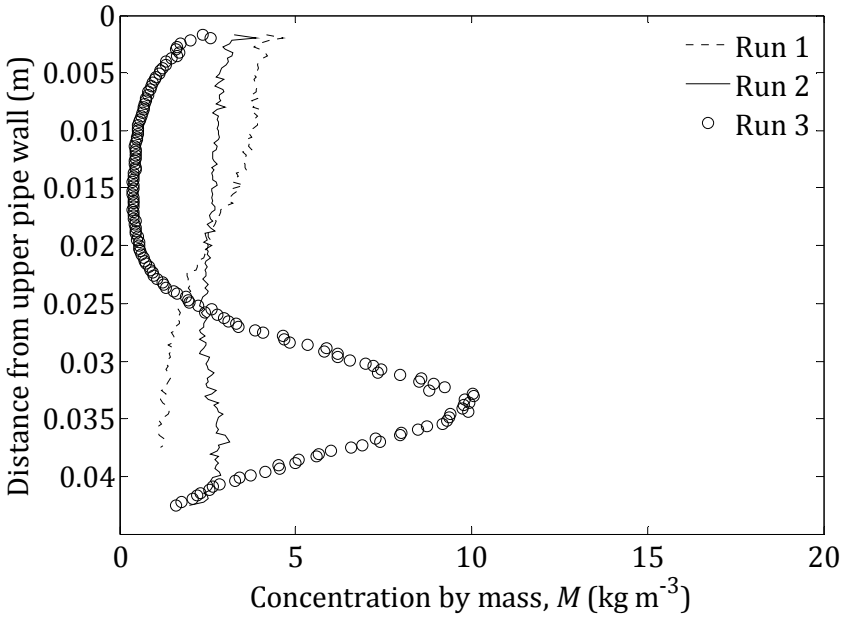

Figure 5-29: Concentration by mass, M, *vs.* vertical distance from upper pipe wall with Guyblast 40/60 plastic beads, ϕ = 1 %; M_w = 14.9 kg m^{-3}; runs 1, 2 and 3 with M_s = 16.9, 17.3 and 11.3 kg m^{-3} at Q = 3.52, 1.73 and 0.838 l s^{-1}, respectively.

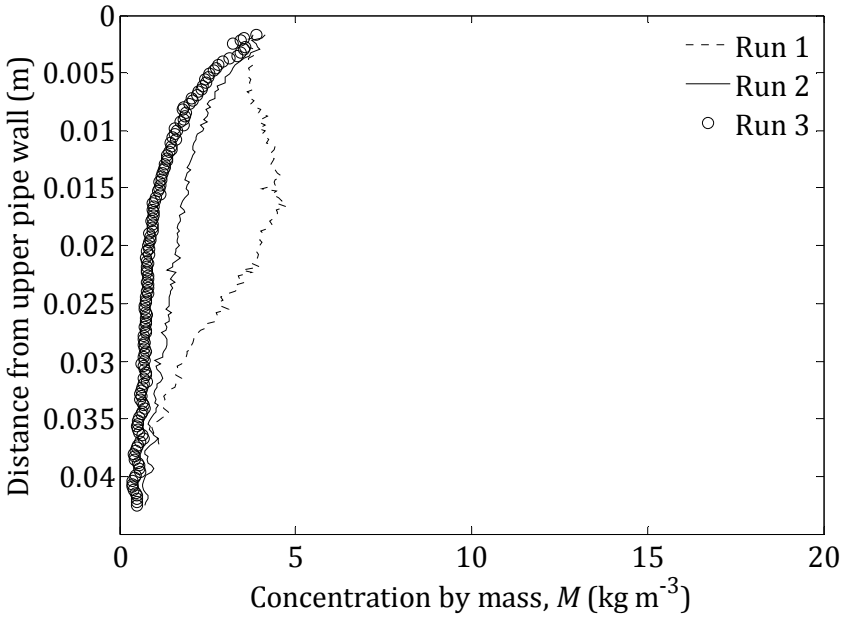

Figure 5-30: Concentration by mass, M, *vs.* vertical distance from upper pipe wall with Guyblast 40/60 plastic beads, ϕ = 3 %; M_w = 43.7 kg m^{-3}; runs 1, 2 and 3 with M_s = 46.9, 40.5 and 21.4 kg m^{-3} at Q = 3.51, 1.72 and 0.826 l s^{-1}, respectively.

5.3.2.4 Guyblast 30/40

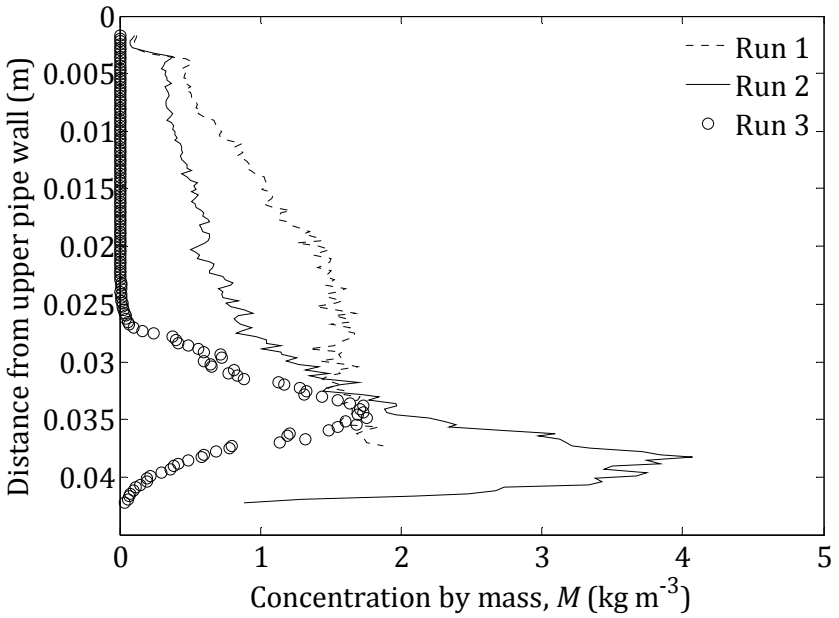

Figure 5-31: Concentration by mass, M, *vs.* vertical distance from upper pipe wall with Guyblast 30/40 plastic beads, ϕ = 0.1 %; M_w = 1.50 kg m^{-3}; runs 1, 2 and 3 with M_s = 2.15, 1.14 and 0.553 kg m^{-3} at Q = 3.46, 1.71 and 0.836 l s^{-1}, respectively.

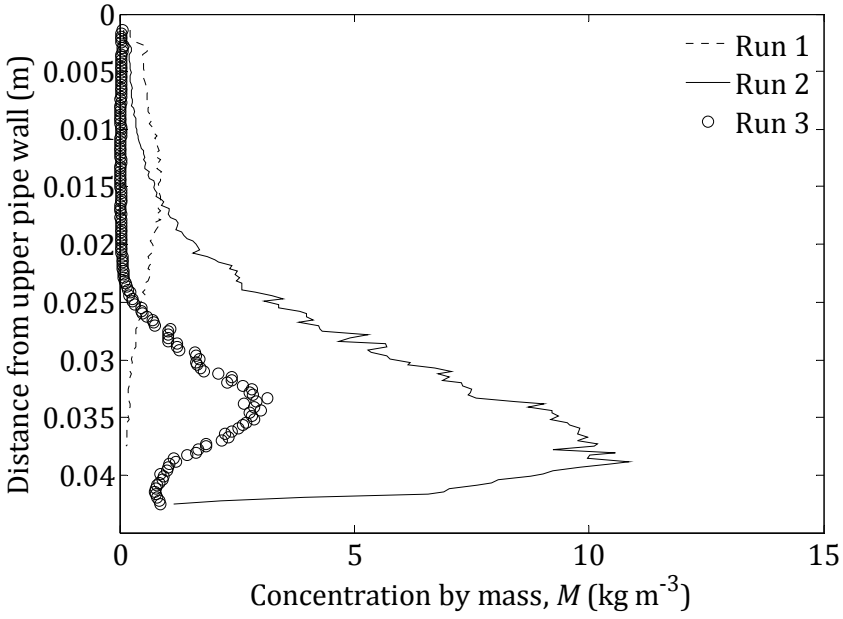

Figure 5-32: Concentration by mass, M, *vs.* vertical distance from upper pipe wall with Guyblast 30/40 plastic beads, ϕ = 0.5 %; M_w = 7.46 kg m^{-3}; runs 1, 2 and 3 with M_s = 8.25, 5.49 and 4.01 kg m^{-3} at Q = 3.39, 1.67 and 0.812 l s^{-1}, respectively.

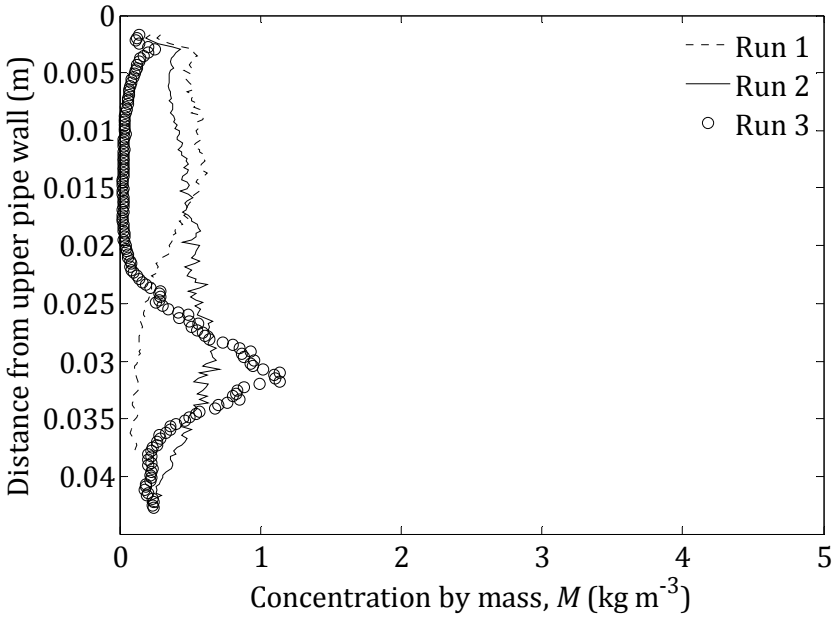

Figure 5-33: Concentration by mass, M, *vs.* vertical distance from upper pipe wall with Guyblast 30/40 plastic beads, ϕ = 1 %; M_w = 14.9 kg m^{-3}; runs 1, 2 and 3 with M_s = 16.1, 11.2 and 7.56 kg m^{-3} at Q = 3.40, 1.68 and 0.812 l s^{-1}, respectively.

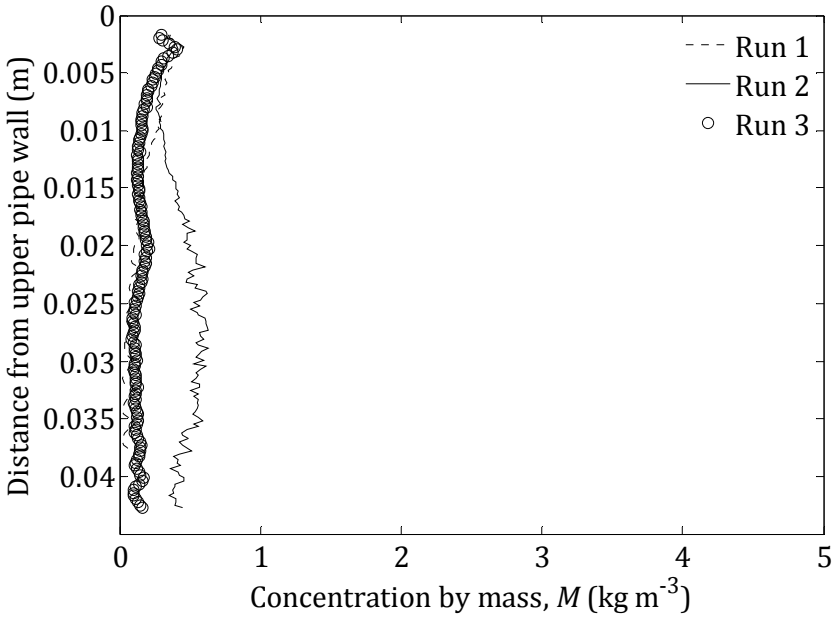

Figure 5-34: Concentration by mass, M, *vs.* vertical distance from upper pipe wall with Guyblast 30/40 plastic beads, ϕ = 3 %; M_w = 43.7 kg m^{-3}; runs 1, 2 and 3 with M_s = 45.5, 34.3 and 15.7 kg m^{-3} at Q = 3.37, 1.63 and 0.755 l s^{-1}, respectively.

5.3.3 Discussion: measured concentration profiles

In this section, the concentration profiles presented in Section 5.3.2 are discussed and some physical arguments are given to account for them. Several interesting trends were observed that were, in general, physically realistic, if qualitative in some cases. The first and most striking trend is that M generally increased with distance from the upper pipe wall, and this increase was stronger at lower flow rates (compare, for example, the profiles at Q = 3.48 and 0.841 l s^{-1} in Figure 5-24, for Honite 16 at ϕ = 0.5 %, M_w = 12.4 kg m^{-3}), as would be expected, except when high attenuation rendered concentration profiles meaningless, as was the case for some Guyblast runs (which is discussed separately later).

Not only was there evidence of segregation at lower flow rates, there was also a decrease in ambient concentration with decreasing flow rate (*e.g.* Guyblast 30/40 at ϕ = 0.1 %, M_w = 1.50 kg m^{-3}: Figure 5-31). Notwithstanding the Reynolds-number effect that is described later, this observation is physically realistic and is supported by physical sample results, which are given in the captions to the figures in Section 5.3.2. To reiterate, these physical samples were taken from the mixing tank and an average over 3 × 60 ml samples was taken for each run, and M_s denotes the sampled concentration.

At the lowest flow rates, M increases very strongly near the lower pipe wall in the majority of cases, suggesting a bed may have been present (as in the run at Q = 0.838 l s^{-1} in Figure 5-26, Honite 16 at ϕ = 3 %, M_w = 72.8 kg m^{-3}). In fact, the runs for which this was found to be the case are at similar flow rates to those in which beds were seen to form, although it should be noted that a more specific method of measuring bed and shear-layer depth, based on the identification of the peak in the echo amplitude, V, is presented in the general methodology (Section 3.7) and is employed in the chapter on bedforms (Chapter 6).

For all particle species at lower values of the nominal volume fraction, ϕ, and weighed concentration, M_w, $M(r)$ is generally lower than M_w at higher flow rates and higher at lower flow rates. These two observations require more explanation,

which follows.

1. *Over-prediction of M at higher flow rates*. This was most severe for Honite 22, although significant for all particle species. For the Guyblast species, the effect appeared to be approximately linear with respect to flow rate, Q (see, for example, Figure 5-27), whereas there seemed to be a threshold for Honite 22 (*e.g.* Figure 5-21: Honite 22, ϕ = 1 %, M_w = 24.7 kg m^{-3}, Q = 3.57 l s^{-1}). It is suggested that this effect is analogous to the apparent extension of fast-moving objects in long-exposure photographs. That is, the transit time of the particles through the emission zone of the probe is similar to or shorter than the pulse length.

   It is important to make clear that this effect, although apparently an artefact of high particle velocities, is distinct from the Doppler effect, since the dominant component of the particle velocity is perpendicular to the axis of the transducer and is expected to be more pronounced for the probe mounted at 90° to the mean flow direction than for the 135° probe.

2. *Under-prediction of M at lower flow rates*. Observed for all species, this effect can be accounted for, at least in part, by actual segregation and bed formation in the test section and settling in the mixing tank, all of which deplete ambient concentration in the upper part of pipe cross-section. However, it is also reasonable to assume that the nonlinearity of ξ_h and K_h at lower concentrations – which is most severe for Honite 16 at 2 MHz (see Figure 5-6 for $\partial G/\partial r$, from the gradient of which ξ_h is calculated, and Figure 5-14 for K_h; in both cases, the nonlinearity is greatest for M_w < 20 kg m^{-3} or so) – contributes to the observed trend and would go some way to explain why it appears to be stronger at lower values of M_w.

The effect of attenuation must also be considered. Even without inspecting the concentration profiles presented in this section, it is to be expected that the larger particle species (*i.e.* Guyblast) would attenuate more strongly than the smaller species (*i.e.* Honite). Indeed, it is clear from the values of ξ_h in Table 5-2: ξ_h is lower

by almost two orders of magnitude for Honite 22 (the species with the smallest diameter) relative to that of Guyblast 30/40 (the largest) at both ultrasonic frequencies.

Results at ϕ = 3 %, M_w = 43.7 kg m^{-3} for Guyblast 40/60 (Figure 5-30) and ϕ = 1 and 3 %, M_w = 14.9 and 43.7 kg m^{-3} for Guyblast 30/40 (Figure 5-33 and Figure 5-34) are very poor and M is under-predicted due to very high attenuation. The fact that this is not observed to the same degree in the Honite profiles, even at much higher concentrations, confirms that the penetration depth (which is proportional to the reciprocal of ξ_h) in the Honite species is much larger than for Guyblast. Alternatively, it should be noted that the range of concentrations over which ξ_h and K_h were calculated for the Guyblast species (*e.g.* in the plot of $\partial G/\partial r$ *vs.* M_w for Guyblast 30/40, the range is roughly $M_w \lesssim 30$ kg m^{-3}: see Figure 5-4) was much narrower than for Honite (*e.g.* the range is $M_w \lesssim 250$ kg m^{-3} or so in the plot of $\partial G/\partial r$ *vs.* M_w for Honite 22: see Figure 5-10; also see text in Sections 5.2.3 and 5.2.5 for more details).

Lastly, the humps observed in some of the Guyblast data (*e.g.* Q = 3.54 l s^{-1} data in Figure 5-28 for Guyblast 40/60 at ϕ = 0.5 %, M_w = 7.46 kg m^{-3}; Q = 3.39 l s^{-1} data in Figure 5-32 for Guyblast 30/40 at ϕ = 0.5 %, M_w = 7.46 kg m^{-3}) at high flow rates at intermediate values of r are not physically realistic and could conceivably be caused by a combination of strong attenuation and the Reynolds-number effect described earlier: at some critical concentration, attenuation in the suspension overcomes backscattering, and if the Reynolds-number effect increases the effective ambient concentration by making the particles appear extended, the observed humps should be considered to be more gentle examples of the peak that is observed at the top of any settled bed or in the shear layer above it (see, for example, the data at Q = 0.855 l s^{-1} for Guyblast 40/60 in Figure 5-28). As with Honite, the observed segregation and settling behaviour is realistic, at least qualitatively.

To conclude, then, the method of using the measured values of ξ_h and K_h in the dual-frequency inversion method was found to be very successful, and the

resulting concentration profiles followed the expected trends. The main limitation appeared to be strong attenuation in suspensions of the Guyblast plastic beads, and this effect meant that concentration profiles in suspensions with $M > 20$ kg m^{-3} or so (see, for example, Figure 5-18) could not be accurately constructed. In particular, the concentration was severely underestimated (*e.g.* Figure 5-34). The limiting concentration in the case of the Honite species, however, was at least $M = 150$ kg m^{-3} (see, for example, Figure 5-12).

It is surprising and disappointing to note that no concentration profile data suitable for comparison could be found in the literature. The data that *are* available are either at too high a concentration (Ekambara *et al.*, 2009; Gillies *et al.*, 2004; Karabelas, 1977; Kaushal and Tomita, 2002), or were gathered in the presence of a bed (Matoušek, 2009; Pugh and Wilson, 1999). The reader is, however, referred to the former papers, which show the same trends as are shown in this study, although no direct comparisons are presented here.

On the other hand, however, the lack of suitable data for comparison demonstrates that the method described in this study has wide potential, and a follow-up study should incorporate runs at similar conditions to some of those in the literature.

6 Bedforms in closed pipe flow

The purpose of this chapter is to describe several interesting aspects of the behaviour of time-dependent bedforms that are produced by the deposition of solid particles from two-phase liquid-solid flows within a closed-pipe flow loop using a novel ultrasonic echo method.

A literature review, supplementary to the general review in Chapter 2, is presented that relates specifically to bedforms (Section 6.1), and the specific experimental techniques used in this chapter are described (Section 6.2). Results are presented for the settled bed and shear layer thicknesses over a range of flow rates (Section 6.3.1). In addition, observations are also presented of path-dependent equilibration and hysteresis, and bi-periodic, possibly cyclical, behaviour in plane beds and ripples (Section 6.3.2). The overall aim, however, is to derive a phase diagram of types of bedforms, including the identification of thresholds between incipient particle motion and various stable and unstable bedform types. To fulfil this aim, the observed bedforms are categorised phenomenologically into five types (Section 6.3.3), and some examples of hysteretic behaviour are presented (Section 6.3.4). The evolution and scaling of bedform heights for three example runs – one for each time-dependent bedform type – and the asymmetry of bedform periods in the same example runs is described (Section 6.3.5). Phase diagrams in terms of the Reynolds number, Re, and the Froude number, Fr, are then presented (Section 6.3.6).

6.1 Literature review: bedforms

Observations of the inception of particle motion on settled beds are described in Section 6.1.1, while the literature relating to bedforms in natural and open channels is briefly reviewed in Section 6.1.2. Theories of the stability of plane beds are described in Section 6.1.3. The focus then moves to bedforms in closed conduits in Section 6.1.4, and in Section 6.1.5 the expected differences between different kinds of conduit are described.

6.1.1 Inception of particle motion and shear flow

There are a variety of definitions of the critical transport velocity in the engineering literature (see, for example, Crowe, 2006; Table 6.2 of Peker and Helvaci, 2007), most commonly defined as either the minimum velocity required for no deposition of solid particles, or the velocity corresponding to minimal pressure loss, and investigations of such critical velocities are described in more detail in Sections 4.2.5 and 4.2.7.

A separate but equally important quantity to know in two-phase liquid-solid flows – and one that has been studied extensively by environmental scientists and civil engineers – is the flow rate necessary to resuspend sediment that has already settled, that is, at the inception of particle motion whereupon particles begin to move, for example by saltation, *i.e.* in "discrete steps" (Graf, 1984). The commonly used Shields diagram, first constructed by Vanoni (1964) with data from the pioneering experiments by Albert F. Shields in the 1930s (the original is not available, but an English translation was written by Ott and van Uchelen, no date), shows the variation in the critical value of a dimensionless shear stress, θ_s, commonly referred to as the Shields parameter and which is the ratio of fluid to gravitational forces on a particle, with either the shear Reynolds number, Re*, or the particle Reynolds number, $\mathrm{Re_p}$, which are defined as follows (García, 2008; van Rijn, 1984a):

$$\theta_s = \frac{\tau_b}{(\rho_s - \rho_w)gd} = \frac{U_\tau^2}{(s-1)gd}, \qquad [6.1]$$

$$\mathrm{Re}^* = \frac{U_\tau d}{\nu}, \qquad [6.2]$$

$$\mathrm{Re}_p = \frac{d[(s-1)gd]^{1/2}}{\nu}, \qquad [6.3]$$

where τ_b is the bed shear stress, U_τ is the (bed) shear velocity, d is the particle diameter and s is the specific gravity of the particle species such that

$$s = \frac{\rho_s}{\rho_w}. \qquad [6.4]$$

From the expressions given above, it is interesting to note the following relationship between $\mathrm{Re_p}$ and Re* (García, 2000):

$$\mathrm{Re}^* = \frac{U_\tau}{[(s-1)gd]^{1/2}} \frac{d[(s-1)gd]^{1/2}}{\nu} = \theta_s^{1/2} \mathrm{Re}_p. \qquad [6.5]$$

A plot of θ_s *vs.* $\mathrm{Re_p}$ (or Re*) shows a broad minimum in the critical value of θ_s corresponding to the inception of particle motion at $\theta_s \approx 0.03$ and $\mathrm{Re_p} \approx 30$. The range of data shown on the plot has been extended by Yalin and Karahan (1979), and it has been adapted by García (2000) to include delineations of other flow regimes, in particular suspension/no suspension and ripples/dunes, forming a simple phase diagram, as shown in Figure 6-1.

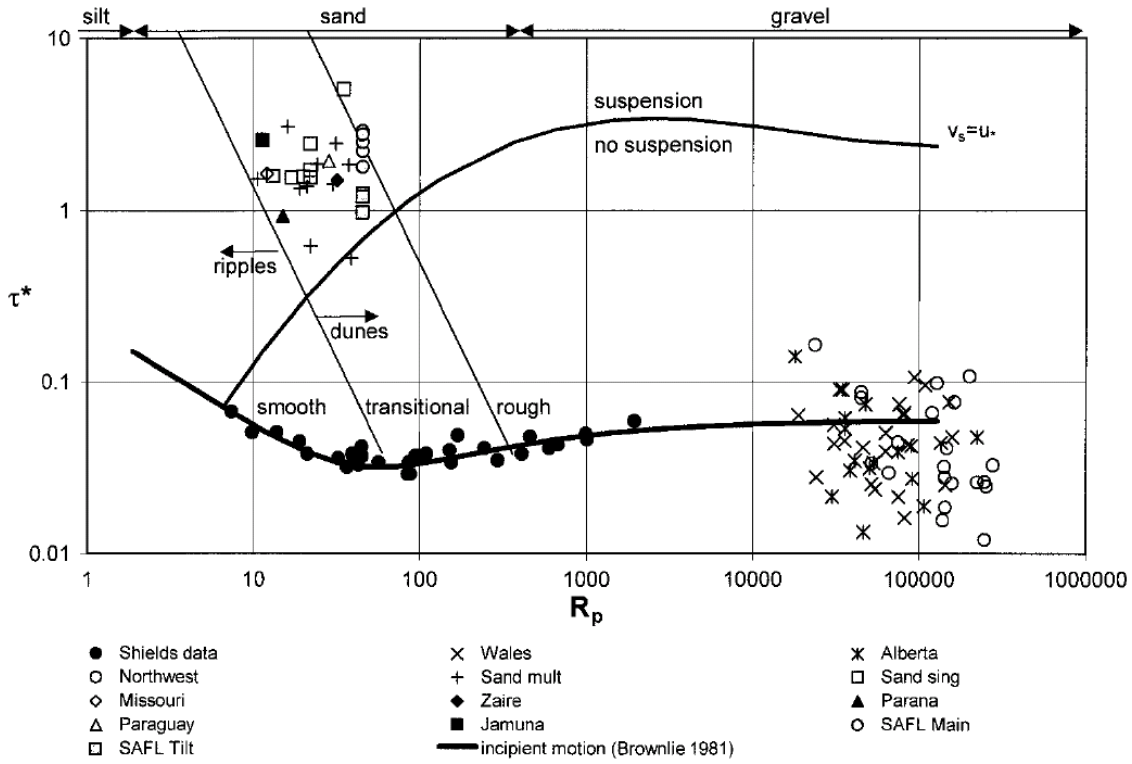

Figure 6-1: Variant of Shields diagram. τ^* (*i.e.* θ_s) is Shields parameter and R_p (*i.e.* Re_p) is particle Reynolds number, as defined in Equation [6.3]. From García (2000).

However, Ouriemi *et al.* (2007) measured a higher value of θ_s for particle motion (θ_s = 0.12) in laminar flow, based on reproducible experiments, while Papista *et al.* (2011) found a very similar value (θ_s = 0.14) in a two-dimensional direct numerical simulation. In fact, the scatter in the available data has been discussed by several researchers (for example, Buffington, 1999). Ouriemi *et al.* suggested a number of methodological differences as an explanation, such as initial bed packing conditions, the definition of shear stress and the difficulties inherent in near-bed measurements. The concept of a saturation timescale may also account for some of the scatter in the available data: Charru *et al.* (2004) found critical Shields numbers of θ_s = 0.04 and 0.12 before and after "armouring", a process by which the bed packing equilibrates.

Sheet flow, on the other hand, is "a granular-fluid flow in which grains are supported by collisions with other grains" and sediment transport proceeds through a combination of saltation and a moving bed (Sumer *et al.*, 1996). Sheet flow differs from pure saltation in terms of momentum transfer, the form of the velocity and concentration profiles and the origin of flow resistance (Gao, 2008). In both environmental and hydraulic-conveying contexts, it is important to know the thickness of the sheet-flow (*i.e.* shear) layer because "the bed load layer serves as an exchange zone between the bed and sediment transported in suspension; the upward flux of sediment at the top of the bed load layer provides the boundary condition for suspended sediment transport calculations" (García, 2008), and sediment flux in this zone may be significant even when the ambient (*i.e.* mean-flow) particle concentration above the shear layer remains low.

The onset of the sheet-flow regime is commonly described by some critical value of θ_s. Above this threshold, which has been constrained to the range $0.4 \leq \theta_s \leq 1$ or so (Gao, 2008) and must – quite obviously – be higher for a given flow than that for the inception of particle motion, dunes and ripples are "washed out" (Wilson, 2005) if any exist, and a plane bed is formed, topped by a shear layer. Gao (2008) has presented visualisations, both schematic and in the form of video images, of the bed-load layer in the vicinity of the shear layer threshold.

Studies in rectangular channels (Pugh and Wilson, 1999; Sumer *et al.*, 1996) have shown that the particle concentration in the shear layer decreases linearly with height, from a maximum at its base that depends on the properties of the particle shape and size distribution, then becoming Rousean across the remainder of the flow depth (Wang and Yu, 2007), as shown in Figure 6-2, with the thickness of the shear layer varying linearly with θ_s (Pugh and Wilson, 1999).

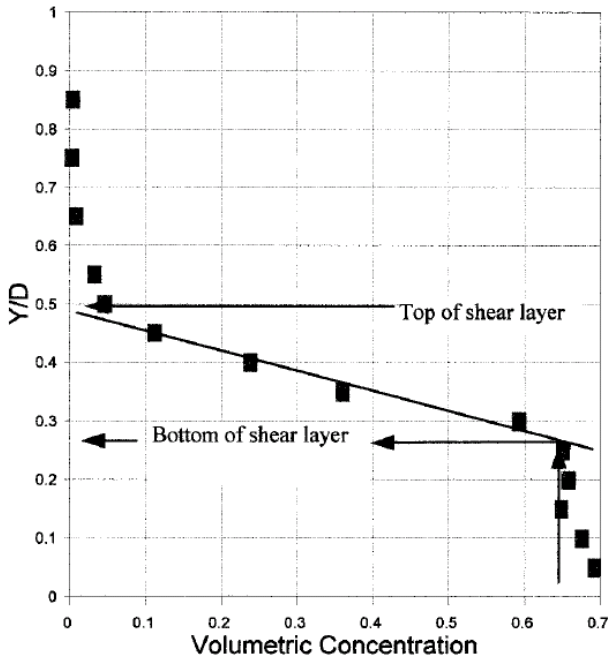

Figure 6-2: Variation of particle concentration with bed height. Y/D (*i.e.* y/D) is distance from pipe bottom relative to pipe diameter. From Pugh and Wilson (1999).

It is important to note that the term "Rousean" is taken to mean varying according to the following expression:

$$\frac{M}{M_a} = \left(\frac{H-y}{y}\frac{a}{H-a}\right)^{\mathrm{Ro}} \qquad [6.6]$$

where M_a is the particle concentration at a reference height a, y is the height above the base (and not wall-normal distance from the upper boundary, as elsewhere in this study) and H is a height at which the concentration is assumed to be zero (*i.e.* the water surface, so that H is the fluid depth); Ro is the Rouse number and is defined as

$$\mathrm{Ro} = w/\kappa U_\tau, \qquad [6.7]$$

where w is the particle settling velocity, κ is the von Kármán constant (κ = 0.41) and U_τ is the shear velocity. For a full derivation of Equation [6.6], see Allen (1997). Some examples of Rousean concentration profiles in an open rectangular channel flow are shown in Figure 6-3 for various values of the Rouse number. It is clear from Figure 6-3 that at high Rouse numbers, the majority of the solid phase is concentrated in the lower part of the channel, whereas at high Rouse numbers, the flow is well approximated as homogeneous.

To the author's knowledge only a small number of equivalent studies in closed pipes exist (for example, Kuru *et al.*, 1995), although several models of analogous slurry flows exist in the engineering literature and have been reviewed thoroughly but succinctly by Ekambara *et al.* (2009).

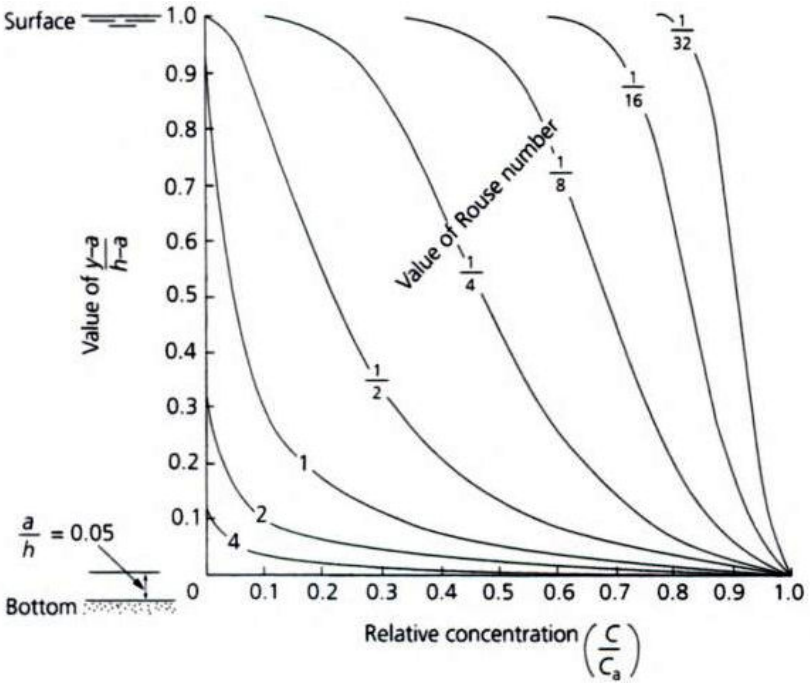

Figure 6-3: Examples of Rousean concentration profiles in an open rectangular channel. C is particle concentration or volume fraction (*i.e.* M or ϕ) and C_a is a reference value at $y = a$. Note y is upwards distance from base, not downwards distance from upper wall as in this study. From Allen (1997).

6.1.2 Bedforms in natural systems and rectangular channels

Bedforms – plane beds, ripples, dunes and other, possibly time-varying, structures formed by settled particulates – are ubiquitous in nature in both sub-aqueous (water-driven) and aeolian (air-driven) environments, and their laboratory analogues have been studied extensively by earth scientists in open and closed rectangular channels. As a result there is a large, mature canon of literature describing their behaviour in natural and laboratory environments (see, for example, the reviews of Best, 2005; Coleman and Nikora, 2011; García, 2008).

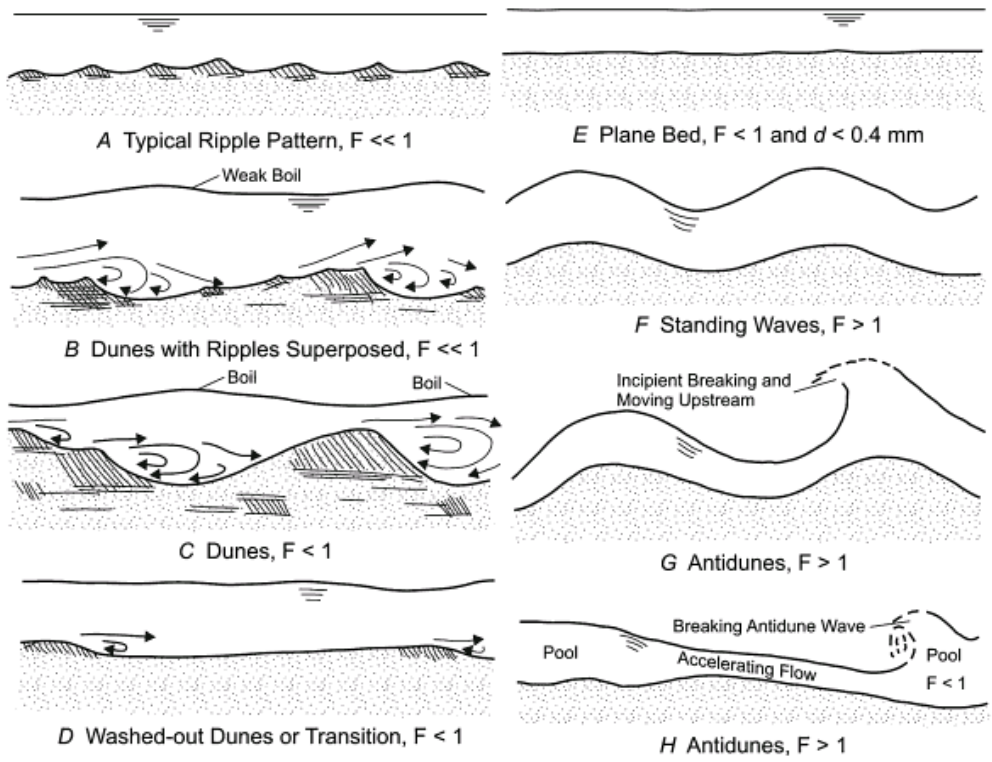

Figure 6-4: Bedforms in open channels with a free water surface. *F* is Froude number (*i.e.* Fr, as defined in Equation [6.17]), and *d* is particle diameter. From García (2008).

Figure 6-4 and Table 6-1 describe common classifications of bedforms in open channels and closed conduits. At low flow rates, ripples and dunes form, provided $d < 0.7$ mm for ripples and $d > 0.1$ mm for dunes (Leeder, 2011, p. 132-137), all configurations of which prograde (*i.e.* progress downstream). At higher flow rates, these bedforms are eroded or "washed out" and form so-called upper plane beds (the name of which is intended to distinguish them from lower plane beds shown on some phase diagrams that are observed over a narrow range of (low) flow rates

and particle sizes). As the Froude number, Fr (Equation [6.17]) approaches unity, the water surface begins to interact with the bed, which forms standing waves. At higher flow rates still, these waves may begin to prograde upstream, in which case they are referred to as anti-dunes; if the water surface breaks the configuration is known as a chute and pool.

Table 6-1: Classification of bedforms in open and closed channels. Adapted from Acaroglu (1968) and Graf (1984).

Flow regime	Bedform type	Mode of particle motion	Mode of sediment transport
Lower regime	Ripples, ripples on dunes, dunes	Discrete steps (saltation)	Bed load
Transition	Washed-out dunes/ripples	Mixed	Bed and suspended load
Upper regime	Plane bed, anti-dunes, chutes and pools (open channels); plane bed, sliding bed (closed conduits)	Continuous	Suspended load (suspension)

Bedforms can very broadly be grouped into three regimes: lower/sub-critical (ripples, ripples on dunes, dunes), transitional (washed-out dunes) and upper or supercritical (plane beds, antidunes, chutes and pools) (Graf, 1984; Simons and Richardson, 1961), as shown in Table 6-1. Barchans, "crescentic" dunes that develop when the sediment supply is limited, are not described in detail here, although a few studies in closed conduits are available (for example, Charru and Franklin, 2012; Franklin and Charru, 2009, 2011).

The transition from planar to periodic bedforms is described in the next section; here it will suffice to review very briefly some properties of ripples and dunes, which are generally identified as different kinds of bedforms of "distinctly separate scales with no gradual transition" (Coleman and Nikora, 2011). García (2008) has reviewed some common ripple and dune scalings in terms of equilibrium height, wavelength and celerity (*i.e.* rate of progradation), and states that dune heights satisfy the following expression:

$$\frac{h_b}{H} \leq \frac{1}{6}, \qquad [6.8]$$

where h_b is the bedform height and H is the fluid depth, whereas Julien and Klaassen (1995) derived the following relationship for dunes based on a compilation of laboratory and field data:

$$\frac{h_b}{H} = 2.5\left(\frac{d_{50}}{H}\right)^{0.3}. \qquad [6.9]$$

Ripples form when the particle size and shear Reynolds number are both small (Raudkivi, 1997) and their equilibrium sizes scale with grain size and are independent of flow depth, whereas those of dunes scale with flow depth. More specifically, van Rijn (1984b) also states that ripple heights are much smaller than, and do not depend strongly on, the flow depth, and ripple lengths are smaller than or comparable to the flow depth; dune lengths, on the other hand, can be much greater than the flow depth, and dune heights depend more strongly on the flow depth, as follows (van Rijn, 1984a):

$$\frac{h_b}{H} = 0.11\left(\frac{h_b}{H}\right)^{0.3}(1 - e^{-0.5T})(25 - T), \qquad [6.10]$$

where T is referred to as the transport stage parameter, which is defined below.

$$T = \frac{(U_\tau')^2 - \left(U_{\tau,cr}\right)^2}{\left(U_{\tau,cr}\right)^2}, \qquad [6.11]$$

where U_τ' and $U_{\tau,cr}$ are the particle bed shear velocity and the critical bed shear velocity (also given in Equation [6.1]), respectively, and are as follows:

$$U_\tau' = \frac{g^{1/2}U_{\text{flow}}}{C'}, \qquad [6.12]$$

$$\frac{\left(U_{\tau,cr}\right)^2}{(s-1)gd_{50}} = \theta_s = \begin{cases} 0.24(d^*)^{-1} & d^* \leq 4 \\ 0.14(d^*)^{-0.64} & 4 < d^* \leq 10 \\ 0.04(d^*)^{-0.10} & 10 < d^* \leq 20 \\ 0.24(d^*)^{0.29} & 20 < d^* \leq 150 \\ 0.055 & d^* > 150 \end{cases} \quad [6.13]$$

where d^* is the particle parameter and C' is the particle Chézy coefficient, which are defined as (García, 2008; van Rijn, 1984a):

$$d^* = d_{50}\left[\frac{(s-1)g}{\nu^2}\right]^{1/3}, \quad [6.14]$$

$$C' = 18\log\left(\frac{4H}{d_{90}}\right), \quad [6.15]$$

where d_{50} and d_{90} are the 50th and 90th percentiles of the particle size distribution, respectively, and s is the specific gravity, as defined in Equation [6.4].

In the sense that they generally incorporate a visualisation of the conditions for incipient motion in addition to other delineations, phase diagrams of bedform types, of which a variety exists, can be seen as extensions of the Shields diagram and similar plots. Such diagrams employ some combination of important suspension parameters, such as flow rate, particle size and density, fluid depth and shear stress, or some dimensionless version of them. García (2008) has reviewed the most commonly used diagrams, such as those of Simons and Richardson (1966) and Ashley (1990), but comments that the diagram of van Rijn (1984b) is "one of the most complete" and "includes both the upper and lower regime". One such plot is presented in Figure 6-5.

García (2008) notes that the purpose of any model of bedform development must, at least, be capable of "determining which equilibrium bed configuration would be established, *i.e.* delineating stability boundaries, as well as being a reliable predictor for bed form dimensions under equilibrium conditions (*i.e.* wavelength and amplitude)." Considering that bed-load transport is a complex phenomenon in which the particle phase behaves like a gas (*i.e.* very dilute, perhaps interacting

infrequently through collisions), liquid (*i.e.* dominated by contact forces) or solid (*i.e.* interacting through contact and friction), depending on the flow regime and a particle's position in it (Frey and Church, 2011), it is not surprising that a unified theory does not yet exist.

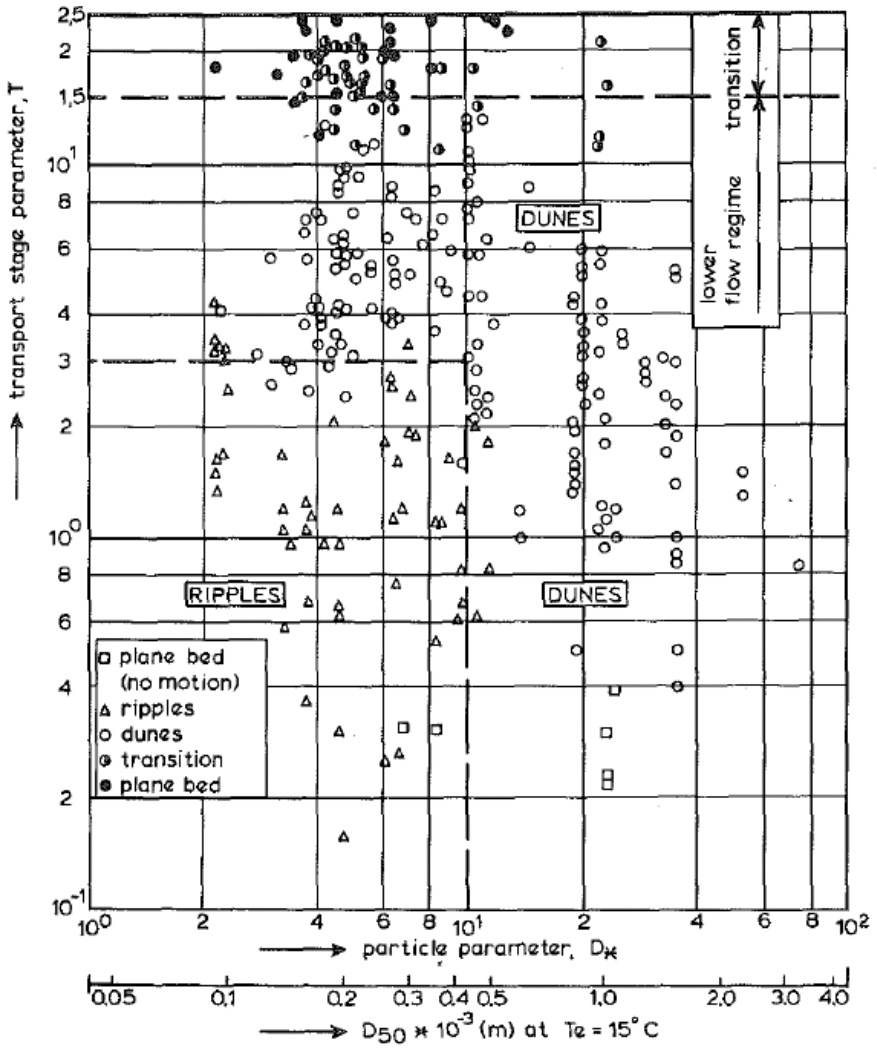

Figure 6-5: Bedform phase diagram, with median particle diameter, d_{50}, and particle parameter, d^*, on x-axis and transport stage parameter, T, on y-axis. From van Rijn (1984b).

6.1.3 Stability of plane beds and evolution of bedforms

The aim of stability analyses as applied to bedforms is to discover whether, and in what manner, an initial (sinusoidal) perturbation applied to a planar bed of particles will be amplified or damped. Several studies that have addressed the

question of how periodic bedforms evolve are described below, although "how and at what rates bed forms change with increasing and decreasing flow remains to be quantified" (García, 2008).

In general, when a bed surface is perturbed, there are two possibilities according to whether the lag between the local sediment transport rate and velocity at the bed, δ, is positive or negative (Engelund and Fredsøe, 1982; García, 2008):

1. The bed is stable ($\delta > 0$): the perturbation is attenuated by changes in the flow and sediment transport rate;
2. The bed is unstable ($\delta < 0$): the perturbation grows, resulting in wave-like bedforms (dunes, ripples, etc.).

In a linear stability analysis of an erodible bed in the presence of a free water surface, Kennedy (1963) incorporated the lag distance, δ, and categorised the resulting bedforms as dunes, plane beds or antidunes depending on the value of $k\delta$ and the flow depth, but the model did not predict ripples. Engelund and Fredsøe (1982) listed five mechanisms that contribute to the stability of a perturbed bed, in decreasing order of importance: fluid friction, the flux of suspended sediment, gravitational forces, inertia of sediment particles and percolation of fluid in the bed.

Richards (1980) extended an earlier model by Engelund (1970) and considered the effects of turbulence more thoroughly, finding two modes of growth corresponding to dunes and ripples respectively – the strength of which were found to depend on the bed roughness and local bed slope – that coalesce into a single mode for $H/z_0 \lesssim 10^2$, where z_0 is the bed roughness length and H is the fluid depth. However, Charru and Mouilleron-Arnould (2002) have commented that these and other models tend to underpredict the wavelength of instabilities when compared to most experimental data. Colombini and Stocchino (2011) have also questioned Richards' identification of a dune mode and ripple mode, but concluded that both ripples and dunes do indeed arise as primary instabilities, rather than dunes forming as a result of "coarsening" of ripples.

The stability problem may be cast alternatively, for example, in terms of the following:

- The forces on the particles: gravity; turbulent diffusion; intergranular forces.
- The timescales over which dynamical process occur: the initial growth rate of "wavelets", the putative precursors of dunes and ripples; percolation and bed consolidation/subsidence timescales; the so-called coarsening time over which the bedform wavelength increases; and equilibration times (of the order of hours, days or weeks), the competition between which has been invoked to account for the scatter in the available data (Charru, 2006; Coleman and Melville, 1996).

As summarised by Ouriemi *et al.* (2009), Sumer and Bakioglu (1984) found an instability occurred at a critical value of the shear Reynolds number, Re* (which they confusingly referred to as the "grain Reynolds number"), as defined in Equation [6.2]. However, Charru and Hinch (2006) delineated stable and unstable plane beds with a critical value of the Galilei number, Ga, which is defined as follows (Ouriemi *et al.*, 2010):

$$\mathrm{Ga} = \frac{d^3(s-1)g}{\nu^2}, \qquad [6.16]$$

where d is the particle diameter, s is the specific gravity of the solid phase and ν is the kinematic viscosity of the fluid. Ga is a measure of the ratio of gravitational to viscous forces, of which gravity tends to be stabilising and viscosity destabilising, and can alternatively be described as "the Reynolds number based on the Stokes settling velocity of the particles" (Ouriemi *et al.*, 2009). However, Charru and Hinch (2006) identified an additional stabilising term ("crest erosion") and found that at small Ga the bed was stable at any shear rate, whereas above a critical value of Ga fluid inertia dominated, and the bed became unstable above a critical Shields number.

García (2008) has stated that the available data on the evolution of bedforms

"seems to suggest that there is self-similarity in the mechanics" of such waves, and notes that a simple and "rather remarkable" relationship between the height and wavelength of the full range of (subcritical) bedforms was found by Flemming (2000). Baas (1994) presented exponential-type expressions for the bedform equilibration times, whereas Coleman *et al.* (2005) combined new and existing data and found equilibration times depended on the Shields parameter in the case of ripples and both the Shields parameter and particle size in the case of dunes. Measurements of changes in bedform dimensions due to changes in flow rate were also presented.

6.1.4 Bedforms in closed conduits

The engineering implications of bedforms in closed conduits are not clear. It is not known, for example, whether time-varying bedforms in pipes increase or decrease the likelihood of blockages. However, it is reasonable to assume that the morphology of bedforms will influence the mean and turbulent velocity fields and particle flux strongly. It is surprising, then, how few studies exist of bedforms in equivalent phase spaces in closed-conduit systems. The author is aware of just 11 such studies, as summarised in Table 6-2, of which four were performed in rectangular channels and the rest in cylindrical pipes. Coleman *et al.* (2003) have described the majority of these studies (with the exception of Acaroglu, 1968; Ouriemi *et al.*, 2009), but state that "data describing bed-form generation and development for closed-conduit flows are limited."

Ouriemi *et al.* (2009) classified time-dependent bedforms observed in pipe flow as either "small", "vortex" or "sinuous dunes", the forms of which are shown in Figure 6-6(a),the latter being observed only in turbulent flow. (However, it is important to note that, in the sedimentology literature, "sinuous" refers to the latitudinal shape of dunes.) They also presented a phase diagram, shown in Figure 6-6(b), of Re *vs.* $\mathrm{Ga}(H/d)^2$, where Ga is the Galilei number, H is the fluid depth (*i.e.* $H = D - h$, where D is the pipe diameter and h is the bed depth) and d is the particle diameter, in which they correctly predicted the thresholds between a stationary and moving bed, and the development of small dunes, according to a linear stability analysis.

Additionally, Ouriemi *et al.* (2009) found that the behaviour of two categories of bedforms ("small" and "vortex") were well separated on a plot of h_b/D *vs.* $U_{ave}t/D$, where h_b is the bedform height (see Section 6.3.3), U_{ave} is the bulk flow rate based on the total pipe cross-section and t is time, as shown in Figure 6-7.

Table 6-2: Studies of bedforms in closed conduits.						
Reference	Type of conduit	Dimensions (mm)	Mean flow velocity ($m\ s^{-1}$) or Re	Particle size (mm)	Particle density ($10^3\ kg\ m^{-3}$)	No. of runs
Ismail (1952) (in Acaroglu, 1968, p. 113)	Rectangular	27 × 7.6	8.93-1.50	0.091, 0.147	2.65	60
Thomas (1964)	Pipe	25.1, 100.4	0.12-0.37	0.05-0.507	1.09, 2.65	~75
Wilson (1965) (in Acaroglu, 1968, p. 113)	Rectangular	9.37 × 9.37	0.69-2.03	0.710	2.65	67
Kriegel and Brauer (1966) (in Acaroglu, 1968, p. 113)	Pipe	53.5	0.72-2.27	1.15-1.90	1.38-1.43	129
Acaroglu (1968)	Pipe	76.2	0.56-6.50	2.00, 2.78	2.67	223
Nakagawa and Tsujimoto (1984)	Rectangular	310 × 75	0.507, 0.676	0.07	Unknown (sand)	2
Takahashi *et al.* (1989)	Pipe	49.7	1.2-1.6	2.18, 3.06	2.74	~40
Kuru *et al.* (1995)	Pipe	31.1	Re = 1,800-12,000	0.1, 0.3	2.4	Not given
Simkhis *et al*. (1999)	Pipe	40	0.3	3	1.24	1
Coleman *et al.* (2003)	Rectangular	300 × 100	0.263-0.703	0.11, 0.87	2.65	12
Ouriemi *et al.* (2009)	Pipe	30	Re = 10^{-1}-10^4	132, 193, 538	2.490, 1.177, 1.070	Not given

(a)

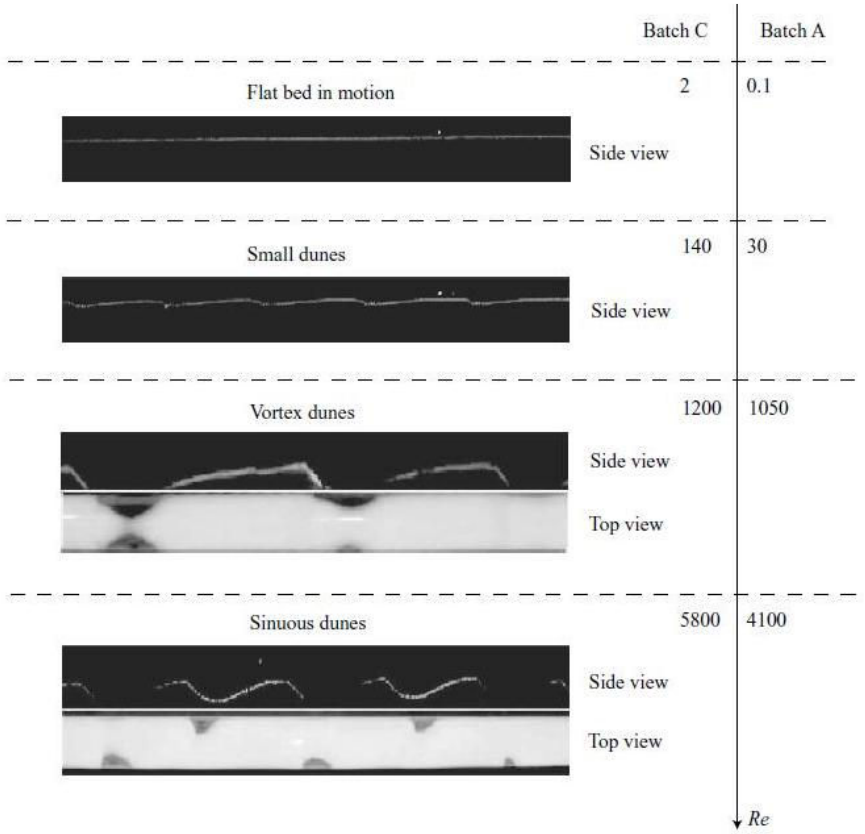

(b)

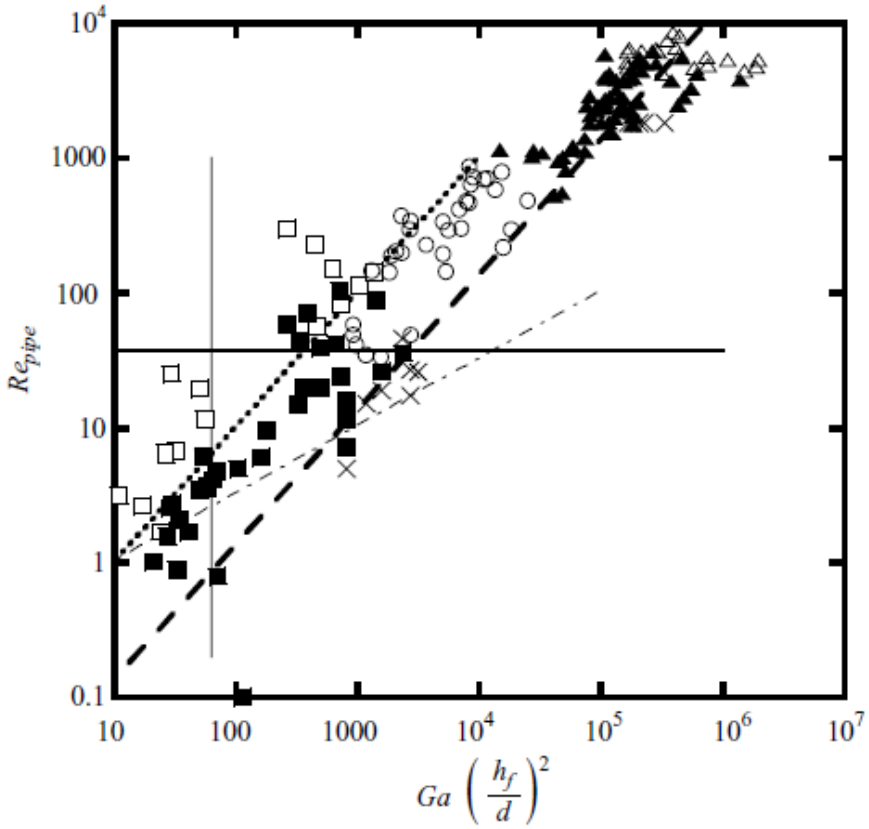

Figure 6-6: (a) Observed bedform types with glass and acrylic beads ("Batch A" and "Batch C", d = 132 and 193 μm), respectively, and (b) bedform phase diagram for pipe flow in terms of Reynolds number, Re_{pipe}, and $Ga(h_f/d)^2$ (*i.e.* $Ga(H/d)^2$ in this study). From Ouriemi *et al.* (2009).

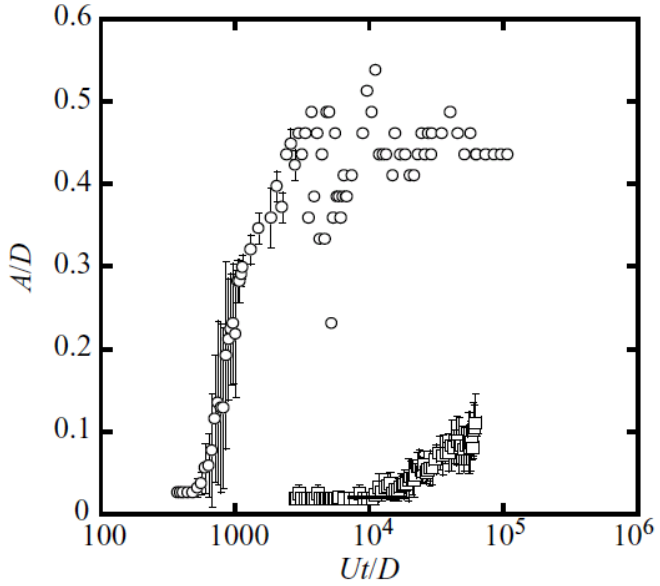

Figure 6-7: Bedform evolution in terms of dimensionless bedform height *vs.* time, A/D (*i.e.* h_b/D) *vs.* Ut/D (*i.e.* $U_{ave}t/D$) for two runs. Circles: "vortex dunes"; squares: "small dunes". From Ouriemi *et al.* (2009), to which the reader is referred for more materials and run information.

6.1.5 Expected and observed differences between types of conduit

There are several differences between open and closed, and cylindrical and rectangular conduits that would be expected to influence the development and equilibrium dimensions of bedforms – and therefore the structure of any phase diagram that describes them – of which a non-exhaustive list follows.

In a conduit with a circular cross-section, the flow structure may be significantly modified by the presence of a thick bed (Adams *et al.*, 2011); secondly, calculations of bulk quantities such as mass flux must take account of the variation in chord length with height, although Kuru *et al.* (1995), for example, in their study of erodible beds in pipes, assumed that "the asymmetric effects of the circular pipe are not significant and the flow is locally two-dimensional" when the shear layer is very thin compared to the pipe diameter.

In any closed conduit, the absence of a free water surface means a no-slip condition exists at all boundaries, and antidunes and chutes/pools, the formation

of which depends on the interaction between the bed and free water surfaces, cannot develop. The Froude number, upon which the delineation of sub- and supercritical flows depends, is defined as follows:

$$\mathrm{Fr} = \frac{U_{\mathrm{flow}}}{(gH)^{1/2}}, \qquad [6.17]$$

where U_{flow} is the mean flow velocity and H is the fluid depth. Although other definitions of the Froude number exist (for example, Gillies *et al.*, 2004), the one above was chosen because it permits comparison of open and closed duct, channel and pipe flows, since U and H can be defined unambiguously in all cases.

These differences aside, Coleman *et al.* (2003) have stated that, although the absence of a free surface causes bedforms to develop more quickly in closed conduits, their equilibrium dimensions appear to be the same as in equivalent open-channels flows: "Bed-form initiation for closed-conduit flows occurs in the same manner as for subcritical open-channel flows, with wavelets on the bed of sediments (solids) instigated by discontinuities in the bed".

6.2 Experimental method

The experimental procedure was to take echo profiles through a vertical cross-section of the horizontal test section of the pipe flow loop. The 4 MHz (mounted at 90 degrees: see Figure 3-2) was used, with a sample rate of approximately 10 Hz. The root-mean square voltage, V, over n samples was then calculated. Suspensions with a range of particle concentrations (ϕ = 0.1 to 3 %) were investigated, with mains water as the carrier fluid and the large plastic particle species (Guyblast 40/60) as the solid phase.

This procedure, including distance calibration, has been described in general terms in the methodology chapter (Section 3.7), to which the reader is referred for more information. However, the method used to generate the results in this section differs from the general case in several simple but important ways: first, the root-

mean-square average was taken of batches of n = 20 samples here (*i.e.* Δt = 1.86s, sample interval = 93 ms), rather than the whole run, so that the time-dependent behaviour of bedforms could be visualised; second, as well as the settled bed thickness, the shear layer thickness was also measured. The concept of a shear layer, and the method by which its thickness was measured, were described in detail in the general methodology (Section 3.7), to which the reader is referred.

6.3 Results and discussion

Results are presented for a variety of time-dependent bedforms and their behaviour under several sets of conditions is described. In Section 6.3.1, plane bed and shear layer thickness measurements are presented for some example runs in order of decreasing flow rate in order to illustrate the method; in Section 6.3.2, the path-dependent behaviour of plane beds is described; in Section 6.3.3, the proposed categories of bedforms are presented, with examples, and some bi-periodic behaviour is shown; in Section 6.3.4, some examples of hysteretic behaviour is shown, in which an initially stable plane bed become unstable when the flow rate is reduced and then becomes planar again when the flow rate is increased; in Section 6.3.5, the evolution and scaling of bedform heights and the asymmetry of adjacent bedforms is investigated for three example runs, each for one of the three time-dependent bedform types; finally, in Section 6.3.6, phase diagrams of bedform types are presented in terms of bed depth, Reynolds number and Froude number.

It is important to note that, whereas in Section 4.1.3 and 4.2.7 (*i.e.* zero-bed depth method and results, respectively, for the determination of the limit deposition velocity, U_{c2}), this contribution from settled ambient sediment was corrected for, the same correction was not applied to the runs in this section in the interests of brevity and for the following reasons: on one hand, the flow rates were often very low, so the contribution to bed depth from settled ambient sediment was very small; on the other hand, the *period* of ripples, which was investigated in depth in the later subsections, would not be affected by the correction anyway.

6.3.1 Thickness of settled, upper plane beds and shear layers

In Figure 3-25, echo amplitude profiles were presented for the whole of three runs. However, in this section the data were generally divided into blocks of n = 20 samples, in order to visualise the time-dependent behaviour of shear layers and moving and settled beds.

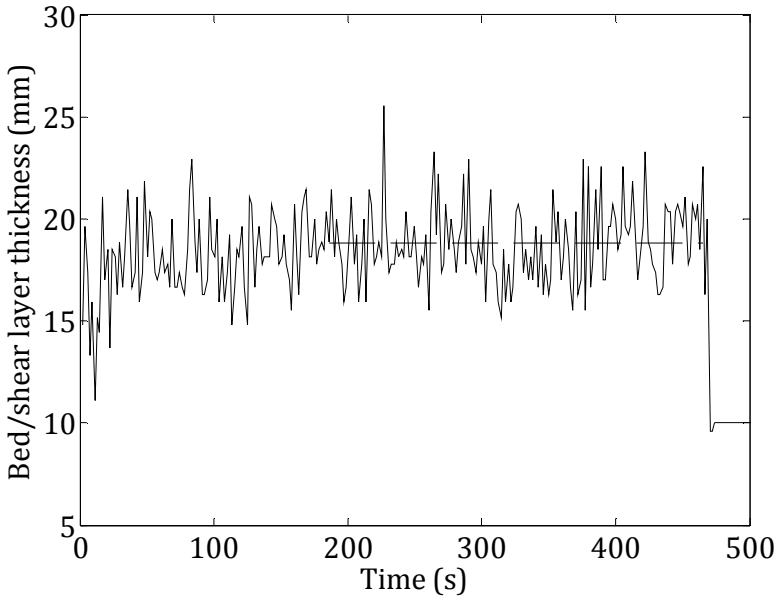

Figure 6-8: Bed/shear layer thickness *vs.* time (Q = 1.07 to 0.856 l s^{-1} at t = 0, ϕ = 3 %) with stop-flow run (to Q = 0 at $t \approx$ 475 s). Horizontal dashed line indicates mean over region shown.

Figure 6-8 to Figure 6-12 show plots of the echo amplitude peak position over time at several flow rates in decreasing order. In Figure 6-8 to Figure 6-10 the suspension equilibrates quickly, whereas in Figure 6-11 and Figure 6-12 the sediment transport rate is such that the suspension takes rather longer to reach equilibrium. For example, in Figure 6-9 the flow rate is reduced from 0.856 to 0.609 l s^{-1} at t = 0 s, and from 0.408 to 0.342 l s^{-1} in Figure 6-11, with the flow equilibrating by $t \approx$ 200 s in Figure 6-9 and by $t \approx$ 350 s in Figure 6-11. At $t \approx$ 470 s in both plots the flow is stopped abruptly and a fully settled, stationary bed forms within seconds. The shear layer thickness is then the difference between the mean distance to the peak during equilibrium flow conditions (in these cases 200 < t < 470 s in Figure 6-9 and 350 < t < 470 s in Figure 6-11), and that to the top of the settled, stationary bed after the flow has been stopped, as described earlier and

shown in Figure 3-25.

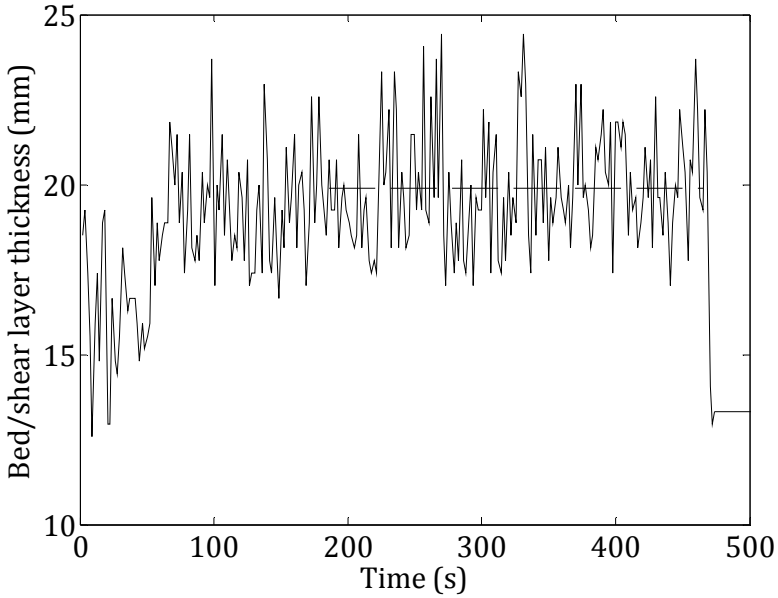

Figure 6-9: Bed/shear layer thickness *vs.* time (Q = 0.856 to 0.609 l s^{-1} at t = 0, ϕ = 3 %) with stop-flow run (to Q = 0 at $t \approx$ 475 s). Horizontal dashed line indicates mean over region shown.

It is interesting to note, then, that the bed thickness overshoots its final equilibrium value in Figure 6-11, a tentative explanation of which is given in Section 6.3.1. Figure 6-12, too, shows interesting behaviour: the bed thickness initially develops ripples of increasing period before being swept over by a thicker plane bed. Such bedforms were investigated in more detail and the results are presented in Sections 6.3.3 to 6.3.6.

Figure 6-13 shows the shear layer and settled, stationary bed thicknesses derived as described above (Figure 6-8 to Figure 6-12) over a range of flow rates. As the flow rate goes to zero, so the stationary bed thickness tends to a maximum value and the shear layer thickness tends to zero, as expected. It is important to note that, once the flow is stopped, any suspended material will settle and contribute to the bed thickness.

The purpose of Figure 6-13 is to validate the method by illustrating several points: firstly, the shear layer thickness increases with flow rate, as expected; secondly, the bed depth decreases with flow rate, as expected, and as was exploited in

Sections 4.1.3 and 4.2.7 in order to measure the critical flow velocity, U_{c2}, corresponding to zero-bed depth, *i.e.* the limit deposition velocity.

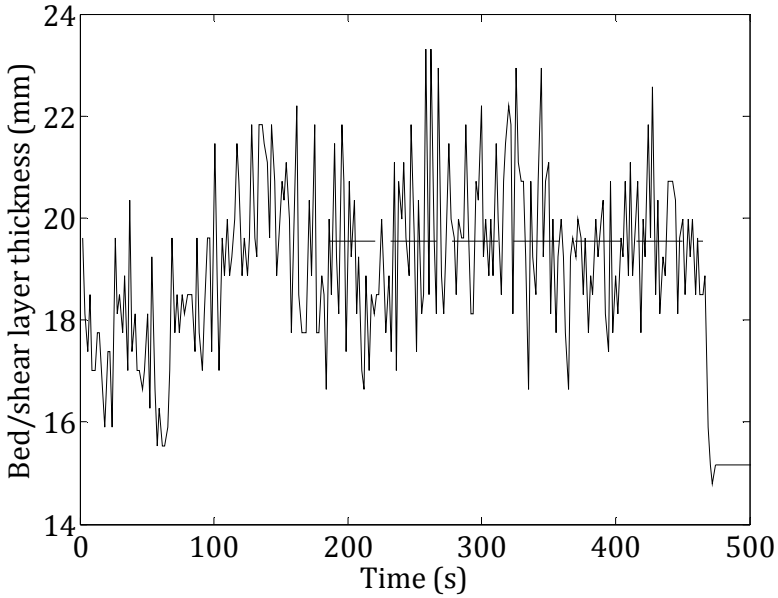

Figure 6-10: Bed/shear layer thickness *vs.* time (Q = 0.609 to 0.509 l s^{-1} at t = 0, ϕ = 3 %) with stop-flow run (to Q = 0 at $t \approx$ 475 s). Horizontal dashed line indicates mean over region shown.

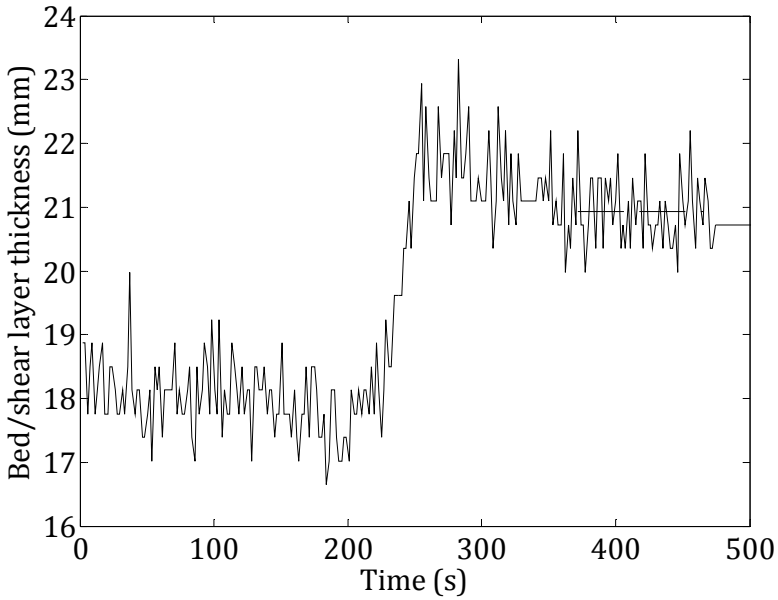

Figure 6-11: Bed/shear layer thickness *vs.* time (Q = 0.408 to 0.342 l s^{-1} at t = 0, ϕ = 3 %) with stop-flow run (to Q = 0 at $t \approx$ 475 s). Horizontal dashed line indicates mean over region shown.

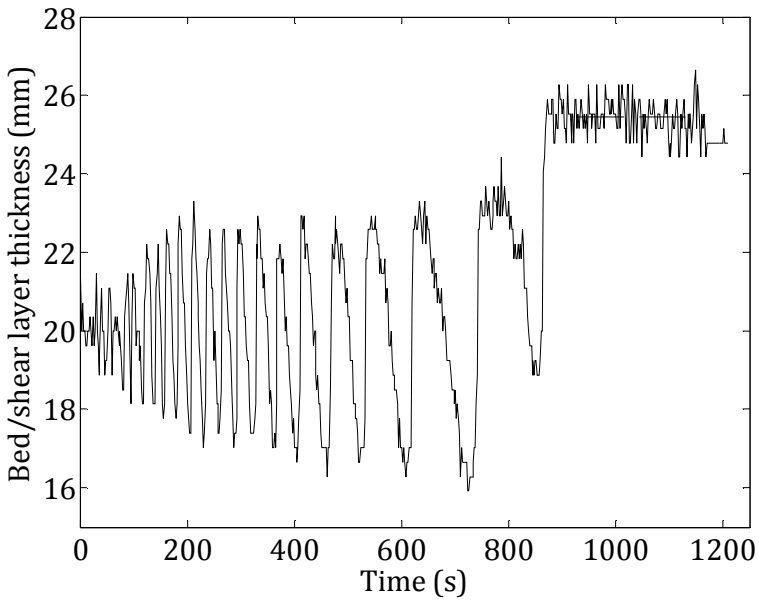

Figure 6-12: Bed/shear layer thickness *vs.* time (Q = 0.342 to 0.277 l s^{-1} at t = 0, ϕ = 3 %) with stop-flow run (to Q = 0 at $t \approx$ 1,150 s). Horizontal dashed line indicates mean over region shown.

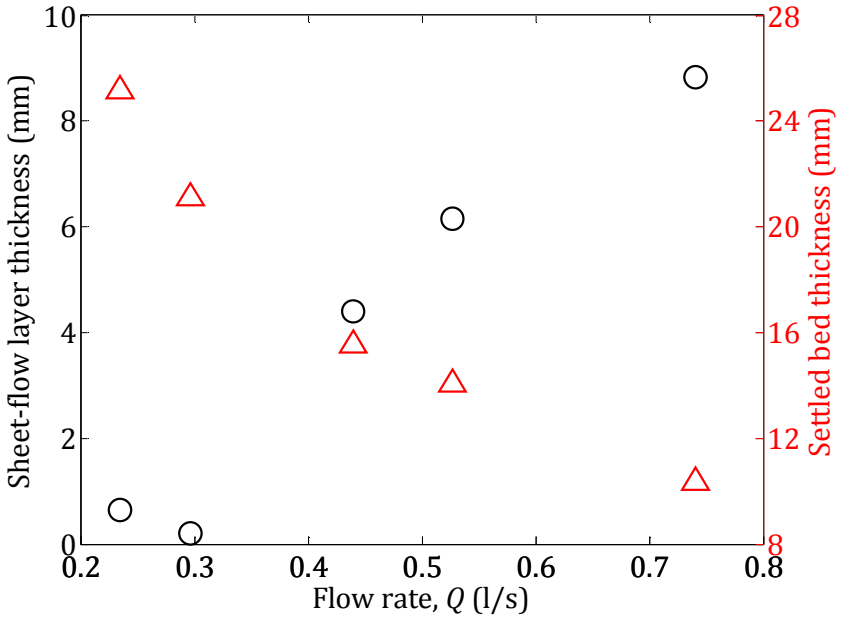

Figure 6-13: Shear layer and settled bed thickness *vs.* flow rate (ϕ = 3 %). Black circles (left axis): shear layer thickness; red triangles (right axis): settled bed thickness.

6.3.2 Path-dependent behaviour of upper plane beds

As demonstrated in Section 6.3.1, at low flow rates the position of the echo amplitude peak corresponds, to within a few millimetres, to the top of the

stationary bed; it is also clear that the equilibration (or lag) time, t_{eq}, of the bedforms is finite and potentially very large in some cases. Moreover, t_{eq} depends on the path taken to reach a particular flow regime. For the sake of clarity, hereafter the symbols Q_i, Q_f and ΔQ are used for the initial and final flow rates and the change in flow rate, respectively. The flow rate was varied from Q_i to Q_f at $t = 0$ in all cases.

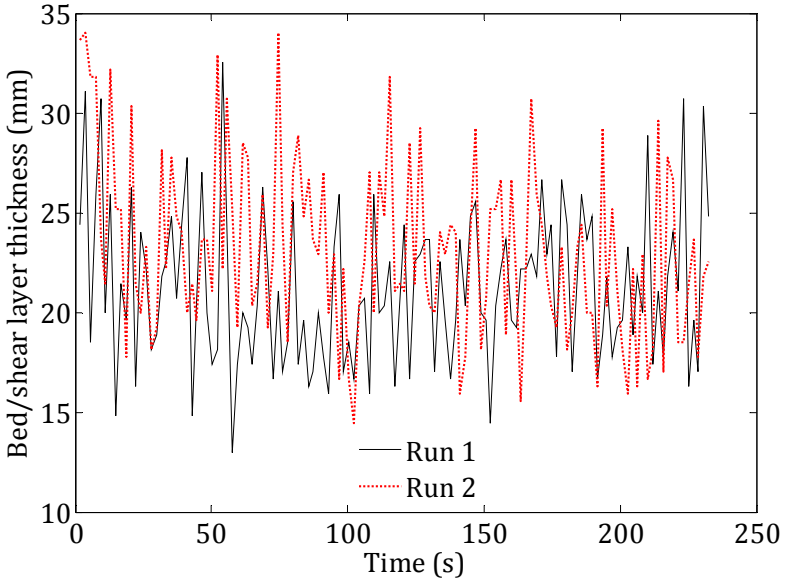

Figure 6-14: Bed/shear layer thickness *vs.* time, showing path-dependent equilibration time (run 1: Q = 1.51 to 1.29 l s^{-1} at $t = 0$, run 2: Q = 2.66 to 1.29 l s^{-1} at $t = 0$, ϕ = 3 %).

The plots in Figure 6-14 (Q_f = 1.29 l s^{-1}) to Figure 6-20 (Q_f = 0.342 l s^{-1}) show, in order of decreasing Q_f, comparisons of the evolution of the echo amplitude peak over a range of flow rates along two paths: *via* an incremental decrease in flow rate (*i.e.* ΔQ is negative and small), and an abrupt decrease from a much higher flow rate at which the particles are fully suspended (*i.e.* ΔQ is negative and large). In each case a bed forms, but while the equilibration times are small (t_{eq} < 100 or so) and indistinguishable between the two cases in Figure 6-14 to Figure 6-16, t_{eq} becomes more significant from Figure 6-17 onwards and differs markedly between the two cases in Figure 6-18 onwards (for example, $t_{eq} \approx$ 150 and 250 s in Figure 6-19). It is also interesting to note that ripples form on the initially planar bed during equilibration in Figure 6-20.

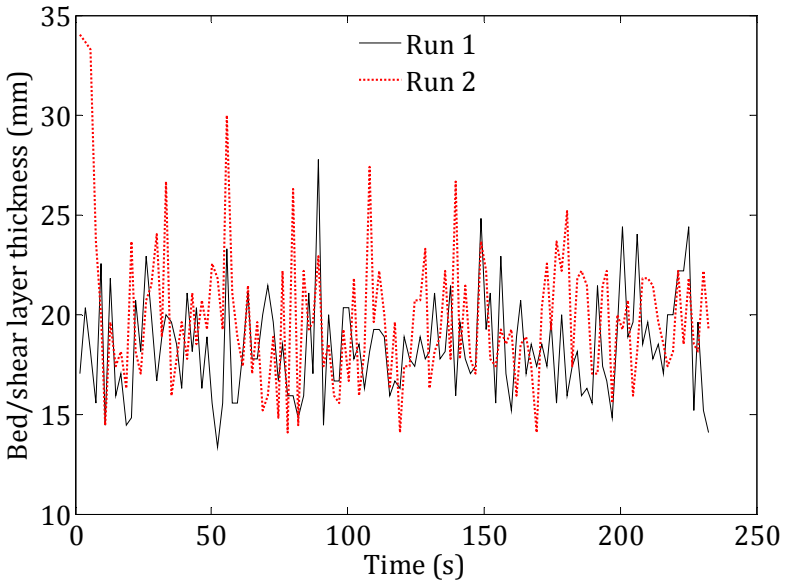

Figure 6-15: Bed/shear layer thickness *vs.* time, showing path-dependent equilibration time (run 1: Q = 1.28 to 1.07 l s^{-1} at t = 0, run 2: Q = 2.66 to 1.07 l s^{-1} at t = 0, ϕ = 3 %).

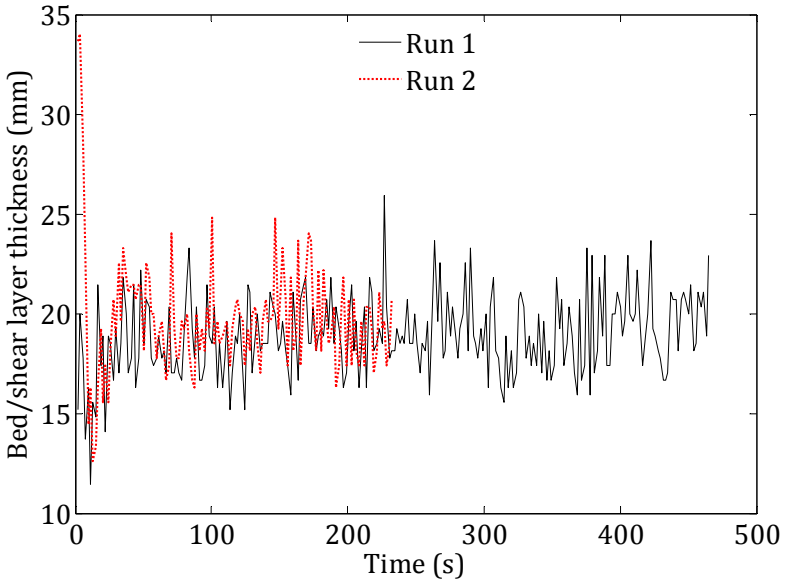

Figure 6-16: Bed/shear layer thickness *vs.* time, showing path-dependent equilibration time (run 1: Q = 1.07 to 0.856 l s^{-1} at t = 0, run 2: Q = 2.66 to 0.856 l s^{-1} at t = 0, ϕ = 3 %).

A simple explanation of the observed path-dependent equilibration follows. When the flow rate is reduced, a certain proportion of the suspended sediment settles onto the top of the bed, thus increasing the bed depth, at a rate that depends on several parameters (for example, the particle settling velocity). However, if the erosion rate at the bed surface (which itself depends on the fluid velocity field at the bed surface and the suspended sediment concentration) is lower than the

sedimentation rate, then the bed depth will overshoot its eventual equilibrium value as the erosion and deposition processes compete. The dashed-line (red) plot in Figure 6-19 clearly shows such an overshoot, whereas the solid-line (black) plot in the same figure shows the simpler case where no significant erosion takes place.

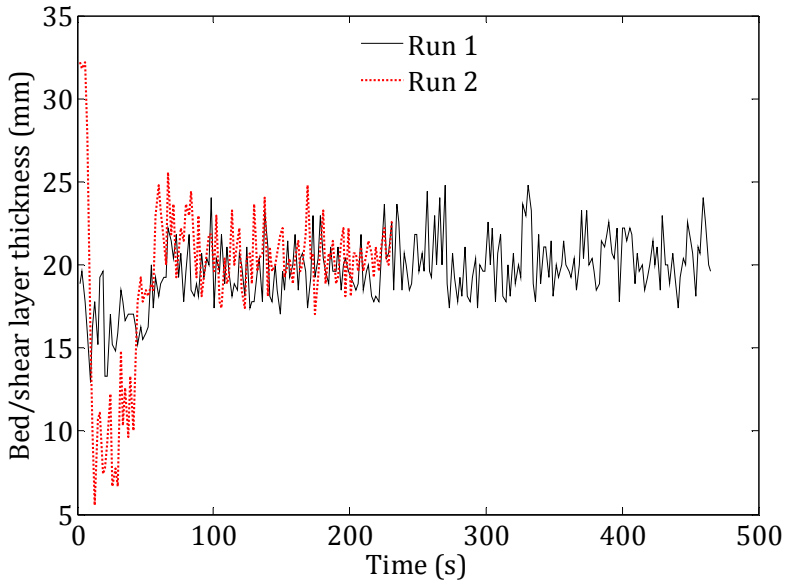

Figure 6-17: Bed/shear layer thickness *vs.* time, showing path-dependent equilibration time (run 1: Q = 0.856 to 0.609 l s^{-1} at t = 0, run 2: Q = 2.66 to 0.609 l s^{-1} at t = 0, ϕ = 3 %).

In general, the higher the suspended sediment concentration and the larger the value of $|\Delta Q|$, the more likely the bed depth is to overshoot its final, equilibrium value. As was the case in the runs described in Section 6.3.1, the thickness of the shear layer and the degree of consequent scatter in the echo amplitude data over time vary with flow rate. Since bed load transport (*i.e.* by moving bed and shear layer) is the dominant transport mechanism at low flow rates when the suspended sediment concentration is very low, it is not surprising that equilibration – whatever the final bed configuration – takes place more slowly at low flow rates because the shear layer is thinnest in that case. The process of equilibration is nothing more than a rearrangement of the distribution of the particulate phase to a change in applied fluid force, and the transport mechanisms by which this rearrangement is effected are bed load and suspended load.

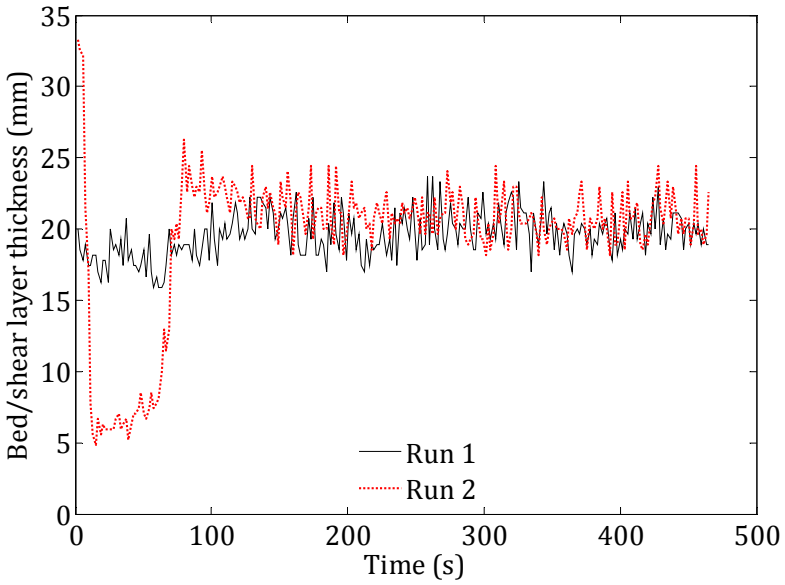

Figure 6-18: Bed/shear layer thickness *vs.* time, showing path-dependent equilibration time (run 1: Q = 0.609 to 0.509 l s^{-1} at t = 0, run 2: Q = 2.66 to 0.509 l s^{-1} at t = 0, ϕ = 3 %).

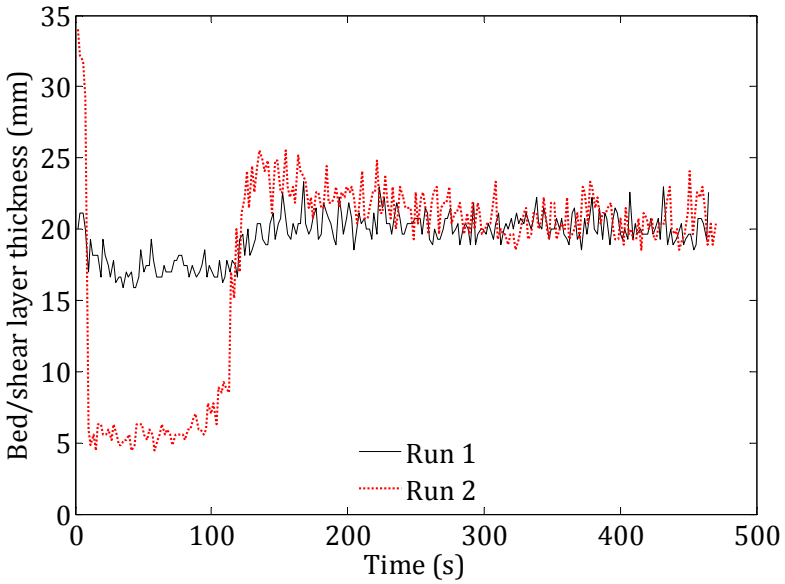

Figure 6-19: Bed/shear layer thickness *vs.* time, showing path-dependent equilibration time (run 1: Q = 0.509 to 0.408 l s^{-1} at t = 0, run 2: Q = 2.66 to 0.408 l s^{-1} at t = 0, ϕ = 3 %).

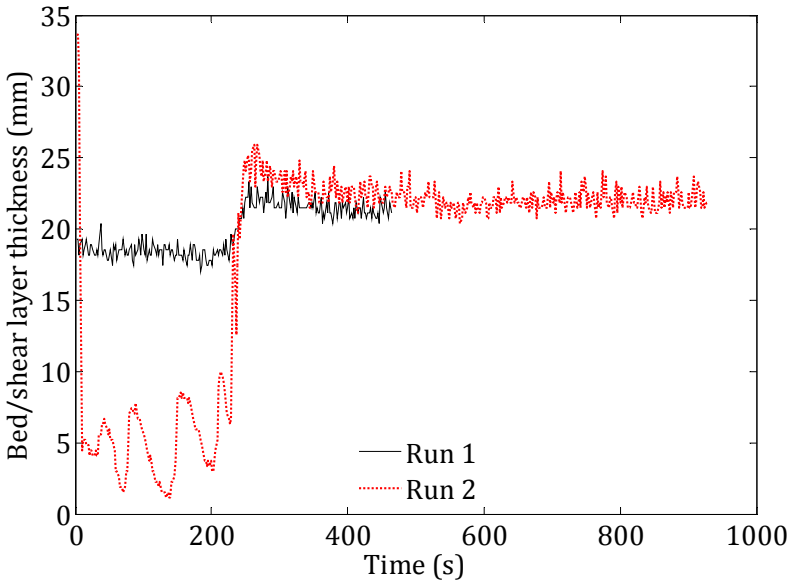

Figure 6-20: Bed/shear layer thickness *vs.* time, showing path-dependent equilibration time (run 1: Q = 0.408 to 0.342 l s^{-1} at t = 0, run 2: Q = 2.66 to 0.342 l s^{-1} at t = 0, ϕ = 3 %).

6.3.3 Categorisation of observed bedforms

In this section, the observed bedforms are categorised into five types, but to begin, several definitions are reiterated or introduced: h, H and D are the bed depth, fluid depth and inner pipe diameter, respectively, as shown in Figure 6-21 and previously presented in Section 3.7.

Geometrically speaking, in a cross-section of the pipe the settled bed is a chord of length, c, where

$$c = D \sin\frac{\theta}{2} \qquad [6.18]$$

and the flow area, A_{flow}, is given by:

$$A_{\text{flow}} = \frac{R^2}{2}(\theta - \sin\theta), \qquad [6.19]$$

where θ, the angle subtended by the bed at the centre of the pipe, is

$$\theta = 2\cos^{-1}[(R - h)/R], \qquad [6.20]$$

and R is the pipe radius (42.6 mm), as shown in Figure 6-21.

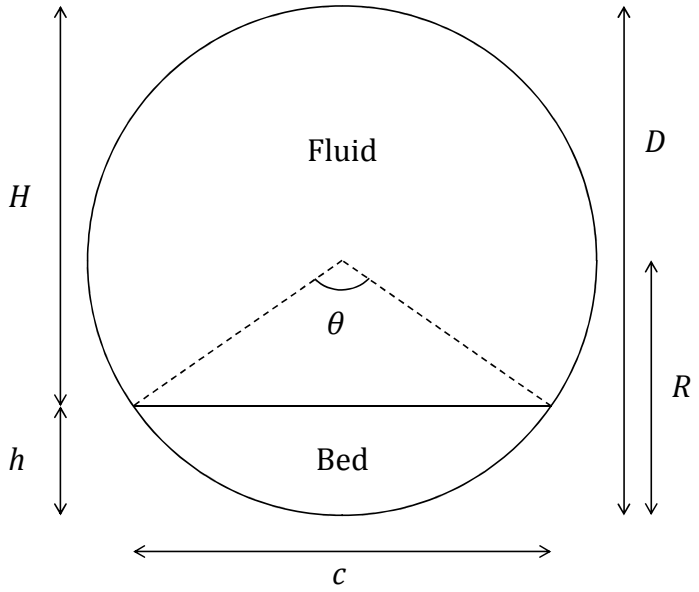

Figure 6-21: Bed geometry and definitions. H and h are fluid and bed depths, respectively; R and D are pipe radius and diameter; θ is angle subtended by bed at pipe centre; and c is chord length (*i.e.* bed width at top of bed). Also shown in Figure 3-24 in general methodology (Section 3.7).

Whereas plane (*i.e.* flat, stable) beds developed in most of the runs described in Sections 6.3.1 and 6.3.2 (with the exception of Figure 6-12 and Figure 6-20, for example), at lower flow rates the top of the bed becomes unstable, and the depth and period of the resulting ripples may vary over time. Since the position of the peak in the echo amplitude profile corresponds to the top of the stationary bed at such low flow rates, and the distance to the opposite pipe wall is known, it becomes straightforward to visualise the bed thickness evolution. For time-dependent bedforms, the total bed depth can then be divided into two components such that

$$h = h_b + h_s, \qquad [6.21]$$

where h_b is the bedform height and h_s is the depth of the settled part of the bed, as illustrated in Figure 6-22.

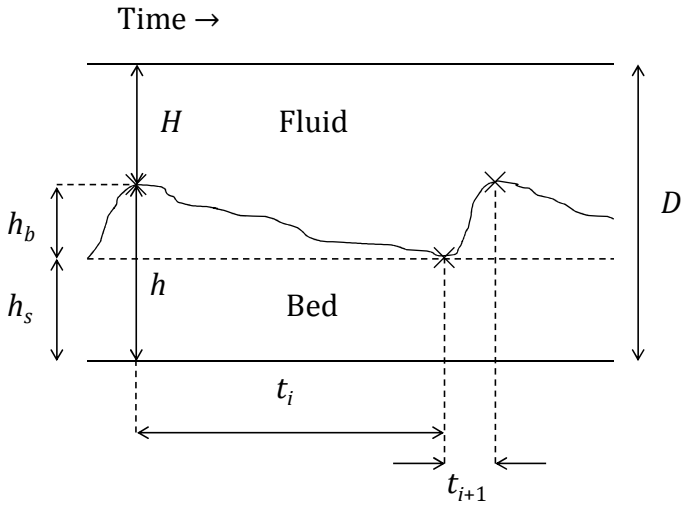

Figure 6-22: Bedform geometry and evolution. H and h are fluid and bed depths, respectively, with $h = h_b + h_s$, where h_b and h_s are the bedform height and settled bed depth, respectively; R and D are pipe radius and diameter; t_i is period between adjacent peak and trough.

Three examples of ripple fields that form from initially planar beds are shown in Figure 6-23, Figure 6-24 and Figure 6-25. In Figure 6-23 (Q = 0.498 to 0.403 l s^{-1} at t = 0, ϕ = 0.1 %) the ripple period remains quite regular, while in Figure 6-24 (Q = 0.483 to 0.323 l s^{-1} at t = 0, ϕ = 0.5 %) the ripple period increases with time.

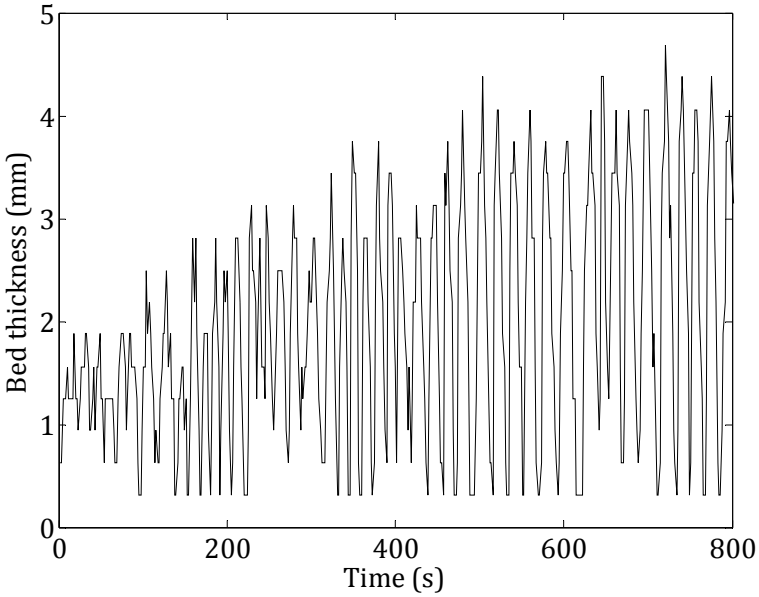

Figure 6-23: Bed thickness *vs.* time: shallow, regular ripples (Q = 0.498 to 0.403 l s^{-1} at t = 0, ϕ = 0.1 %).

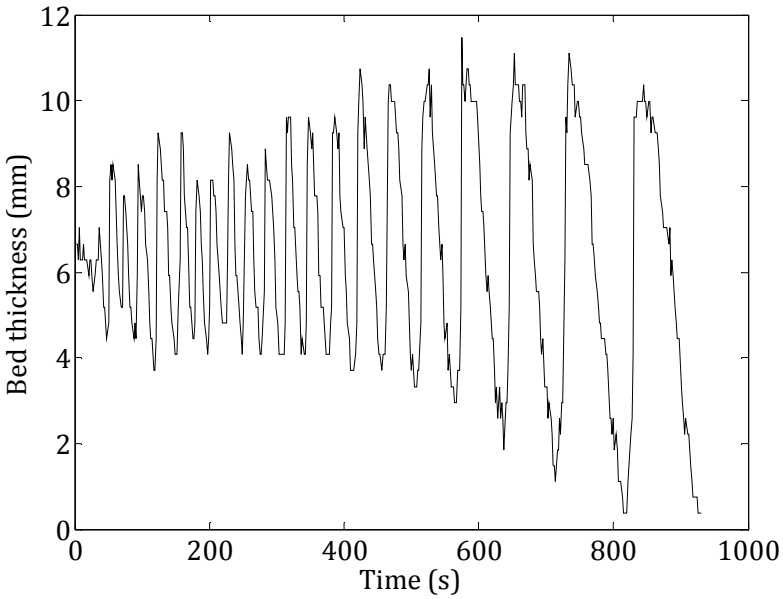

Figure 6-24: Bed thickness *vs.* time: ripples of increasing period (Q = 0.483 to 0.323 l s^{-1} at t = 0, ϕ = 0.5 %).

The bed thickness in Figure 6-25 (Q = 0.383 to 0.287 l s^{-1} at t = 0, ϕ = 1 %), however, exhibits even more complex behaviour, varying strongly and unpredictably, and the ripple field is not at equilibrium at the end of the run (more than 30 minutes). The bed thickness exhibits cyclical, bi-periodic behaviour that suggests two competing instabilities are present. Figure 6-26 shows a histogram of the frequencies of the ripples (*i.e.* the reciprocal of the periods between the peaks) shown in Figure 6-25. It appears there may be two clusters of frequency (around 0.02 and 0.05 Hz) implying bi-periodicity. However, there is a significant amount of scatter and more data are required to determine whether these observations represent universal dynamical processes or are artefacts of the flow loop configuration (such as transient deposits which, although not known to occur, may have developed in opaque sections of the pipework).

For the purpose of consolidation and summary, a list of observed bedform types is given in Table 6-3, categorised broadly and phenomenologically and in order of decreasing flow rate.

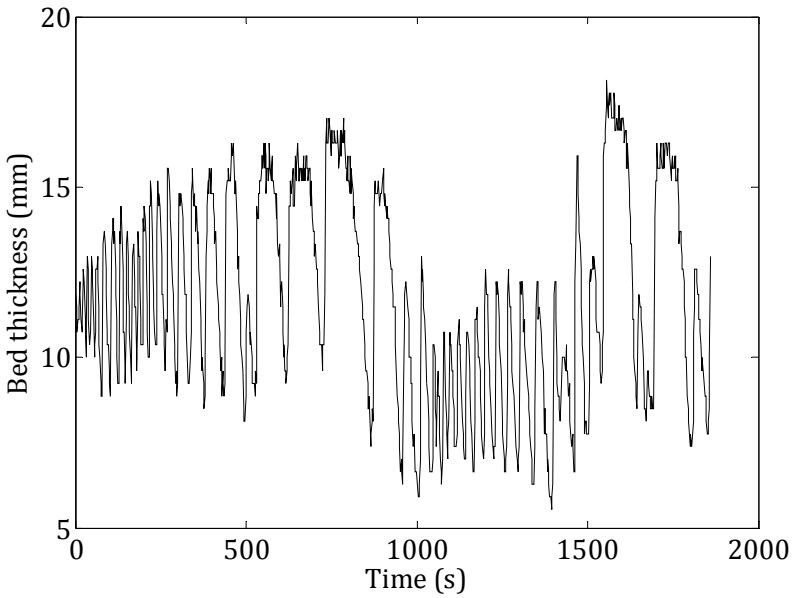

Figure 6-25: Bed thickness *vs.* time: unstable/chaotic ripples (Q = 0.383 to 0.287 l s^{-1} at t = 0, ϕ = 1 %).

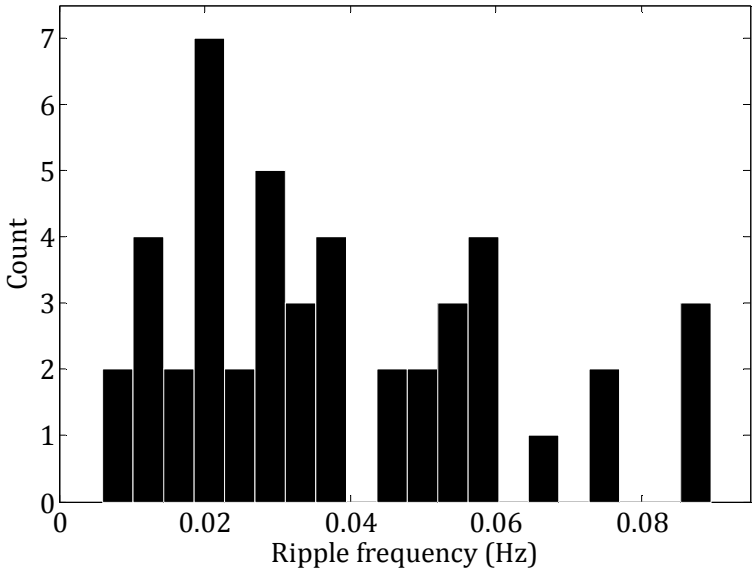

Figure 6-26: Histogram of ripple frequencies from Figure 6-25 (Q = 0.383 to 0.287 l s^{-1} at t = 0, ϕ = 1 %).

It is important to note that ripples of increasing period may, in fact, be of the same kind as unstable/chaotic ripples. There are similarities between them, but further investigation would be required to be able to draw a definite conclusion. For example, it is not clear why the ripple bed is over-swept by a plane bed in some cases, as in Figure 6-12, but continues to be unstable and does not equilibrate in others, as in Figure 6-25.

Table 6-3: Categories of bed/bedform identified in this study.	
Bed/bedform type	Description
1 Upper plane bed	Planar (*i.e.* flat) bed: depth does not vary over time, once equilibrated. Transitional between time-varying bedforms and heterogeneous suspension. Examples: Figure 6-8 to Figure 6-11, and Figure 6-14 to Figure 6-20.
2 Bedforms of regular period	Ripples of time-independent period: period of ripples remains constant; depth may increase with time. Example: Figure 6-23.
3 Bedforms of increasing period	Ripples of time-dependent period: period increases with time; depth may also increase with time. Example: Figure 6-24.
4 Bedforms with unstable/chaotic period	Ripples of complex time-dependent periodicity, suggesting two competing instabilities. Example: Figure 6-25 (plot) and Figure 6-26 (histogram).
5 Bed with no particle motion	No particle motion occurs on surface of bed; determined visually. (Plots of such runs show a flat line, so no example is provided.)

6.3.4 Hysteresis and ripple wash-out

As well as path-dependent behaviour, as shown in Section 6.3.2, hysteresis was also observed, of which Figure 6-27 (Q = 0.483 to 0.323 to 0.483 l s^{-1} at t = 0, $|\Delta Q|$ = 0.160 l s^{-1}, ϕ = 0.5 %) and Figure 6-28 (Q = 0.342 to 0.277 to 0.342 l s^{-1} at t = 0, $|\Delta Q|$ = 0.065 l s^{-1}, ϕ = 3 %) are two examples.

Upon reduction of the flow rate (first frame of each figure), the initially planar beds develop an instability in the form of ripples of increasing period; upon increase of the flow rate (second frame), the ripples are washed out and the bed tends towards a planar configuration: in Figure 6-28 this occurs monotonically, whereas in Figure 6-27 periodicity remains on the bed surface. This periodicity is transient and is likely to represent simple erosion of existing ripples, rather than an example of overshoot – as seen in Section 6.3.2 – *i.e.* the result of a competition between erosion and sedimentation: the net sedimentation rate decreases (which tends to be destabilising) and the erosion rate increases (stabilising) when $\Delta Q > 0$.

It should be noted that the runs shown in Figure 6-27 were performed concurrently, but those in Figure 6-28 were not, although such hysteretic behaviour was found to be very reproducible at all flow rates. The data are noisier in the second frames of Figure 6-27 and Figure 6-28 than the first because the shear layer – the region in which both turbulent motions and intergranular contact are significant – is thicker.

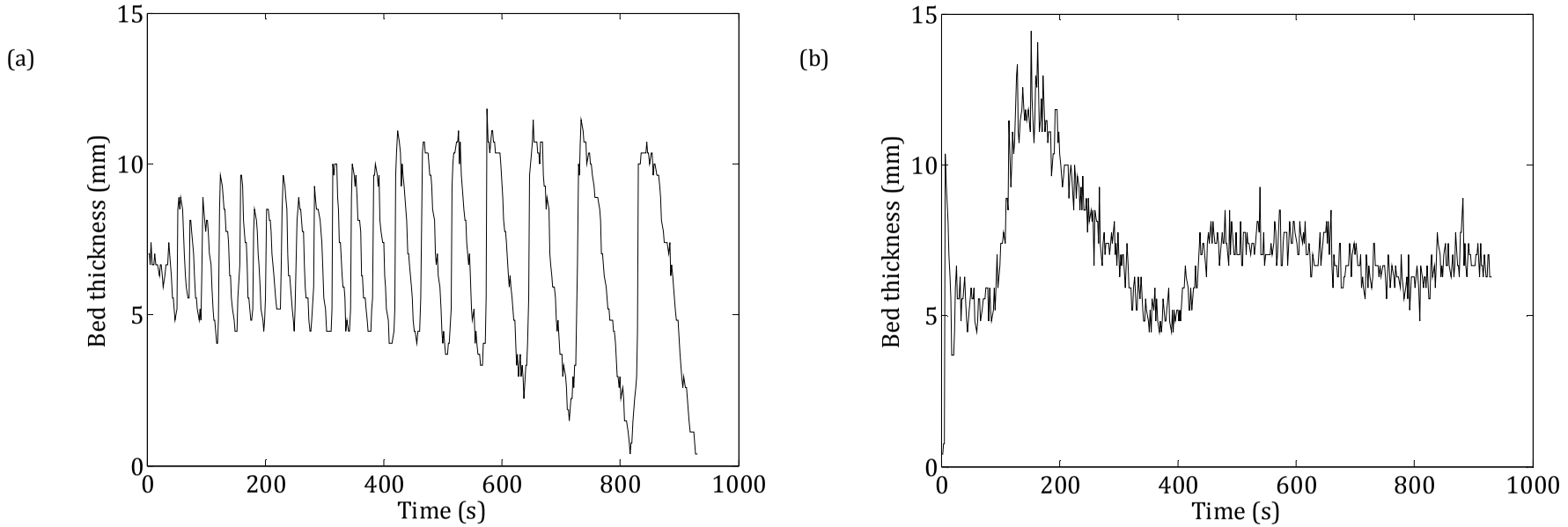

Figure 6-27: Bed thickness *vs.* time, showing hysteresis behaviour, (a) Q = 0.483 to 0.323 l s^{-1} at t = 0, (b) Q = 0.323 to 0.483 l s^{-1} at t = 0 ($|\Delta Q|$ = 0.160 l s^{-1}, ϕ = 0.5 %). Runs were performed concurrently.

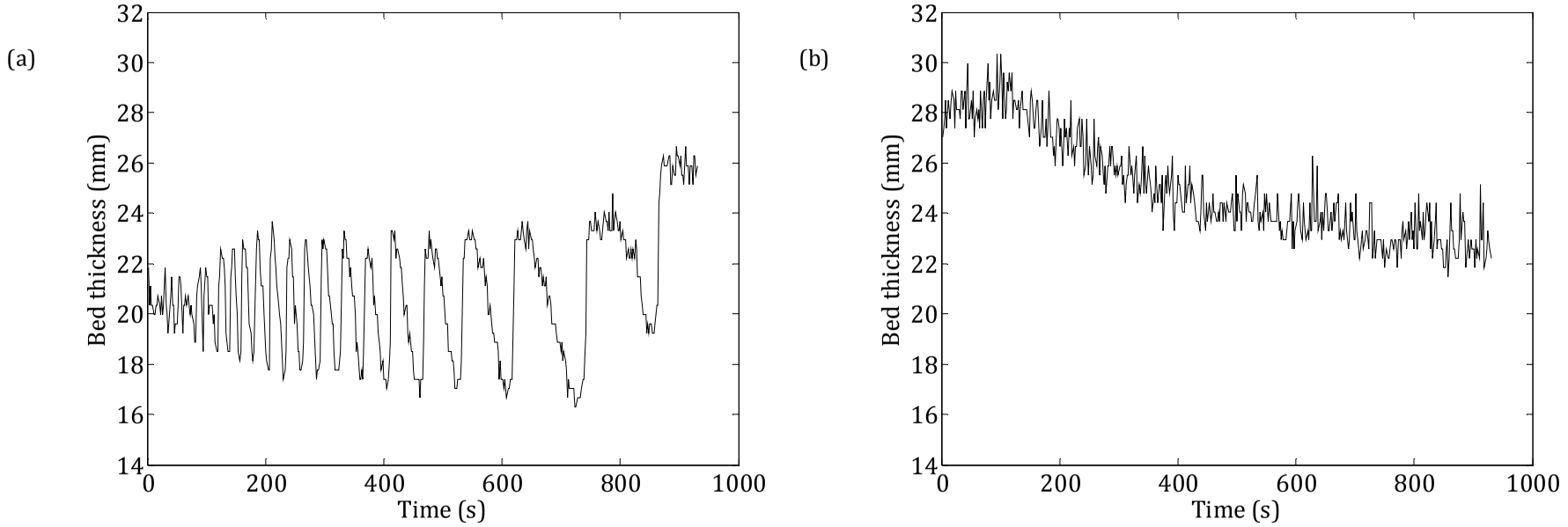

Figure 6-28: Bed thickness *vs.* time, showing hysteresis behaviour, (a) Q = 0.342 to 0.277 l s^{-1} at t = 0, (b) Q = 0.277 to 0.342 l s^{-1} at t = 0 ($|\Delta Q|$ = 0.065 l s^{-1}, ϕ = 3 %). Runs were *not* performed concurrently.

6.3.5 Evolution and scaling of height and axial symmetry of time-dependent bedforms

In this section, the evolution of the height and axial symmetry of the three types of time-dependent bedforms identified in Section 6.3.3 (*i.e.* regular, increasing and unstable) is investigated, with reference to a range of scalings from the literature that was described in Sections 6.1.2 and 6.1.4. The three example runs are the same as those used in Section 6.3.3, the details of which are summarised in Table 6-4, and were chosen as being representative of their bedform type.

Table 6-4: Summary of example runs investigated in this section.

Type	Flow rate, Q (l s^{-1})	Conc., ϕ	See for h_b scaling, f_b evolution
Regular	0.498 to 0.402	0.1	Figure 6-32, Figure 6-36
Increasing	0.483 to 0.323	0.5	Figure 6-33, Figure 6-37
Unstable/chaotic	0.383 to 0.287	1	Figure 6-34, Figure 6-38

The structure of this section is as follows. First, the smoothing and peak-finding algorithm for identifying local minima and maxima in the bed depth with respect to time is described. Then, the algorithm is applied to each of the three example runs in order to (a) demonstrate its efficiency, and (b) illustrate some properties of the data in detail. Next, the evolution of the height, h_b, of individual bedforms in each bedform field is quantified and compared to several expressions available in the sedimentology and engineering literature for predicting the scaling of h_b relative to the fluid depth, H, and pipe diameter, D. Lastly, the symmetry (or rather, lack of symmetry) of the bedform fields is investigated through the bedform asymmetry factor, f_b, which is the ratio of adjacent bedform periods and is presented as a proxy for the ratio of adjacent bedform wavelengths.

A MATLAB algorithm was used to smooth the calculated bed depth data with respect to time and then identify the local minima and maxima that correspond to the peaks and troughs of each bedform. The smoothing was necessary to eliminate scatter of the order of a few seconds (*i.e.* tens of samples), but was not found to affect the position or amplitude of peaks and troughs. The algorithm is described in more detail below.

1. The total bed depth (*i.e.* $h = h_b + h_s$) was smoothed using a polynomial filter of the Savitzky-Golay type (MATLAB function "sgolayfilt") which took two arguments for polynomial order, k, and frame size, f;
2. The position and amplitude of local minima and maxima were identified (MATLAB function "findpeaks") which took one optional argument for minimum peak separation, m;
3. The periods, t_i, between adjacent peaks and troughs were calculated in order to quantify the period of successive lees and stosses.

The optimal values of k, f and m, which differed for each example run ($3 \leq k \leq 7$; $3 \leq f \leq 5$; $5 \leq m \leq 7$) were found by trial and error, based on visual assessment, according to whether all peaks were resolved, and with the condition of minimal loss of peak sharpness.

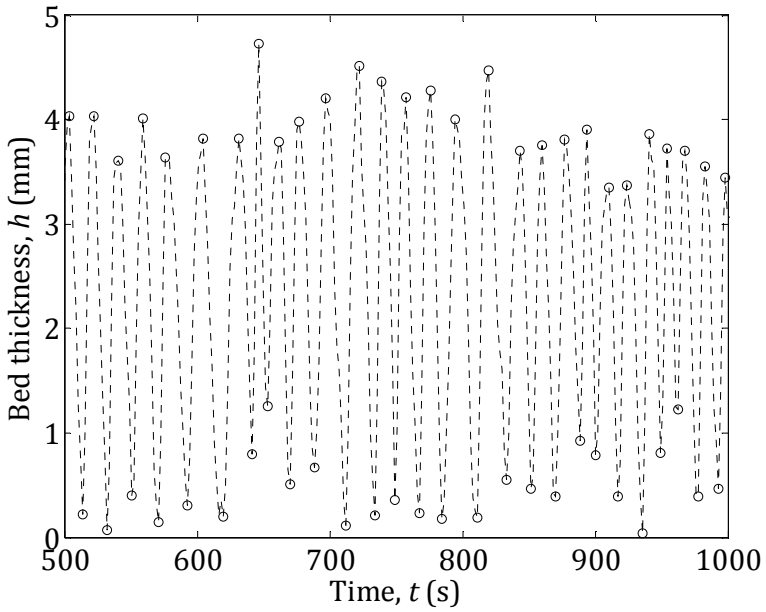

Figure 6-29: Total bed thickness, h, for case of bedform field of regular period (Q = 0.498 to 0.402 l s^{-1} at t = 0, ϕ = 0.1 %). Circles indicate local minima and maxima (*i.e.* peaks and troughs).

The results of the algorithm are shown for bedforms of regular, increasing and unstable period in Figure 6-29, Figure 6-30 and Figure 6-31, respectively, from which a number of interesting observations can be made. From Figure 6-29 and

Figure 6-30, it is clear that the algorithm efficiently identifies the peaks – which are signified by circles – of simple regular bedforms and bedforms of increasing period. A short period – 500 < t (s) < 1000 – was chosen for the former in order to show the regularity of the bedforms. A short period was also chosen for the case of bedforms of unstable period (Figure 6-31) in order to illustrate: (a) the apparent presence of smaller bedforms on larger ones, which is posited as evidence of ripples on dunes (and the reader is referred to the bi-periodicity observed in the same run and visualised in Figure 6-26); and (b) the ability of the algorithm – using suitable values of the parameters k, f and m – to identify the position and amplitude of such complex bedforms, which were not observed on bedforms in the other four categories.

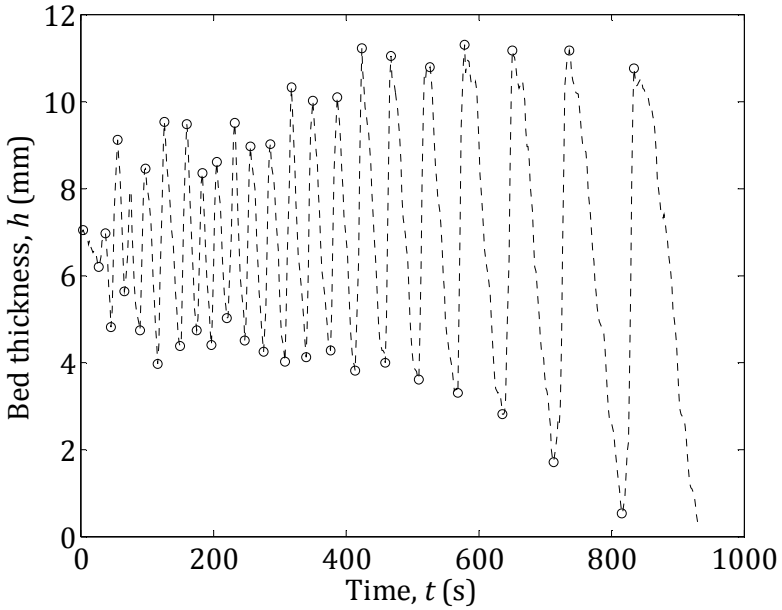

Figure 6-30: Total bed thickness, h, for case of bedform field of increasing period (Q = 0.483 to 0.323 l s^{-1} at t = 0, ϕ = 0.5 %). Circles indicate local minima and maxima (*i.e.* peaks and troughs).

Next, the evolution and scaling of bedform height, h_b, with respect to time is investigated. As shown in Figure 6-7, Ouriemi *et al.* (2009) found that the relative height (h_b/H) of different bedform types (specifically, "vortex" and "small dunes") were very well delineated when plotted against a dimensionless measure of time ($U_{ave}t/D$). Furthermore, several expressions available in the sedimentology literature for the equilibrium dimensions, h_b/H, of bedforms were given in Section

6.1.2 (García, 2008; Julien and Klaassen, 1995; Ouriemi *et al.*, 2009; van Rijn, 1984a, b) and the aim in this section is to compare and contrast the calculated bedform depths for each bedform type to those expressions, at which point it should be noted that U_{flow} and the initial value of H were used when calculating predictions of h_b/H – and therefore C', U_*' and T – according to Equations [6.8], [6.9] and [6.10]. The predictions are overlaid on plots of the data as horizontal lines in frame (b) of each of the three figures.

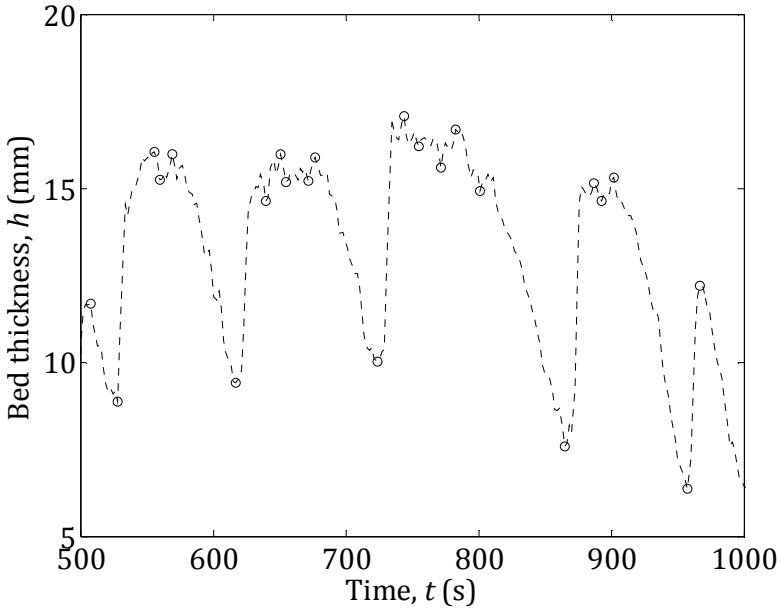

Figure 6-31: Total bed thickness, h, for case of chaotic, unstable bedform field (Q = 0.383 to 0.287 l s^{-1} at t = 0, ϕ = 1 %). Circles indicate local minima and maxima (*i.e.* peaks and troughs). Time period was chosen to show ripples on dunes.

The evolution of h_b/D *vs.* $U_{ave}t/H$ and h_b/H *vs.* t is shown in Figure 6-32, Figure 6-33 and Figure 6-34. The first clear observation to be made is that the bedform height is significantly smaller, with less scatter (with the exception of a small anomaly around $U_{ave}t/D$ = 7,000, or t = 1,000 s), in the case of regular ripples (Figure 6-32) and appears to be at equilibrium by $U_{ave}t/D$ = 3,000 or so, or t = 500 s. In the sense that h_b/H and h_b/D remain below 1/6, the observed behaviour satisfies the definition of dunes given by García (2008) in Equation [6.8], but is significantly below the predictions of Julien and Klaassen (1995) and van Rijn (1984a), as given in Equations [6.9] and [6.10].

Inspection of Figure 6-33 (bedforms of increasing period) and Figure 6-34 (unstable/chaotic bedforms) reveals very similar behaviour – a monotonic increase in bedform height, albeit with some scatter, for $0 < U_{ave}t/D < 2{,}000$ or $0 < t$ (s) < 500. At that point, however, the behaviour of the two bedform types diverges: in the first (Figure 6-33), h_b continues to rise monotonically; in the second (Figure 6-34), h_b becomes unstable and, in addition to the bi-periodicity seen in the same run and illustrated earlier (Section 6.3.2), evidence for putative ripples on dunes is shown in Figure 6-31: clusters of very small-amplitude bedforms are present in Figure 6-34(a) in the regions $3{,}000 < U_{ave}t/D < 5{,}000$ and $7{,}000 < U_{ave}t/D < 9{,}000$, and in Figure 6-34(b) in the regions $500 < t$ (s) $< 1{,}000$ and $1{,}500 < t$ (s) $< 1{,}800$.

However, although Coleman and Nikora (Coleman and Nikora, 2011) have stated that ripples and dunes in occupy "distinctly separate scales with no gradual transition" (see Section 6.1.2), the relationship between wavelets, ripples and dunes in pipe flow is not clear from the results presented in this section. Of the three time-dependent bedform types described in this section, only one satisfies the definition of dunes given by García (2008) – *i.e.* $h_b/H \leq 1/6$ (Equation [6.8]) – despite exhibiting the smallest amplitudes of the three bedform types. Moreover, it is not clear whether the bedforms-on-bedforms seen in Figure 6-31 and Figure 6-34 are of kind distinct from the small, regular bedforms shown in Figure 6-29 and Figure 6-32.

What is clear, however, is that the best predictor of equilibrium bedform depth for bedforms with increasing period, and for unstable/chaotic bedforms (although neither example given in Figure 6-33 and Figure 6-34 appear to be at equilibrium, as the measurement time was too short), is that given by van Rijn (1984a, b) – *i.e.* Equation [6.10] - whereas that given by Julien and Klaassen (1995) – *i.e.* Equation [6.9] – overestimates the equilibrium dimensions for all three time-dependent bedform types. While some discrepancy between these expressions and the laboratory data presented in this study would be expected, since the flow conditions are very different (natural systems and lab flumes *vs.* closed pipe flow), the van Rijn (1984a, b) model contains a larger number of flow-specific parameters, and so it is not surprising that the agreement is good.

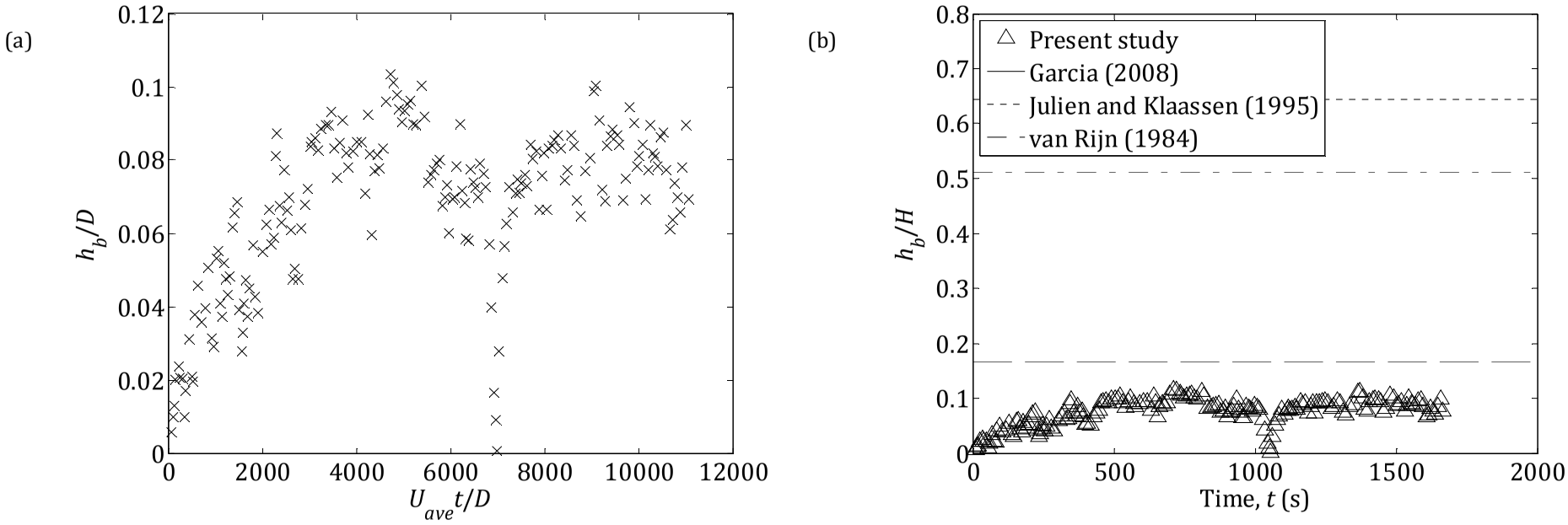

Figure 6-32: Scaling and evolution of bedform height, h_b, relative to (a) pipe diameter, D, and (b) fluid height, H, *vs.* (a) dimensionless time variable, $U_{ave}t/D$, and (b) time, t, for case of bedform field of regular period (Q = 0.498 to 0.402 l s^{-1} at t = 0, ϕ = 0.1 %).

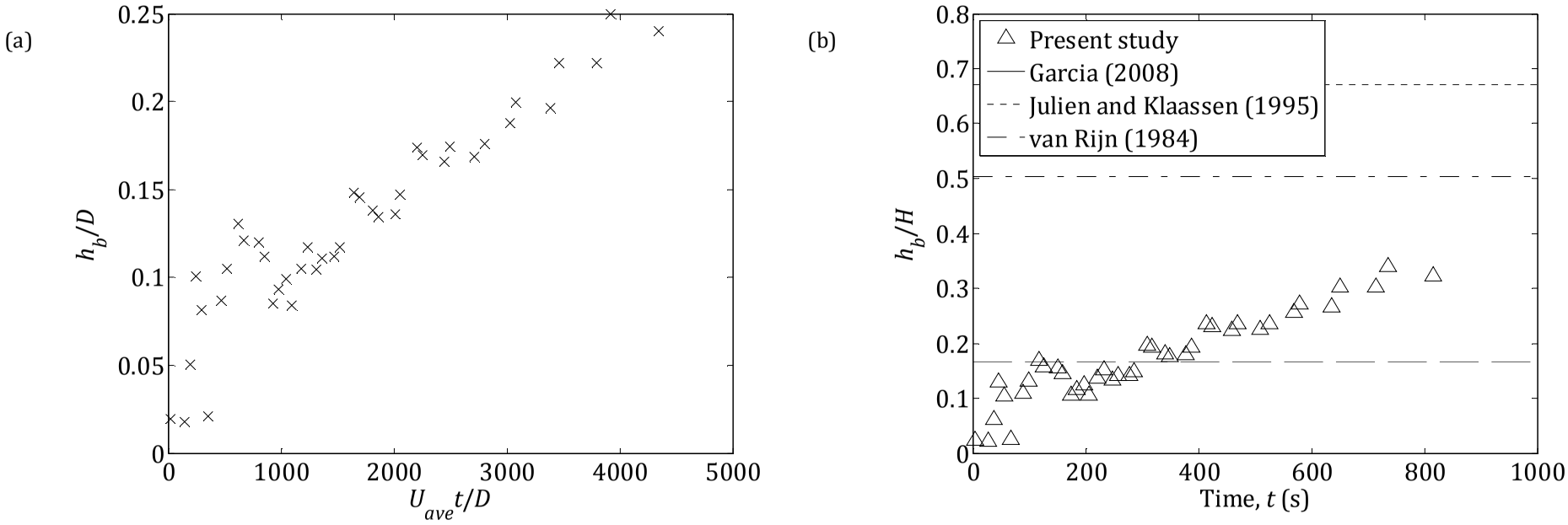

Figure 6-33: Scaling and evolution of bedform height, h_b, relative to (a) pipe diameter, D, and (b) fluid height, H, *vs.* (a) dimensionless time variable, $U_{ave}t/D$, and (b) time, t, for case of bedform field of increasing period (Q = 0.483 to 0.323 l s^{-1} at t = 0, ϕ = 0.5 %).

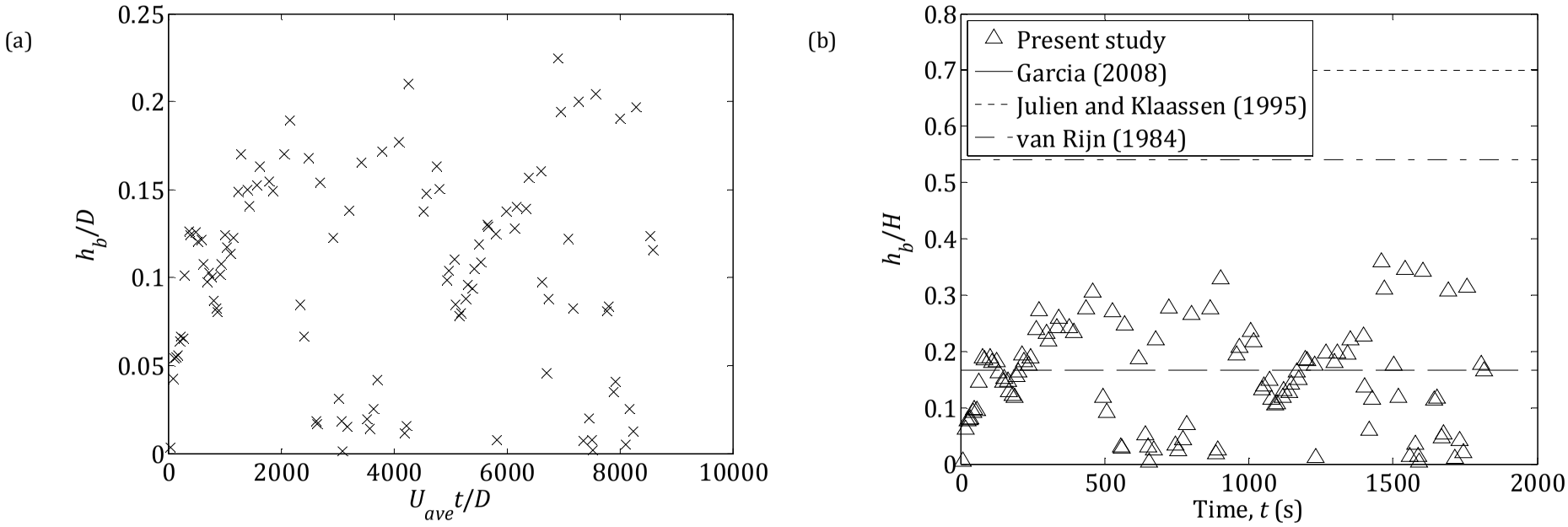

Figure 6-34: Scaling and evolution of bedform height, h_b, relative to (a) pipe diameter, D, and (b) fluid height, H, *vs.* (a) dimensionless time variable, $U_{ave}t/D$, and (b) time, t, for case of chaotic, unstable bedform field (Q = 0.383 to 0.287 l s^{-1} at t = 0, ϕ = 1 %).

When comparing data from natural and laboratory systems, and from conduits with rectangular, circular and other cross-sectional shapes, it is clear from the results presented in this section that many time- and length scales can be used, but that not all are universal because the geometry – and therefore flow field and particle concentration profile – differs. For example, a finite bed depth in pipe flow modifies the chord length at the bed surface and the shape of the flow area, whereas in rectangular channel flow it does not. This issue is discussed in more detail, with the aim of suggesting scalings that are more universal and allow more direct comparison of data from different flow geometries at low flow rates.

The first and most important point to note is that total bed depth, h, and pipe diameter, D, are irrelevant, since the particles in the bed interact with fluid only at, or within a thin layer above, the surface of bed (if it is assumed that secondary fluid motions caused by the non-rectangular shape of the flow area are insufficient to influence the behaviour of particles in/at the surface of the bed). At first glance, then, the three quantities of that will influence the behaviour of the bed, and which ought to be chosen to allow comparison between various flow geometries, are (a) the fluid depth above the bed, (b) the fluid velocity at or near the bed surface, and (c) the size of the particles.

So, some combination of (a) H, (b) U_{ave}, and (c) d_{50} may appear optimal. However, it suggested that more physically meaningful choices can be made. In the case of (a) an equivalent fluid depth, H_e, is proposed and is as illustrated in Figure 6-35. H_e is calculated by conserving the chord length, c – *i.e.* the cross-sectional width of the bed at its surface – and the flow area, A_{flow}, between flow geometries, since these two quantities are posited as being of principal importance in terms of their influence on bedform behaviour. That is,

$$cH_e = A_{\text{flow}} = \frac{Q}{U_{\text{flow}}}, \qquad [6.22]$$

where c and A_{flow} are calculated from the measured value of h according to Equations [3.46] and [3.49], respectively. The choice of H_e also naturally yields the second parameter, (b) U_{flow}, as the most appropriate.

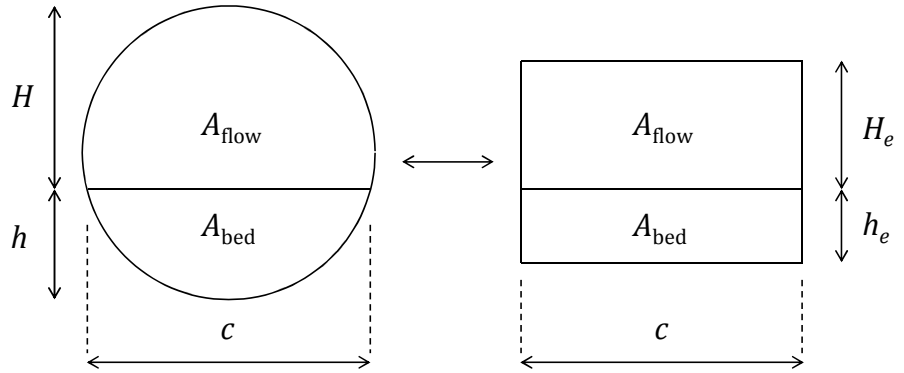

Figure 6-35: Illustration of a suggested universal scaling for closed-conduit flows of any cross-sectional shape.

The third choice to be made, then, is a representative particle size at the bed surface. Although d_{50} is the most obvious choice, it may be a poor one: if the particle size distribution is wide, then then the particles deposited at the surface of the bed may be significantly larger than d_{50}, since larger particles will tend to deposit more readily than smaller ones. For this reason, d_{90}, may be a better choice.

However, the size of particles at the bed surface may depend in a more complex way on the flow rate and ambient particle concentration, and the processes of armouring and overpassing, well known by sedimentologists (García, 2008; Raudkivi, 1998), may also play a role. (The first is a process by which larger particles constitute the top layer of the bed, and smaller particles are thereby "armoured" from the influence of fluid flow; in the second, larger particles skip over a bed of smaller particles.)

The issue of representative particle size in systems that produce time-dependent bedforms is, therefore, left as one for future study, although d_{90} is offered as a suggestion. It is also interesting to note that d_{90}, rather than d_{50}, was chosen by van Rijn (1984a) as a representative particle size at the bed surface when calculating C', the particle Chézy coeffient. The resulting expressions for the transport stage parameter, T, and h_b/H (Equation [6.10]) were found to predict equilibrium bedform dimensions more accurately than others earlier in this section.

So, it is suggested that choosing H_e, U_{flow} and, say, d_{90} – rather than, say, H or D, U_{ave}

and d_{50} without further consideration – has the advantages of (a) capturing all the relevant scales, and (b) allowing more direct comparison between data obtained in conduits of different cross-sectional shapes. For example, in conduits with rectangular cross-sections, $H_e \equiv H$.

When applied to a specific case, in particular the evolution of bedform height, h_b, with time, t, as described in this section, the corresponding choice of parameters would be h_b/H_e *vs.* $U_{\text{flow}}t/H_e$ (rather than h_b/H or h_b/D *vs.* $U_{ave}t/D$, as shown in Figure 6-32 to Figure 6-34). Both parameters have universal, unambiguous meanings in many flow geometries and accurately represent the physical situation in the flow, because as many important flow parameters as possible are taken in to account, and because results can readily be compared to the expressions for h_b given in Section 6.1.2, for example.

The question of whether the quantities suggested in this section are, indeed, the most appropriate for comparison of different flow conditions and geometries, can only be answered by whether the data collapse onto one set and show similar behaviour. This question, along with a full dimensional analysis – which, it is suggested, must include d_{90}, h_b, H_e, t, U_{flow}, and the viscosity, ν, as a minimum – is left as a subject for future work.

Lastly for this section, the axial symmetry of the three time-dependent types of bedforms was investigated, and was quantified by the bedform asymmetry factor, f_b, defined as the ratio of the periods between adjacent minima and maxima in the bed depth, as illustrated by t_i and t_{i+1} in Figure 6-22. Specifically,

$$f_b = \frac{t_1}{t_2}, \qquad [6.23]$$

where t_1 and t_2 are the larger and smaller of t_i and t_{i+1}, respectively (which are illustrated in Figure 6-22). It is clear, then, that f_b was contrived to be the ratio of the larger to the smaller of adjacent periods, so that $f_b \geq 1$, in order to allow a clearer illustration of the development of asymmetry with time. Celerity and wavelength could not be measured in this study, as a single probe was used to

measure bed depth. However, f_b, although a ratio of periods, is intended to be a proxy for the ratio of wavelengths of the same bedforms, which is reasonable if it assumed that the change in celerity between adjacent bedforms is small.

Plots of the bedform asymmetry factor, f_b, are shown for the three example runs in Figure 6-36 (bedforms with regular period), Figure 6-37 (increasing period) and Figure 6-38 (unstable/chaotic). In the first figure (Figure 6-36), f_b remains small (f_b < 2 for the vast majority of bedforms) and shows no significant trend over time. Inspection of Figure 6-32 (h_b/D and h_b/H *vs.* time) and Figure 6-36, then, confirms that in this case the bedforms remain stable, quite axially symmetrical and of small amplitude relative to the dimensions of the pipe diameter and fluid depth.

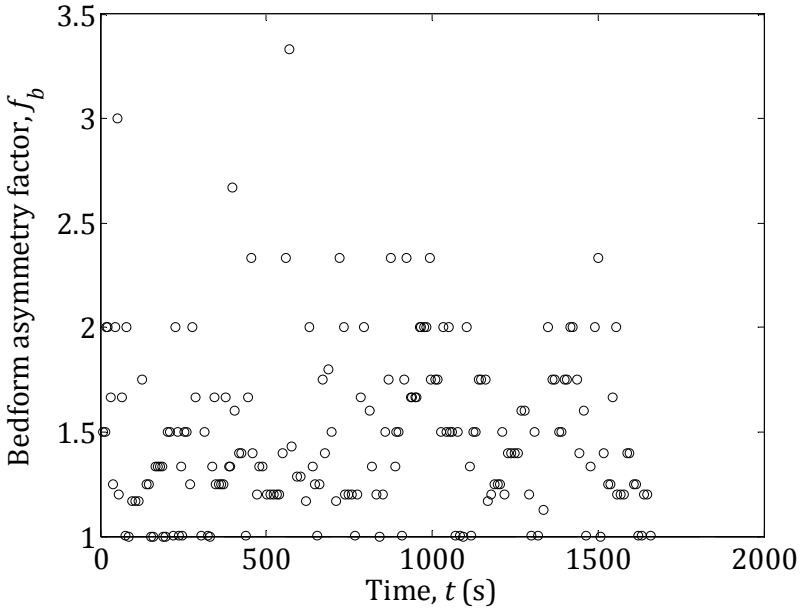

Figure 6-36: Bedform asymmetry factor, f_b, for case of bedform field of regular period (Q = 0.498 to 0.402 l s^{-1} at t = 0, ϕ = 0.1 %).

The trends for the second (Figure 6-37) and third cases (Figure 6-38) are: an increase in asymmetry over the first few hundred seconds, followed by significant scatter; and much higher values of f_b compared to the first case (regular bedforms). By comparing the evolution of bedform height, h_b (Figure 6-33 and Figure 6-34) with that of bedform asymmetry, f_b (Figure 6-37 and Figure 6-38), there is a broad correlation: deeper bedforms are more axially asymmetrical.

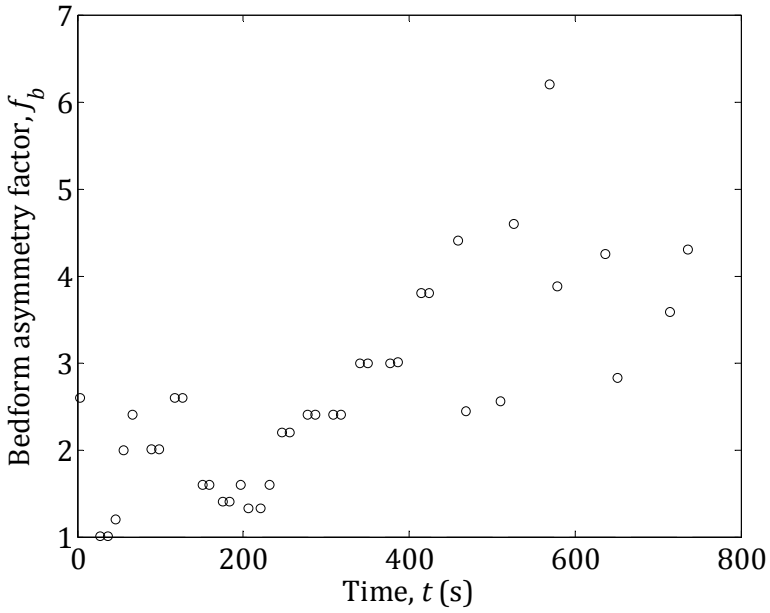

Figure 6-37: Bedform asymmetry factor, f_b, for case of bedform field of increasing period (Q = 0.483 to 0.323 l s^{-1} at t = 0, ϕ = 0.5 %).

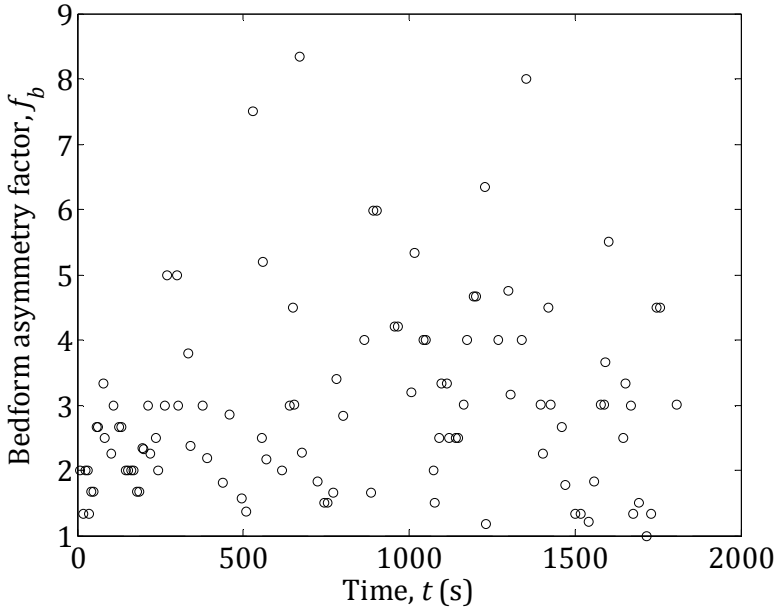

Figure 6-38: Bedform asymmetry factor, f_b, for case of unstable, chaotic bedform field (Q = 0.383 to 0.287 l s^{-1} at t = 0, ϕ = 1 %).

6.3.6 Phase diagrams of bedforms in closed pipe flow

In this section, three phase diagrams of bedform types are presented in terms of the flow Reynolds number, Re_{flow}, the flow Froude number, Fr, and the bulk

Reynolds number, $\mathrm{Re}_{\mathrm{pipe}}$, *vs.* h/D and $\mathrm{Ga}(H/d)^2$, and a summary table of the 58 runs presented in the phase diagrams is also given (Table 6-5). To reiterate, the various definitions of flow Reynolds number, *etc.*, presented below are exactly as in Section 3.7 but are repeated here for the reader. In particular:

$$\mathrm{Re}_{\mathrm{flow}} = \frac{U_{\mathrm{flow}} H}{\nu}, \qquad [6.24]$$

$$\mathrm{Fr} = \frac{U_{\mathrm{flow}}}{(gH)^{1/2}}, \qquad [6.25]$$

where h, H and D are the bed depth, fluid depth and inner pipe diameter, respectively, as shown in Figure 6-21. It should be noted that h and H are the initial values before the bed surface is perturbed by a change in flow rate. These quantities were chosen because they have a common interpretation in all the runs and could be evaluated in a consistent way. U_{flow} is the mean axial flow velocity in the flow area, A_{flow}, *i.e.* the cross-sectional area not occupied by the bed, and is calculated as follows:

$$U_{\mathrm{flow}} = \frac{Q}{A_{\mathrm{flow}}}. \qquad [6.26]$$

The Galilei number, Ga, defined earlier in Equation [6.16], is:

$$\mathrm{Ga} = \frac{d^3(s-1)g}{\nu^2}. \qquad [6.27]$$

Lastly, $\mathrm{Re}_{\mathrm{pipe}}$ is the bulk Reynolds number, *i.e.* that based on the total cross-sectional area, A_{total}, and the bulk velocity, U_{ave}, averaged over A_{total} such that

$$\mathrm{Re}_{\mathrm{pipe}} = \frac{U_{ave} D}{\nu} = \frac{4Q}{\pi D \nu}. \qquad [6.28]$$

To reiterature, the bedforms have been categorised into five types: flat beds with no particle motion; ripples with regular period; ripples with periods that increase

monotonically over time; unstable/chaotic ripples, the periods of which vary in an unpredictable way; and upper plane beds, *i.e.* flat beds on which ripples have been washed out and above which a shear layer exists. These categories were described in more detail, with examples, in Section 6.3.3.

A summary of the flow conditions in the 58 runs that were categorised and compiled into the phase diagrams is given in Table 6-5 at the end of this section.

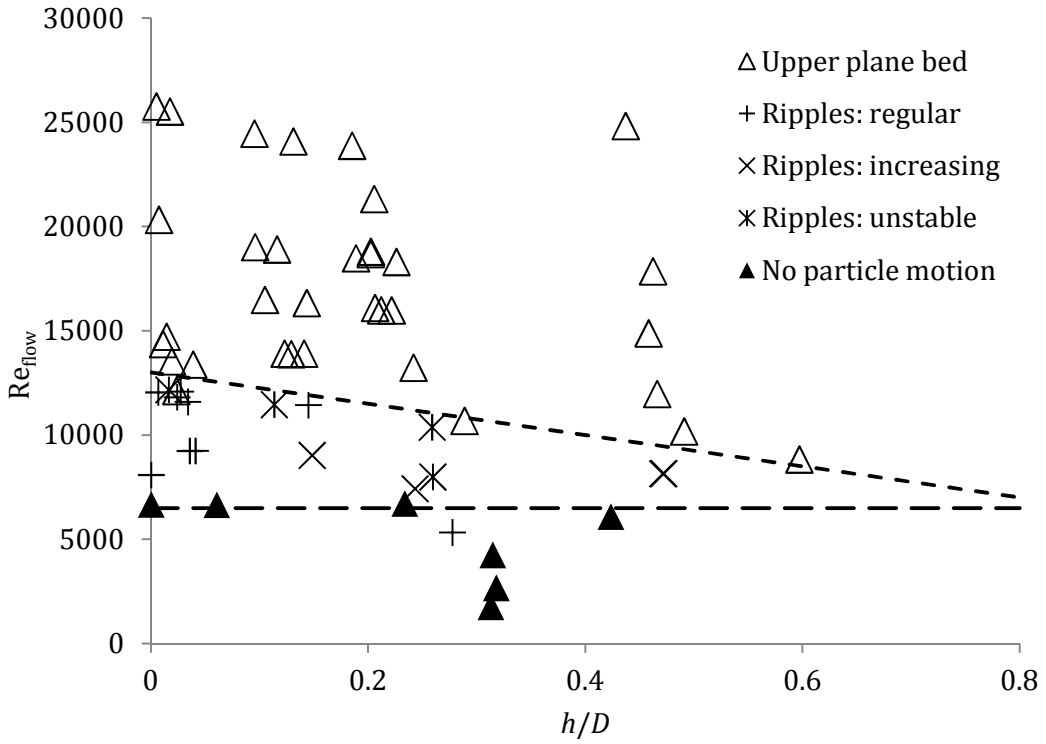

Figure 6-39: Phase diagram of bedforms in pipe flow according to flow Reynolds number, Re_{flow}. Unfilled triangles: upper plane bed; stars: variable ripples; pluses: regular ripples; crosses: ripples with increasing period; filled triangles: no particle motion. Dashed lines indicate transitions between no particle motion, ripples and upper plane beds.

The flow Reynolds number, Re_{flow}, and Froude number, Fr, have been plotted against h/D in Figure 6-39 and Figure 6-40, respectively. The bulk Reynolds number, Re_{pipe}, is plotted against $Ga(H/d)^2$ in Figure 6-41, for direct comparison with the phase diagram presented by Ouriemi *et al.* (2009; 2010) in which the same variables were used (see Section 6.1.4 and Figure 6-6(b)). In each of these three phase diagrams of stable and unstable bedforms, the categorisation described in Section 6.3.3 and reiterated above was used. Data from a total of 58

runs at several concentrations (0.1 % < ϕ < 3 %) are presented. It should be noted that the three-dimensional "sinuous dunes" observed by Ouriemi *et al.* (2009; 2010) were not observed in the present study: all bedforms were two-dimensional (by visual inspection).

The regions corresponding to no particle motion and upper plane beds are well delineated in Figure 6-39 (dashed lines), with a region in between in which ripples form. Ripples with regular periods appear to be distributed across the unstable region at smaller bed depths (h/D < 0.1), but at larger bed depths the situation is less clear due to a lack of data.

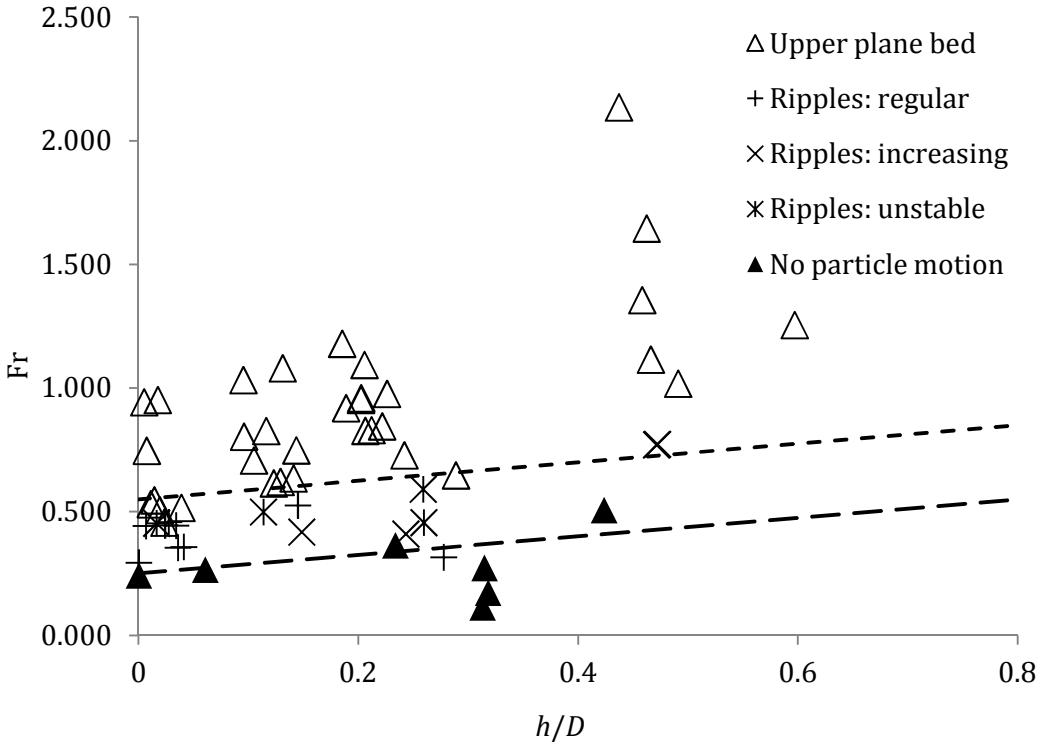

Figure 6-40: Phase diagram of bedforms in pipe flow according to Froude number, Fr. Unfilled triangles: upper plane bed; stars: variable ripples; pluses: regular ripples; crosses: ripples with increasing period; filled triangles: no particle motion. Dashed lines indicate transitions between no particle motion, ripples and upper plane beds.

On the other hand, ripples with increasing periods appear to be clustered towards the lower parts of the unstable region, suggesting they are transitional between beds with no particle motion and ripples; ripples with highly variable periods appear to be clustered towards the top of the unstable region, suggesting they are

transitional between ripples and upper plane beds (although this hypothesis was not confirmed or ruled out visually). There is a clear dependence of bedform type on Reynolds number, but the dependence on bed depth is weaker and less clear.

Equally clear from a comparison of Figure 6-39 ($\mathrm{Re}_{\mathrm{flow}}$ *vs.* h/D) and Figure 6-40 (Fr *vs.* h/D) is that the regions corresponding to each kind of bedform and the critical values delineating them have different dependences on the parameters in each case. The same is true when comparing those figures to Figure 6-41 ($\mathrm{Re}_{\mathrm{pipe}}$ *vs.* $\mathrm{Ga}(H/d)^2$), in which it should be noted that both axes are logarithmic.

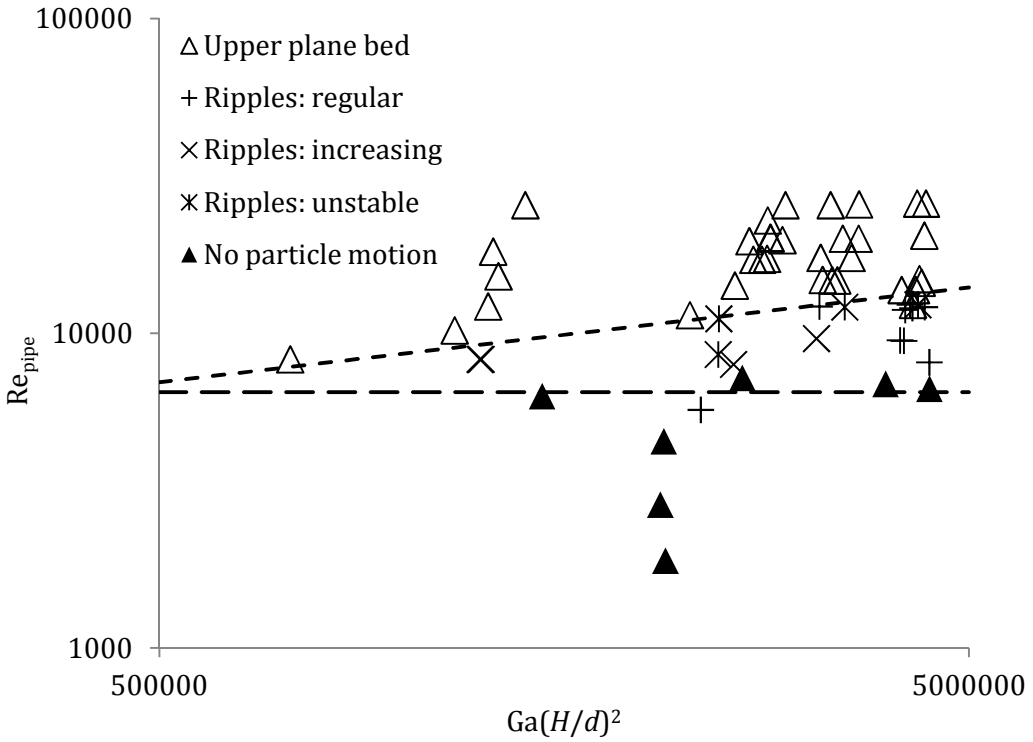

Figure 6-41: Phase diagram of bedforms in pipe flow according to bulk Reynolds number, $\mathrm{Re}_{\mathrm{pipe}}$ *vs.* $\mathrm{Ga}(H/d)^2$, as presented by Ouriemi *et al.* (2009). Unfilled triangles: upper plane bed; stars: variable ripples; pluses: regular ripples; crosses: ripples with increasing period; filled triangles: no particle motion. Dashed lines indicate transitions between no particle motion, ripples and upper plane beds.

A number of observations and conclusions can be drawn from Figure 6-41, which is plotted with the same variables as the phase diagram of Ouriemi *et al.* (2009), which is shown in Figure 6-6(b). First, the threshold for particle motion ($\mathrm{Re}_{\mathrm{pipe}} \approx$ 6,500) does not vary with $\mathrm{Ga}(H/d)^2$. Second, the threshold between unstable

bedforms and upper plane beds appears to increase with Re_{pipe}. Third, the same threshold vanishes at low flow $Ga(H/d)^2$, although this observation is tentative as it is based on rather few data. Fourth, and most importantly, the observed thresholds do not appear to closely match those given by Ouriemi *et al.* (2009; 2010), although it is difficult to gauge the closeness of the match as the results presented here fall into a small area in the upper reaches of the parameter space investigated by Ouriemi *et al*.

The last observation is the most significant and suggests that the variables chosen – Re_{pipe} and $Ga(H/d)^2$ – may not be able to capture the universal behaviour of bedforms in closed pipes. It was suggested in Section 6.3.5, with reference to the scaling of bedform heights, that some combination of the most important variables (d_{90}, h_b, H_e, t, U_{flow} and ν, at least) be made that accounts a range of flow rates, particle properties and flow geometries. The same principle appplies to the bedform diagrams presented in this section. However, here, as there, a dimensional analysis is left as a subject for future work.

Table 6-5 follows and contains a summary of the most important measured and calculated flow and bed parameters in the runs presented in the phase diagrams (Figure 6-39, Figure 6-40 and Figure 6-41).

Table 6-5: Summary of experimental parameters of runs used to construct phase diagrams. (Total: 58.)							
Q (l s^{-1})	U_{ave} (m s^{-1})	U_{flow} (m s^{-1})	H/D	Re_{pipe}	Re_{flow}	Fr_{flow}	$\text{Ga}(H/d)^2$
Category: No particle motion (7 runs)							
0.063	0.045	0.061	0.687	1896	1779	0.113	2108359
0.096	0.067	0.092	0.682	2859	2684	0.173	2077766
0.152	0.107	0.146	0.685	4545	4264	0.273	2097711
0.224	0.157	0.157	1.000	6682	6680	0.243	4465407
0.232	0.162	0.167	0.939	6922	6669	0.266	3942286
0.242	0.170	0.206	0.766	7223	6732	0.364	2623640
0.211	0.148	0.249	0.576	6320	6103	0.506	1484578
Category: Bedforms of unstable period (4 runs)							
0.287	0.201	0.254	0.740	8578	8000	0.456	2449037
0.413	0.290	0.291	0.984	12340	12181	0.453	4322015
0.406	0.285	0.304	0.886	12129	11471	0.499	3510062
0.373	0.261	0.329	0.741	11136	10386	0.591	2453480
Category: Bedforms of increasing period (4 runs)							
0.322	0.226	0.249	0.852	9631	9039	0.418	3239304
0.267	0.187	0.231	0.757	7976	7434	0.410	2558773
0.277	0.194	0.363	0.528	8277	8160	0.773	1244449

Table 6-5: Summary of experimental parameters of runs used to construct phase diagrams. (Total: 58.)							
Q (l s^{-1})	U_{ave} (m s^{-1})	U_{flow} (m s^{-1})	H/D	Re_{pipe}	Re_{flow}	Fr_{flow}	$\text{Ga}(H/d)^2$
0.277	0.194	0.362	0.529	8277	8156	0.770	1248615
Category: Bedforms of regular period (9 runs)							
0.191	0.134	0.174	0.722	5719	5341	0.316	2330998
0.413	0.290	0.292	0.973	12340	12094	0.458	4225640
0.318	0.223	0.226	0.959	9511	9249	0.358	4107835
0.271	0.190	0.190	1.000	8096	8094	0.294	4465407
0.403	0.283	0.284	0.976	12039	11823	0.445	4254819
0.317	0.223	0.225	0.964	9481	9246	0.355	4153334
0.408	0.286	0.314	0.855	12189	11447	0.526	3266149
0.398	0.279	0.282	0.966	11889	11606	0.444	4168203
0.406	0.285	0.285	0.993	12129	12058	0.442	4406916
Category: Upper plane beds (34 runs)							
0.856	0.601	0.688	0.815	25583	23891	1.180	2965622
0.765	0.537	0.630	0.794	22874	21330	1.094	2819281
0.658	0.461	0.556	0.774	19654	18316	0.977	2676138
0.574	0.403	0.482	0.778	17156	15989	0.845	2706499
0.475	0.333	0.410	0.758	14206	13240	0.728	2567940
0.383	0.268	0.353	0.711	11437	10693	0.647	2259828

Table 6-5: Summary of experimental parameters of runs used to construct phase diagrams. (Total: 58.)							
Q (l s^{-1})	U_{ave} (m s^{-1})	U_{flow} (m s^{-1})	H/D	Re_{pipe}	Re_{flow}	Fr_{flow}	$\text{Ga}(H/d)^2$
0.866	0.608	0.608	0.995	25884	25769	0.943	4422586
0.685	0.480	0.481	0.993	20466	20337	0.747	4401597
0.498	0.350	0.351	0.986	14898	14727	0.546	4340251
0.460	0.323	0.324	0.981	13755	13550	0.507	4296534
0.413	0.290	0.291	0.977	12340	12125	0.456	4261085
0.460	0.323	0.327	0.961	13755	13392	0.516	4126541
0.861	0.604	0.635	0.905	25733	24467	1.033	3656268
0.670	0.470	0.502	0.884	20015	18916	0.827	3490458
0.582	0.408	0.448	0.857	17396	16341	0.749	3277385
0.495	0.348	0.380	0.859	14808	13917	0.635	3296365
0.670	0.470	0.494	0.904	20015	19026	0.804	3651507
0.582	0.408	0.433	0.895	17396	16492	0.707	3578793
0.493	0.346	0.372	0.877	14748	13914	0.615	3436147
0.493	0.346	0.375	0.871	14748	13894	0.621	3387885
0.856	0.601	1.036	0.563	25583	24834	2.136	1415268
0.609	0.427	0.780	0.538	18209	17868	1.646	1291523
0.509	0.357	0.645	0.542	15199	14888	1.356	1311107
0.408	0.286	0.527	0.534	12189	11982	1.115	1273352

Table 6-5: Summary of experimental parameters of runs used to construct phase diagrams. (Total: 58.)							
Q (l s^{-1})	U_{ave} (m s^{-1})	U_{flow} (m s^{-1})	H/D	Re_{pipe}	Re_{flow}	Fr_{flow}	$\text{Ga}(H/d)^2$
0.342	0.240	0.470	0.509	10233	10184	1.018	1157669
0.277	0.194	0.515	0.403	8277	8842	1.255	725294
0.856	0.601	0.651	0.869	25583	24092	1.080	3372532
0.675	0.473	0.554	0.797	20165	18808	0.959	2841146
0.663	0.465	0.535	0.811	19804	18489	0.919	2939888
0.574	0.403	0.476	0.788	17156	15993	0.830	2774083
0.485	0.341	0.341	0.989	14507	14374	0.531	4368681
0.866	0.608	0.610	0.983	25884	25531	0.952	4312596
0.671	0.471	0.550	0.798	20045	18695	0.953	2842254
0.578	0.406	0.476	0.794	17276	16110	0.827	2814344

6.4 Summary and conclusions

Measurements of time-dependent bedforms produced by the deposition of solid particles from two-phase liquid-solid flows have been studied using an ultrasonic echo method in a horizontal test section of closed pipe flow loop. Results were presented for settled bed and shear layer thicknesses over a range of flow rates, with the path-dependent equilibration, hysteresis and bi-periodic, and possibly cyclical, behaviour in plane beds and ripples also considered.

The evolution and scaling of bedform heights were then investigated. It was found that: (a) the van Rijn (1984a, b) model best describes equilibrium bedform height, but no clear distinction between ripples and dunes is evident in the results presented; (b) no single model, either from the sedimentology or engineering/fluid mechanics literature is able to fully account for the observed bedform types in terms of a phase diagram; (c) any model must necessarily incorporate the dynamic nature of bedforms, including the hysteretic and path-dependent behaviour described in this chapter, and the influence of initial and resultant bed/fluid depth and changes in flow rate, which are strongly linked; and (d) the effect of the shape of the pipe cross-section must be taken into account, and suitable scalings (*e.g.* U_{flow} in place of U_{ave}; H in place of D; see Section 6.3.5) should be chosen and justified if a range of flow geometries and particle types are to be accounted for.

Time-dependent bedforms were found to be axially asymmetrical in all cases in terms of the period taken to pass the probe, but only slightly so in the case of small, regular ripples. In general, the degree of asymmetry between adjacent bedforms was correlated with bedform height.

In the concluding part of the chapter, data gathered in a wide range of experiments were used to derive phase diagram of bedforms in closed pipes in terms of the bulk and flow Reynolds and Froude numbers – Re_{pipe}, Re_{flow} and Fr – in which the thresholds between incipient particle motion and different bedform types were established and compared to a similar phase diagram presented by Ouriemi *et al.* (2009).

The ultimate aim of the work described in this chapter is to characterise the effect of bedforms on the magnitude and variability of particle flux in closed pipe flow. In the future, the author intends to combine the results and methods presented in this chapter with measurements of Doppler velocity and Reynolds stress profiles described in Chapter 4 and concentration profiles described in Chapter 5 in order to quantify the particle flux as a function of height through the flow.

Several suggestions are made for the exploitation of the methods described in this chapter. The procedure for measuring bed depth and evolution appears to be relatively novel, in the engineering literature, at least. Although many related acoustic methods are commonly used by earth and marine scientists (see, for example, Thorne and Hanes, 2002), the author is aware of only one other study (McLelland, 2010) in which exactly the same method (*i.e.* the RMS of the backscattered signal) has been used to measure bed depth.

A simple modification of the flow loop – in particular, using two parallel transducers - would allow not only the depth and period of ripples to be measured, as presented here, but also their wavelength and rate of progradation. Alternatively, the evolution of bedform shapes could be tracked using particle image velocimetry with a suitable high-quality video camera and compared to acoustic measurements of bed depth.

7 Conclusions

In this final chapter, the findings are broadly summarised by topic, conclusions regarding the success of the project are drawn (Section 7.1) and several suggestions for future work are made (Section 7.2).

7.1 Review of methods and results

The methods that were developed for and employed in this study were intended to be applicable to a broad range of flow and particle properties, and several were either partly or wholly novel. The successes and limitations of each part of this study are discussed by topic, in terms of: the experimental method (Section 7.1.1); first- and second-order flow statistics and critical velocities (Section 7.1.2); the determination of acoustic backscatter and attenuation coefficients and construction of particle concentration profiles (Section 7.1.3); and the possibility of devising universal scalings for bedform behaviour and the limit deposition velocity, U_{c2} (Section 7.1.4).

7.1.1 Experimental method

The main measurement system used in this study was the *UVP-DUO* ultrasonic signal processing unit, which, although intended by the manufacturer to be used primarily as a Doppler velocimeter, was also used as a very capable acoustic backscatter system (particularly in Chapter 5). It was chosen for several reasons, the principal ones being that much higher particle concentrations can be investigated than with optical systems, the equipment is highly mobile and versatile, and the associated data processing requirements are low enough that analysis can be performed rapidly and *in situ* if necessary.

The *UVP-DUO* system was operated at the limit of its measurement ability in this study, in terms of accuracy and spatial and temporal resolution, which were discussed in detail in Section 3.6.2 for some idealised particle species at three flow rates (very low, intermediate and very high). It was found that the *UVP-DUO* would

be unable to resolve the finest turbulent motions, either spatially or temporally, based on estimates of the Kolmogorov time- and length scales. The ability of the *UVP-DUO* system is ultimately limited, through the equations given in Sections Section 2.2.3 and 3.2.2, by the following: (a) the speed of sound, which determines the transit time of pulses across the measurement domain, and therefore the maximum sampling rate, F (Equation [3.6]); (b) the chosen acoustic frequency, f (or wavelength, λ), which determines the maximum measurement distance, r_{max} and the velocity bandwidth, U_{bw} (through Equation [3.12]); (c) the sampling theorem (Equation [3.9]); and (d) the radius of the active face of the transducer, a_t, which, along with the measurement channel width, w (Equation [3.5]), influences the spatial resolution since they determine the size of the measurement volume.

The measurement quality can be increased in a number of ways: the velocity resolution, by increasing the number of bits used for digitisation (14 in this study, as set by the *UVP-DUO* software); the temporal resolution, by using a higher repetition rate, which in practice requires using a single repetition per pulse (*i.e.* $N = 1$) and as low an ultrasonic frequency as possible (Equations [3.6] and [3.12]); the spatial resolution, by using as high a frequency as possible (Equation [3.5]). However, it quickly becomes clear that there is a trade-off between spatial and temporal resolution in terms of emitted frequency. Moreover, although a high frequency will allow a higher spatial resolution, it would reduce the maximum measurable distance directly, through Equation [3.12], and indirectly as a result of attenuation if the particle concentration is sufficiently high. It should also be noted, however, that reducing the number of cycles per pulse would reduce the statistical accuracy of measurements, so a balance must always be found.

The experimental parameters used in this study were chosen carefully in order to maximise the measurement quality, according to the considerations described in this section and Section 3.6.2.

7.1.2 Flow statistics, critical velocities and bed depth

That the *UVP-DUO* was operated at the limit of its ability, as discussed in the

previous section, was particularly evident from the results presented in Chapter 4. For example, the balance between maximum measurement distance and velocity bandwidth – as quantified by Equation [3.12] – can clearly be seen in Figure 4-10(b): the maximum measurable distance is truncated at $y/R \approx 1.8$ because of the high flow rate/bulk flow velocity (Re = 104,000, U_{ave} = 2.43 m s^{-1}).

It is clear from the results presented in Chapter 4 that the axial mean ($\overline{U}$) and RMS velocity (u') fields were measured accurately (notwithstanding some flow disturbance caused by the probes themselves) and a shear layer was resolved in some cases (see, for example, Figure 4-8). However, the radial RMS velocity (w') and shear Reynolds stress ($\overline{uw}$) fields were generally underestimated by a factor of order unity and two possible reasons are suggested for this: (a) the spatial and temporal resolution of the measurement system was insufficient, as described in the previous section and in Section 3.6.2; and (b) the magnitude of the fluctuating part of the Doppler velocity time series was very small compared to the mean, so it is possible that the peak in the Doppler spectrum generated by Fourier transform was weak. However, the latter is speculative and is left as a subject for future study.

The method of measuring the thickness of beds and shear layers (Section 4.2.7 and Chapter 6) was very successful and precise (to 0.37 mm at f = 4 MHz) for this purpose and, although not entirely novel in itself (McLelland, 2010), had not previously been used in an engineering context. However, the method of calculating the limit deposition velocity, U_{c2}, by extrapolation of the bed depth to zero is novel and gave clear and unambiguous results. It can be applied to any bed-forming suspension at low flow rates, *i.e.* in the absence of a large shear layer. (The method can also be used in the presence of shear layers, but the results require more interpretation.) The measured values of U_{c2} agreed very well with values calculated according to one correlation from the literature but not another, more widely used one.

A full error analysis for wall-normal distance and mean axial velocity was performed and is given in the appendix (Appendix A). Errors were generally of the

order of a few per cent, and suggestions are given in the appendix for reducing them. It should be noted that one limiting factor in the measurement system – namely the size of the measurement volume, as dictated by the diameter of the active faces of the transducers, could not be reduced in this study, but could be reduced in future studies to some extent by using narrower probes.

7.1.3 Acoustic coefficients and concentration profiles

A novel method for measuring the backscattering and attenuation properties of arbitrary particles was derived and tested with four particles species (Section 5.2). One aim was to use the results to provide the basis of a reference database for a variety of particle types – in terms of size, density and shape – for engineers and scientists in situations where direct sampling and particle characterisation is not possible.

It was found that signal attenuation was significant over just a few centimetres of penetration depth at volume fractions of a few per cent for the plastic particle species (see, for example, Figure 5-8), which was to be expected since the backscatter and attenuation coefficients increase very strongly with particle size. In order to apply the methods described in this study to either highly concentrated suspensions or much larger suspension vessels in an industrial setting, much lower ultrasonic frequencies could be used, although the corresponding reduction in the spatial resolution of measurements would have to be considered.

Particular note must be made of the very strong influence of particle size, and the width and shape of the particle size distribution (PSD), on the strength of backscatter and attenuation (see discussion in Section 5.2.5). It was found that using d_{50} as a representative particle size, rather than integrating over the entire PSD, generally yielded under- or overestimates of the attenuation at low and high values of ka, respectively, as expected (Thorne and Meral, 2008). This finding underlines the importance of knowing the PSD – and accounting for it in any model used – as accurately as possible. The industrial implications of this are obvious: if physical samples cannot be taken, then the PSD must be estimated, and the wider

the PSD, the greater the associated uncertainties. On the other hand, reasonable estimates of the width and shape of the PSD can usually be made (in terms of σ/μ, for example), and a suitable choice of the insonification frequency can always be made.

The trends in the measured concentration profiles (Section 5.3.2) were realistic, but a Reynolds number-dependent effect was observed whereby the concentration was often overestimated at very high Reynolds numbers. This could form the basis of a very interesting study in terms of particle transit time *vs.* pulse length. On the other hand, it is noteworthy that this effect simply would not be present in many industrial applications at low flow rates and in freely settling suspensions.

Lastly, an analysis of the effect of the uncertainty in measured laboratory temperature – the greatest source of error – on the acoustic attenuation was described in the appendix (Section A.7), in which it was found that dT could, indeed, influence results at lower particle concentrations for particles with smaller diameters and should therefore generally be measured as accurately as possible and explicitly accounted for in calculations.

7.1.4 Universal scalings

The topic of universality arose twice in this study: in the context of (a) the limit deposition velocity, U_{c2} (Section 4.2.7); and (b) bedform heights and delineations between bedform types (Sections 6.3.5 and 6.3.6). In the case of U_{c2}, it was found that a commonly used correlation for predicting U_{c2} (Oroskar and Turian, 1980) was not accurate for the plastic species used in this study, and so cannot be said to be universal. In this context, "universal" is taken to mean "applying to all pipe-flow conditions and particle species", and in particular the density of particle species was posited as being accounted for unsatisfactorily in the Oroskar and Turian (1980) correlation.

In the case of bedforms, it was found that, of the scalings for bedform height given by García (2008), Julien and Klaassen (1995) and van Rijn (1984a), the last was

found to most accurately predict bedform height. In this context, "universal" is taken to mean "applying to all flow conditions, particle species and geometries". Clearly then, the expressions given García (2008) and Julien and Klaassen (1995) cannot be said to be universal: many of the bedforms encountered in this study were much larger than the limit of $h_b/H = 1/6$ given by García (2008), for example. The absence of a universal scaling for delineations between types of bedforms, in the form of a suitable phase diagram, was apparent when the results from this study were not found to coincide closely with those of Ouriemi *et al.* (2009). An equivalent fluid depth, H_e, that can be identified in any flow geometry was suggested in Section 6.3.5 and is explored as a subject for future study in Section 7.2.

7.2 Suggestions for future exploitation

There follows a numbered list of suggestions, by topic, for future work, based on the findings of this study.

1. *Probe mounting.* An intrusive probe mounting was used in this study (see Section 3.2), the main advantage of which was an efficient transfer of acoustic energy from the probes into the suspension and, after interaction with the fluid and scatterers, back into the probes. The main shortcoming of this arrangement, however, was that the presence of the probes influenced the flow field.

   In an alternative probe mounting used by Admiraal and García (2000) and shown in Figure 7-1, there is no physical contact between the probes and the flow. Instead, the probes are positioned in a transmission tube that is separated from the flow by a thin film through which the ultrasound can pass. A similar mounting, with a Mylar film, was used by Lemmin and Rolland (1997). If incorporated into the flow loop used in this study, such a mounting would minimise flow disturbances caused by the probes and errors in position calibration, but would increase the effects of beam divergence – and, correspondingly, reduce the spatial resolution with distance from probe – as

the probe(s) would have to be recessed and would therefore be further from the measurement points.

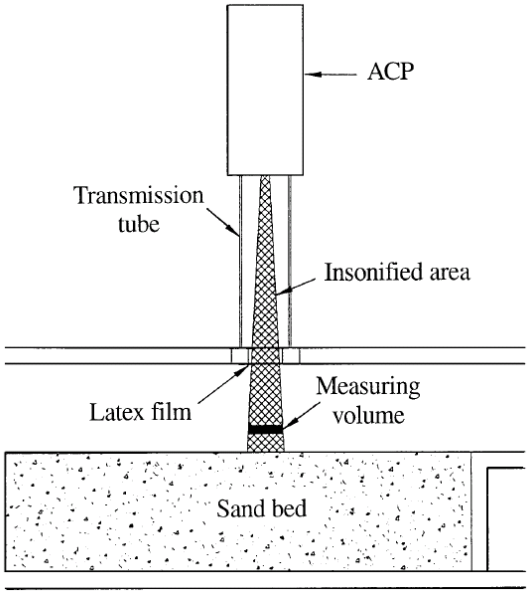

Figure 7-1: Probe mounting used by Admiral and García to investigate sand beds in a rectangular channel. "ACP" is an acoustic concentration profiler.

2. *Pressure transducers.* The installation of pressure transducers on the main flop loop would allow the bed shear stress (and therefore the Shields parameter, θ_s) to be measured, and the friction factor, f, to be measured directly, rather than *via* the correlation of Haaland (1983), as was the case in this study (Section 3.6.6). Although this correlation appears to produce very good estimates of the friction factor (as demonstrated by the results presented in Figure 3-22), it is based on single-phase (*i.e.* water-only) measurements and so direct measurement would be preferable.

3. *Three-probe system.* Although the probe arrangement that was chosen (two probes, at 90° and 135° to the flow direction) was efficient in the sense that two components of the velocity field, vertical concentration profiles *and* bed thickness could be measured, it is suggested that a three-probe system would allow an even greater range of measurements to be taken. In particular, the third probe should ideally provide the ability to measure the wavelength and rate of progradation of time-dependent bedforms (which would require that

it be directed approximately perpendicular to the bed surface) and a component of the axial velocity field (which requires that it be directed at as small an angle to the mean flow direction as possible) in order that a less computationally intensive method of measuring the velocity and stress fields, as described by Lhermitte and Lemmin (1994) and Lemmin and Rolland (1997), could be employed.

4. *Digital-image particle tracking.* High-quality video footage of solid-liquid suspensions under a range of conditions, when combined with the kind of complementary acoustic data presented in this study, would allow a great deal of additional dynamic flow characterisation to be done, as well as providing a separate measurement method for the purpose of calibration and validation. For example, the wavelength and celerity of bedforms could be measured (as suggested in Chapter 6). If the images were of sufficiently high quality, saltation distance – *i.e.* the distance travelled by particles as they skip along the surface of the bed – in bed-forming flows could also be measured.

5. *Combination of complementary data.* Complementary sets of different data could be combined and compared. For example, since both the mean axial velocity and particle concentration profiles were measured, the mass flux could be calculated over the same range of flow parameters. Moreover, in that case a detailed investigation of the evolution of the turbulence and particle concentration fields above time-dependent bedforms could be carried out (as was done by Charru and Franklin, 2012; Zedel and Hay, 1999): the corresponding fluid dynamics in natural streams and rectangular flume-type channels has been studied extensively, but there are far fewer studies in engineering-related, closed-pipe conditions.

6. *Polydensity.* The assumption that the density does not vary within a particle species is implicit in all the models used in this study. Although this was clearly a valid assumption for the manufactured particle species used in this study, the same may not be true for some complex, polydisperse nuclear waste slurries described in the relevant literature (see Section 1.1). It is

suggested that, in the first instance, a study could be conducted using two particle types of different densities simultaneously, using and building on the experimental and computational methods developed in this study. Such a mixture of particle species represents the simplest case of a polydense suspension. Moreover, if one species were very fine (*i.e.* were chosen to have a very small mean diameter), a great deal of interesting analysis could be performed by assuming the larger species were suspended in a pseudo-fluid consisting of the fluid and the finer species. In particular, the strength of inter-particle interactions could be quantified.

7. *Acoustic coefficients.* Backscatter and attenuation coefficients were presented in Section 5.2 for the four particle species used in this study (glass spheres and jagged plastic beads). The author intends to expand the database by testing a larger range of particle species that are representative of the particles that constitute nuclear slurries, for example, and those commonly encountered in minerals processing and other industries. The focus of future work on this topic would be to determine whether the expressions for f and χ by Thorne and Meral (2008) actually apply to all materials. It may be possible, for example, to generalise those expressions by applying factors that account for the differences between materials, such as a shape or sphericity factor.

8. *Modelling of concentration profiles and PSD.* Particle concentration profiles in pipe flow were presented in Chapter 5, but no data – either experimental or numerical – could be found in the literature in similar flow conditions and so none could be used for comparison. Also presented in Chapter 5 were estimates of the acoustic backscatter and attenuation coefficients based on the median measured particle size, d_{50}, and quartz-sand data available in the literature (Thorne and Meral, 2008). It is suggested that future studies that employ the dual-frequency inversion method to construct particle concentration profiles in pipe flow should contain: (a) a comparison to predictions of particle concentration profiles from a suitable model, such as that of Kaushal and Tomita (2013), which agreed extremely well with several

experimental studies; and (b) a more detailed estimate of the acoustic coefficients based on a numerical integration of the entire particle size distribution (PSD), for validation purposes.

9. *Universal scalings.* Phase diagrams of bedforms consisting of jagged plastic beads in pipe flow were presented in Chapter 6. One (Figure 6-41) was directly comparable to that given by Ouriemi *et al.* (2009) for glass spheres, but it was found that the thresholds delineating various bedform types, as well as the characteristics of the bedform types themselves, did not coincide, presumably because of the differences in flow conditions and the physical properties of the particle species. It was suggested (in Section 6.3.5) that both a full set of initial conditions – at least d_{90}, h_b, H_e, t, U_{flow} and ν, where H_e is an equivalent fluid depth, as illustrated in Figure 6-35 – as well as the magnitude and type of perturbation applied to the bed be included in any dimensional analysis that is performed in order to derive a universal scaling for bedform dimensions, *etc*. However, it is also suggested that a similar universal scaling could be found, using arguments similar to those provided in Section 6.3.5, for the limit deposition velocity, U_{c2}, results for which were given in Section 4.2.7.

8 References

ACAROGLU, E. R. 1968. *Sediment Transport in Conveyance Systems.* Ph.D., Cornell University.

ADAMS, J. F. W., FAIRWEATHER, M. and YAO, J. 2011. Particle deposition in circular pipes with variable bed height. *Journal of Physics: Conference Series,* 318**,** 052001.

ADMIRAAL, D. M. and GARCÍA, M. H. 2000. Laboratory measurement of suspended sediment concentration using an Acoustic Concentration Profiler (ACP). *Exp. Fluids,* 28**,** 116-127.

AINSLIE, M. A. and MCCOLM, J. G. 1998. A simplified formula for viscous and chemical absorption in sea water. *J. Acoust. Soc. Am.,* 103**,** 1671-1672.

ALLEGRA, J. R. and HAWLEY, S. A. 1972. Attenuation of sound in suspensions and emulsions - theory and experiments. *J. Acoust. Soc. Am.,* 51**,** 1545-1564.

ALLEN, P. A. 1997. *Earth Surface Processes,* Oxford, Blackwell Science.

ASHLEY, G. M. 1990. Classification of large-scale subaqueous bedforms: a new look an old problem. *J. Sediment. Petrol.,* 60**,** 160-172.

BAAS, J. H. 1994. A flume study on the development and equilibrium morphology of current ripples in very fine sand. *Sedimentology,* 41**,** 185-209.

BABICK, F., HINZE, F., STINTZ, M. and RIPPERGER, S. 1998. Ultrasonic spectrometry for particle size analysis in dense submicron suspensions. *Part. Part. Syst. Charact.,* 15**,** 230-236.

BACHALO, W. D. 1994. Experimental methods in multiphase flows. *Int. J. Multiphas. Flow,* 20**,** 261-295.

BEST, J. 2005. The fluid dynamics of river dunes: A review and some future research directions. *J. Geophys. Res.-Earth,* 110.

BETTERIDGE, K. F. E., THORNE, P. D. and COOKE, R. D. 2008. Calibrating multi-frequency acoustic backscatter systems for studying near-bed suspended sediment transport processes. *Cont. Shelf Res.,* 28**,** 227-235.

BUFFINGTON, J. M. 1999. The legend of A. F. Shields. *J. Hydraul. Eng.-ASCE,* 125**,** 376-387.

CARLSON, J. 2002. *Ultrasonic characterization of materials and multiphase flows.* Ph.D., Lulea University.

CHALLIS, R. E., POVEY, M. J. W., MATHER, M. L. and HOLMES, A. K. 2005. Ultrasound techniques for characterizing colloidal dispersions. *Rep. Prog. Phys.,* 68**,** 1541-1637.

CHANG, C. Y. and POWELL, R. L. 1994. The rheology of bimodal hard-sphere suspensions. *Phys. Fluids,* 6**,** 1628-1636.

CHARRU, F. 2006. Selection of the ripple length on a granular bed sheared by a liquid flow. *Phys. Fluids,* 18.

CHARRU, F. and FRANKLIN, E. M. 2012. Subaqueous barchan dunes in turbulent shear flow. Part 2. Fluid flow. *J. Fluid Mech.,* 694**,** 131-154.

CHARRU, F. and HINCH, E. J. 2006. Ripple formation on a particle bed sheared by a viscous liquid. Part 1. Steady flow. *J. Fluid Mech.,* 550**,** 111-121.

CHARRU, F. and MOUILLERON-ARNOULD, H. 2002. Instability of a bed of particles sheared by a viscous flow. *J. Fluid Mech.,* 452**,** 303-323.

CHARRU, F., MOUILLERON, H. and EIFF, O. 2004. Erosion and deposition of particles on a bed sheared by a viscous flow. *J. Fluid Mech.,* 519**,** 55-80.

COLEMAN, S. E., FEDELE, J. J. and GARCÍA, M. H. 2003. Closed-conduit bed-form

initiation and development. *J. Hydraul. Eng.-ASCE,* 129**,** 956-965.
COLEMAN, S. E. and MELVILLE, B. W. 1996. Initiation of bed forms on a flat sand bed. *J. Hydraul. Eng.-ASCE,* 122**,** 301-310.
COLEMAN, S. E. and NIKORA, V. I. 2011. Fluvial dunes: initiation, characterization, flow structure. *Earth Surf. Proc. Land.,* 36**,** 39-57.
COLEMAN, S. E., ZHANG, M. H. and CLUNIE, T. M. 2005. Sediment-wave development in subcritical water flow. *J. Hydraul. Eng.-ASCE,* 131**,** 106-111.
COLOMBINI, M. and STOCCHINO, A. 2011. Ripple and dune formation in rivers. *J. Fluid Mech.,* 673**,** 121-131.
CROWE, C. R. E. 2006. *Multiphase flow handbook,* Boca Raton, Florida, CRC: Taylor & Francis.
DEN TOONDER, J. M. J. and NIEUWSTADT, F. T. M. 1997. Reynolds number effects in a turbulent pipe flow for low to moderate Re. *Phys. Fluids,* 9**,** 3398-3409.
DORON, P. and BARNEA, D. 1993. A three-layer model for solid-liquid flow in horizontal pipes. *Int. J. Multiphas. Flow,* 19**,** 1029-1043.
DORON, P. and BARNEA, D. 1995. Pressure drop and limit deposit velocity for solid-liquid flow in pipes. *Chem. Eng. Sci.,* 50**,** 1595-1604.
DORON, P. and BARNEA, D. 1996. Flow pattern maps for solid-liquid flow in pipes. *Int. J. Multiphas. Flow,* 22**,** 273-283.
DORON, P., GRANICA, D. and BARNEA, D. 1987. Slurry flow in horizontal pipes - experimental and modeling. *Int. J. Multiphas. Flow,* 13**,** 535-547.
DOWNING, A., THORNE, P. D. and VINCENT, C. E. 1995. Backscattering from a suspension in the near field of a piston transducer. *J. Acoust. Soc. Am.,* 97**,** 1614-1620.
DUKHIN, A. S. and GOETZ, P. J. 2002. *Ultrasound for Characterizing Colloids: Particle Sizing, Zeta Potential, Rheology,* Amsterdam, Elsevier Science.
DURAND, R. 1953. Basic relationships of the transportation of solids in pipes - experimental research. *Proceedings: Minnesota International Hydraulic Convention.* University of Minnesota, Minneapolis, Minnesota.
DURAND, R. and CONDOLIOS, E. 1952. Paper VI: The hydraulic transport of coal and solids materials in pipes. *Colloquium on the Hydraulic Transport of Coal.* National Coal Board, London.
EATON, J. K. and FESSLER, J. R. 1994. Preferential concentration of particles by turbulence. *Int. J. Multiphas. Flow,* 20**,** 169-209.
EGGELS, J. G. M., UNGER, F., WEISS, M. H., WESTERWEEL, J., ADRIAN, R. J., FRIEDRICH, R. and NIEUWSTADT, F. T. M. 1994. Fully developed turbulent pipe flow - a comparison between direct numerical simulation and experiment. *J. Fluid Mech.,* 268**,** 175-209.
EKAMBARA, K., SANDERS, R. S., NANDAKUMAR, K. and MASLIYAH, J. H. 2009. Hydrodynamic simulation of horizontal slurry pipeline flow using ANSYS-CFX. *Ind. Eng. Chem. Res.,* 48**,** 8159-8171.
ENGELUND, F. and FREDSØE, J. 1970. Instability of erodible beds. *J. Fluid Mech.,* 42**,** 225-244.
ENGELUND, F. and FREDSØE, J. 1982. Sediment ripples and dunes. *Annu. Rev. Fluid Mech.,* 14**,** 13-37.
EPSTEIN, P. S. and CARHART, R. R. 1953. The absorption of sound in suspensions and emulsions: 1. Water fog in air. *J. Acoust. Soc. Am.,* 25**,** 553-565.
ESKIN, D., LEONENKO, Y. and VINOGRADOV, O. 2004. On a turbulence model for slurry flow in pipelines. *Chem. Eng. Sci.,* 59**,** 557-565.
ESKIN, D. and SCARLETT, B. 2005. Model of the solids deposition in hydrotransport:

An energy approach. *Ind. Eng. Chem. Res.,* 44**,** 1284-1290.

ESTEY, S. D. and HU, T. A. 1998. Flow velocity analysis for avoidance of solids deposition during transport of Hanford tank waste slurries. Richland, WA: Lockheed Martin Hanford Corporation.

FLEMMING, B. W. Year. The role of grain size, water depth and flow velocity as scaling factors controlling the size of subaqueous dunes. *In:* TRENTESAUX, A. and GARLAN, T., eds. Proceedings of Marine Sandwave Dynamics, 2000 University of Lille. Lille, France, 23-24.

FRANCOIS, R. E. and GARRISON, G. R. 1982. Sound absorption based on ocean measurements: Part I: Pure water and magnesium sulfate contributions. *J. Acoust. Soc. Am.,* 72**,** 896-907.

FRANKLIN, E. M. and CHARRU, F. 2009. Morphology and displacement of dunes in a closed-conduit flow. *Powder Technol.,* 190**,** 247-251.

FRANKLIN, E. M. and CHARRU, F. 2011. Subaqueous barchan dunes in turbulent shear flow. Part 1. Dune motion. *J. Fluid Mech.,* 675**,** 199-222.

FREY, P. and CHURCH, M. 2011. Bedload: a granular phenomenon. *Earth Surf. Proc. Land.,* 36**,** 58-69.

FURLAN, J. M., MUNDLA, V., KADAMBI, J., HOYT, N., VISINTAINER, R. and ADDIE, G. 2012. Development of A-scan ultrasound technique for measuring local particle concentration in slurry flows. *Powder Technol.,* 215-16**,** 174-184.

GAD-EL-HAK, M. and BANDYOPADHYAY, P. R. 1994. Reynolds number effects in wall-bounded turbulent flows. *Appl. Mech. Rev.,* 47**,** 307-365.

GAO, P. 2008. Transition between two bed-load transport regimes: Saltation and sheet flow. *J. Hydraul. Eng.-ASCE,* 134**,** 340-349.

GARCÍA, M. H. 2000. The legend of A.F. Shields. *J. Hydraul. Eng.-ASCE,* 126**,** 718-720.

GARCÍA, M. H. (ed.) 2008. *Sedimentation Engineering: Process, Measurements, Modeling and Practice,* Reston, Virginia: American Society of Civil Engineers.

GEORGE, W. K. 2007. Is there a universal log law for turbulent wall-bounded flows? *Philos. Trans. R. Soc. Lond. A-Math. Phys. Sci.,* 365**,** 789-806.

GILLIES, R. G., SCHAAN, J., SUMNER, R. J., MCKIBBEN, M. J. and SHOOK, C. A. 2000. Deposition velocities for Newtonian slurries in turbulent flow. *Can. J. Chem. Eng.,* 78**,** 704-708.

GILLIES, R. G. and SHOOK, C. A. 1994. Concentration distributions of sand slurries in horizontal pipe flow. *Part. Sci. Technol.,* 12**,** 45-69.

GILLIES, R. G. and SHOOK, C. A. 2000. Modelling high concentration settling slurry flows. *Can. J. Chem. Eng.,* 78**,** 709-716.

GILLIES, R. G., SHOOK, C. A. and WILSON, K. C. 1991. An improved two layer model for horizontal slurry pipeline flow. *Can. J. Chem. Eng.,* 69**,** 173-178.

GILLIES, R. G., SHOOK, C. A. and XU, J. H. 2004. Modelling heterogeneous slurry flows at high velocities. *Can. J. Chem. Eng.,* 82**,** 1060-1065.

GORE, R. A. and CROWE, C. T. 1989. Effect of particle size on modulating turbulent intensity. *Int. J. Multiphas. Flow,* 15**,** 279-285.

GORE, R. A. and CROWE, C. T. 1991. Modulation of turbulence by a dispersed phase. *J. Fluid. Eng.-T. ASME,* 113**,** 304-307.

GRAF, W. H. 1984. *Hydraulics of Sediment Transport*, Water Resources Publications.

GREENWOOD, M. S., MAI, J. L. and GOOD, M. S. 1993. Attenuation measurements of ultrasound in a kaolin-water slurry: A linear dependence upon frequency. *J. Acoust. Soc. Am.,* 94**,** 908-916.

HA, H. K., MAA, J. P. Y., PARK, K. and KIM, Y. H. 2011. Estimation of high-resolution sediment concentration profiles in bottom boundary layer using pulse-

coherent acoustic Doppler current profilers. *Mar. Geol.,* 279**,** 199-209.
HAALAND, S. E. 1983. Simple and explicit formulas for the friction factor in turbulent pipe flow. *J. Fluid. Eng.-T. ASME,* 105**,** 89-90.
HARBOTTLE, D. 2008. *Physical modelling of colloidal slurry flow.* Ph.D., University of Leeds.
HASTINGS, J. J., RHODES, D., FELLERMAN, A. S., MCKENDRICK, D. and DIXON, C. 2007. New approaches for sludge management in the nuclear industry. *Powder Technol.,* 174**,** 18-24.
HAY, A. E. 1983. On the remote acoustic detection of suspended sediment at long wavelengths. *J. Geophys. Res.-Oc. Atm.,* 88**,** 7525-7542.
HAY, A. E. 1991. Sound scattering from a particle-laden, turbulent jet. *J. Acoust. Soc. Am.,* 90**,** 2055-2074.
HAY, A. E. and SHENG, J. Y. 1992. Vertical profiles of suspended sand concentration and size from multifrequency acoustic backscatter. *J. Geophys. Res.-Oceans,* 97**,** 15661-15677.
HINZE, J. O. 1959. *Turbulence: an introduction to its mechanism and theory,* New York, McGraw-Hill.
HIPP, A. K., STORTI, G. and MORBIDELLI, M. 2002. Acoustic characterization of concentrated suspensions and emulsions. 2. Experimental validation. *Langmuir,* 18**,** 405-412.
HULTMARK, M., BAILEY, S. C. C. and SMITS, A. J. 2010. Scaling of near-wall turbulence in pipe flow. *J. Fluid Mech.,* 649**,** 103-113.
HULTMARK, M., VALLIKIVI, M., BAILEY, S. C. C. and SMITS, A. J. 2012. Turbulent pipe flow at extreme Reynolds numbers. *Phys. Rev. Lett.,* 108.
HUNTER, T. N., DARLISON, L., PEAKALL, J. and BIGGS, S. 2012a. Using a multi-frequency acoustic backscatter system as an in situ high concentration dispersion monitor. *Chem. Eng. Sci.,* 80**,** 409-418.
HUNTER, T. N., PEAKALL, J. and BIGGS, S. 2012b. An acoustic backscatter system for in situ concentration profiling of settling flocculated dispersions. *Miner. Eng.,* 27**,** 20-27.
HUNTER, T. N., PEAKALL, J. and BIGGS, S. R. 2011. Ultrasonic velocimetry for the in situ characterisation of particulate settling and sedimentation. *Miner. Eng.,* 24**,** 416-423.
HURTHER, D., THORNE, P. D., BRICAULT, M., LEMMIN, U. and BARNOUD, J.-M. 2011. A multi-frequency Acoustic Concentration and Velocity Profiler (ACVP) for boundary layer measurements of fine-scale flow and sediment transport processes. *Coast. Eng.,* 58**,** 594-605.
ISMAIL, H. M. 1952. Turbulent transfer mechanism and suspended sediment in closed channels. *Trans. Am. Soc. Civ. Eng.,* 117**,** 409-434.
JULIEN, P. Y. and KLAASSEN, G. J. 1995. Sand-dune geometry of large rivers during floods. *J. Hydraul. Eng.-ASCE,* 121**,** 657-663.
KARABELAS, A. J. 1977. Vertical distribution of dilute suspensions in turbulent pipe flow. *AlChE J.,* 23**,** 426-434.
KAUSHAL, D. R., SESHADRI, V. and SINGH, S. N. 2002. Prediction of concentration and particle size distribution in the flow of multi-sized particulate slurry through rectangular duct. *Appl. Math. Model.,* 26**,** 941-952.
KAUSHAL, D. R. and TOMITA, Y. 2002. Solids concentration profiles and pressure drop in pipeline flow of multisized particulate slurries. *Int. J. Multiphas. Flow,* 28**,** 1697-1717.
KAUSHAL, D. R. and TOMITA, Y. 2013. Prediction of concentration distribution in

pipeline flow of highly concentrated slurry. *Part. Sci. Technol.,* 31**,** 28-34.
KAYE, G. W. C. and LABY, T. H. 1995. *Tables of physical and chemical constants,* London, Longman.
KENNEDY, J. F. 1963. The mechanics of dunes and antidunes in erodible-bed channels. *J. Fluid Mech.,* 16**,** 521-544.
KIM, J., MOIN, P. and MOSER, R. 1987. Turbulence statistics in fully developed channel flow at low Reynolds number. *J. Fluid Mech.,* 177**,** 133-166.
KOLMOGOROV, A. N. 1991a. Dissipation of energy in the locally isotropic turbulence. *Proc. R. Soc. London Ser. A,* 434**,** 15-17.
KOLMOGOROV, A. N. 1991b. The local structure of turbulence in incompressible viscous fluid for very large Reynolds numbers. *Proc. R. Soc. London Ser. A,* 434**,** 9-13.
KRIEGEL, E. and BRAUER, H. 1966. *Hydraulischer Transport körniger Feststoffe durch waagerechte Rohrleitungen,* Düsseldorf, VDI-Verlag.
KULICK, J. D., FESSLER, J. R. and EATON, J. K. 1994. Particle response and turbulence modification in fully developed channel flow. *J. Fluid Mech.,* 277**,** 109-134.
KURU, W. C., LEIGHTON, D. T. and MCCREADY, M. J. 1995. Formation of waves on a horizontal erodible bed of particles. *Int. J. Multiphas. Flow,* 21**,** 1123-1140.
KYTÖMAA, H. K. 1995. Theory of sound propagation in suspensions - a guide to particle size and concentration characterization. *Powder Technol.,* 82**,** 115-121.
LAUFER, J. 1954. Report 1174: The structure of turbulence in fully developed pipe flow. Washington, D.C.: National Bureau of Standards.
LAWN, C. J. 1971. Determination of rate of dissipation in turbulent pipe flow. *J. Fluid Mech.,* 48**,** 477-505.
LEEDER, M. 2011. *Sedimentology and Sedimentary Basins: From Turbulence to Tectonics,* Oxford, Wiley-Blackwell.
LEMMIN, U. and ROLLAND, T. 1997. Acoustic velocity profiler for laboratory and field studies. *J. Hydraul. Eng.-ASCE,* 123**,** 1089-1098.
LHERMITTE, R. and LEMMIN, U. 1994. Open-channel flow and turbulence measurement by high-resolution Doppler sonar. *J. Atmos. Ocean. Tech.,* 11**,** 1295-1308.
LIN, C. W. and TRUSLER, J. P. M. 2012. The speed of sound and derived thermodynamic properties of pure water at temperatures between (253 and 473) K and at pressures up to 400 MPa. *J. Chem. Phys.,* 136.
MAJUMDER, A. K. 2007. Settling velocities of particulate systems - a critical review of some useful models. *Miner. Metall. Process,* 24**,** 237-242.
MARTIENSSEN, W. and WARLIMONT, H. 2006. *Springer Handbook of Condensed Matter and Materials Data*, Springer.
MARUSIC, I., MONTY, J. P., HULTMARK, M. and SMITS, A. J. 2013. On the logarithmic region in wall turbulence. *J. Fluid Mech.,* 716.
MATOUŠEK, V. 2005. Research developments in pipeline transport of settling slurries. *Powder Technol.,* 156**,** 43-51.
MATOUŠEK, V. 2009. Concentration profiles and solids transport above stationary deposit in enclosed conduit. *J. Hydraul. Eng.-ASCE,* 135**,** 1101-1106.
MCCLEMENTS, D. J. 1991. Ultrasonic characterization of emulsions and suspensions. *Adv. Colloid Interface Sci.,* 37**,** 33-72.
MCKEON, B. J., LI, J., JIANG, W., MORRISON, J. F. and SMITS, A. J. 2004a. Further observations on the mean velocity distribution in fully developed pipe flow. *J. Fluid Mech.,* 501**,** 135-147.

McKeon, B. J., Swanson, C. J., Zagarola, M. V., Donnelly, R. J. and Smits, A. J. 2004b. Friction factors for smooth pipe flow. *J. Fluid Mech.,* 511**,** 41-44.

McLelland, S. J. 2010. Observing bedload/suspended load using multi-frequency acoustic backscatter. *In:* Gray, J. R., Laronne, J. B. and Marr, J. D. G. (eds.) *Bedload-surrogate monitoring technologies: U.S. Geological Survey Scientific Investigations Report 2010-5091.*

Met-Flow 2002. UVP monitor model UVP-Duo with software version 3. Revision 5 ed. Lausanne, Switzerland: *Met-Flow* SA.

Moate, B. D. and Thorne, P. D. 2009. Measurements and inversion of acoustic scattering from suspensions having broad size distributions. *J. Acoust. Soc. Am.,* 126**,** 2905-2917.

Moate, B. D. and Thorne, P. D. 2013. Scattering from suspended sediments having different and mixed mineralogical compositions: Comparison of laboratory measurements and theoretical predictions. *J. Acoust. Soc. Am.,* 133**,** 1320-34.

Monty, J. P., Hutchins, N., Ng, H. C. H., Marusic, I. and Chong, M. S. 2009. A comparison of turbulent pipe, channel and boundary layer flows. *J. Fluid Mech.,* 632**,** 431-442.

Moody, L. F. 1944. Friction factors for pipe flow. *Transactions of the American Society of Mechanical Engineers,* November**,** 671-684.

Morrison, J. F., McKeon, B. J., Jiang, W. and Smits, A. J. 2004. Scaling of the streamwise velocity component in turbulent pipe flow. *J. Fluid Mech.,* 508**,** 99-131.

Nakagawa, H. and Tsujimoto, T. 1984. Spectral analysis of sand bed instability. *J. Hydraul. Eng.-ASCE,* 110**,** 467-483.

NDA 2011. The 2010 UK Radioactive Waste Inventory: Main Report, URN 10D/985, NDA/ST/STY (11) 0004.

NDA. 2013. *RE: Detailed water stream-specific information sheets, by personal communication.*

Orfanidis, S. J. 1996. *Introduction to signal processing*, Prentice Hall.

Oroskar, A. R. and Turian, R. M. 1980. The critical velocity in pipeline flows of slurries. *AlChE J.,* 26**,** 550-558.

Ott, W. P. and van Uchelen, J. C. no date. Application of similarity principles and turbulence research to bed-load movement, Publication no. 167. Pasadena: California Institute of Technology.

Ouellette, N. T., Xu, H. T., Bourgoin, M. and Bodenschatz, E. 2006. An experimental study of turbulent relative dispersion models. *New J. Phys.,* 8**,** 109.

Ouriemi, M., Aussillous, P. and Guazzelli, E. 2009. Sediment dynamics. Part 2. Dune formation in pipe flow. *J. Fluid Mech.,* 636**,** 321-336.

Ouriemi, M., Aussillous, P., Medale, M., Peysson, Y. and Guazzelli, E. 2007. Determination of the critical Shields number for particle erosion in laminar flow. *Phys. Fluids,* 19.

Ouriemi, M., Chauchat, J., Aussillous, P., Medale, M. and Guazzelli, E. 2010. Sediment transport and dunes in pipe flow. *"ICMF 2010", 7th International Conference on Multiphase Flow.* Tampa, Florida.

Papista, E., Dimitrakis, D. and Yiantsios, S. G. 2011. Direct numerical simulation of incipient sediment motion and hydraulic conveying. *Ind. Eng. Chem. Res.,* 50**,** 630-638.

Pedocchi, F. and Garcia, M. H. 2012. Acoustic measurement of suspended sediment concentration profiles in an oscillatory boundary layer. *Cont. Shelf Res.,* 46**,** 87-95.

PEKER, S. M. and HELVACI, S. S. 2007. *Solid-Liquid Two Phase Flow*, Elsevier.
PERRY, A. E., HENBEST, S. and CHONG, M. S. 1986. A theoretical and experimental study of wall turbulence. *J. Fluid Mech.,* 165**,** 163-199.
POELMA, C. and OOMS, G. 2006. Particle-turbulence interaction in a homogeneous, isotropic turbulent suspension. *Appl. Mech. Rev.,* 59**,** 78-90.
POELMA, C., WESTERWEEL, J. and OOMS, G. 2007. Particle-fluid interactions in grid-generated turbulence. *J. Fluid Mech.,* 589**,** 315-351.
POLOSKI, A. P., ETCHELLS, A. W., CHUN, J., ADKINS, H. E., CASELLA, A. M., MINETTE, M. J. and YOKUDA, S. T. 2010. A pipeline transport correlation for slurries with small but dense particles. *Can. J. Chem. Eng.,* 88**,** 182-189.
POVEY, M. J. W. 1997. *Ultrasonic Techniques for Fluids Characterization,* San Diego, Academic Press.
PUGH, F. J. and WILSON, K. C. 1999. Velocity and concentration distributions in sheet flow above plane beds. *J. Hydraul. Eng.-ASCE,* 125**,** 117-125.
RAUDKIVI, A. J. 1997. Ripples on stream bed. *J. Hydraul. Eng.-ASCE,* 123**,** 58-64.
RAUDKIVI, A. J. 1998. *Loose Boundary Hydraulics*, Balkema.
RICHARDS, K. J. 1980. The formation of ripples and dunes on an erodible bed. *J. Fluid Mech.,* 99**,** 597-618.
RICHARDS, S. D., HEATHERSHAW, A. D. and THORNE, P. D. 1996. The effect of suspended particulate matter on sound attenuation in seawater. *J. Acoust. Soc. Am.,* 100**,** 1447-1450.
RICHARDSON, J. F. and ZAKI, W. N. 1954. The sedimentation of a suspension of uniform spheres under conditions of viscous flow. *Chem. Eng. Sci.,* 3**,** 65-73.
RICHTER, A., VOIGT, T. and RIPPERGER, S. 2007. Ultrasonic attenuation spectroscopy of emulsions with droplet sizes greater than 10 μm. *J. Colloid Interface Sci.,* 315**,** 482-492.
RILEY, K. K. F., HOBSON, M. P. and BENCE, S. S. J. 2006. *Mathematical Methods for Physics and Engineering,* Cambridge, Cambridge University Press.
ROBERSON, J. A. and CROWE, C. T. 1996. *Engineering Fluid Mechanics,* New York, John Wiley & Sons.
SCHLICHTING, H. and GERSTEN, K. 2000. *Boundary-Layer Theory,* New Delhi, Springer.
SHAMES, I. H. 2003. *Mechanics of fluids,* New York, McGraw-Hill.
SHIROLKAR, J. S., COIMBRA, C. F. M. and MCQUAY, M. Q. 1996. Fundamental aspects of modeling turbulent particle dispersion in dilute flows. *Prog. Energy Combust. Sci.,* 22**,** 363-399.
SHOOK, C. A., DANIEL, S. M., SCOTT, J. A. and HOLGATE, J. P. 1968. Flow of suspensions in pipelines, Part 2: Two mechanisms of particle suspensions. *Can. J. Chem. Eng.,* 46**,** 238-244.
SHUKLA, A., PRAKASH, A. and ROHANI, S. 2007. Particles settling studies using ultrasonic techniques. *Powder Technol.,* 177**,** 102-111.
SHUKLA, A., PRAKASH, A. and ROHANI, S. 2010. Particle size monitoring in dense suspension using ultrasound with an improved model accounting for low-angle scattering. *AlChE J.,* 56**,** 2825-2837.
SIMONS, D. B. and RICHARDSON, E. V. 1961. Forms of bed roughness in alluvial channels. *J. Hydr. Div.-ASCE,* 87**,** 87-105.
SIMONS, D. B. and RICHARDSON, E. V. 1966. Professional Paper 422-J: Resistance to flow in alluvial channels. Washington: U.S. Geological Survey.
STAKUTIS, V. J., MORSE, R. W., DILL, M. and BEYER, R. T. 1955. Attenuation of ultrasound in aqueous suspensions. *J. Acoust. Soc. Am.,* 27**,** 539-546.
STICKEL, J. J. and POWELL, R. L. 2005. Fluid mechanics and rheology of dense

suspensions. *Annu. Rev. Fluid Mech.,* 37**,** 129-149.
SUMER, B. M. and BAKIOGLU, M. 1984. On the formation of ripples on an erodible bed. *J. Fluid Mech.,* 144**,** 177-190.
SUMER, B. M., KOZAKIEWICZ, A., FREDSOE, J. and DEIGAARD, R. 1996. Velocity and concentration profiles in sheet-flow layer of movable bed. *J. Hydraul. Eng.-ASCE,* 122**,** 549-558.
SUNG, C. C., HUANG, Y. J., LAI, J. S. and HWANG, G. W. 2008. Ultrasonic measurement of suspended sediment concentrations: an experimental validation of the approach using kaolin suspensions and reservoir sediments under variable thermal conditions. *Hydrol. Process.,* 22**,** 3149-3154.
TAKAHASHI, H., MASUYAMA, T. and NODA, K. 1989. Unstable flow of a solid-liquid mixture in a horizontal pipe. *Int. J. Multiphas. Flow,* 15**,** 831-841.
TENNEKES, H. and LUMLEY, J. L. 1972. *A First Course in Turbulence,* Cambridge, Mass., MIT Press.
THOMAS, D. G. 1964. Periodic phenomena observed with spherical particles in horizontal pipes. *Science,* 144**,** 534-536.
THORNE, P. D. and BUCKINGHAM, M. J. 2004. Measurements of scattering by suspensions of irregularly shaped sand particles and comparison with a single parameter modified sphere model. *J. Acoust. Soc. Am.,* 116**,** 2876-2889.
THORNE, P. D. and HANES, D. M. 2002. A review of acoustic measurement of small-scale sediment processes. *Cont. Shelf Res.,* 22**,** 603-632.
THORNE, P. D., HURTHER, D. and MOATE, B. D. 2011. Acoustic inversions for measuring boundary layer suspended sediment processes. *J. Acoust. Soc. Am.,* 130**,** 1188-1200.
THORNE, P. D. and MERAL, R. 2008. Formulations for the scattering properties of suspended sandy sediments for use in the application of acoustics to sediment transport processes. *Cont. Shelf Res.,* 28**,** 309-317.
TSUJI, Y. 2000. Activities in discrete particle simulation in Japan. *Powder Technol.,* 113**,** 278-286.
TSUJI, Y. and MORIKAWA, Y. 1982. LDV measurement of an air-solid two-phase flow in a horizontal pipe. *J. Fluid Mech.,* 120**,** 385-409.
TURIAN, R. M., HSU, F. L. and MA, T. W. 1987. Estimation of the critical velocity in pipeline flow in slurries. *Powder Technol.,* 51**,** 35-47.
TURIAN, R. M. and YUAN, T. F. 1977. Flow of slurries in pipelines. *AlChE J.,* 23**,** 232-243.
URICK, R. J. 1948. The absorption of sound in suspensions of irregular particles. *J. Acoust. Soc. Am.,* 20**,** 283-289.
VAN RIJN, L. C. 1984a. Sediment transport, part I: bed load transport. *J. Hydraul. Eng.-ASCE,* 110**,** 1431-1456.
VAN RIJN, L. C. 1984b. Sediment transport, part III: bed forms and alluvial roughness. *J. Hydraul. Eng.-ASCE,* 110**,** 1733-1754.
VANONI, V. A. 1964. Report KH-R-7: Measurements of critical shear stress for entraining fine sediments in a boundary layer. Pasadena: California Institute of Technology.
WANG, Y. H. and YU, G. H. 2007. Velocity and concentration profiles of particle movement in sheet flows. *Adv. Water Resour.,* 30**,** 1355-1359.
WASP, E. J., KENNY, J. P. and GANDHI, R. L. 1977. *Solid-liquid flow slurry pipeline transportation,* University of Michigan, Ann Arbor, Trans Tech Publications.
WEISSTEIN, E. W. *"Circular Segment." From MathWorld--A Wolfram Web Resource*

[Online]. Available: http://mathworld.wolfram.com/CircularSegment.html [Accessed 11/01/2013].

WILLIAMS, R. A., XIE, C. G., BRAGG, R. and AMARASINGHE, W. P. K. 1990. Experimental techniques for monitoring sedimentation in optically opaque systems. *Colloid. Surface.,* 43**,** 1-32.

WILSON, K. C. 1965. Derivation of the regime equations from relationships for pressurized flow by use of the principle of minimum energy - degradation rate, Civil Engineering Research Report No. 51. Kingston, Ontario: Queen's University.

WILSON, K. C. 2005. Rapid increase in suspended load at high bed shear. *J. Hydraul. Eng.-ASCE,* 131**,** 46-51.

WOSNIK, M., CASTILLO, L. and GEORGE, W. K. 2000. A theory for turbulent pipe and channel flows. *J. Fluid Mech.,* 421**,** 115-145.

WU, X. H. and MOIN, P. 2008. A direct numerical simulation study on the mean velocity characteristics in turbulent pipe flow. *J. Fluid Mech.,* 608**,** 81-112.

YALIN, M. S. and KARAHAN, E. 1979. Inception of sediment transport. *J. Hydr. Div.-ASCE,* 105**,** 1433-1443.

ZAGAROLA, M. V. and SMITS, A. J. 1998. Mean-flow scaling of turbulent pipe flow. *J. Fluid Mech.,* 373**,** 33-79.

ZEDEL, L. and HAY, A. E. 1999. A coherent Doppler profiler for high-resolution particle velocimetry in the ocean: Laboratory measurements of turbulence and particle flux. *J. Atmos. Ocean. Tech.,* 16**,** 1102-1117.

ZEMANEK, J. 1971. Beam behavior within the nearfield of a vibrating piston. *J. Acoust. Soc. Am.,* 49**,** 181-191.

ZISSELMAR, R. and MOLERUS, O. 1979. Investigation of solid-liquid pipe flow with regard to turbulence modulation. *Chem. Eng. J.,* 18**,** 233-239.

A Appendix: Propagation of experimental errors

The most likely sources of experimental uncertainties are identified and quantified algebraically. The four directly measured quantities most likely to affect the results in this study were as follows: beam divergence angle, probe mounting angle, pressure and temperature. The effect of these uncertainties on calculated quantities – the distance from the probe, the mean axial flow velocity and the acoustic attenuation due to water – are assessed for a representative example run, and the total and relative contribution of the various uncertainties are compared and discussed.

The example run for which errors have been quantified is a pipe-flow run with Honite 16 glass beads (*i.e.* a species with an intermediate mean particle size, and therefore subject to attenuation of intermediate severity relative to all the species used) at a nominal volume fraction of ϕ = 1% (*i.e.* an intermediate value) at a flow rate/velocity of Q = 1.72 l s^{-1}/U_{ave} = 1.21 m s^{-1} in which the computed mass concentration varies through the pipe cross-section within the range of $10 \lesssim M \lesssim$ 20 kg m^{-3} (see Figure 5-25). Data from the f = 2 MHz probe mounted at ψ_1 = 135° were used, although extensive reference is made to other particle species and other flow conditions.

In Sections A.1 to A.3, the uncertainties due to acoustic beam divergence, probe mounting angle and the speed of sound, respectively, are derived. Nominal values of the most important experimental parameters, and their associated uncertainties, are summarised in Section A.4. In Sections A.5 to A.7, the effect of these uncertainties on the measurement distance, the mean axial flow velocity and the attenuation due to water, respectively, are quantified and discussed in detail.

A.1 Beam divergence angle

For measurement purposes, the acoustic beam emitted from an ideal transducer would excite scatterers in a very narrow cylindrical region. However, in reality the beam diverges with distance from the probe, and in order to estimate the

corresponding uncertainty in perpendicular distance, a probe is modelled here as a point source and the acoustic pulse as diverging linearly with distance from it (but see Section 3.2.2 for a more accurate description).

At a nominal measurement distance, r, from the probe, with a beam divergence of γ_0 radians, the beam will excite scatterers along an arc made up of points equidistant from the probe, as illustrated in Figure A-1 (and Figure 3-3(b)). The maximum possible deviation in the position of the measurement point, r, from the perpendicular distance from the probe along its axis is denoted as $\mathrm{d}r_1$.

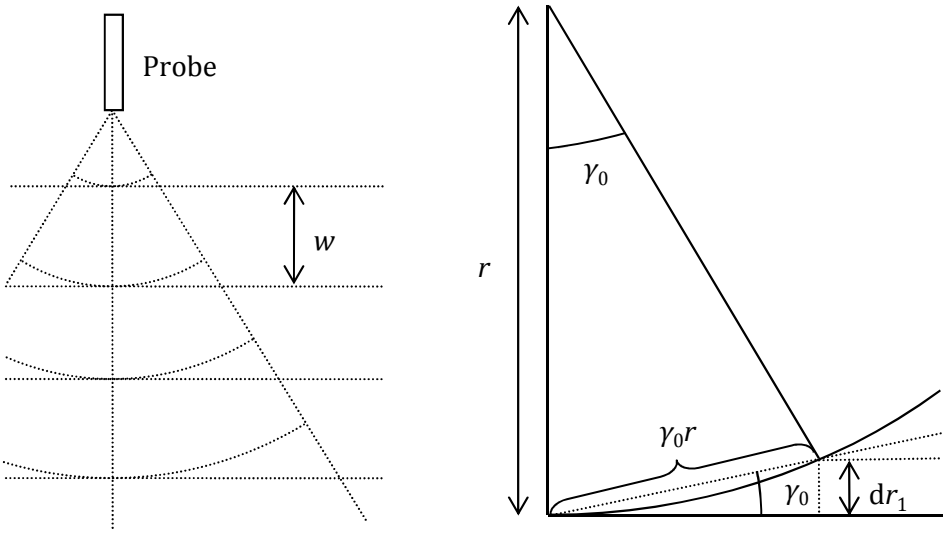

Figure A-1: Linear beam divergence from a point source, where r is distance from probe to measurement point, w is distance between measurement points, γ_0 is beam divergence angle, $\mathrm{d}r_1$ is resulting uncertainty in r.

If the chord length is approximated as the arc length, $\gamma_0 r$, then the following expression can be written:

$$\sin\gamma_0 \approx \frac{\mathrm{d}r_1}{\gamma_0 r}, \qquad [A.1]$$

and if $\gamma_0 \ll 1$, so that $\sin\gamma_0 \approx \gamma_0$, then

$$\mathrm{d}r_1 = r\gamma_0^2. \qquad [A.2]$$

A.2 Probe mounting angle

The uncertainty in the mounting angle for the 2 MHz probe could not be measured directly, so instead an estimate was made based on that for the 4 MHz probe, as follows. In turbulent pipe flow, the mean radial (or wall-normal) velocity ought to be zero at all points through the pipe cross-section. However, a small transverse mean velocity was generally observed of the order of millimetres to tens of millimetres per second with the 4 MHz probe.

That is, the angle at which the probe is mounted onto the pipe has an associated uncertainty that is due purely to imperfect machining of the holes in the pipe wall and plastic clasp through which the probes are inserted. The error in the mounting angle for the 4 MHz (90°) probe is $\mathrm{d}\psi_2$, such that

$$\sin \mathrm{d}\psi_2 \approx \frac{\bar{V}_{\max}}{\bar{U}_{\max}}, \qquad [A.3]$$

where $\bar{U}_{\max}$ and $\bar{V}_{\max}$ are the maxima (*i.e.* centreline values) of the mean velocity profiles in the axial and wall-normal directions and are measured with probes 1 (f = 2 MHz, ψ_1 = 135°) and 2 (f = 4 MHz, ψ_2 = 90°), respectively. In the run chosen as an example, $\bar{V}_{\max} \lesssim 0.01\ \bar{U}_{\max}$ through the whole pipe cross-section, from which a value of $\mathrm{d}\psi_2$ = 0.01 radians = 0.6° was calculated. However, the machining of the hole for the 135° (2 MHz) probe is more difficult mechanically and so it was assumed that $\mathrm{d}\psi_1 = 5\mathrm{d}\psi_2$ = 3°.

The uncertainty in the mounting angle causes errors in both the wall-normal distance, y, and the Doppler velocity, $\bar{U}$, as described in Sections A.5 and A.6, respectively, since data from the 2 MHz probe must be projected onto the wall-normal axis, which transformation requires that the mounting angle, ψ_1, and offset distance, a_{off}, be known, according to Equation [3.28], *i.e.*:

$$y = y' \sin\psi - a_{off}. \qquad [A.4]$$

A.3 Speed of sound

The speed of sound, c, is a function of both temperature, T, and pressure, P. The total uncertainty in c, dc, is then the sum of the components due to temperature and pressure, *i.e.*:

$$\mathrm{d}c = \left[\left(\frac{\partial c}{\partial T}\right)^2 (\mathrm{d}T)^2 + \left(\frac{\partial c}{\partial P}\right)^2 (\mathrm{d}P)^2\right]^{1/2} = [(\mathrm{d}c_1)^2 + (\mathrm{d}c_2)^2]^{1/2}. \quad [A.5]$$

According to Kaye and Laby (1995), at T = 10, 20 and 30 °C, c = 1447.28, 1482.36 and 1509.14 m s^{-1}, respectively, in distilled water. Using the values of c at T = 10 and 30 °C, an estimate of $\partial c/\partial T$ can be made, as follows:

$$\frac{\partial c}{\partial T} \approx \frac{c(T = 30\ ℃) - c(T = 10\ ℃)}{30 - 10}, \quad [A.6]$$

which yields a value of $\partial c/\partial T \approx 3.10$ m s^{-1} K^{-1} at T = 20 °C (*i.e.* standard ambient temperature in the laboratory).

Table A-1: List of temperature measurements over three days. Example run was performed on second day.

Day	Time (24 hr)	Temperature (°C)
13th August 2012	14:30	21.6
	16:30	23.6
14th August 2012	10:00	22.6
	12:30	24.2
	17:00	25.5
15th August 2012	10:00	23.1
	11:45	24.7
	14:00	26.4

The temperature of the fluid was not controlled during experiments, but regular measurements were taken from the mixing tank during experiments using a

thermocouple-type probe thermometer. The uncertainty in temperature, dT, was estimated by reviewing the variation in temperature over the course of three days (13th-15th August 2012), and the example run was performed on the second of the three. The recorded temperatures are listed in Table A-1. It was found that the temperature varied during each day and from day to day due to ambient changes and due to dumping of heat into the fluid from the pump. The average temperature recorded on the second day (14th August) was T = 24.1 °C. However, a nominal temperature of T = 20 °C was used in all calculations, so a value of dT = 4 K is used hereafter.

According to Lin and Trusler (2012), at T = 293.16 K and p = 0.99 and 5.01 MPa, c = 1483.9 and 1490.4 m s^{-1}, respectively, in "high-purity water". Using these values of c, an estimate of $\partial c/\partial p$ can be made, as follows:

$$\frac{\partial c}{\partial P} \approx \frac{c(P = 5.01\ \text{MPa}) - c(P = 0.99\ \text{MPa})}{(5.01 - 0.99) \times 10^6} \qquad [A.7]$$

which yields a value of $\partial c/\partial P \approx 1.62 \times 10^{-6}$ m s^{-1} Pa^{-1} at $P = 10^5$ Pa (*i.e.* standard atmospheric pressure).

The uncertainty, dP, in the pressure, P, was estimated as the pressure drop due to viscous losses, such that (Roberson and Crowe, 1996)

$$\mathrm{d}P = h_p \rho_f g = f \frac{L_p}{D} \frac{\rho_f U_{ave}^2}{2}, \qquad [A.8]$$

where h_p is the head loss, ρ_f is the fluid density, g is the acceleration due to gravity, f is the friction factor and L_p is the length of pipe, which was approximated as L_p = 10 m.

The uncertainty in the speed of sound influences measurement distance through Equation [3.4], which is incorporated into the *UVP-DUO* software, *i.e.*

$$r = \frac{ct}{2}, \qquad [A.9]$$

so if dr_2 is the error in the position of the measurement point, r, due to uncertainties in the speed of sound, then dr_2 is found by differentiating Equation [A.9] with respect to c, to give:

$$dr_2 = dc\frac{t}{2} = dc\frac{r}{c}. \qquad [A.10]$$

A.4 Summary of uncertainties

The nominal values of the beam divergence angle, probe mounting angle, ambient laboratory temperature and pressure, with corresponding uncertainties as estimated in the preceding sections, are summarised in Table A-2. It should be noted that no uncertainty is given for the beam divergence angle, since it is the cause of an error itself.

Table A-2: Summary of nominal values of measured quantities in example run, with corresponding uncertainties. All results for f = 2 MHz at T = 20 °C and P = 10^5 Pa, with Honite 16 glass spheres (d_{50} = 77.0 μm, ρ_s = 2.46 × 10^3 kg m^{-3}) at volume fraction ϕ = 1 %.

Quantity	Symbol	Nominal value	Uncertainty	
			Symbol	Estimated value
Volumetric flow rate	Q	1.72 l s^{-1}	-	-
Bulk flow velocity	U_{ave}	1.21 m s^{-1}	-	-
Reynolds number	Re	51,400	-	-
Friction factor	f	0.0207	-	-
Beam divergence angle	γ_0	4.33°	-	-
Probe mounting angle	ψ_1	135°	$d\psi_1$	± 3°
Temperature	T	20 °C	dT	± 4 °C
Pressure	P	10^5 Pa	dP	± 3530 Pa
Speed of sound	c	1480 m s^{-1}	dc	± 12.4 m s^{-1}
Attenuation due to water	α_w	0.1076 Np m^{-1}	$d\alpha_w$	± 0.00796 Np m^{-1}

It was found that, under the conditions of the example run, dc_1 – the error in the

speed of sound due to temperature variations – was several orders of magnitude greater than dc_2 – *i.e.* that due to pressure variations. These observations demonstrate that T must be measured as precisely as possible. On the other hand, dT was quite large in the example run (dT = ± 4 °C), and dP depends strongly on flow velocity ($dP \propto Q \propto U_{ave}^2$), so at high flow rates the error due to both temperature and pressure should generally be considered.

A.5 Wall-normal distance

The total uncertainty in the measured distance from the probe, r, is found by adding the various components in quadrature as follow:

$$dr = [(dr_1)^2 + (dr_2)^2]^{1/2} \qquad [A.11]$$

where dr_1 and dr_2 are the uncertainties due to beam divergence and the speed of sound, respectively, which were defined earlier. The wall-normal distance, y, depends on both the distance from the probe, r, and the mounting angle, ψ, according to the transformation in Equation [A.4], and so the error in y, dy, is as follows:

$$dy = \left[\left(\frac{\partial y}{\partial r}\right)^2 (dr)^2 + \left(\frac{\partial y}{\partial \psi}\right)^2 (d\psi)^2\right]^{1/2} + [(dy_1)^2 + (dy_2)^2]^{1/2}, \qquad [A.12]$$

where dr and $d\psi$ are known and the derivatives are, by inspection of Equation [A.4], as follows:

$$\frac{\partial y}{\partial \psi} = r \cos \psi_1, \qquad [A.13]$$

$$\frac{\partial y}{\partial r} = \sin \psi_1. \qquad [A.14]$$

The error in the wall-normal distance, y, is shown in Figure A-2 for the example

run. The error, dy, increased in absolute terms with y, and was generally in the range 5 % $\lesssim$ dy/y $\lesssim$ 10 %, with a value of dy/y = 6.3 % at the pipe centreline. It is interesting to note that dr_1 and dr_2, the contributions from beam divergence and the uncertainty in the speed of sound, respectively, were of very similar magnitudes at all distances. Whereas dr_1 cannot be reduced significantly – because it is determined by the mechanical property of the probe – dr_2 can be reduced by more precise measurement of the temperature.

It was also found that dy_2, the contribution to dy from the uncertainty in the mounting angle, exceeded dy_1, the contribution from the distance from the probe by a factor of about five at all distances. Considering that dy_1 incorporates errors in temperature, dT, through dc_1, it is perhaps surprising that an uncertainty in the mounting angle as small as dψ_1 = 3° was able to produce an error of greater magnitude than that due to temperature variations of ± 4 °C.

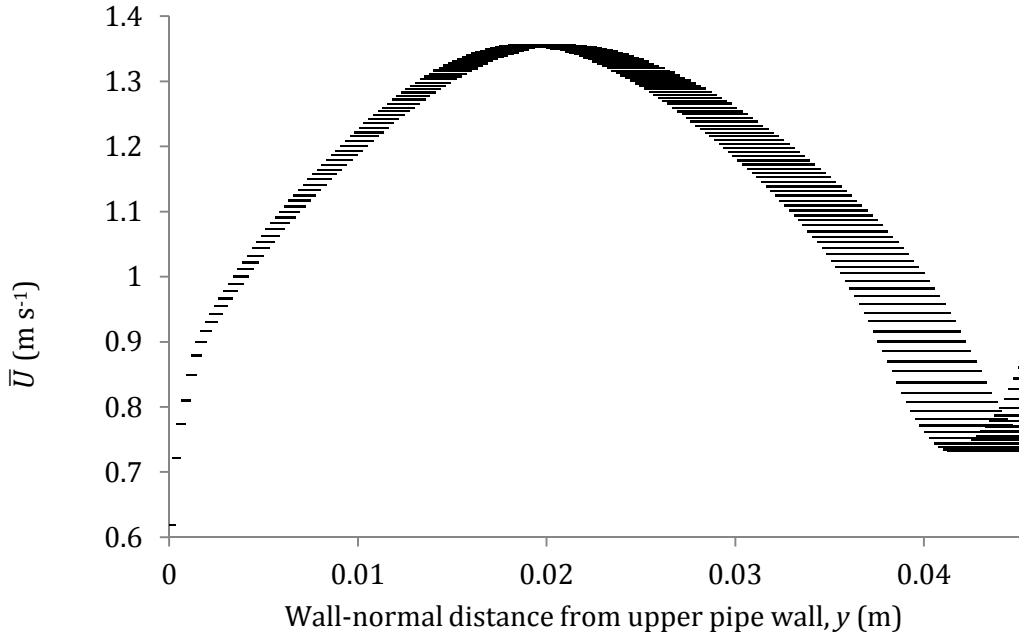

Figure A-2: Mean axial flow velocity, $\overline{U}$, *vs.* wall-normal distance, y, for example run (Honite 16, ϕ = 1%, Q = 1.72 l s^{-1}, U_{ave} = 1.21 m s^{-1}), with errors in y, dy, shown (horizontal bars). Note x-axis is truncated for better visualisation.

A.6 Mean axial velocity

The total error in the mean axial velocity, $\overline{U}$, include contributions from uncertainties in the probe angle, dψ, and speed of sound, dc, such that

$$\mathrm{d}\overline{U} = \left[\left(\frac{\partial \overline{U}}{\partial \psi}\right)^2 (\mathrm{d}\psi)^2 + \left(\frac{\partial \overline{U}}{\partial c}\right)^2 (\mathrm{d}c)^2\right]^{1/2} = [(\mathrm{d}\overline{U}_1)^2 + (\mathrm{d}\overline{U}_2)^2]^{1/2}. \quad [A.15]$$

The instantaneous measured velocity, U_{p1}, measured by probe 1 (*i.e.* the 2 MHz probe), which is positioned at ψ_1 = 135° = 3π/4 radians, depends on the speed of sound as follows, and as described in more detail in Section 3.2.2:

$$U_{p1} = c\frac{\Delta f}{2f_0}, \quad [A.16]$$

and the axial mean velocity, $\overline{U}$, is calculated according to the following expression (Equation 4.1.1):

$$\overline{U_{p1}} = \overline{U}\cos\psi_1. \quad [A.17]$$

The two derivatives in Equation [A.15] are as follows:

$$\frac{\partial \overline{U}}{\partial \psi} = \frac{\partial}{\partial \psi}\left(\frac{\overline{U_{p1}}}{\cos\psi_1}\right) = \overline{U_{p1}}\frac{\tan\psi_1}{\cos\psi_1} = \overline{U}\tan\psi_1, \quad [A.18]$$

$$\frac{\partial \overline{U}}{\partial c} = \frac{\partial \overline{U}}{\partial \overline{U_{p1}}}\frac{\mathrm{d}\overline{U_{p1}}}{\mathrm{d}c} = \frac{1}{\cos\psi_1}\overline{\left(\frac{\Delta f}{2f_0}\right)} = \frac{\overline{U_{p1}}}{c\cos\psi_1} = \frac{\overline{U}}{c}, \quad [A.19]$$

and so all the terms in Equation [A.15] are accounted for.

The error in the mean axial flow velocity, $\overline{U}$, is shown in Figure A-3 for the example run. It is clear from Figure A-3 that, as expected from Equations [A.18] and [A.19],

the error in the mean axial velocity varies linearly with it, reaching a maximum of $d\overline{U} \approx 7.2$ cm s^{-1} at the pipe centreline ($y \approx 0.02$ m). The relative error, which was independent of y, was $d\overline{U}/\overline{U} = 5.3$ %. The upward curvature near the lower pipe wall (*i.e.* beyond $y \approx 0.042$ m), however, is thought to be the result of beam divergence(which, although modelled in this section as being linear, is nonlinear in reality) and reflections from the lower pipe wall, as discussed in Sections 3.6.3 and 4.2.1, and not a result of the experimental errors described in this appendix.

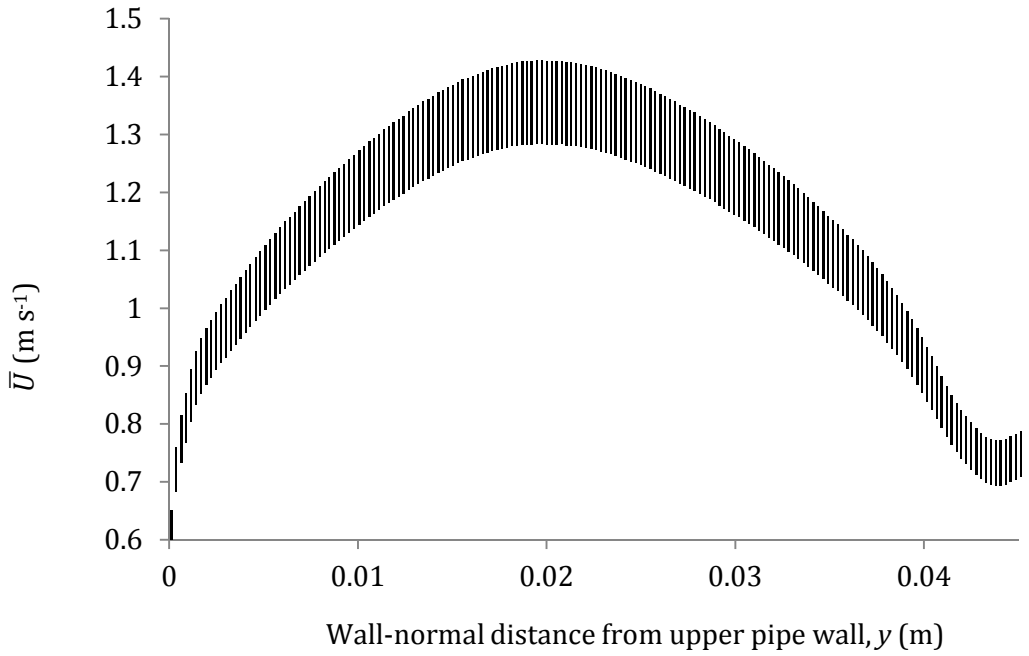

Figure A-3: Mean axial flow velocity, $\overline{U}$, *vs.* wall-normal distance, y, for example run (Honite 16, $\phi = 1\%$, $Q = 1.72$ l s^{-1}, $U_{ave} = 1.21$ m s^{-1}), with errors in $\overline{U}$, $d\overline{U}$, shown (vertical bars). Note x-axis is truncated for better visualisation.

The contributions $d\overline{U}_1$ and $d\overline{U}_2$ from uncertainties in the mounting angle and speed of sound, respectively, were found to be of comparable magnitudes at all distances, $d\overline{U}_1$ generally exceeding $d\overline{U}_2$ by a factor of around five at all points. The condition for the two contributions to be roughly equal, by inspection of Equations [A.18] and [A.19], is as follows:

$$d\psi \tan\psi \approx \frac{dc}{c}. \qquad [A.20]$$

A.7 Acoustic attenuation due to water

As stated in Equation [5.19], which is a modification of the expression given by Ainslie and McColm (1998) at zero salinity, the attenuation due to water depends on both insonification frequency and temperature, as follows:

$$\alpha_w = 0.05641 f^2 \exp\left(-\frac{T}{27}\right), \qquad [A.21]$$

where α_w is in Np m^{-1}, f is in MHz and T is in °C. The dependence on pressure in the expression given by Ainslie and McColm (1998) is extremely weak and was therefore ignored; the uncertainty in frequency was also assumed to be small. The error in α_w is therefore calculated as follows:

$$\mathrm{d}\alpha_w \approx \mathrm{d}T \left|\frac{\partial \alpha_w}{\partial T}\right|. \qquad [A.22]$$

Taking the derivative of Equation [A.21] with respect to temperature gives the following:

$$\frac{\partial \alpha_w}{\partial T} = -2.098 \times 10^{-3} f^2 \exp\left(-\frac{T}{27}\right), \qquad [A.23]$$

which yields a value of $\partial\alpha_w/\partial T \approx$ -3.98 × 10^{-3} Np m^{-1} K^{-1} for f = 2 MHz at T = 20 °C.

The error in the attenuation due to water can be considered to be significant if it is comparable to the attenuation due to suspended particles, *i.e.* if

$$\mathrm{d}\alpha_w \sim \alpha_s. \qquad [A.24]$$

With Honite 16 at f = 2 MHz (ξ_h = 0.0212: see Table 5-2) and with dT = 4 °C, if it is assumed that $\alpha_s \approx \xi_h M_w$, then d$\alpha_w$ = ± 0.0160 Np m^{-1}. So, the condition in Equation [A.24] is satisfied when $M \lesssim 0.75$ kg m^{-3} or $\phi \lesssim 0.03\%$. The error in the attenuation due to water is therefore likely to have influenced the measured values of ξ_h and K_h

(as described in Section 5.2) because $\phi \approx 0.03\%$ is within the range of nominal volume fractions used, albeit towards the lower limit. It should also be noted that the temperature on 10th September 2012 on which the Honite 16 calibration runs were performed varied between 20.3 °C (time: 10:30) and 21.4 °C (12:30), so a value of $\mathrm{d}T = \pm 4$ °C is very conservative. For comparison, with Honite 22, the smallest species, insonified at $f = 4$ MHz, the limiting volume fraction is $\phi \approx 0.04\%$, *i.e.* very similar to that for Honite 16 at $f = 2$ MHz.

It is important to note that the uncertainty in temperature can be invoked to account for the variation in K_h with concentration in the Honite species that was described in Section 5.2.5: an underestimate of T would produce a corresponding overestimate of α_w (since $\partial\alpha_w/\partial T$ is negative) and K_h, as was observed.

The effect of an uncertainty in the temperature on the acoustic coefficient ξ_h is much less significant for the Guyblast species, since ξ_h, and therefore the attenuation due to particles at any nominal concentration, is at least an order of magnitude higher. Correspondingly, the limiting concentration below which the uncertainty in the attenuation due to water becomes significant is at least an order of magnitude lower, and the effect is therefore not restrictive.

To summarise, it was found that the uncertainties in the temperature could significantly affect the total attenuation at lower volume fractions with smaller particles (*i.e.* the Honite species) but not larger particles (*i.e.* Guyblast). These observations demonstrate that the temperature must be controlled, or at least recorded, quite accurately: it is suggested that in future experiments the temperature be measured *in every run* to an accuracy of $\mathrm{d}T = \pm 1$ °C or better, and that the exact temperature be accounted for explicitly at the data processing stage. In the results presented in this study, a nominal temperature of $T = 20$ °C was assumed throughout.

A.8 Discussion

An analysis of the uncertainties in four measured experimental quantities – beam

divergence angle, probe mounting angle, pressure and temperature – was performed and applied to one example run with particles of intermediate size (Honite 16) under specific flow conditions (ϕ = 1%, Q = 1.72 l s^{-1}, U_{ave} = 1.21 m s^{-1}), and the influence of these uncertainties on the nominal distance from the probe, the calculated mean axial velocity and the attenuation of sound in water was assessed. Although results are only presented for one example run, this run was chosen as being intermediate and representative. The analysis that was presented in this section, then, can be applied to all the runs described in this study. Although the magnitude of errors is likely to vary slightly between runs, the trends presented in this appendix apply for all runs.

Of all the experimental variables that were chosen, the uncertainty in the pressure was found to produce an insignificant error in y and $\overline{U}$. Acoustic beam divergence and the uncertainty in temperature were found to produce errors of very similar magnitudes of the order of a few percent in the distance from the probe (and wall-normal distance) and mean axial flow velocity. However, the uncertainty in the probe mounting angle was found to produce the largest error in both wall-normal distance and mean axial velocity. It was also found that uncertainties in the temperature is likely to signficantly influence the total acoustic attenuation in suspensions of smaller particles at lower concentrations.

The main conclusions are that: (a) temperature should be measured and accounted for as accurately as possible in every run, since it influences all the calculated variables considered here, but particularly the inferred acoustic coefficients of the particle species; and (b) the mounting angle should be known precisely as it is responsible for the largest errors in y and $\overline{U}$, and so machining of the probe mounting apparatus should be done as finely as possible, to within half a degree or less, if possible.